Measurement of blood analytes in turbid biological tissue using near-infrared Raman spectroscopy

by

Tae-Woong Koo

S.M., Mechanical Engineering
Massachusetts Institute of Technology
(1998)

B.S., Mechanical Design and Production Engineering
Seoul National University
(1996)

Submitted to the Department of Mechanical Engineering
in partial fulfillment of the requirements for the degree of

Doctor of Philosophy in Mechanical Engineering

at the

Massachusetts Institute of Technology

August, 2001
[September 2001]

Author .....
Department of Mechanical Engineering
August 10, 2001

Certified by .....
Michael S. Feld
Professor of Physics, Thesis Supervisor

Certified by .....
Peter T. C. So
Associate Professor of Mechanical Engineering, Thesis Reader

Accepted by .....
Ain A. Sonin
Chairman, Department Committee on Graduate Students

Measurement of blood analytes in turbid biological tissue using near-infrared Raman spectroscopy

by

Tae-Woong Koo

Submitted to the Department of Mechanical Engineering on August 10, 2001
in partial fulfillment of the requirements for the degree of
Doctor of Philosophy in Mechanical Engineering

ABSTRACT

Concentrations of blood constituents provide diagnostic information in clinical procedures. Among the medical community, there is great interest in developing an optical method of concentration measurements that eliminates reagents required in the current clinical chemistry techniques and is non-invasive.

This thesis describes the methodology to develop a measurement technique of blood component concentrations using Raman spectroscopy. The sources of prediction error were identified. A Monte Carlo simulation model was developed to study the distribution of the Raman signal from turbid biological samples. A high sensitivity system for Raman spectroscopy of blood analytes was designed by optimizing the optical components. The new system had higher collection efficiency than the previous state-of-the-art system. Experiments were performed using the new system in order to collect Raman spectra of human whole blood. The collected Raman spectra were analyzed with multivariate calibration techniques, and compared with hospital measurements.

The analysis of the spectra of whole blood samples demonstrate that many chemical components in *ex vivo* whole blood samples can be measured accurately with near-infrared Raman spectroscopy. A preliminary analysis based on the results of this thesis indicates that it is feasible to measure blood analytes non-invasively.

Thesis Supervisor: Michael S. Feld
Title: Professor of Physics

Acknowledgments

Many people contributed to my growth as a scientist and engineering during my time in graduate school. First, I would like to thank my advisor, Michael S. Feld, for providing guidance, questioning details and providing larger vision. Both he and Ramachandra Dasari have helped me learn science and research. I would like to thank them for support and friendship.

Andrew Berger introduced me to this project. His research provided the base where I could add my own contribution. Irving Itzkan served as an optics guru, and I enjoyed learning optics and sailing from him.

Gary Horowitz at Beth Israel Deaconess Medical Center played a crucial role in this research. He provided not only whole blood samples and reference measurements, but also his vast knowledge of clinical pathology and enthusiasm for our research.

A team of people helped me advance this research. Martin Hunter helped me design the instrument. Annika M. K. Enejder improved and validated the Monte Carlo simulation code. Slobodan Sasic and Jason T. Motz investigated the laser dosimetry. Karen Shafer's chemical model was used to analyze tissue spectra. Jeankun Oh worked with me in every aspect of this research as he will advance this research further into transcutaneous measurements. It was my pleasure to work with them.

I thank mechanical engineering department for allowing me to work on this interesting project outside the conventional scope of mechanical engineering. I especially thank Peter So, C. Forbes Dewey, George Barbastathis, Kamal Youcef-Toumi, and Haruhiko Asada for providing valuable feedback.

I learned a lot from discussions with Gordon Thomas, Eugene B. Hanlon, Geurt Deinum, Ramasamy Manoharan, and Joe Gardecki. I would like to thank the members of Spectroscopy Laboratory for their friendship and help over the years, and I learned much from all of you. I especially thank Andrew, Karen, Jason, Abi, and Jeankun for providing immense moral support and keeping 6-018 a great place to work.

I would like to thank NIH NCRR (grant P41 RR022594-15) and Bayer Diagnostics Corporation for funding this research.

Finally, I want to thank my parents and my wife for their love and support. Without them, the past years could have been more challenging.

Contents

List of Figures

List of Tables

Chapter 1

Introduction

This thesis describes development of an optical method of measuring concentration levels of important blood constituents ("analytes") in whole blood using Raman spectroscopy. Every chemical has its own unique Raman spectrum that can be used to distinguish different chemicals. The intensity of the Raman signal bears a linear relationship to the chemical concentration, and therefore, Raman spectroscopy can be used as a tool in concentration measurements, as well. Since Raman spectroscopy is an optical technique, it can collect signals without damaging samples. The ultimate application of this technique will be noninvasive and continuous monitoring of clinically important substances *in vivo*. Non-invasive measurements of this kind will be valuable in a wide variety of clinical settings. The goals of this thesis are measurements of analytes in biological fluids, development of a methodology for using spectroscopy techniques for extracting analyte concentration information in the presence of turbidity, and better understanding of the detection limits of spectroscopy techniques. This thesis will also serve as a resource for other researchers who are interested in concentration measurements using optical techniques.

1.1 Objectives

Turbidity effect study

When this thesis research began, it had been demonstrated that chemicals in human serum can be measured using Raman spectroscopy with clinical accuracy. However, measurements in whole blood were not as accurate, and thus, the differences between serum and whole blood had to be investigated. The major difference between serum and whole blood is the presence of blood cells. The blood cells scatter and absorb light, and the effect of such optical events on Raman scattering was studied. We needed a tool to study scattering and absorption in whole blood. It was essential to validate the whole blood model.

Multivariate analysis of Raman spectra

Multivariate techniques were used to analyze Raman spectral data and extract concentrations. We wanted to confirm that Raman spectra of serum and whole blood are linear superpositions of component spectra, which allowed the use of linear spectral analysis techniques. To investigate the spectral differences between serum and whole blood, we wanted to find out whether the same chemical has the identical Raman spectrum in serum and whole blood. Component spectra extracted from serum and whole blood by a multivariate technique were compared. Moreover, we wanted to have a better understanding of prediction errors. An analytical equation derived for error in multivariate analysis will indicate what factors are important in improving the prediction accuracy.

Optical system development

In order to collect high signal-to-noise ratio Raman spectra rapidly, a spectroscopy system with high throughput was required. The throughput of the system was optimized by numerical simulations. Based on the distribution of the Raman signal in whole blood, a collection geometry that allows for the maximum collection efficiency was designed. Optical design software was used to select the optimal combination of optical components.

Measurements in whole blood

The principal objective of this research was to demonstrate that chemical concentrations could be measured at physiological concentrations in whole blood. We performed experiments on whole blood. The presence of scattering and absorbing particles, the interference of multiple components, and the shot noise of the background were the challenges in these measurements.

Preliminary estimation of prospects for transcutaneous measurements

We wanted to estimate the prospects for transcutaneous measurements of blood analytes using near-infrared Raman spectroscopy. Raman spectra of various body parts were collected and analyzed. With the analytical equation derived for error in multivariate analysis, prediction accuracy in transcutaneous measurements was calculated.

1.2 Accomplishments

The results of the experiments described in the following chapters show that Raman spectroscopy can be used to measure chemical concentrations with clinical accuracy from a Raman spectrum of human whole blood. Our technique measured concentrations of eight analytes: glucose, urea, cholesterol, triglyceride, albumin, total protein, hemoglobin, and hematocrit, using a calibration data base of spectra from 31 human subjects.

In addition to demonstrating the ability to use Raman spectroscopy to measure chemical concentrations, we have also developed important tools. First, we developed a Monte Carlo simulation code that models light propagation and Raman scattering in turbid samples. The code provides the distribution of Raman signals on the surface and inside the medium. The code was designed with the capability of modeling various geometries. It can be easily modified to add additional constraints or calculate new quantities of interest, and it provided a clear picture of light propagation in whole blood.

Also, the methodology of designing a spectroscopy system by optimizing the throughput was developed. Experimental measurements, statistical simulations, and optical principles and optical design software were used to design an optimal throughput system in a step-by-step procedure. The methodology developed in this research can be applied to the design of other optical components and systems.

Finally, we derived an analytical equation that estimates the error of multivariate techniques in concentration measurements. The equation identified noise as the limiting source of error, guiding the direction of research.

This equation was also used to estimate the prediction error in transcutaneous measurements. Raman spectra of various body parts were collected and analyzed. The preliminary calculation indicates that it is feasible to measure blood analytes transcutaneously.

1.3 Outline

The work that has been performed is presented in the following sequence:

Chapter 2: Background

This chapter provides background information about both clinical chemistry and Raman spectroscopy. A review of literature on optical measurement techniques is included, and Raman spectroscopy and other non-invasive techniques are compared. Techniques that are described are mid-infrared and near-infrared absorption spectroscopy, Raman spectroscopy, other optical techniques, and minimally invasive techniques. Previous accomplishments in this project are also summarized. Previous accomplishments include development of a sensitive instrument for serum analysis, measurements of chemical concentrations in serum and preliminary measurements in whole blood.

Chapter 3: Understanding turbidity using Monte Carlo simulations

The need for understanding turbidity is explained. The development and validation of the Monte Carlo simulation for Raman scattering is presented. Then, experiments were performed to measure the surface distribution of the Raman signal in whole blood. The

measurements and simulation results were compared, and they matched well. To show the effect of turbidity on signal intensity, simulation results for various turbidity samples are presented.

Chapter 4: Raman spectra of biological samples and multivariate analysis

Fundamentals of multivariate analysis and their applications are described. The whole blood spectra are analyzed with multivariate techniques. The Raman spectra of chemicals in serum and whole blood are compared. An analytical equation for estimating prediction error was derived.

Chapter 5: Design of a high-sensitivity system for Raman spectroscopy

The need for a high-sensitivity spectroscopy system is presented. Basic principles of radiometry are explained. How an optimal design can be obtained using simulations, measurements, optical design software, and optical principles is discussed. The performance of the new system is also presented in terms of the increased sensitivity and the reduced noise.

Chapter 6: Experiments to measure analytes in whole blood using the high-sensitivity system for Raman spectroscopy

This chapter reports measurements of multiple components in whole blood. These studies comprise the core experimental work in this thesis. Preliminary experiments were performed using samples prepared in the laboratory with whole blood from a single subject.

A large study was performed using blood samples from 31 subjects at the Beth Israel Deaconess Medical Center (BIDMC). The results of the experiment demonstrate that analytes can be measured with clinical accuracy in whole blood.

Chapter 7: Toward transcutaneous measurements

A non-invasive measurement of analytes in blood-tissue matrix is presented as the future direction. Challenges in non-invasive measurements are discussed. Results from a preliminary measurement of skin are presented. The analysis indicates that it is feasible to measure blood analytes non-invasively.

Chapter 8: Conclusion

The accomplishments in this thesis research are summarized, and final statements are made.

Chapter 2

Background

2.1 Overview

Blood analyte concentrations provide important clinical information in diagnostic procedures. There is a great benefit in developing an optical method, which does not require reagents for analysis and is non-invasive, of measuring clinically important substances, as current clinical chemistry methods require blood withdrawal for determining analyte concentrations.

This chapter explains basic concepts and terms in clinical chemistry, discusses some analytes of interest and clinical chemistry techniques to determine their concentrations. In addition, efforts made to develop non-invasive optical measurement techniques are reviewed. Raman spectroscopy, a common tool in analytical chemistry, is found to have advantages over other optical techniques. Prior accomplishments achieved using Raman spectroscopy are also summarized.

2.2 Clinical chemistry of blood analytes

Clinical chemistry is the field of chemistry related to medical science, and it provides chemical information needed in medical diagnosis. Clinical chemistry analysis is performed in many body fluids. Blood is the most frequently used medium. It has many

components whose concentration levels provide essential clinical information. Among them, this thesis research measured glucose, hematocrit, cholesterol, urea, albumin, total protein, hemoglobin, and triglycerides. The following subsections review the significance of these analytes, describe current measurement techniques, and discuss advantages offered by an optical measurement.

2.2.1 Specimens for clinical chemistry

This thesis research mainly used whole blood as the specimen, as many analytes in whole blood (and its derivatives, plasma or serum) are frequently measured in diagnostic procedures. However, other body fluids are also available and used as specimens in clinical chemistry. This subsection discusses various specimens, their advantages and limits in clinical chemistry.

Blood is the body fluid that is most frequently used for analytical purposes. Blood is obtained by venipuncture (puncture of a vein), arterial puncture, and skin puncture. In addition, indwelling catheters provide continuous access to venous blood. It is important to use the same technique to obtain blood samples in order to compare concentrations in the blood samples. Oxygen concentrations, pH, carbon dioxide concentration, hematocrit are different in venous blood and arterial blood. Also, concentrations of glucose, lactic acid, chloride, and ammonia may vary [Henry and Kurec 1996].

Obtained blood samples can be processed further, depending on the type of tests required. Many analytes are determined in serum. Serum is obtained by allowing blood to clot and centrifuging the clotted blood to remove fibrinogen as well as other blood cells

[Miller 1996]. Plasma is the fluid component of blood. It is similar to serum, and many chemicals are also determined in plasma. Plasma is obtained by centrifuging whole blood to remove blood cells [Boral and Henry 1996]. Whole blood, with the addition of an anticoagulant, is used for hematology studies, such as complete blood count and platelet count. An anticoagulant, such as heparin, ethylenediaminetetraacetic acid (EDTA), sodium fluoride oxalate, or sodium citrate, prevent coagulation. It may interfere with concentration determinations, and therefore, extra care is needed in selecting anticoagulants.

Concentrations of analytes may vary in serum, plasma, and whole blood. Certain analytes, such as glucose and urea, can be determined in both serum and plasma, and concentrations in serum and plasma are similar. Concentrations of analytes can be lower in whole blood due to the volume displaced by the solid content of blood cells. For example, concentrations of glucose in whole blood are about 12 ~ 16% lower than concentrations in serum or plasma [Fogh-Andersen et al. 2000]. Hematological analytes, such as hemoglobin or hematocrit, can be only determined in whole blood due to the absence of red blood cells or hemoglobin in serum and plasma.

Urine is another biological fluid frequently used in medical diagnosis. Generally, urine is obtained without pain or danger. Analysis of urine provides diagnostic information regarding kidney and urinary tract functions [Henry et al. 1996]. Cerebrospinal fluid (CSF) is collected from spinal cord, and analysis of CSF may provide diagnostic information of infection, hemorrhage, and multiple sclerosis. However, collection of CSF is painful and may cause serious complications, such as paralysis, infection, and asphyxiation. CSF

analysis is performed only when it is necessary, because of the chance of complications [Henry and Kurec 1996].

Other biological fluids include sweat and interstitial fluid. Sweat is analyzed for determination of electrolytes, but it is not suitable for other analytes as they are not present in sweat. Interstitial fluid is present in the space between cells. It contains many blood analytes (such as proteins, glucose, lactate), as it allows analytes to pass between capillaries and cells. Determination of analytes in interstitial fluid could provide bloodless measurements of blood analytes. However, invasive measurements in interstitial fluid are challenging due to the lack of reliable sample extraction methods and the small volume of interstitial fluid samples. A non-invasive measurement in interstitial fluid might be a solution for the sample extraction issue.

The conventional methods most widely used to obtain concentration information rely on removing samples of blood from patients and then subjecting these samples to many chemical techniques. Many clinical chemistry techniques are performed in four steps: withdrawing blood from patients, centrifuging blood to obtain serum or plasma, adding specific reagents for chemicals whose concentrations are of interest, and measuring concentrations using optical techniques. Although these methods can be used to detect a wide variety of substances and have evolved to the point where they can be done relatively quickly and accurately on small quantities of blood, they usually require transport to a laboratory and multiple processes before analysis can be initiated. Thus, from a practical perspective, clinicians frequently have to wait hours to get results. Thus, if one could

measure blood analytes non-invasively, it would be that much more convenient for everyone involved.

Furthermore, the body of clinical knowledge about analytes focuses upon monitoring their concentrations in biological fluids (mainly blood or its derivatives), rather than in the blood-tissue matrix. This is because the regular withdrawal of certain biological fluids is relatively harmless, whereas the repeated removal of tissue samples for chemical analysis is clearly unfeasible. For this reason, the clinical value of monitoring tissue analyte concentrations has not been assessed. An optical technique, which probes tissue directly, offers the opportunity to perform such measurements. Accurate monitoring of tissue analyte concentrations would provide clinicians with new and potentially powerful diagnostic information. These concentrations would be useful not only in monitoring overall health, but also in studying the viability of particular tissue regions, such as would be necessary in choosing the proper site for an amputation.

2.2.2 Clinically important blood analytes

Blood has many components whose concentration levels provide essential clinical information. These include blood gases, glucose, hematocrit, cholesterol, urea, albumin, total protein, and many others that were not measured in this thesis research. The following paragraphs review the significance of these quantities, describe current measurement

Glucose and insulin

Glucose is the carbohydrate essential to all body cells as an energy source (Figure 2.1). It is introduced into the body by direct ingestion of glucose or ingestion of other

carbohydrates. Large carbohydrate molecules are broken into smaller molecules, one of which is glucose [Stryer 1995]. Its concentration is precisely regulated by a variety of hormones, the most important of which is insulin. When glucose levels in the blood stream rise, insulin is secreted by the pancreas, which enables the glucose to move into cells. In the absence, or lack, of insulin, the glucose cannot move into the cells and levels rise in the bloodstream, and the cells begin to catabolize (break down) fat [Benett 1994]. Ketones are products of fat metabolism, and many ketones are toxic. Accumulation of glucose and ketones in the body can lead to a life-threatening syndrome called diabetic ketoacidosis, the symptoms of which include frequent thirst, nausea, vomiting, excessive urination, tiredness, and, eventually, diabetic coma. The therapy for diabetic ketoacidosis is administration of insulin. However, the amount of insulin must be carefully titrated to the glucose concentration, and a variety of other factors come into play as well [Govoni and Hayes 1985, Scipien and Barnard 1983]. Thus, the American Diabetes Association recommends that glucose levels be measured frequently and accurately in all patients taking insulin.

The glucose concentration in a normal human subject typically ranges from 45 to 180 mg/dL (2.5 to 10.0 mM) in plasma [Threatte and Henry 1996]. Glucose concentration is affected by the age and gender of the subject and the delay between a meal and the measurement. Glucose concentrations higher than the normal range are classified as hyperglycemia and glucose concentrations lower than the normal range are classified as hypoglycemia. Extreme concentrations as high as 1000 mg/dL (56 mM) have been observed. Glucose concentrations can be measured with many techniques, one of which is spectrophotometry (Section 2.2.4).

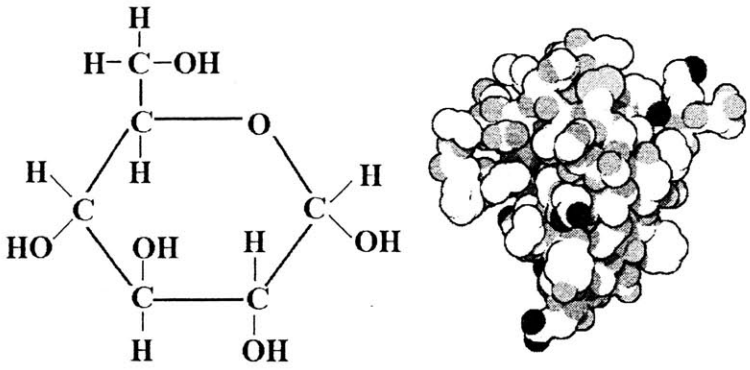

Figure 2.1. Structure of glucose (left) (© Mountcollyer Technology Center) and insulin (right) (© D. S. Goodsell, Research Collaboratory for Structural Bioinformatics)

The insulin concentration is associated with the glucose concentration in normal subjects, and it ranges between 79 and 1722 pM (11 to 240 μU/ml). Determinations of insulin concentrations in addition to glucose concentrations may provide better control of glucose concentrations. However, insulin concentrations are not measured often, probably due to the high cost of insulin measurements and difficulties in data interpretation [Threatte and Henry 1996]. Radioimmunoassay is the method commonly used to measure insulin concentrations, but this, in general, cannot differentiate low insulin levels from normal levels. An affordable and accurate technique to determine insulin concentration could become an important tool in diabetes management.

Hemoglobin and hematocrit

Hemoglobin is the major component of red blood cells, and its main function is to transport oxygen and carbon dioxide. In the pulmonary capillaries, more than 98% of the hemoglobin is combined with oxygen. When red blood cells are transported near tissues, the oxygen is dissociated from hemoglobin. The normal hemoglobin concentration is 14.0

~ 17.5 g/dL in males and 12.3 ~ 15.3 g/dL in females [Morris and Davey 1996]. In extreme cases, concentrations ranging from 4 to 20 g/dL can be observed.

Another important factor in one's capacity to carry oxygen for body needs is hematocrit. Technically, the hematocrit is the volume proportion of whole blood represented by red blood cells. That is, if one centrifuges whole blood from a normal individual, it will separate into two major components, plasma and red blood cells, and a very small third component, which consists of other cellular components, such as white blood cells and platelets. The normal hematocrit in adults is 41.5 ~ 50.4% in males and 35.9 ~ 44.6% in females [Morris and Davey 1996]. Extreme levels of hematocrit ranging from 5% to 70% are sometimes found.

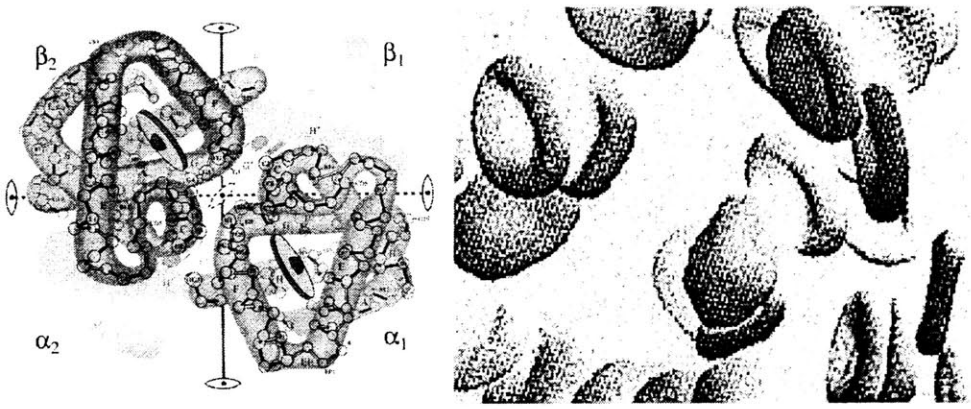

Figure 2.2. Structure of hemoglobin (left) (© A. M. Jarosz, Michigan State University) and the image of red blood cells (© S. Berg, Winona State University)

A wide variety of patients have hemoglobin and hematocrit determinations. It is used to check for anemia in patients who complain of fatigue, and in newborns to check for nutritional deficiencies. More relevant to our technique is its use in monitoring patients who are bleeding in emergency or operation and its use in following the adequacy of transfusion to correct deficiencies [Treseler 1995].

Although one can measure the hematocrit by centrifugation, it is most frequently done in modern laboratories in an indirect but much more sophisticated way. Using a very small amount of blood, modern Complete Blood Count (CBC) analyzers monitor individual cells passing through an aperture. The instrument can count the number of cells per unit volume as well as estimate the size of each cell. By multiplying the number of cells per unit volume by their average size, the instrument calculates the hematocrit [Morris and Davey 1996].

Cholesterol, triglycerides, and lipoproteins

Coronary artery disease is the leading cause of death in this country [Murray and Lopez 1996], and the most important risk factors are cholesterol and triglycerides [Harvey et al. 1988]. The American Heart Association recommends that all adults get their cholesterol levels measured regularly, and treated if appropriate.

Roughly 50% of the American population have cholesterol levels that are considered abnormal (i.e., fasting levels greater than 200 mg/dL). While some people may respond to diet and exercise regimens, many patients will be treated with a variety of drugs, most commonly, inhibitors of the enzyme governing the rate-limiting step in cholesterol synthesis [Sodeman and Sodeman 1982, Howard and Herbold 1982]. In either case, periodic monitoring of such patients' cholesterol levels is required. There are near-patient testing devices for measuring these parameters, but, again, these require withdrawing a sample of blood from the patient.

Although cholesterol and triglycerides are related to cardiovascular disease, they are important molecules in human body. Both cholesterol and triglycerides are introduced into

the body through food ingestion and biosynthesis in the liver and intestines. Cholesterol and triglyceride concentrations can be measured with many techniques, one of which is spectrophotometry (Section 2.2.4).

Cholesterol (Figure 2.3) is a part of cell membranes, and also a precursor for the synthesis of steroid hormones and bile acids [Stryer 1995]. Typical total cholesterol concentrations (without fasting) are between 150 and 250 mg/dL (3.88 to 6.47 mM) are considered normal. A fasting cholesterol concentration higher than 200 mg/dL (5.18 mM) may indicate higher risk of cardiovascular disease [Bachorik et al. 1996]. A high level of cholesterol may contribute to cardiovascular disease. A low level of cholesterol may not be sufficient to promote growth in children. Extreme concentrations in the range between 50 mg/dL and 800 mg/dL are observed.

Triglycerides (Figure 2.3) are the storage form of energy, and also the largest proportion of fat in blood and adipose tissue (connective tissue for fat storage) [NIH Medline]. A typical concentration of triglycerides ranges from 10 to 190 mg/dL (0.11 to 2.15 mM). A greater than normal level of triglycerides may indicate cirrhosis, hypothyroidism, high carbohydrate diet, poorly controlled diabetes, and pancreatitis. A lower than normal level of triglycerides may indicate hyperthyroidism, malnutrition, and low fat diet [Treseler 1995]. Extreme levels of triglycerides as high as 10,000 mg/dL are infrequently found.

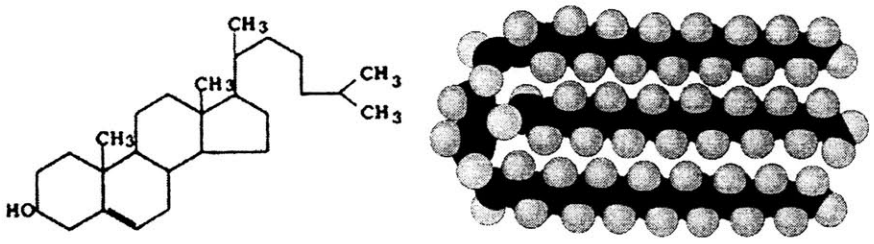

Figure 2.3. Structure of a cholesterol molecule (left) (© 2000 McGraw-Hill) and a triglyceride molecule (© 2000 Houghton Mifflin College) [Zumdahl and Zumdahl 2000]

Cholesterol and triglycerides are transported in body by lipoproteins. Lipoproteins consist of proteins (called apolipoproteins), cholesterol, cholesterol esters, triglyceride, and phospholipids (Figure 2.4). Four major lipoprotein classes are called chylomicrons, very low density lipoproteins, low density lipoproteins (LDL), and high density lipoproteins (HDL) [Bachorik et al. 1996]. The main function of HDL appears to carry excess cholesterol to the liver for processing or excretion, while the main function of LDL appears to carry cholesterol to various tissues. In general, cholesterol contents of lipoproteins are reported rather than the actual concentration of lipoproteins. A typical concentration of HDL cholesterol ranges from 29 to 62 mg/dL in males and from 34 to 82 mg/dL in females. A typical concentration of LDL cholesterol is between 60 and 180 mg/dL [NIH Medline]. Decreased levels of HDL cholesterol and elevated levels of LDL cholesterol may indicate the increased risk of cardiovascular disease.

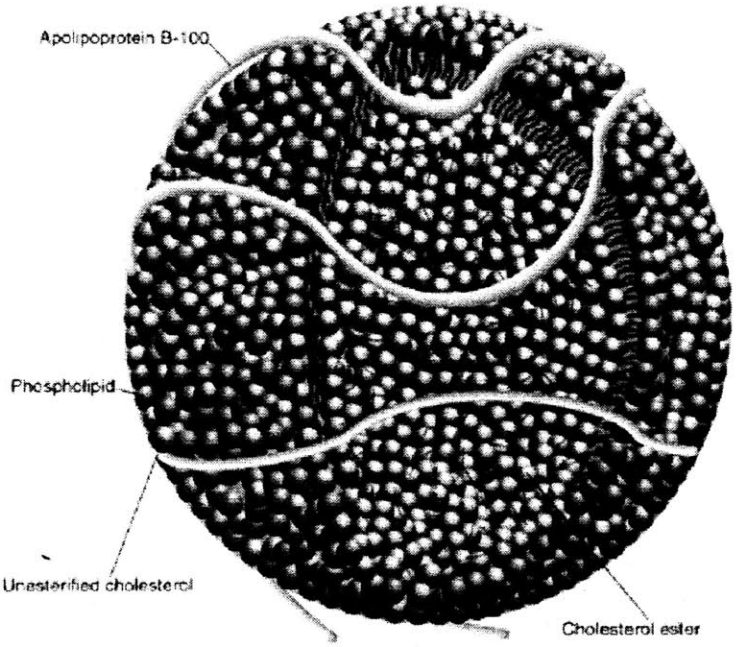

Figure 2.4. Structure of low density lipoprotein (© 1999 John Wiley and Sons)

Urea

Urea is synthesized in the liver during the deamination of protein (removal of nitrogen from amino acids). Determination of plasma urea is used most frequently as a kidney function test [Woo and Henry 1996]. This is because urea does not circulate for long in the bloodstream but rather is filtered through the kidneys and excreted in the urine. With deterioration of kidney function, the rate and effectiveness of filtration falls and the urea concentration increases. Physicians use urea concentration to screen for renal problems and to monitor their progression [Treseler 1995].

Urea concentrations can be measured with many techniques, one of which is spectrophotometry (Section 2.2.4). Historically, the nitrogen content of urea has been reported instead of the actual urea concentration. Due to this reason, urea concentrations in

blood are reported in concentrations of "blood urea nitrogen" (BUN). To convert a blood urea nitrogen concentration to a urea concentration, the conversion factor 2.14 is multiplied. A typical concentration of urea nitrogen is 8 ~ 23 mg/dL (2.9 ~ 8.2 mM) in plasma and 60 ~ 90 mg/dL (21.4 ~ 32.1 mM) in urine. Extreme levels in the range of 0 ~ 150 mg/dL in plasma are rarely observed. Low levels of urea in urine may indicate malnutrition and kidney dysfunction, whereas high levels may indicate excessive protein intake [NIH Medline].

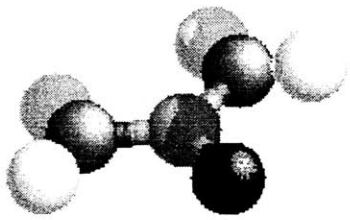

Figure 2.5. Structure of urea (© S. Fairall, DeMontfort University)

Bilirubin

Bilirubin is the major metabolic product of hemoglobin [NIH Medline]. Hemoglobin is broken into heme and globin. Heme is converted to bilirubin, and albumin in blood transports bilirubin to the liver. The liver conjugates most of bilirubin, and conjugated bilirubin is stored in the gall bladder or transferred to intestines where the conjugated bilirubin is metabolized and excreted. Determination of bilirubin is performed to test liver or gall bladder dysfunction.

Bilirubin is measured by a spectrophotometry technique called the van den Bergh method (section 2.2.4) [Pincus 1996a]. A typical concentration of conjugated (direct)

bilirubin in serum is between 0 to 0.3 mg/dL (0 ~ 5 μM), and a concentration of total bilirubin (conjugated and unconjugated) ranges from 0.1 to 1.2 mg/dL (2 ~ 17 μM). Increased unconjugated or total bilirubin may indicate hemolytic (hemoglobin breakdown) diseases and hematoma (formation of blood clot due to a broken blood vessel). Increased direct bilirubin may indicate bile duct obstruction, hepatitis, and cirrhosis [NIH Medline].

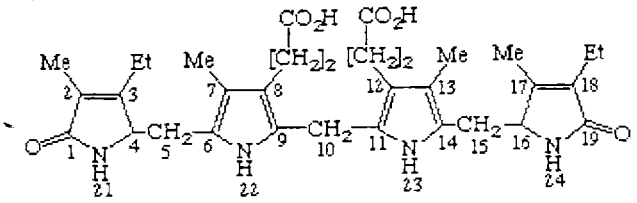

Figure 2.6. Structure of bilirubin (© G. P. Moss, Queen Mary, University of London)

Total protein, albumin, and globulin

Total protein is a measure of serum protein, and its concentration reflects liver state, kidney state, nutritional state, and many other conditions. [Treseler 1995, McCance and Huether 1990, Sabiston 1981]. Many serum proteins can be measured individually, but frequently physicians want to know the total protein concentration first.

Albumin is the principal protein (roughly 55%) found in plasma. It is synthesized in the liver, and its concentration falls in liver disease or with poor nutrition. Albumin carries many small molecules, and plays an important role in maintaining the oncotic pressure of the blood [McPherson 1996].

The difference between the total protein and albumin is sometimes called "globulin", because the majority of the remaining protein is comprised of

immunoglobulins. Immunoglobulins serve as antibodies in immune systems and target antigens that stimulate immune systems.

Protein concentrations can be measured with many techniques, one of which is spectrophotometry (Section 2.2.4). A typical concentration in serum is 6.0 ~ 8.3 g/dL for total protein, 3.2 ~ 4.5 g/dL for albumin, and 2.3 ~ 3.5 g/dL for globulin. Extreme levels are 3 ~ 12 g/dL for total protein and 1 ~ 5 g/dL for albumin. A greater than normal level of total protein may indicate chronic inflammation or infection and multiple myeloma (a cancer of bone marrow), while a lower than normal level may indicate extensive burns, hemorrhage, liver disease, malnutrition, malabsorption, and glomerulonephritis (a type of kidney disease) [NIH Medline]. A lower than normal level of albumin may indicate burns, malnutrition, kidney diseases, and liver diseases, such as hepatitis, cirrhosis, and hepatocellular necrosis (liver cell death). If the globulin concentration is abnormally high, physicians may suspect active inflammation or even a malignant proliferation of immunoglobulin-producing cells [McPherson 1996].

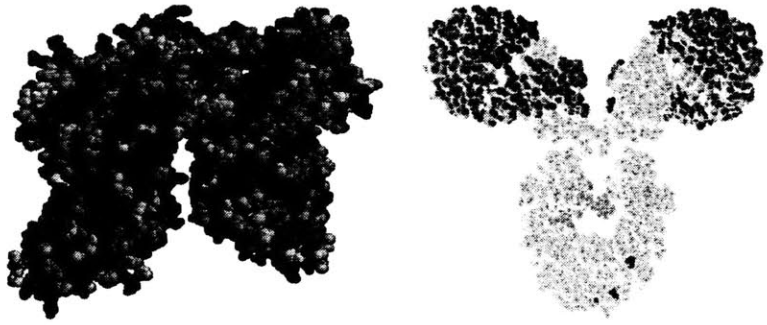

Figure 2.7. Structure of albumin (left) (© University of Aarhus) and IgG1, a type of immunoglobulin (right) (© M. Clark, University of Cambridge)

Blood gases: pH, partial pressures of oxygen and carbon dioxide

Oxygen plays important roles in many physiological processes, including aerobic generation of adenosine triphosphate (ATP) in muscles. Carbon dioxide is the product of many aerobic processes. The respiratory system delivers oxygen to and removes carbon dioxide from the blood through the gas exchange process in lungs. The interaction between the lung and the kidney regulates the acid-base balance in body.

Partial pressures of blood gases are often determined by measuring volume, pressure (in the manometer), or color of reagents, or by using electrodes [Pincus et al 1996]. A typical partial pressure of oxygen is 75 to 100 mm Hg (10 ~ 13 kPa), a typical partial pressure of carbon dioxide is 35 to 45 mm Hg (4.7 ~ 6.0 kPa), and a typical pH is 7.35 to 7.45. The partial pressures of oxygen and carbon dioxide also vary in different body locations. The oxygen pressure is higher in artery than in vein, and the carbon dioxide pressure is higher in vein than in artery. Abnormal levels of blood gases may indicate diseases in respiratory system, renal system, metabolic system, or trauma. A lower than normal pressure of oxygen may lead to fatigue, dizziness, weakness, irritability, and even heart failure in extreme cases.

2.2.3 Units in clinical chemistry

In this subsection, we would like to clarify the units used in clinical chemistry. Along the advances in clinical chemistry, many conventional units were adopted or developed. These conventional units are different from international standard (SI) units. For many analytes, many units, such as mass-density (e.g. mg/dL), molar units (e.g. mole/L, or M), and other

units (e.g. IU/L[1]), have been used. Simple conversion factors can be often used to convert one unit to the other. For example, the molar concentration of 18 mg/dL glucose is 1 mM. Although efforts are being made to adopt SI units, many physicians are still more familiar with conventional units. Due to this reason, both conventional units and SI units are presented in this thesis. When either one is presented, Table 2.1 can be used to calculate concentrations in the other unit.

Table 2.1. Conversion of analyte concentrations from conventional units to international standard (SI) units

Analyte	Conventional Unit	SI Unit
glucose	18 mg/dL	1 mM
insulin	1 μIU/mL	7.175 pM
hemoglobin	1 g/dL	10 g/dL
hematocrit	1%	0.01
total cholesterol	38.67 mg/dL	1 mM
triglycerides	88.57 mg/dL[+]	1 mM
urea nitrogen	2.8 mg/dL	1 mM
bilirubin	1 mg/dL	17.1 μM
proteins	1 g/dL	10 g/dL
gas pressure	7.5 mm Hg	1 kPa

[+] The conventional conversion factor is for triolein, a type of triglyceride.

[1] International Unit (IU) is the unit of analytes for which functional activity is measured instead of the molarity (e.g. enzymatic activity). 1 IU is the quantity of enzyme that will catalize the reaction of one micromole of substrate per minute [Pincus 1996].

2.2.4 Clinical chemistry techniques

Many analytes discussed above can be measured using absorbance spectrophotometry. The blood sample is centrifuged to separate the liquid phase (plasma) from the cellular components (blood cells and platelets). The plasma is then treated with reagents (Table 2.2) that cause a change in absorbance at a specific wavelength proportional to the analyte concentration in the sample [Nguyen et al. 1996]. By measuring absorbance using a spectrophotometer, the analyte concentration can be determined.

Table 2.2. Reagents for absorbance spectrophotometry of some important blood analytes

Target Chemical	*Reagents*
Glucose	hexokinase, glucose-6-phosphate dehydrogenase, NADP
Cholesterol	cholesterol esterase, cholesterol oxidase, phenol, peroxidase
Triglyceride	lipase, glycerol kinase, glycerol phosphate oxidase, peroxidase
Urea	urease, ketoglutarate, glutamate dehydrogenase, NADH
Bilirubin	van den Bergh reagent (diazotized sulfanilic acid)
Albumin	bromcresol green
Total Protein	biuret reagent (copper ion at alkaline pH)

2.2.5 Accuracy, precision, and prediction error

There are multiple methods for quantifying the levels of analytes in body fluids, and levels measured by two methods are often compared to determine how reliable and reproducible the measurements are.

In clinical chemistry, accuracy refers to the reliability of the method in determining the actual or true value of the level of the analyte [Pincus 1996]. If there is a method that serves as a standard for determining the actual concentration, the levels determined by a second method can be compared with the levels determined by the standard. The correlation coefficient (also called Pearson product moment correlation [Sharma 1996]) is often used to quantify the accuracy of the other method. Although the tolerable limits of correlation are somewhat arbitrary, "correlation coefficients of over 0.9 are usually deemed acceptable, and indicate that new method agrees satisfactorily with the reference method." [Pincus 1996] This requirement of the correlation coefficient higher than 0.9 was used as a test of accuracy.

In this thesis, we also use prediction error and prediction accuracy to quantify the reliability of measurement techniques. The prediction error is calculated by comparing the concentrations of an analyte in multiple samples determined by a reference technique (the standard technique) and a new technique. The differences in analyte concentrations in multiple samples can be calculated, and the standard deviation of the differences is called the root mean standard error of prediction (RMSEP), or prediction error[2] in this thesis. For a single sample, the prediction error is simply the difference in concentrations of an analyte determined by the two techniques. The prediction accuracy is closely associated with the prediction error. For multiple samples, the prediction accuracy is the average concentration divided by the prediction error. For each sample, the prediction accuracy is the reference concentration divided by the prediction error.

[2] The prediction error is discussed in detail in Chapter 4. Eq. (4.6) is the formula of prediction error.

Precision refers to the reproducibility of the method. The reproducibility is often expressed in the coefficient of variation, or CV. The coefficient of variation can be calculated in the following way. The level of an analyte in the same sample is determined several times over a period. The standard deviation of the measurements is calculated, and the standard deviation divided by the average of the measurements is the coefficient of variation.

Method sensitivity refers to the lowest level of an analyte that can be detected by a given method with a certain precision. The concentration ranges of analytes are summarized in Table 2.3 in the order of decreasing average density. The table can be used to estimate the method sensitivity of blood analyte measurement techniques. If we hypothesize that the all analytes of unit density (1 mg/dL) can be measured with the same precision using the same technique (which is not always the case, of course), the precision of detecting an analyte would increase with its mean concentration. Although many other factors, such as noise and interference, play a role in determination of the method sensitivity in practice, the difficulty in determination of analytes can be roughly compared. This table is used in Section 2.4, Chapter 6, and Chapter 7 to evaluate the sensitivity of Raman spectroscopy instruments. The method sensitivity should be distinguished from the sensitivity of an optical system, which is discussed in Chapter 5.

Table 2.3. Normal range and mean of the normal range for blood analytes

Analyte	Normal range (mg/dL)	Mean of normal range (mg/dL)
Hemoglobin	14,000~17,500	16,250
Total Protein	6,000~8,300	7,150
Albumin	3,200~4,500	4,350
Globulin	2,300~3,500	2,900
Cholesterol	150~250[a]	200
LDL Cholesterol	60~180	120
Glucose	45~180	117
Triglyceride	10~190	100
HDL Cholesterol	29~82	56
Urea[b]	17~50	34
Oxygen	16~17[c]	~16
Carbon Dioxide	8~11[d]	~10
Total Bilirubin	0.1~1.2	0.7
Direct Bilirubin	0~0.3	0.15
Insulin	0.0005~0.01	0.005

[a] Random (non-fasting) normal range of cholesterol. Fasting normal values are less than 200 mg/dL. For other analytes, fasting values are listed.

[b] The range for urea is listed instead of the range of urea nitrogen.

[c] The concentration of oxygen in artery is listed.

[d] Combined range of carbon dioxide concentration in artery and vein is listed.

2.3 Optical techniques for clinical chemistry

A variety of optical techniques for measuring concentrations of blood analytes are being developed. Since only light contacts the tissue and blood in optical measurements, instrumental parts do not degrade with use and do not need to be cleaned or replaced regularly. It is also easy to obtain multi-channel optical data simply by adding additional wavelengths. Many analytes are present in biological samples, and they may interfere with measurements of the analyte of interest, if they have spectral features similar to those of the target analyte. Similarities in the spectral features are also called spectral overlap and can be quantified (Chapter 4). A single-variable measurement is influenced by interferences from other analytes, and multiple variables in which the contributions of interfering analytes vary can be used to make accurate measurements in the presence of interfering analytes. Also, many optical techniques do not require chemical reagents, and this would make the measurement process simple and easy. Finally, optical techniques have the potential of measuring analytes in blood-tissue matrix (either in whole blood or in interstitial fluid) non-invasively, and the process of whole blood withdrawal can be eliminated when such measurement techniques are developed.

Vibrational spectroscopy is a promising tool for blood analysis, because it uses molecular vibrations that are unique for each chemical. All of the information is gathered in a single spectral measurement, which can provide concentration information about multiple analytes simultaneously. At least two vibrational spectroscopic techniques are of interest, absorption and Raman scattering. Other optical phenomena, such as reflectance spectroscopy and polarization spectroscopy, are also being studied.

The optical techniques measure either transmitted light through or diffuse reflected light from various parts of human body. These can be classified into three groups: thin skin, such as arm, webbing of a hand, earlobe, and lip; thick skin, such as inside finger; and the eye.

Thin skin parts have normal or thin epidermis (outer skin). Lip and ear may be good candidates for non-invasive measurements. The epidermis is as thin as 40 μm in inner lips, and capillary blood would seem to be easily accessible for optical measurements, although interference from saliva is a potential concern. Blood is abundant and accessible in the earlobe, which is one of the reasons the earlobe is for used for blood withdrawal. Also, the blood flow in the earlobe can be easily increased by applying heat, chemicals, and physical stimulations. The webbing of a hand has been studied in transmission geometry, as it is the body part for which the transmission distance is the minimum, and thus, the optical signal is the least attenuated. However, measurement in the webbing is not suitable for every subject, as the webbing may be difficult to access for some people. Simultaneous measurement in webbing in both transmission and reflectance geometries might provide more information about analyte concentrations, but it has not bee reported yet to the best of our knowledge.

Thick skin parts have a relatively thick epidermal layer. Due to the thickness of the epidermis, capillary blood is less accessible in thick skins, and they are not ideal parts of the body if analytes in blood are to be measured.

The eye is quite different from the body parts discussed above. Through the iris and inside, eyes are clear and do not attenuate light, which simplifies the optical collection.

Furthermore, fewer analytes may be present in the eye. This may result in reduced interference, which may make eye measurements more attractive, as long as the analyte of interest is present. However, a more serious challenge is present in eye measurements. The level of safe irradiance in the eye is much lower than for any other body part. This is because the retina is very sensitive and vulnerable to excess exposure to light. According to the ANSI standards, only a beam of 18 mJ/cm^2 at 830 nm wavelength is permissible for a 10 second exposure [ANSI Z136-1 2000, ANSI Z136-3 1996], which is probably too short time and a low power to make any sensitive detection.

2.3.1 Mid-infrared (mid-IR) absorption spectroscopy

Excitation wavelength is critical in absorption spectroscopy. Mid-infrared absorption spectroscopy (also called mid-infrared spectroscopy) measures the fundamental vibrations of biological molecules. Mid-IR absorption spectra contain sharp peaks, and therefore provide good contrast among chemicals. However, water strongly absorbs light in this wavelength regime (Figure 2.8), and penetration depths are generally less 100 μm. Hence, mid-IR penetration depths are too shallow to probe deep tissue. Mid-IR absorption spectroscopy is not practical for measuring light transmitted through biological tissue, and is often performed in diffuse reflectance geometry, in which the reflectivity is more important than the penetration depth.

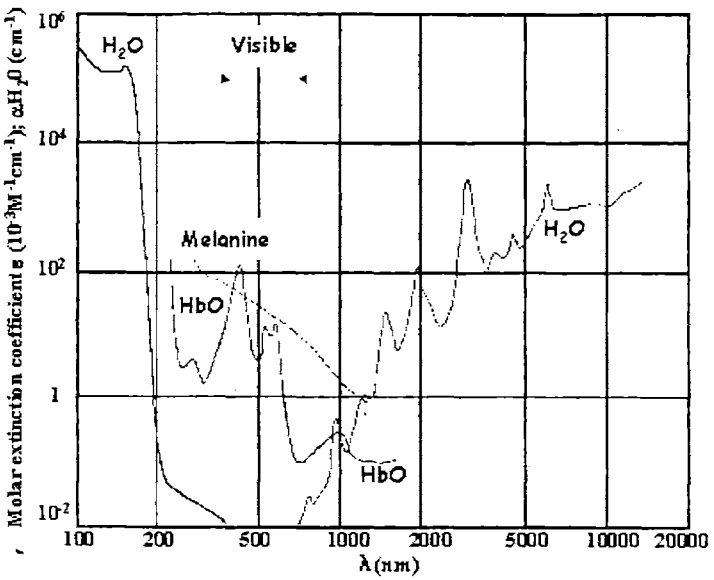

Figure 2.8. Absorption spectrum of major absorbers in human body
[Hale and Querry 1973, Boulnois 1986, Itzkan and Izatt 1994]

In 1987, the correlation between the concentration of glucose and the intensity of the glucose absorption band at 1036 cm^{-1} in doped serum and spinal fluid samples was found [Bauer and Floyd 1987]. Attenuated total reflection (ATR), which measures absorption of the evanescent wave generated from total internal reflection of light in a crystal (typically Zinc Selenide or Germanium), was used in the mid-infrared (1.5-6 μm) to measure concentrations of blood analytes in human blood plasma [Janatsch et al. 1989] and glucose in whole blood [Heise et al. 1989]. The glucose peak around 1030 cm^{-1} in doped pig blood was measured using a CO_2 laser [Mendelson et al. 1990]. In 1995, a large scale experiment was performed with plasma samples from 126 subjects, and a chemometric technique was used to extract concentration information [Heise and Bittner 1995]. A direct mid-IR transmission measurement was made on evaporated serum and whole blood samples [Budínová et al. 1997].

Although mid-IR absorption spectroscopy can extract clinical information from blood, its penetration depth is severely limited. Since mid-IR techniques cannot probe deep into any biological sample, mid-IR absorption is restricted to near-surface measurements [Heise et al. 1999].

2.3.2 Near-infrared (near-IR) absorption spectroscopy

Near-IR absorption has been studied by many researchers, because near-infrared light (770-1500 nm [RCA 1974]) is optimal for probing human tissue. Near-IR light can penetrate significant distances without being absorbed (Figure 2.8). Near-IR spectra in general have good signal-to-noise ratios. However, near-IR absorption measures only the weak overtone and combination bands of the analytes of interest. Absorption bands are broad, with no distinct peaks, and they can be easily confused by background or an overlapping band from an interfering molecule. Features in the measured spectra are not well understood. This can lead to severe calibration difficulties. Stability of measuring instruments becomes critical. Absorption is also temperature sensitive on the fine scale on which measurements are made.

In 1987, one of the earliest papers measuring serum cholesterol using light from 1200-2400 nm was published [Peuchant et al. 1987]. In the following year, total serum protein was measured by near-infrared spectroscopy [Toorenenbergen et al. 1988]. Glucose concentrations in aqueous samples were also measured [Arnold and Small 1990]. Many groups began to measure analytes in serum and whole blood using near-IR techniques [Hall and Pollard 1992, 1993; Haaland et al. 1992]. Accurate measurements of analytes in

human plasma were performed using a multivariate calibration technique [Bittner et al. 1995]. Non-invasive measurements of glucose *in vivo* were attempted by irradiating near-IR on the finger [Robinson et al. 1992]. In 1999, blood pH was also measured [Alam et al. 1999].

Although near-IR spectroscopy is promising for non-invasive measurements of blood analytes, the lack of sharp spectral features, the extreme sensitivity to temperature fluctuation, and the drift of near-IR spectra remain as major challenges.

2.3.3 Other infrared absorption spectroscopy techniques

Other methods based on IR absorption have also been explored. The correlation between the glucose concentration and the absorption spectrum of mid-infrared light radiated from the human body was reported [Klonoff et al. 1998]. In this study, thermal radiation from the body was used, and no external radiation source was necessary. However, due to the strong absorption of MID-IR in body, the source of the spectral signal is generated within a few hundred microns layer of skin, and again, precluding probing of deep tissue.

Recently, a method called Kromoscopy was used to measure concentrations of glucose and urea in aqueous samples [Helwig et al. 2000, Misner and Block 2000]. In Kromoscopy, a "Kromoscope", a filter-based 4-channel detector, is used instead of a conventional dispersive or interferometric spectrograph. The "Kromoscope" sacrifices spectral resolution in order to obtain a high throughput. Kromoscopy has the potential to be a useful tool for analyte measurements, if the enough number of filters (potentially more than 4) are used and the transmittance of each filter is designed in the manner that

interferences can be isolated and the signal intensity is optimized. The concept of throughput and optimal system design is discussed in detail in Chapter 5.

While absorption is by far the most widely studied optical technique for blood analysis, other methods have also shown promise. Fundamental mechanisms of light-matter interaction have also been investigated, including Raman scattering, reflectance, scattering, the rotation of polarization, and photoacoustic effect.

2.3.4 Raman spectroscopy

Raman spectroscopy is another technique to measure molecular vibrations (Figure 2.9). In Raman scattering, monochromatic excitation light is inelastically scattered from a molecular sample, which means that the wavelength of the scattered light shifts to either longer wavelengths (Stokes Raman) or shorter wavelengths (anti-Stokes Raman) (Figure 2.10). In Stokes Raman scattering, a portion of the excitation light's energy is transferred to excite the molecule to a vibrational level. In anti-Stokes Raman scattering, energy is transferred from the vibrating molecule to the Raman scattered light.

Raman shifts are independent of excitation wavelength. Therefore, one has the freedom to choose an optimal excitation wavelength in the near IR for deep sampling, and still observe the fundamental vibrations of analyte molecules. Raman spectra are sharp and distinct for each molecule, so one analyte can be distinguished easily from another, and from a broad fluorescence background, even if the Raman signal intensity is smaller than the background. Since the major optical absorbers in the human body, melanin, hemoglobin and water, absorb near-IR light the least (Figure 2.8), near-IR Raman

spectroscopy can probe deeply into tissue. Also, the near-IR excitation reduces the fluorescence the intensity of which is much higher than that of Raman scattered light. Since shot noise of fluorescence is typically the dominating noise in Raman spectra, it is desirable to minimize the fluorescence.

However, Raman scattering is a rare event, and the intensity of the Raman signals is generally weak. This weak signal intensity is the challenge in Raman spectroscopy of biological tissue.

In principle, the probability of certain Raman scattering events can be increased by using resonance Raman techniques, stimulated Raman spectroscopy, or surface enhanced Raman spectroscopy (SERS). Generally speaking, resonance Raman spectroscopy of biological molecules requires short wavelength excitation, typically in ultra-violet (UV). When the wavelength of the excitation beam is close to that of the electronic absorption band, intensities of Raman signals can be increased by orders of magnitudes. However, the use of UV excitation is not desirable in *in vivo* measurements, as UV radiation can damage DNA molecules.

In contrast with ordinary (spontaneous) Raman scattering, stimulated Raman spectroscopy employs a high power excitation beam. If the intensity of the Stokes Raman scattered light becomes sufficiently large, it creates a strong Raman radiation field (i.e. many photons in each mode of the radiation field), and mixing of the Raman radiation field and the field of excitation light causes strong light emission at the Raman scattered frequency [Diem 1993]. The conversion of the excitation light to the Raman scattered light

is more efficient in stimulated Raman scattering. However, the use of high power laser light can damage tissue.

SERS is a technique to enhance the intensity of Raman signals by using SERS active particles, such as gold or silver colloids. The electromagnetic field near the surface of SERS particles amplifies the probability of Raman scattering by several orders of magnitude [Diem 1993]. However, not all Raman signals can be enhanced by SERS, and certain analytes may not benefit from its use. Furthermore, it is not safe to inject the SERS active particles into human subjects, and its application in *in vivo* measurements is limited.

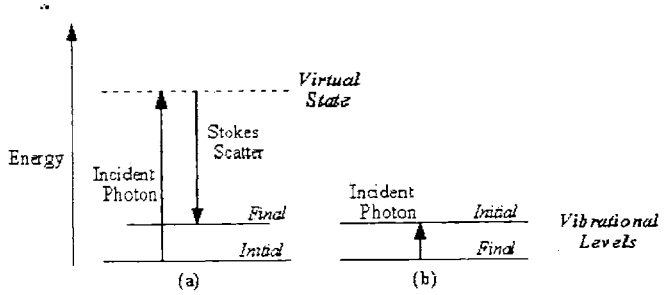

Figure 2.9. Comparison of (Stokes) Raman scattering (a) and absorption (b). Both Raman spectroscopy and absorption spectroscopy provide information about the same molecular vibration levels.

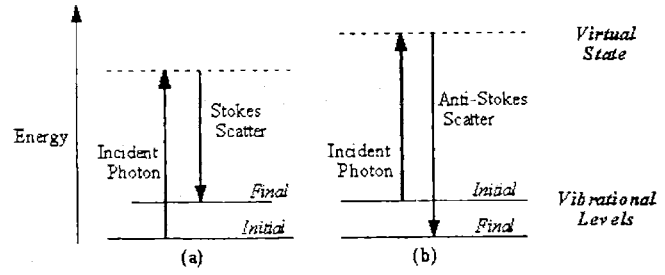

Figure 2.10. Energy level diagram of Stokes (a) and anti-Stokes (b) Raman scattering

The use of Raman spectroscopy for measuring blood analytes has been studied by several investigators. The group at MIT has pioneered in using Raman spectroscopy for analyte measurements, and our recent research is discussed in Section 2.4.

Raman spectroscopy has been suggested as a tool to measure glucose in aqueous humor of the eye in 1993 [Tarr and Steffes 1993]. They proposed use of stimulated Raman spectroscopy and suggested the aqueous humor in the eye as the location of measurements, since eyes have fewer interfering chemicals than in blood or skin. Furthermore, optical scattering and absorption are negligible in the visible and near-infrared wavelength range, and difficulties related to measurements in turbid medium are not present in eye measurements. However, the risk of damaging the retina during measurements remains as a challenge [ANSI Z136-1 2000, ANSI Z136-3 1996], and no *in vivo* experiment using stimulated Raman spectroscopy has been reported as of yet. In addition, the glucose concentration in the eye follows that in the blood with some time lag, due to diffusion. This delay may be a problem when accurate and rapid measurements are necessary, and it needs to be understood better.

In 1996, it was demonstrated that anti-Stokes Raman spectroscopy (Raman shifts to shorter wavelengths) is capable of quantitative analysis of glucose in blood plasma and serum [Dou et al. 1996]. With anti-Stokes Raman the fluorescence background is suppressed, but the signal intensity is weak. To obtain sufficient signals, an integrating sphere was employed. However, an integrating sphere, which only holds a small volume of sample, is not suitable for *in vivo* measurements.

In 1999, two groups reported the measurements of multiple blood analytes in human serum using Stokes Raman spectroscopy [Berger et al. 1999, Qu et al. 1999]. In addition, Qu et al. mechanically filtered large molecules in their samples, such as proteins and lipids, and demonstrated that fluorescence backgrounds in serum spectra are due to serum proteins and lipids.

In the same year, glucose concentrations in rabbit eyes were measured using Stokes Raman spectroscopy [Brochert et al. 1999]. Again, the risk associated with eye exposure to laser radiation remains a challenge. In this study, safety issues need to be addressed.

2.3.5 Other optical techniques

Reflectance spectroscopy measures light reflected by sample. Both techniques often use a broadband light source and collect reflected or back-scattered light. Chromopores in the sample absorb the light, and changes in the index of refraction scatter light. Reflectance spectroscopy measures mainly absorption and scattering rather than molecular vibrations. Reflectance spectroscopy can measure specular reflected light and diffuse reflected light. Diffuse reflectance spectroscopy can probe deep tissue, whereas specular reflectance spectroscopy can only probe a near-surface region. Therefore, diffuse reflectance spectroscopy is preferred to specular reflectance spectroscopy in biological studies.

In 1990, a non-invasive method of measuring bilirubin concentration in neonates using diffuse reflectance was suggested [Saidi et al. 1990]. Non-invasive measurement of glucose *in vivo* was attempted by employing diffuse reflectance spectroscopy from the human inner lip [Marbach et al. 1993], but the accuracy was not applicable for clinical

settings. Other groups also investigated the possibility of correlating optical properties and glucose concentrations [Kohl et al. 1994, Maier et al. 1994]. In a study of 41 diabetic volunteers, a correlation between glucose concentrations and scattering properties calculated from diffuse reflectance data was reported [Bruusema et al. 1996, 1997].

Diffuse reflectance spectroscopy in the near-infrared cannot measure fundamental vibrational bands as in near-IR absorption spectroscopy. However, scattering and absorption properties can be obtained from diffuse reflectance data, and it is a promising technique to measure analytes which change scattering and absorption properties.

Polarimetry estimates the chemical concentration by measuring the rotation of polarization. Since scattering depolarizes light and other analytes can rotate polarization, polarimetry is also performed in the eye where scattering is low and fewer analytes are present. It was demonstrated that the glucose concentration is proportional to the angle of polarization rotation [Coté et al. 1992]. However, other chemicals can also rotate polarization, and single channel polarimetry is limited by this overlap. A multi-wavelength polarimeter was designed to eliminate such overlap [King et al. 1994]. Also, in an attempt to reduce the required laser power and increase the safety, a magnetic rotator scheme was devised to double the signal intensity at the same laser power [Jang et al. 1998].

Photoacoustic spectroscopy measures the pressure wave that results from heat expansion. A rapid pulse of excitation light is absorbed by tissue, and an acoustic pressure wave is generated. The acoustic pressure wave may have correlations to analyte concentrations. In a preliminary study, photoacoustic spectroscopy was used to measure

glucose concentrations *in vivo* [Spanner and Niessner 1996], but the prediction accuracy was not acceptable.

This wealth of research activity underscores the interest, promise and importance of developing non-invasive techniques to measure concentrations of blood analytes.

2.3.6 Minimally invasive techniques

Minimally invasive techniques require some form of sample extraction, and are not considered to be non-invasive. However, they differ from invasive techniques, since they do not require puncture of blood vessels to obtain samples.

Interstitial fluid (ISF) is the medium most extensively studied by minimally invasive techniques, since ISF can be obtained relatively painlessly. Methods to extract ISF include skin puncture, chemical enhancement, reverse iontophoresis, and sonophoresis [Roe and Smoller 1998]. In skin puncture, a small hole is made in the skin to obtain ISF without bleeding. Companies are developing micro-lancets and focused laser beams to puncture such small holes. In other methods, chemicals, electricity (current), and ultrasound extract ISF without puncture. Chemical enhancement patches are being developed to enhance the transport of ISF through the skin and absorb the extracted ISF from the surface of the skin. Reverse iontophoresis is also called electro-osmosis. Electric current is applied on skin, and ISF is extracted from the skin. In sonophoresis, ultrasound applied to the skin produces a local pressure gradient, and ISF is extracted. The extracted ISF can be analyzed chemically, electrochemically, or optically. Another method suggested to collect ISF is implanted sensors. Sensors implanted on or under the skin

remains in contact with the ISF, and may be used for continuous measurement of analytes. However, implanted foreign objects can cause undesired reactions in the body, and issues related to the implantation need to be addressed.

Measurements of analytes in ISF need more investigation. Concentrations of analytes in ISF and in blood are different, and many diagnostic criteria in conventional clinical chemistry may have to be translated. Concentrations of analytes in ISF are also affected by stress, exercise, diet, sweating, illness, and aging. A proper calibration is needed to provide accurate analyte concentrations under such interferences. Furthermore, concentrations of certain analytes in ISF, such as glucose, exhibit a time lag in following the concentrations in blood, since many analytes diffuse from the blood to the ISF. An average delay time of 20 minutes was reported for glucose [Tamada et al. 1995].

Although there are many challenges in the interstitial fluid measurements, efforts are being made by many researchers to develop an accurate ISF measurement technique. The recent FDA approval of a minimally invasive technique for glucose measurements (GlucoWatch, Cygnus) may be a result of such efforts. Measurements of glucose using this technique are not as accurate as other clinical chemistry techniques, but further development may improve its accuracy. Studies performed using minimally invasive instruments will provide useful information in development of non-invasive techniques.

2.4 Prior research using Raman spectroscopy

The Stokes Raman spectroscopy of blood analytes has been studied for several years at the MIT Spectroscopy Laboratory. Feasibility study demonstrated that it is possible to measure

dissolved blood gases and biological analytes in aqueous samples [Berger et al. 1995, 1996]. Also, higher than physiological concentrations of glucose in whole blood were measured [Berger et al. 1997], which demonstrated the feasibility of measuring glucose in whole blood using Raman spectroscopy. A new method of spectral analysis was developed [Berger et al. 1998]. A numerical simulation was performed to show how the prediction error in chemometric algorithms is affected by signal-to-noise ratio (S/N) [Berger and Feld 1997].

2.4.1 Experimental setup

An experimental setup was developed for the study of biological fluids (Figure 2.11) [Berger 1998]. The system specifications are summarized in Table 2.4. A compact, portable CW gallium aluminum arsenide (GaAlAs) diode laser at 830 nm was the light source. In multi-mode operation, the light from the source contained several frequencies. To block frequencies other than 830 nm, a holographic notch filter was used. The light passing through the filter was focused onto the sample, which is contained in a quartz cuvette (10 mm x 10 mm x 20 mm). A magnetic stir-bar kept the sample uniform, and prevented particles from settling. Because of the size of the stir-bar, a sample-volume of about 1 mL was used. However, this volume was not mandatory, and could be reduced by using a smaller cuvette and a smaller stir-bar.

The sample generated Raman light, and the back-scattered light was collected by a reflective microscope objective (a Cassegrain objective [Born and Wolf 1997]). It had a high numerical aperture (NA 0.5), and it could collect light from a 0.7 mm spot at angles

between 14 and 33 to the normal. A later analysis indicated that this objective could collect about 11% of all photons emerging from whole blood (the method of collection efficiency calculation is discussed in Chapter 5). However, it was not optimized for collecting spectra from turbid biological samples. This led to the development of a spectroscopy system optimized for whole blood, which is discussed in Chapter 5.

A holographic bandpass filter rejected 830 nm from the collected light to avoid Raman scattering from the subsequent optical components. It was determined to use a fiber bundle to deliver more light into the spectrograph. The light emerging from the filter was focused to a fiber bundle, which transferred the beam pattern from circular to linear to match the geometry of the spectrograph entrance slit. The optical fiber bundle had 177 optical fibers, and the fibers were circularly packed on one side and linearly packed on the other side. Each fiber had 100 μm diameter core and 110 μm diameter cladding. The diameter of the circular end was 1.7 mm, and the height and width of the active area on the linear end were 19.7 mm and 0.1 mm, respectively. The packing fraction was 0.6125 on the circular side and 0.7057 on the linear side. The use of the fiber bundle enabled more efficient collection of Raman signals, as the efficiency of light collection is low when a circularly distributed light is passed through the linear slit inside the spectrograph.

The light coming out of the far end of the fiber was focused to the entrance slit of the spectrometer by means of two lenses. The purpose of having these two lenses, called connection optics, was to change the NA of the light (0.22) to match the NA of the spectrograph (0.28). However, these lenses had aberrations, and half of the focused light could not enter the slit according to a numerical calculation. By matching the NA of the

fiber bundle to the NA of the spectrograph, these connection optics could be eliminated and the loss of light prevented, as discussed in Chapter 5.

The holographic grating inside the spectrometer dispersed the light horizontally, and the front-illuminated, deep-depleted CCD camera collected the image of the light. The spectrograph distorts the image of the optical slit inside the spectrograph to a curve, and a curvature correction was needed to obtain the true spectrum. If there was no distortion, a spectrum of a single wavelength band would appear like a line on the CCD camera (Figure 2.12), and the spectrograph distorts the image. The horizontal dimension on the CCD displays the wavelength, and the vertical dimension represents the fiber height. To correct for the curvature, the CCD output was broken into multiple horizontal strips, which were read out separately and shifted in software to compensate for the curvature. All data points in a strip were shifted by the same number of pixels (or wavelengths). Then, the shift-corrected strips were summed to create a single spectrum.

The camera was connected to a computer by means of a controller. The collected images were binned, and the spectra were analyzed by mathematical algorithms [Berger 1998]. The S/N of a 10 mM glucose spectrum in whole blood collected for 10 seconds with this system was 1.1.

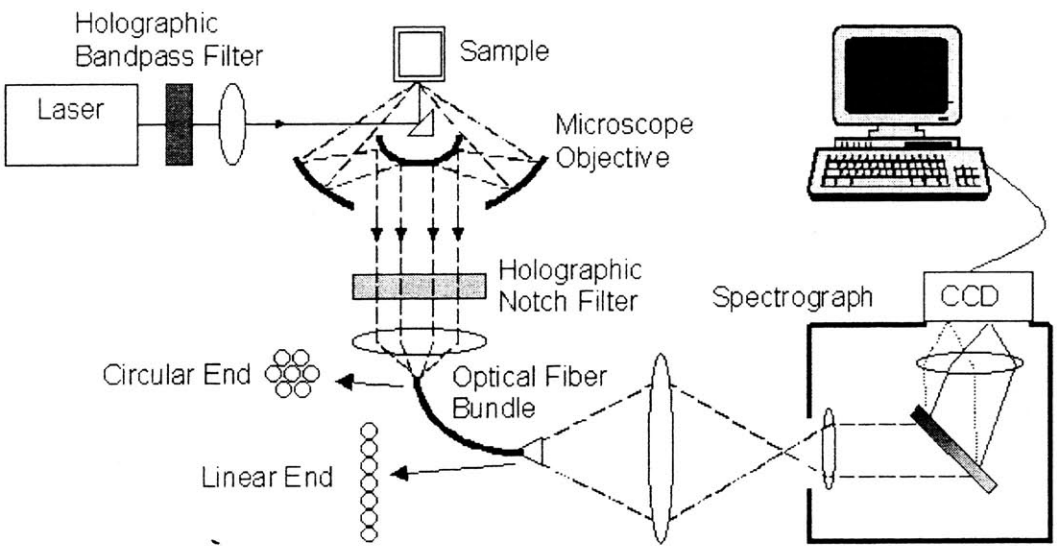

Figure 2.11. Previous experimental setup

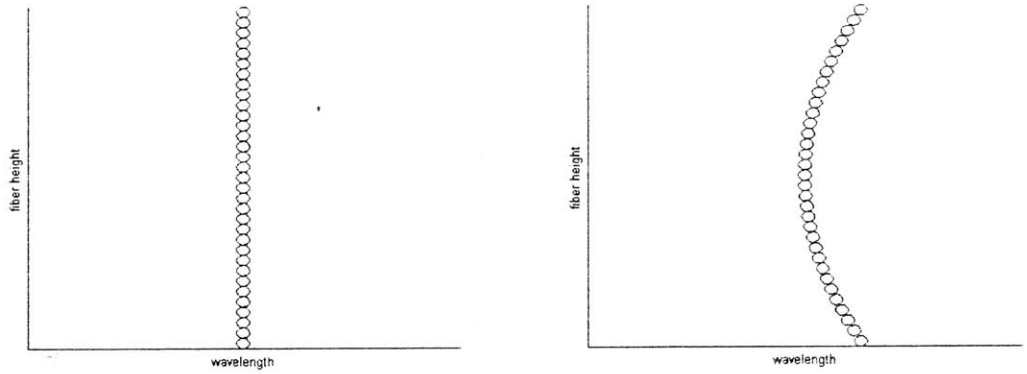

Figure 2.12. Undistorted image of fiber array on CCD (left), and the image distorted by the spectrograph (right).

Table 2.4. Summary of system specifications

Component	*specification*
Laser	wavelength • 830 nm
	power output • 500 mW
Sample	volume • 2 ml
	excitation power on sample • 300 mW
	excitation beam diameter • 100 μm
Cassegrain microscope	magnification • 15x
	NA • 0.5
	minimum acceptance angle • 14°
	maximum acceptance angle • 33°
	obscuration • 19.5%
Fiber bundle	core diameter • 100 μm
	cladding diameter • 110 μm
	number of optical fibers • 177
	NA • 0.22
	packing fraction • 0.6125
	circular end diameter • 1.7 mm
	linear end height • 19.7 mm
Coupling lens	focal length • 82 mm
	diameter • 105 mm
Spectrograph	NA • 0.27
	dispersion • 16.5 m/cm^{-1}
CCD detector	height • 17 mm
	pixel size • 22 μm x 22 μm
	quantum efficiency • 20% @ 900 nm

2.4.2 Experiment and results

Using this system, multiple analytes including glucose, urea, cholesterol, triglyceride, albumin, total protein and hematocrit were measured in serum and whole blood samples from sixty-nine patients over a seven-week period. Measurements of analytes in serum were clinically accurate or near-clinically accurate [Berger et al. 1999], as the correlation coefficient r is higher than, or close to, 0.9 (thus r^2 is higher than, or close to, 0.81). However, analytes could not be measured accurately in whole blood, and prediction errors were higher than those in serum.

The following describes the experimental procedure of this study. Approximately ten blood samples were collected once each week at the Beth Israel Deaconess Medical Center for a period of seven weeks, totaling sixty-nine samples from different individuals. The blood drawn from each individual was divided into two samples. EDTA was added to one sample to prevent clotting. This sample remained at room temperature before the hematology analysis. The other was left to clot, and centrifuged to generate blood serum. Chemical analyses were performed on the serum sample, and chemical concentrations were measured. The whole blood sample and blood serum sample pairs were then stored in a refrigerator at 4°C overnight. Because glucose can break down after withdrawal from the body, a portion of the whole blood sample was centrifuged, and the concentration of the plasma glucose was also measured. The samples were brought to MIT in a refrigerated state, and the samples were again stored at 4°C before spectral measurement. Collected Raman spectra were analyzed using a standard partial least squares algorithm.

Table 2.5 lists the prediction errors of analyte concentration measurements obtained in this experiment. The prediction errors in serum were accurate, but the prediction errors in whole blood were larger. Using Table 2.3, we can also qualitatively discuss the method sensitivity. This instrument could measure analytes of concentrations as low as that of triglyceride in serum with r^2=0.81. However, it could measure only analytes of high concentrations, such as hematocrit and albumin, in whole blood with r^2 higher than or near 0.81.

Table 2.5 Prediction errors and correlation coefficients from analyte concentration measurements obtained in the previous experiment

Analyte (unit)	*In Whole Blood* (r^2)	*In Serum* (r^2)
Glucose (mg/dL)	77 (0.15[1])	26 (0.83)
BUN (mg/dL)	6.5 (0.59)	3.8 (0.74)
Cholesterol (mg/dL)	45 (0.12[1])	12 (0.83)
Triglyceride (mg/dL)	81 (0.56)	29 (0.88)
Total Protein (g/dL)	0.38 (0.55)	0.19 (0.77)
Albumin (g/dL)	0.21 (0.76)	0.12 (0.86)
Hematocrit (%)	1.5 (0.92)	N/A[2]

[1] No statistical significance was achieved.

[2] Hematocrit, the volume fraction of red blood cells, is always zero in serum samples, since red blood cells are not present in serum samples. Determination of hematocrit in serum does not have any statistical or clinical significance.

Importantly, the intensities of the Raman signals in whole blood were reduced by a factor of four compared to those in serum [Berger 1998], while the background and noise did not change much (Figure 2.13). This indicates that the major source of the fluorescence background is not the sample medium (serum or whole blood). As a result, the S/N was reduced by a factor of four, as well. This led to the study of the differences between serum and whole blood (Chapter 3). The experimental results obtained by using a higher sensitivity spectroscopy system are presented in Chapter 6 and 7.

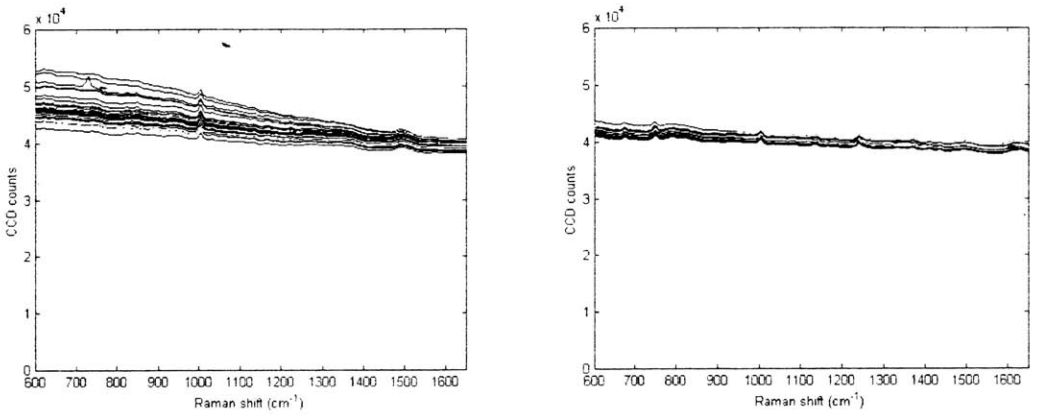

Figure 2.13 Raman spectra of serum (left) and whole blood (right) samples. The backgrounds in the two types of media are similar. In addition, the background noise did not change much.

References

M. K. Alam, M. R. Rohrscheib, J. E. Franke, T. M. Niemczyk, J. D. Maynard, and M. R. Robinson, "Measurement of pH in whole blood by near-infrared spectroscopy," *Applied* Spectroscopy, volume 53, 3 1999, pp. 316-324.

American Heart Association, *Heart and Stroke Guide*, 2001.

American National Standards Institute, Z136-1, *Safe Use of Lasers*, 2000.

American National Standards Institute, Z136-3, *Safe Use of Lasers in Health Care Facilities*, 1996.

M. A. Arnold and G. W. Small, "Determination of physiological levels of glucose in an aqueous matrix with digitally filtered Fourier transform near-infrared spectra," *Analytical Chemistry*, volume 62, 1990, pp. 1457-1464.

P. S. Bachorik, B. M. Rifkind, and P. O. Kwiterovich, "Lipids and Dyslipoproteinemia," in *Clinical Diagnosis and Management by Laboratory Methods*, J. B. Henry, ed. (Philadelphia: W. B. Saunders Company, 1996).

D. E. Battey, J. B. Slater, R. Wludyka, H. Owen, D. M. Pallister, and M. D. Morris, "Axial transmissive *f*/1.8 imaging Raman spectrograph with volume-phase holographic filter and grating," *Applied Spectroscopy*, volume 47, 11 1993, pp. 1913 –1919.

B. Bauer and T. A. Floyd, "Monitoring of glucose in biological fluids by Fourier-transform infrared spectrometry with a cylindrical internal reflectance cell, " *Analytica Chimica Acta*, volume 197, 1987, pp. 295-301.

P. H. Benett, "Definition, diagnosis, and classification of diabetes mellitus and impaired glucose tolerance" in *John's Diabetes Mellitus*, C. R. Kahn and G. C. Weir, eds. (New York: Lippincott, Williams & Wilkins, 1994).

A. J. Berger, Y. Wang, D. M. Sammeth, I. Itzkan, K. Kneipp and M. S. Feld, "Aqueous Dissolved-Gas Measurements Using near-Infrared Raman-Spectroscopy," *Applied Spectroscopy*, volume 49, 8 1995, pp. 1164-1169.

A. J. Berger, Y. Wang and M. S. Feld, "Rapid, noninvasive concentration measurements of aqueous biological analytes by near-infrared Raman spectroscopy," *Applied Optics*, volume 35, 1 1996, pp. 209-212.

A. J. Berger, I. Itzkan, and M. S. Feld, "Feasibility of measuring blood glucose concentration by near- infrared Raman spectroscopy," *Spectrochimica Acta Part a-Molecular and Biomolecular Spectroscopy*, volume 53, 2 1997, pp. 287-292.

A. J. Berger and M. S. Feld, "Analytical method of estimating chemometric prediction error," *Applied Spectroscopy*, volume 51, 5 1997, pp. 725-732.

A. J. Berger, T. W. Koo, I. Itzkan and M. S. Feld, "An enhanced algorithm for linear multivariate calibration," *Analytical Chemistry*, volume 70, 3 1998, pp. 623-627.

A. J. Berger, T. W. Koo, I. Itzkan, G. Horowitz and M. S. Feld, "Multicomponent blood analysis by near-infrared Raman spectroscopy," *Applied Optics*, volume 38, 13 1999, pp. 2916-2926.

A. Bittner, R. Marbach, and H. M. Heise, "Multivariate calibration for protein, cholesterol, and triglycerides in human plasma using short-wave near-infrared spectrometry, " *Journal of Molecular Structure*, volume 349, 1995, pp. 341-344.

J. L. Boulnois, "Time-irradiance reciprocity relationship as a model for laser-tissue interactions," Lasers in Surgery and Medicine, volume 6, 2 1986, pp. 168 -168.

L. I. Boral and J. B. Henry, "Transfusion Medicine," in *Clinical Diagnosis and Management by Laboratory Methods*, J. B. Henry, ed. (Philadelphia: W. B. Saunders Company, 1996).

M. Born and E. Wolf, *Principes of Optics* (New York: Cambridge University Press, 1997).

M. S. Brochert, M. C. Storrie-Lombardi, and J. L. Lambert, "A Noninvasive Glucose Monitor: Preliminary Results in Rabbits", *Diabetes Technology & Therapeutics*, volume 1, 2 1999, pp. 145-152.

J. T. Bruulsema, M. Essenpreis, L. Heinemann, J. E. Hayward, M. Berger, F. A. Greis, T. Koschinsky, J. Sandahl-Christiansen, H. Orskov, T. J. Farrell, M. S. Patterson, and D. Bocker, "Detection of changes in blood glucose concentration *in vivo* with spatially resolved diffuse reflectance," *OSA Conf. On Biomedical Optical Spectroscopy and Diagnostics* 1996.

J. T. Bruulsema, J. E. Hayward, T. J. Farrell, M. S. Patterson, L. Heinemann, M. Berger, T. Koschinsky, J. SandahlChristiansen, H. Orskov, "Correlation between blood glucose concentration in diabetics and noninvasively measured tissue optical scattering coefficient ," *Optics Letters*, volume 22, 3 1997, pp. 190-192.

G. Budinova, J. Salva and K. Volka, "Application of molecular spectroscopy in the mid-infrared region to the determination of glucose and cholesterol in whole blood and in blood serum," *Applied Spectroscopy*, volume 51, 5 1997, pp. 631-635.

X. Dou, Y. Yamaguchi, H. Yamamoto, S. Doi and Y. Ozaki, "Quantitative analysis of metabolites in urine using a highly precise, compact near-infrared Raman spectrometer," *Vibrational Spectroscopy*, volume 13, 1 1996, pp. 83-89.

N. Fogh-Andersen, P. D'Orazio, K. Kuwa, W. R. Külpmann, G. Mager, and L. Larsson, "Recommendation on Reporting Results for Blood Glucose," *Journal of the International Federation of Clinical Chemistry*, volume 12, 4 2000.

L. E. Govoni and J. E. Hayes, *Drugs and nursing implications* (E. Norwalk, CT: Appleton-Century-Crofts, 1985).

D. M. Haaland, M. R. Robinson, G. W. Koepp, E. V. Thomas, and R. P. Eaton, "Reagentless near-infrared determination of glucose using multivariate calibration," Applied Spectroscopy, volume 46, 1992, pp. 1575 –1578.

G. M. Hale and M. R. Querry, "Optical constants of water in the 200 nm to 200 µm wavelength region," in *Applied Optics*, volume 12, 1973, pp. 555-563.

J. W. Hall and A. Pollard, "Near-infrared spectrophotometry: A new dimension in clinical chemistry," Clinical Chemistry, volume 38, 1992, pp. 1623 –1631.

J. W. Hall and A. Pollard, "Near-infrared spectroscopic determination of serum total proteins, albumin, globulins, and urea," *Clinical Biochemistry*, volume 26, 1993, pp. 483 –490.

D. M. Haaland, M. R. Robinson, G. W. Koepp, E. V. Thomas and R. P. Eaton, "Reagentless near-Infrared determination of glucose in whole-blood using multivariate calibration," *Applied Spectroscopy*, volume 46, 10 1992, pp. 1575-1578.

A. M. Harvey, R. J. Johns, and V. A. McKusick, *The principles and practice of medicine* (E. Norwalk, CT: Appleton & Lange, 1988).

H. M. Heise, R. Marbach, G. Janatsch, J. D. Kruse-Jarres, "Multivariate determination of glucose in whole blood by attenuated total reflection Infrared spectroscopy", *Analytical Chemistry*, volume 61, 1989, pp. 2009 - 2015.

H. M. Heise and A. Bittner, "Investigation of experimental errors in the quantitative analysis of glucose in human blood plasma by ATR-IR spectroscopy", *Journal of Molecular Structure*, volume 348, 1995, pp. 21-24.

H. M. Heise, L. Kuepper, and R. Marbach, "Limitations of infrared spectroscopy for non-invasive metabolite monitoring using the attenuated total reflection technique," *IEEE LEOS Newsletter*, volume 13, 5 1999.

A. M. Helwig, M. A. Arnold and G. W. Small, "Evaluation of Kromoscopy: resolution of glucose and urea," *Applied Optics*, volume 39, 25 2000, pp. 4715-4720.

J. B. Henry and A. S. Kurec, "The Clinical Laboratory: Organization, Purposes, and Practice," in *Clinical Diagnosis and Management by Laboratory Methods*, J. B. Henry, ed. (Philadelphia: W. B. Saunders Company, 1996).

J. B. Henry, R. B. Lauzon, and G. B. Schumann, "Basic Examination of Urine," in *Clinical Diagnosis and Management by Laboratory Methods*, J. B. Henry, ed. (Philadelphia: W. B. Saunders Company, 1996).

R. B. Howard and N. H. Herbold, *Nutrition in clinical care* (New York: McGraw-Hill, 1982).

I. Itzkan and J. A. Izatt, "Medical Use of Lasers," in *Encyclopedia of Applied Physics*, Volume 10, G. L. Trigg, ed. (Washington, D.C. : Wiley - VCH & American Institute of Physics, 1994).

G. Janatsch, J. D. Kruse-Jarres, R. Marbach, and H. M. Heise, "Multivariate calibration for assays in clinical chemistry using attenuated total reflection infrared spectra of human blood plasma", *Analytical Chemistry,* 1989, volume 61, pp. 2016 - 2023.

D. C. Klonoff, J. B Braig, B. Sterling, C. Kramer, D. Goldberger, and R. Trebino, "Mid-infrared spectroscopy for noninvasive blood glucose monitoring," *IEEE LEOS Newsletter*, volume 12, 2 1998, pp. 13 - 14.

R. Marbach, T. Koschinsky, F. A. Gries and H. M. Heise, "Noninvasive blood-glucose assay by near-Infrared diffuse-reflectance spectroscopy of the Human Inner Lip," *Applied Spectroscopy*, volume 47, 7 1993, pp. 875-881.

K. L. McCance and S. E. Huether, *Pathophysiology: Clinical concepts of disease processes* (St. Louis, MO: Mosby, 1990).

R. A. McPherson, "Specific Proteins," in *Clinical Diagnosis and Management by Laboratory Methods*, J. B. Henry, ed. (Philadelphia: W. B. Saunders Company, 1996).

Y. Mendelson, A. C. Clermont, R. A. Peura RA, and B. C. Lin, "Blood glucose measurement by multiple attenuated total reflection and infrared absorption spectroscopy", *IEEE Transactions on Biomedical Engineering*, volume 37, 5 1990, pp. 458-465.

J. L. Miller, "Blood Coagulation and Fibrinolysis," in *Clinical Diagnosis and Management by Laboratory Methods*, J. B. Henry, ed. (Philadelphia: W. B. Saunders Company, 1996).

M. W. Misner and M. J. Block, "Noninvasive measurement by Kromoscopic analysis," *Spectroscopy*, volume 15, 11 2000, pp. 51-55.

M. W. Morris and F. R. Davey, "Basic Examination of Blood," in *Clinical Diagnosis and Management by Laboratory Methods*, J. B. Henry, ed. (Philadelphia: W. B. Saunders Company, 1996).

C. J. L. Murray and A. D. Lopez, *The global burden of disease : a comprehensive assessment of mortality and disability from diseases, injuries, and risk factors in 1990 and projected to 2020* (Cambridge, MA: Harvard School of Public Health, 1996).

National Institute of Health National Library of Medicine, *Medline plus Medical Encyclopedia*, http://www.nlm.nih.gov/medlineplus/ency.

A. N. D. Nguyen, J. B. Henry, and R. L. Sunheimer, "Principles of Instrumentation," in *Clinical Diagnosis and Management by Laboratory Methods*, J. B. Henry, ed. (Philadelphia: W. B. Saunders Company, 1996).

E. Peuchant, C. Salles, and R. Jensen, "Determination of serum cholesterol by near-infrared reflectance spectrometry," *Analytical Chemistry*, volume 59, 1987, pp. 1816 –1819.

M. R. Pincus, "Assessment of Liver Function," in *Clinical Diagnosis and Management by Laboratory Methods*, J. B. Henry, ed.. (Philadelphia: W. B. Saunders Company, 1996a).

M. R. Pincus, "Interpreting Laboratory Results: Reference Values and Decision Making," in *Clinical Diagnosis and Management by Laboratory Methods*, J. B. Henry, ed. (Philadelphia: W. B. Saunders Company, 1996b).

M. R. Pincus, H. G. Preuss, and J. B. Henry, "Evaluation of Renal Function, Water, Electrolytes, Acid-Base Balance, and Blood Gases," in *Clinical Diagnosis and Management by Laboratory Methods*, J. B. Henry, ed. (Philadelphia: W. B. Saunders Company, 1996).

J. N. Y. Qu, B. C. Wilson and D. Suria, "Concentration measurements of multiple analytes in human sera by near-infrared laser Raman spectroscopy," *Applied Optics*, volume 38, 25 1999, pp. 5491-5498.

M. R. Robinson, R. P. Eaton, D. M. Haaland, G. W. Koepp, E. V. Thomas, B. R. Stallard and P. L. Robinson, "Noninvasive glucose monitoring in diabetic-patients - a preliminary evaluation," *Clinical Chemistry*, volume 38, 9 1992, pp. 1618-1622.

RCA, *Electro-Optics Handbook* (Harrison, NJ: RCA Corporation, 1974).

D. C. Sabiston, *Davis-Christopher textbook of surgery: Biological basis of modern surgical practice* (Philadelphia: Saunders, 1981).

I. S. Saidi, S. L. Jacques, and F. K. Tittel, "Monitoring neonatal bilirubinemia using an optical patch," *SPIE Proceedings of Optical Fibers in Medicine V,* A. Katzir, ed. volume 1201, 1990, pp. 569-578.

G. Scipien G and M. V. Barnard, *Comprehensive pediatric nursing* (New York: McGraw-Hill, 1983).

S. Sharma, Applied Multivariate Techniques, (New York: John Wiley & Sons, 1996).

W. A. Sodeman and T. M. Sodeman, *Pathologic physiology: Mechanisms of diseases*, (Philadelphia: Saunders, 1982).

L. Stryer, *Biochemistry* (New York: W. H. Freeman and Co., 1995).

J. A. Tamada, N. J. V. Bohannon, and R. O. Potts, "Measurement of glucose in diabetic subjects using noninvasive transdermal extraction," *Nature Medicine*, volume 1, 11 1995.

R. V. Tarr and P. G. Steffes, "Non-invasive blood glucose measurement system and method using stimulated Raman spectroscopy", United States Patent #5,243,983 (1993).

G. A. Threatte and J. B. Henry, "Carbohydrates," in *Clinical Diagnosis and Management by Laboratory Methods*, J. B. Henry, ed. (Philadelphia: W. B. Saunders Company, 1996).

A. W. van Toorenenbergen, B. G. Blijenberg, and B. Leijnse, "Measurement of total serum protein by near-infrared reflectance spectroscopy," Journal of Clinical Chemistry and Clinical Biochemistry, volume 26, 1988, pp. 209 –211.

K. M. Treseler, *Clinical Laboratory and Diagnostic Tests: Significance and Nursing Implications* (East Norwalk, CT: Appleton & Lange, 1995).

J. Woo and J. B. Henry, "Metabolic Intermediates and Inorganic Ions," in *Clinical Diagnosis and Management by Laboratory Methods*, J. B. Henry, ed. (Philadelphia: W. B. Saunders Company, 1996).

S. S. Zumdahl and S. Zumdahl, *Chemistry* (Boston: Houghton Mifflin College, 2000).

Chapter 3

Understanding the role of turbidity in Raman scattering using Monte Carlo simulations

3.1 Overview

The earlier experiments (Chapter 2) demonstrated that Raman spectroscopy can measure concentrations of analytes in aqueous and serum samples. However, prediction accuracies were reduced in whole blood. The difference between serum and whole blood is the presence of blood cells and fibrinogen. The presence of red blood cells in whole blood complicates optical measurements of blood analytes. In terms of the light propagation, the blood cells make samples optically turbid. Scattering and absorption alter the propagation of excitation and Raman light, and thus, a different optical collection scheme is required.

It is critical to understand the effect of scattering and absorption in whole blood to study the generation of the Raman signal inside the sample and the distribution and intensity of the Raman signal on the surface.

The research in this chapter was performed in collaboration with Dr. Annika M. K. Enejder, whose research is funded by the Swedish Research Council.

We, therefore, undertook to build a model of the light propagation in turbid biological tissue. Such a model would allow us to study the differences in light propagation and Raman scattering in clear media (e.g. serum and plasma) versus turbid media (e.g. whole blood). It would also allow us to study the surface distribution of Raman light and to determine if our measurements of surface distributions are reasonable. In addition, the surface distribution would be critical in designing a new collection system (Chapter 5) in order to optimize the light collection. Furthermore, the model could be applied to the study of light propagation in blood-tissue matrix, which would lead to transcutaneous measurements.

The propagation of light in turbid media has been studied extensively. Many analytical formulae, numerical simulations, and experimental measurements were studied in various geometries [Prahl et al. 1989, Wu et al. 1993, Fantini et al. 1997, Farrell et al. 1998, Venugopalan et al. 1998]. Their work provides fundamentals on which our model of Raman scattering is based. In this chapter, we developed a steady-state Monte Carlo simulation model for Raman scattering in turbid media.

By evaluating the Monte Carlo simulation results, we have developed a better understanding of Raman scattering in turbid biological tissue. We have determined how deeply we can probe into whole blood using Raman spectroscopy. We have also confirmed the surface distribution of Raman scattered light in whole blood with simulation results. The Monte Carlo simulation model was used to develop an insight into the angular and spatial distributions, and it was found that the coupling of the two can be approximated in certain ranges.

The first part of this chapter describes conceptually how light propagates in biological tissue and how it is studied. Physical phenomena, terminology, conventions, and methods of other researchers are discussed. In the second part, the development and validation of a Monte Carlo simulation model are described. Implementation of the software code to model Raman scattering is presented. The final part of this chapter discusses experimental measurements of surface distribution of Raman signal in whole blood, and compares the measurements and Monte Carlo simulation results. Also, simulation results are used to study the differences in light propagation between serum and whole blood.

3.2 Background

3.2.1 Optical properties

Light propagation in tissue is governed mainly by the elastic scattering[1] and absorption of photons by the tissue. Elastic scattering is a phenomenon in which the direction of light is changed without changes in its energy level when the light encounters discontinuities (e.g. index of refraction changes) in the medium, and absorption is the conversion of light into another form of energy (usually thermal energy). Mathematical models of the light propagation process often use macroscopic optical properties, including the absorption coefficient, μ_a, the scattering coefficient, μ_s, and the average cosine of single scattering angle θ, $g = \langle \cos\theta \rangle$. The absorption and scattering coefficients are the probability of

[1] In this thesis, "scattering" generally refers to elastic scattering, in which incoming photons are redirected but suffer no change in energy. Raman scattering, an inelastic process, is always called Raman scattering.

absorption and scattering per unit pathlength. In a similar manner, the Raman scattering coefficient, μ_r, is the probability of Raman scattering per unit pathlength. The sum of μ_a and μ_s is called the total attenuation coefficient, μ_t. In this thesis, we define the total attenuation coefficient, μ_t, as the sum of the three coefficients, μ_a, μ_s, and μ_r[2]. The reciprocal of these is the average distance that light will travel before being absorbed, elastically scattered, or Raman scattered, respectively. The scattering angle is the angle by which the direction of light changes at a scattering event. The reduced scattering coefficient is defined as $\mu_s' = \mu_s(1-g)$. The scattering angle in a single scattering event is calculated by a phase function. The phase function is a probability density function of the scattering angle, describing the probability of a scattering angle at which scattering occurs. Optical properties are functions of the wavelength.

3.2.2 Methods

When the wave properties of light are not relevant, light propagation can be described by the radiative transport equation [Ishimaru 1997]. The radiative transport equation is an integro-differential equation derived on the basis of the energy equilibrium in a scattering and attenuating medium. The analytical solution to the transport equation is usually not available, and the diffusion approximation is often used to study the light propagation in turbid media [Ishimaru 1997].

[2] When Raman scattering is not the phenomenon of interest, the Raman scattering coefficient is often neglected, as it is much smaller than the absorption and scattering coefficients in biological tissue.

In the diffusion approximation, the phase function often is approximated by two terms; one that accounts for the strong scattering in the forward direction and the other for the diffuse scattering. In the near-infrared range (770~1500 nm), the absorption coefficient is 0.01~1 mm^{-1} [van Gamert et al. 1990, Cheong et al. 1990]. The absorption coefficient in this wavelength range is very small compared to the tissue scattering coefficient, μ_s, which is on the order of 10 mm^{-1} [Cheong et al. 1990]. Since g is ~0.9 in many biological tissues, in the wavelength range 770~1200 nm, the reduced scattering coefficient, μ_s' is still greater than the absorption coefficient, which makes the diffusion theory an appropriate approximation for many biomedical applications [Prahl 1995, Chance and Alfano 1995]. The steady-state diffusion theory has long been used in interpreting multiply-scattered light from turbid media [Ishimaru 1997, Van de Hulst 1980]. Thereafter, numerous research work, varying from basic theoretical analysis [Schotland et al. 1993] to more clinically oriented applications [Peters et al. 1990, Sevick et al. 1991], has been reported to extract spectroscopic information and to image inhomogeneities embedded in turbid media using the diffusion approximation. As this approach has been extensively studied, its limitations have also been noted. In particular, the diffusion approximation is inaccurate at positions close to the source or boundary [Venugopalan et al. 1998], and for small inhomogeneities. In addition, although the solution of the diffusion equation is well known in an infinite medium, in many practical situations the physical boundary conditions often preclude a simple determination of the solution.

The diffusion approximation was also used in modeling the propagation of Raman scattered light in turbid tissue [Berger 1998]. The model consisted of two parts: calculation

of the steady-state energy density of the excitation beam throughout the volume, and propagation of Raman light radiated by from each small fraction of the volume. In the study of light propagation in whole blood, the model was not accurate due to the use of diffusion approximation and a simple phase function (delta-Eddington [Ishimaru 1997]). The calculation of the internal distribution of light showed discrepancies with a Monte Carlo simulation model (Appendix A).

Probabilistic methods have also been explored as tools to study the light distribution in tissue. One of the probabilistic methods is the photon migration model, introduced in 1987 [Bonner et al. 1987]. It models the light propagation in turbid media as the ensemble average of the "probabilistic photon migration paths" distributed within the turbid media, and the realization of the full path of each individual photon is governed by the scattering and absorption properties [Wu 1992], as well as the boundary conditions of the medium. A more traditional probabilistic model for photon propagation in general is the Monte Carlo simulation method. The Monte Carlo simulation is a statistical approach used to study the behavior of a complex system. In a Monte Carlo simulation of the radiative transfer equation, the scattering, absorption, and propagation of each photon or each packet of photons is determined by probability density functions. Each photon path is computationally formed by a number of consecutive events from the launch of a photon into the medium and the termination of the photon (either by absorption or exiting the medium).

The accuracy of a Monte Carlo simulation result is often determined by the statistics of its simulations. A large number of photons is necessary to obtain good statistics and

accurately model the distribution of light [Enejder 1997]. Running a simulation with many photons sometimes takes long run-time, and it is less of a problem as fast computers are readily available.

Furthermore, the Monte Carlo simulation method is flexible, and it can be easily adopted for the study of other optical phenomena, such as modeling of fluorescence light [Wu 1992, Welch et al. 1997] and Raman light. Many additional constraints can be implemented, and complex geometries can be used in simulations. As we aimed to develop a tool to study various biological tissues in various geometries, this flexibility made the Monte Carlo simulation method an attractive and powerful tool.

3.3 Monte Carlo simulation model for Raman scattering

In this section, a steady-state Monte Carlo simulation model for Raman scattering is described. The model enabled the study of the surface and internal distributions of Raman light. Computation results showed good agreement with experimental measurements. Therefore, it could be relied upon the design of an optimal system for Raman signal collection (Chapter 5).

3.3.1 Development of a Monte Carlo simulation model for Raman scattering

Our Monte Carlo simulation algorithm takes the geometry and optical properties, such as μ_a, μ_s, g, and μ_r, and calculates the surface and internal distribution of both excitation and Raman scattered light. Additional information (e.g. the distribution of Raman scattering events) can be obtained with a minor modification of the code.

This Monte Carlo simulation code consists of three parts: (i) the propagation of photons in turbid media, (ii) the Raman scattering event (i.e. conversion of the excitation photon to a Raman scattered photon), followed by (iii) the propagation of Raman scattered photons in the media and re-emergence at the surface. Initially, a packet of excitation photons enters the media. On average, photons travel a distance $1/\mu_{t,excitation}$ ($\mu_{t,excitation}$ is the total attenuation coefficient at the excitation wavelength) in each step, hit a scatterer, and change direction. In addition, some portion of the photon packet is absorbed. There is also a chance of Raman scattering, the probability of which is based on the Raman scattering coefficient, μ_r. The Raman scattered photons propagate inside the media with the average travel distance of $1/\mu_{t,Raman}$ ($\mu_{t,Raman}$ is the total attenuation coefficient for the Raman scattered wavelength) in each step, and experience scattering and absorption events. This is repeated until all the remaining excitation and Raman photons exit the media, or are absorbed. A flow chart of the Monte Carlo simulation summarizes the sequence of events the photons experience (Figure 3.1).

The probability density functions for the light propagation were adopted from standard Monte Carlo simulation code [Keijzer et al. 1989, Prahl et al. 1989, Wang et al. 1995]. From the probability density functions, the step size was calculated:

$$s = -\frac{ln(\xi)}{\mu_t}, \tag{3.1}$$

where ξ is a random number in a uniform probability density function between 0 and 1.

Each photon packet has a weight, which is proportional to the number of photons in the packet. For each step, the absorption of the photon packets' weight was determined from:

$$\Delta W = \frac{\mu_a}{\mu_t} W , \tag{3.2}$$

where W is the weight of the photon packet and ΔW is the weight absorbed in each step.

A phase function was used to calculate scattering angles. The selection of the proper phase function is important in Monte Carlo simulations of photon transport in turbid media [Roggan et al. 1999]. We used the Reynolds-McCormick phase function (also called Gegenbauer-Kernel phase function) [Reynolds and McCormick 1980, Yaroslavsky et al. 1996]:

$$p(\theta) = \frac{\alpha \cdot g}{\pi((1+g)^{2\alpha} - (1-g)^{2\alpha})} \times \frac{(1-g^2)^{2\alpha}}{(1+g^2-2g\cos\theta)^{\alpha+1}}, \tag{3.3}$$

where α is a free parameter. Due to this degree of freedom, the Reynolds-McCormick phase function is sometimes more accurate in modeling scattering due to various scatterers than Henyey-Greenstein phase function, which is a special case of the Reynolds-McCormick phase function when α=0.5. The Henyey-Greenstein phase function is formulated as:

$$p(\theta) = (1-g^2)(1+g^2-2g\cos\theta)^{-3/2} , \tag{3.4}$$

[Henyey and Greenstein 1941, van de Hulst 1980]. The Henyey-Greenstein phase function is often used in biomedical optics because it matches well with goniophotometric measurements of tissues for a limited range of angles [Prahl 1988, van Gemert et al. 1989].

In modeling light propagation in whole blood (refractive index 1.333 for the surrounding medium and 1.402 for the red blood cells), the Reynolds-McCormick phase function with α=1 and g=0.9924 approximates a Mie phase function for a 5.56 μm particle at 633 nm [Roggan et al. 1999]. The Mie phase function is based on the calculation of electromagnetic waves scattered and absorbed by a small particle. The Mie phase function is usually difficult to calculate for non-spherical particles, and the solutions for spherical and spheroidal particles are used as an approximation [Malfait 1999].

For each photon at the excitation wavelength, a probabilistic test is performed to decide whether the photon will experience Raman scattering or not. The probability for Raman scattering is determined by the ratio of the Raman scattering coefficient and the total attenuation coefficient:

$$p_{Raman} = \mu_r / \mu_t , \tag{3.5}$$

where P_{Raman} is the propability of Raman scattering. The Raman scattering coefficient, μ_r, is a function of the concentration and composition of the Raman scatterers and their Raman cross-section. The Raman cross-section, σ, is associated with the probability of Raman scattering for a unit concentration of Raman scatterers and a unit path length:

$$\mu_R = c \cdot \sigma . \tag{3.6}$$

The Raman scattering coefficient, μ_r, is orders of magnitude smaller than μ_s or μ_a in most biological samples. The Raman cross-section of biological molecules is typically on the order of $10^{-29} \sim 10^{-31}$ cm^2/mole [Schrötter and Klöckner 1979]. When the concentration of the Raman scatter is 10 mmole/L (which is within the physiological range of a blood

analyte, glucose), the Raman scattering coefficient is on the order of $10^{-34} \sim 10^{-36}$ cm^{-1}. In Monte Carlo simulations, μ_r values higher than physical levels are used to reduce the computation time. As long as μ_r is orders of magnitude smaller than μ_a or μ_s, an increase in μ_r does not affect the pattern of elastic scattering and absorption in the media.

From the comparison of Eq. (3.2) and Eq. (3.5), we find that the absorption of the excitation light and the Raman scattering event are associated. For each incoming photon, absorption and Raman scattering may occur with their given probabilities, respectively. Thus, the ratio of absorption and Raman scattering events is determined by the ratio of the absorption and Raman scattering coefficients, and the distribution of absorbed excitation light and the distribution of Raman scattering events should match, on average. This principle was used in the validation of the Monte Carlo simulation code.

The Raman scattering is assumed to be an isotropic event, and the direction of the light is randomized after each Raman scattering. This assumption is valid for non-polarized excitation light [Schrötter and Klöckner 1979]. It is also a good approximation for polarized excitation light in turbid media, because polarized excitation light (e.g. laser beam) becomes depolarized after multiple scattering events.

The Raman scattered light is then propagated in a similar manner in which the excitation light is propagated. The Raman scattering shifts the wavelength of light, and accordingly, the optical properties, since they are wavelength dependent.

Both excitation and Raman scattered photons can be terminated before they emerge on the surface when their weights are small. This is to reduce the computation time by discarding photons that do not contribute significantly to overall computation results.

When the weight of a photon packet is lower than its initial weight by factor of 10^4, it was subject to "roulette test [Wang et al. 1995]" which is a statistical test to determine the termination of the packet. In the test, nine out of ten photon packets are randomly selected and terminated. The weight of the remaining one photon packet is increased by ten times, and the packet continues to propagate until its becomes subject to the test again.

When a photon packet strikes the boundary, another probabilistic test is performed using Fresnel's formula [Born and Wolfe 1997] to determine whether the photon packet passes the boundary or undergoes an internal reflection. The direction of the packet traversing the boundary is calculated from the Snell's law, which determines the angle changes of refracted light. The direction of the internally reflected light is determined in a manner that the average of direction cosines before and after the internal reflection is perpendicular to the boundary surface.

Typical simulations were performed with one million photon packets. The computation time depends on optical properties of media, and it took about one hour to calculate propagation of Raman light in whole blood with one million photon packets. The internal and surface distribution of excitation and Raman scattered light was recorded. The simulation results are shown in the following sections.

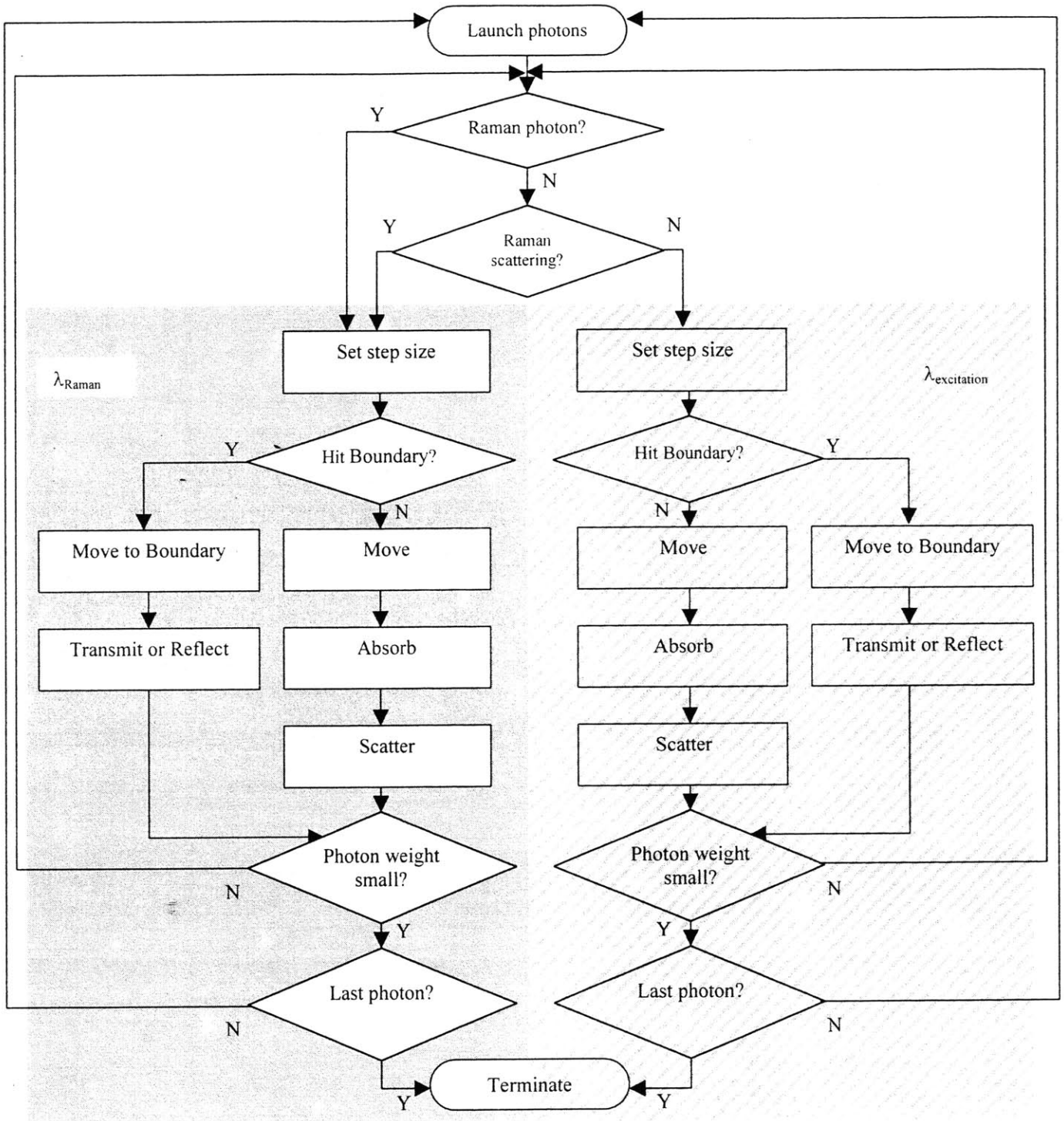

Figure 3.1. Flow chart of a Monte Carlo simulation algorithm

3.3.2 Validation of the Monte Carlo simulation model for Raman scattering

This subsection describes how the Monte Carlo simulation code was validated. We used a standard Monte Carlo simulation code [Wang et al. 1995] for comparison, as the standard code has been tested by many researchers. Each part of the Monte Carlo simulation model was validated separately. First, the propagation of excitation and Raman scattered light was validated by comparing the results calculated by our Monte Carlo simulation code and the standard Monte Carlo simulation code. The surface distribution of light calculated by our Monte Carlo simulation code was compared with that calculated by the standard Monte Carlo simulation code. Second, the generation of Raman scattering was compared with the energy distribution of excitation light. The internal distribution of absorbed excitation light and the distribution of Raman scattering event were calculated by our Monte Carlo simulation code, and the two were compared. Third, the propagation of Raman scattered light and the propagation of light from an isotropic source was compared.

Figure 3.2 shows the surface distribution of excitation light emerging from turbid media with various optical properties calculated by our Monte Carlo simulation code and the standard Monte Carlo simulation code. The geometry of the sample was a semi-infinte medium, and the excitation beam was an infinitely narrow and collimated (pencil) beam. The properties used in this simulation were μ_a=0.5 mm^{-1}, μ_s=100 mm^{-1}, and α=0.5, and g values were 0.86, 0.93, and 0.995. Also tested were absorption coefficients (0.05 and 5 mm^{-1}) and another scattering coefficient (300 mm^{-1}). In all cases, the reflectance and transmittance curves calculated by the two Monte Carlo simulation codes matched well.

This indicates that the light propagation part of the Monte Carlo simulation code for Raman scattering works closely related to the standard Monte Carlo simulation code, and thus, is validated, over the range of optical properties tested (μ_a=0.05~0.5 mm^{-1}, μ_s=100~300 mm^{-1}, and g=0.86~0.995).

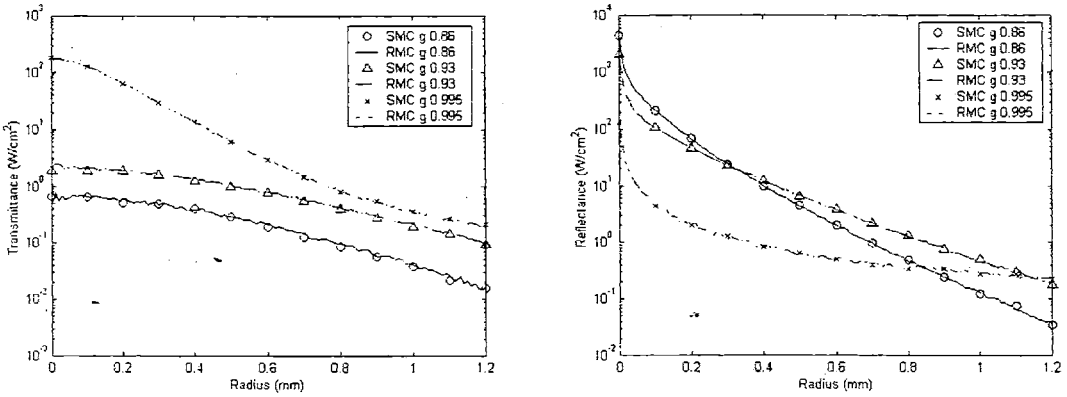

Figure 3.2. Transmittance (left) and reflectance (right) of excitation light calculated for various mean cosine scattering angles by the standard Monte Carlo simulation model (SMC) and our Monte Carlo simulation model for Raman scattering (RMC).

Figure 3.3 shows the distribution of excitation light absorbed by the media and the distribution of Raman scattering events. The distribution of excitation light absorbed by the media was available as one of the standard outputs of the simulation code. The location of Raman scattering events was obtained by modifying our Monte Carlo simulation code. The geometry of the sample was a semi-infinite medium, and the excitation beam was an infinitely narrow and collimated (pencil) beam. The properties used in this simulation were μ_a=0.8 mm^{-1}, μ_s=172 mm^{-1}, g=0.99, and α=0.5. The distributions in Figure 3.3 show traces of certain photons, which could be averaged by using more photons in the simulation. Figure 3.3. was generated from the simulation result with one million photons, and the run-time was approximately one hour. As discussed before, the distribution of absorbed

excitation light and the distribution of Raman scattering events should match well as the numbers of absorption and Raman scattering events are proportional to the number of incoming photons. The two distributions matched well (Figure 3.3). This indicates that the frequency of Raman scattering events is proportional to the energy of the incoming light, and thus, the Raman scattering part of the Monte Carlo simulation code is validated.

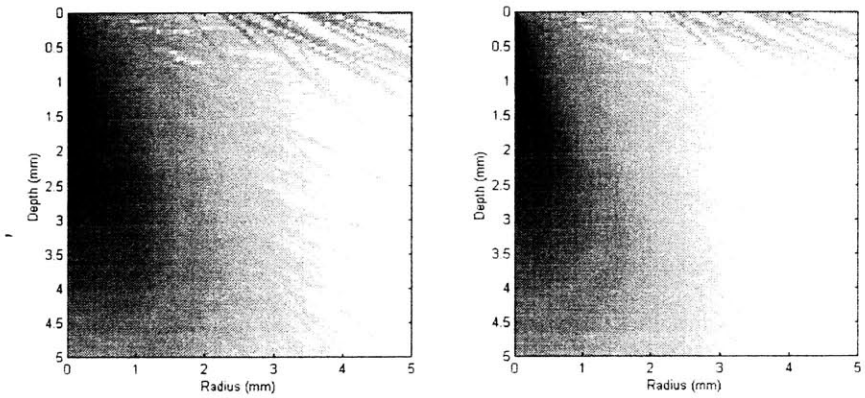

Figure 3.3. The distribution of excitation light absorbed by the media (left) and the distribution of Raman scattering events in the media (right).

Finally, the propagation of Raman scattered light was tested. Since Raman scattering is modeled as an isotropic process [Schrötter and Klöckner 1979], we compared the propagation of Raman scattered light and the propagation of light from an isotropic source inside the medium. The comparison confirmed that the propagation of Raman scattered light and light emerging from an isotropic source are identical, and the propagation of Raman scattered light was validated.

In summary, we have validated our Monte Carlo simulation model by validating each part (light propagation and Raman scattering). This validated model was used in study of the surface distribution of Raman light and the radiant power of the Raman signal

generated in media of various optical properties relevant for tissue. Further validation with whole blood experiments is discussed in the next section.

3.4 Monte Carlo simulation results

3.4.1 Angular and spatial distribution of Raman signal in whole blood

Experiments were performed to measure the surface distribution of Raman signals in whole blood. The measurements were compared with Monte Carlo simulation results, and showed good agreement. Also, the measurements were used in the design of a high sensitivity system for Raman spectroscopy (Chapter 5).

Measurements of the spatial distribution of the Raman signal in whole blood

The Raman spectroscopy system described in Chapter 2 was used to measure the spatial distribution of Raman signal in whole blood. The system was used in a manner different from the way Raman spectra are collected. Since the aim of this study was to measure the Raman signal distribution with high spatial resolution, the Raman signal collected by a single fiber in the fiber bundle was recorded. The core diameter of the collection fiber was 100 μm, and it imaged a 44 μm-diameter spot on the sample by means of the optical components in the system. The reflective objective, the focusing lens, and the optical components in the collection system, were used as imaging optics. They collect light between 14 and 33 degrees, and image the distribution of the Raman signal from the whole blood surface onto the front surface of the optical collection fiber bundle. By translating

the fiber bundle along one axis while the sample was irradiated by the laser beam, Raman spectra from various regions of the whole blood sample were collected. Each Raman spectrum corresponded to a region of the sample with a certain distance from the laser excitation beam. Since the geometry was considered to be independent on the azimuthal angle, measuring the spatial distribution from a single scan was sufficient to describe the distribution over the entire surface. For each spectrum, the position of the fiber bundle was recorded from readings on the micrometer of the translation stage. The intensity of Raman signal was measured by counting the intensity of a given Raman peak after fluorescence background subtraction. The distribution of the Raman signal on the fiber bundle surface was plotted. By scaling this distribution with the magnification ratio of the optical components, the distribution of the Raman signal on whole blood was obtained (Figure 3.4).

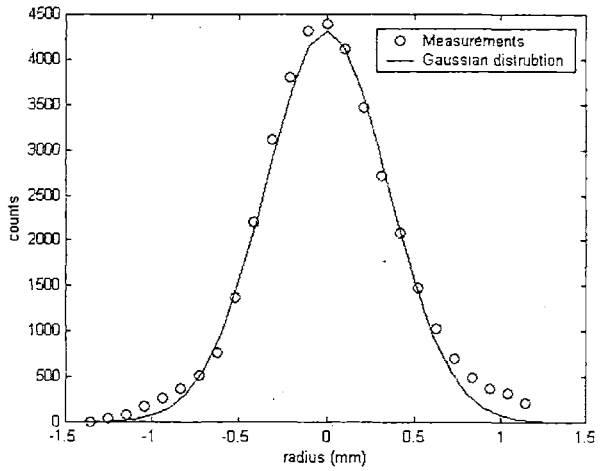

Figure 3.4. Spatial distribution of Raman signal emerging from the surface of whole blood. The dots are experimental measurements, and the line is a Gaussian fit. Monte Carlo simulation was not used.

The Raman signal emerging from a whole blood sample is similar to a Gaussian distribution. The full-width-at-half-maximum (FWHM) of the Raman signal is 0.8 mm. The FWHM of the excitation beam was 100 μm, which is much narrower than the width of the Raman distribution. The fact that the Raman distribution is wider than the excitation beam indicates that multiple elastic scattering in whole blood spreads the photons, and resulted in a broad distribution of light.

Measurements of angular distribution of Raman signals in whole blood

The experimental setup described in Chapter 2 was useful in measuring the spatial distribution of the Raman signal. However, it was not suitable for measuring the angular distribution of the Raman signal, because the umbra of the reflective objective blocked the light emerging at an angle smaller than 17°. Thus, a different system was employed to measure the angular distribution of the Raman signal emerging from a whole blood sample.

Figure 3.5 displays the schematic diagram of the system used for the angular distribution measurement. The excitation beam was delivered to the sample at 30°. By employing an off-axis geometry, we avoided blocking the low angle beams. A camera lens was used to collect the Raman signal from the sample, and two apertures were placed between the sample and the camera lens. The first aperture was placed close to the sample, and the "near sample" aperture set the size of the spot from which the Raman signal was collected. The second aperture was placed close to the camera lens, and the size of this aperture could be varied. Varying the size of this "near lens" aperture enabled collection of Raman spectra with different collection angle limits. Photons emerging within the

collection angle limit were collected, and Raman spectra of the sample were collected with incremental aperture sizes. The collection angle was calculated from the "near lens" aperture size and the distance between the sample and the lens, which was the focal length of the lens. Using this data, the angular distribution of the Raman signal emerging from the whole blood sample was generated (Figure 3.6). The distribution in Figure 3.6 is the cumulative angular distribution.

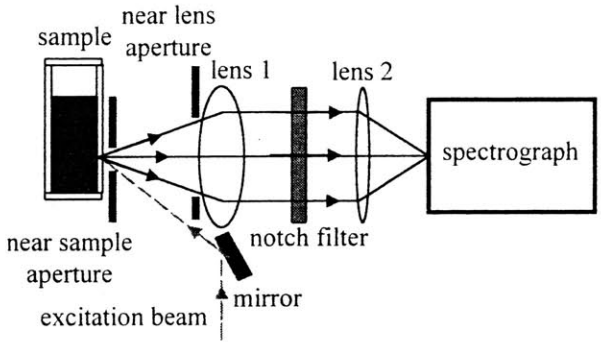

Figure 3.5. Schematic diagram of the experimental setup used for measuring the angular distribution of the Raman signal emerging from the surface of whole blood

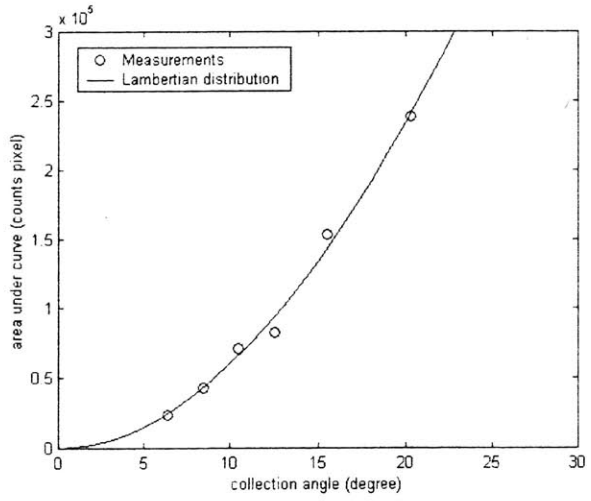

Figure 3.6. Cumulative angular distribution of Raman signal emerging from the surface of whole blood. The dots are measurements, and the line is a Lambertian fit. In a Lambertian distribution, the angular distribution function of light is cosine.

3.4.2 Comparison of Monte Carlo simulation results and experimental measurements

The experimental measurements were compared with the Monte Carlo simulation results. The Monte Carlo simulation code accepted scattering and absorption properties of a sample as input variables and provided the angular and spatial distribution of the Raman light as output variables. Many researchers have studied the optical properties of biological samples, including whole blood [Cheong et al. 1990]. For instance, the absorption coefficient of lysed blood samples was measured [Zijlstra et al. 1991], and the scattering coefficient of diluted blood samples was measured using a laser Doppler technique [Kienle et al. 1996]. Among many measurements, the optical properties of whole blood measured by Roggan were most suitable for the Monte Carlo simulations, since these measurements were performed on samples that were not manipulated (lysed or diluted) [Roggan et al. 1999]. The properties used in the Monte Carlo simulation are listed in Table 3.1.

Table 3.1. Input parameters used in the Monte Carlo simulation

	wavelength	μ_a	μ_s	g	n
Excitation wavelength	830 nm	1.04/mm	216/mm	0.990	1.37
Raman-scattered wavelength	910 nm	1.36/mm	192/mm	0.985	1.37

The optical properties of whole blood change monotonically over the wavelength range of interest (830~1000 nm). Over this wavelength range, μ_a ranges from 0.8 to 1.6/mm, μ_s varies from 180 to 240/mm, and the range of g is from 0.98~0.99. The changes in the optical properties were not significant, and a single Raman-scattered wavelength was

assumed to be sufficient to study the effect of the turbidity using Monte Carlo simulations. If needed, the Monte Carlo simulation model could be modified to model multiple Raman-scattered wavelengths.

The spatial and angular distribution of the Raman signal emerging from whole blood was computed in a simulation with 1,000,000 photons. The Raman scattering coefficient, μ_R, used was 0.02 mm^{-1}, whereas the physical range of μ_R for blood analytes is typically on the order of 10^{-34} ~10^{-40} mm^{-1}. Although this was higher than the Raman scattering coefficient of blood analytes, it was still much smaller than the absorption and scattering coefficients, and did not interfere with the elastic scattering and absorption in the sample. Furthermore, a high μ_R enables a good statistics in a simulation with fewer photons, which leads to shorter computation times.

The Monte Carlo simulation results indicated that the angular distribution was not always Gaussian and Lambertian, respectively. For a small radius spot the angular distribution was much narrower than the Lambertian distribution, and for a large radius spot it was wider than the Lambertian distribution. However, on average over our region of interest, the angular distribution was similar to the Lambertian distribution. The simulation results and the experimental measurements are plotted together in Figure 3.7, and the curves overlap well. This demonstrates that the Monte Carlo simulation code can be used to model light propagation in whole blood. Thus, this information could be used in the design of a high-sensitivity spectroscopy system (Chapter 5).

When a narrow input beam irradiated the medium, a broad surface distribution of Raman scattered light is observed. The broad surface distribution of Raman scattered light

is due to multiple scattering in whole blood. If the medium had a higher scattering coefficient without a higher absorption coefficient, it could increase the width of the surface distribution and the number of Raman scattered photons emerging from the whole blood surface, whereas a higher absorption coefficient can decrease the width of distribution and the number of photons.

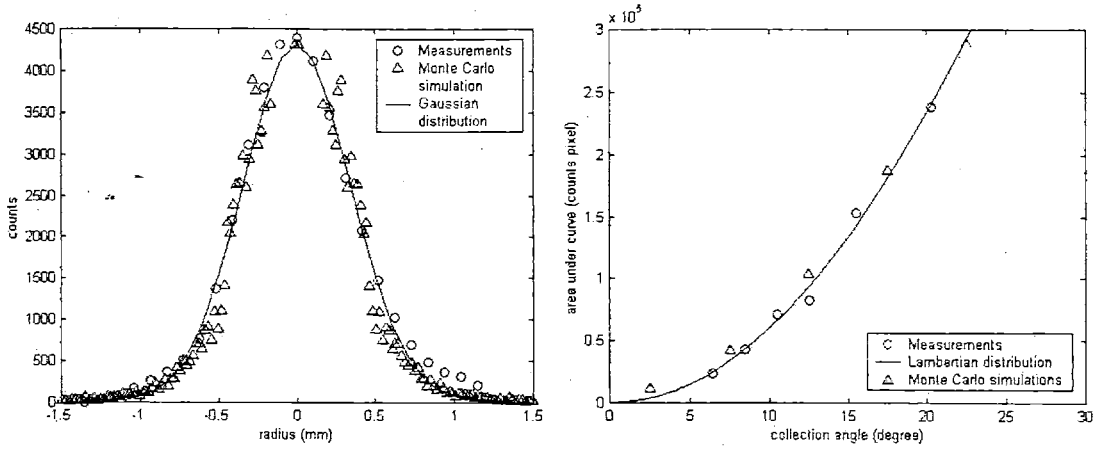

Figure 3.7. Comparison of Monte Carlo simulation results and experimental measurements. The experimental measurements overlap with the simulation results both in spatial distribution (left) and angular distribution (right).

3.5 Effect of scattering and absorption in Raman signal intensity

The experimental results in Chapter 2 showed that the intensity of Raman signal was lower in whole blood than in serum by factor of 4, and it was necessary to understand the differences between serum and whole blood. The difference between serum and whole blood is the presence of red blood cells and fibrinogen, in terms of their compositions.

While serum has negligible absorption and scattering coefficients in the wavelength range of our interest, the scattering and absorption in whole blood are significant (e.g. μ_a = 1.06 mm^{-1} and μ_s = 216 mm^{-1} at 900 nm for 45% hematocrit [Roggan 1999]). The scattering and absorption coefficients in whole blood are associated with the hematocrit, the volume fraction of red blood cells in whole blood. This is because the red blood cells are the major source of scattering in whole blood, and hemoglobin within red blood cells is the major source of absorption. Thus, in our studies, serum can be considered as whole blood with zero hematocrit.

On-the positive side, for blood analyte measurements the scattering increases the pathlength, which in turn increases the chance of Raman scattering. However, the scattering spreads out the Raman photons, while the absorption attenuates the intensity of Raman signal. Absorption and scattering affect the intensity of the emitted Raman signal in a complex way. Thus, the effect of various hematocrit was studied using the Monte Carlo simulation model, and the simulation results explained the difference in signal intensity between serum and whole blood, as well as the effect of hematocrit changes in whole blood samples. Due to the complex nature of competing but related processes, Monte Carlo simulations were helpful in understanding the effect of turbidity on Raman signal intensity.

In a Monte Carlo simulation, the scattering and absorption properties were varied to model different hematocrit values. The amount and the size of red blood cells determine the scattering and absorption properties of whole blood. Although the physiological normal range of hematocrit is 35 ~ 50%, simulations were performed to model the hematocrit range between 1 ~ 50%. The simulation for 1% hematocrit was performed to approximate

serum. Figure 3.8 shows the power (W) of the Raman scattered light emerging from the sample surface for various hematocrit samples. It does not include extreme levels of hematocrit, such as 70%. However, such extreme levels are rare, and also, Figure 3.8 indicates that the difference in power of the Raman scattered light at 50% and 70% can be small.

Two facts are notable in Figure 3.8. First, the power of the Raman signal emerging from the sample surface decreased with increasing hematocrit. In a turbid sample absorption and scattering attenuated the Raman signal, and therefore, fewer Raman photons emerged from the sample surface. The radiant power at a physiological hematocrit was significantly reduced from the power in a clear sample. This indicates that the presence of red blood cells reduced the intensity of Raman signal in whole blood. Also, this explains the reduced signal intensity in whole blood versus serum. According to the Monte Carlo simulations with consideration of the collection optics, the power of Raman scattered light is reduced by a factor of 3 in whole blood (when light is collected by the previous system), compared with the power in serum. This reduction factor is similar to the factor of 4 reduction observed using the previous experimental setup (Chapter 2). Second, the change in radiant power was not significant over a physiological range of hematocrit. The radiant power varied by less than 30% over the hematocrit range between 35% and 50%, and the effect of this variation on prediction error was less than 10% of the average concentration. For extreme levels of hematocrit, such as 5% and 70%, the effect of the hematocrit variation on prediction error would be greater, and it could be a significant part of the total

prediction error. A calibration would be needed to deal with samples of extreme hematocrit values. The prediction error is discussed in detail in Chapter 4.

In other biological tissue, absorption coefficient is not as strong as that in whole blood and scattering coefficient is comparable (μ_a <0.1/mm, μ_s' ~2/mm, and $g \sim 0.9$) and [Cheong et al. 1990]. As the absorption is weaker, the intensity of Raman signal in such tissue could be stronger than that in whole blood.

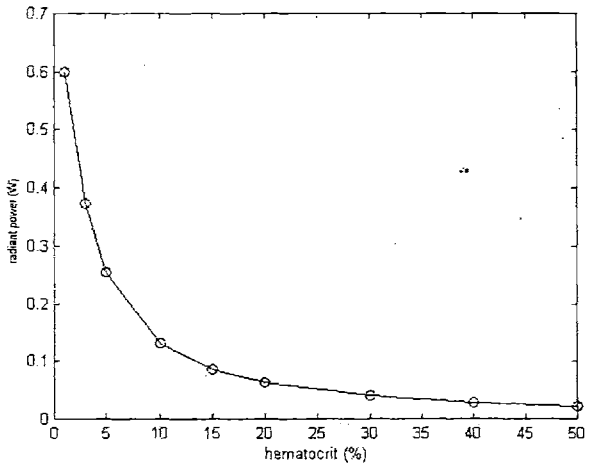

Figure 3.8. The power of the emerging Raman signal in samples with various hematocrit values. The Monte Carlo simulation model was used to compute the power.

3.6 Conclusion

To study the effect of turbidity on the Raman signal, a Monte Carlo simulation model was developed. The simulation results and the experimental measurements matched well, confirming the accuracy of the simulation in modeling whole blood. Both the simulation and the experiment characterized the distribution of the Raman signal emerging from a whole blood sample irradiated with a 100 μm excitation beam. The FWHM of the spatial

distribution was 0.9 mm diameter, and the angular distribution was similar to the Lambertian distribution. This information about the signal distribution was used to design a system with optimal collection efficiency (see Chapter 5).

Furthermore, the Raman signal intensity in various hematocrit samples was simulated. Samples with high hematocrit had high scattering and absorption properties, reducing the radiant power of the Raman signal emerging from whole blood. The red blood cells reduced the radiant power in whole blood significantly, when compared with the radiant power in serum or aqueous samples. However, the variation of radiant power in whole blood samples was small over a representative range of hematocrit, and such a change in radiant power has little effect on the prediction error.

References

A. J. Berger, "Measurement of analytes in human serum and whole blood samples by near-infrared Raman spectroscopy" (Cambridge: Massachusetts Institute of Technology, doctoral thesis, 1998).

R. Bonner, R. Nossal, and S. Havlin, and G. Weiss, "Model for photon migration in turbid biological media," *Journal of Optical Society of America A*, volume 4, 3 1987, pp. 423-432.

M. Born and E. Wolf, *Principes of Optics* (New York: Cambridge University Press, 1997).

B. Chance and R. Alfano, *Proceedings of Optical Tomography, Photon Migration, and Spectroscopy of Tissue and Model Media: Theory, Human Studies, and Instrumentation*, SPIE 2389 (1995).

W.-F. Cheong, S. A. Prahl, and A. J. Welch, "A review of the optical properties of biological tissues," *IEEE Journal of Quantum Electronics*, volume 26, 12, 1990, pp. 2166 –2185.

A. M. K. Enejder, "Light scattering and absorption in tissue - models and measurements" (Lund Institute of Technology, doctoral thesis, 1997).

S. Fantini, M. A. Franceschini, and E. Gratton, "Effective source term in the diffusion equation for photon transport in turbid media," *Applied Optics*, volume 36, 1997, pp. 156 –163.

T. J. Farrell, R. P. Hawkes, M. S. Patterson, and B. C. Wilson, "Modeling of photosensitizer fluorescence emission and photobleaching for photodynamic therapy dosimetry," Applied Optics, volume 37, 1998, pp. 7168 – 7183.

M. J. C. van Gemert, S. L. Jacques, H. J. C. M. Sterenborg, and W. M. Star, "Skin optics," *IEEE Transactions on Biomedical Engineering*, volume 36, 1989, pp. 1146-1154.

M. J. C. van Gemert, A. J. Welch, S. L. Jacques, Q. F. Cheong, W. M. Star, "Light distribution, optical properties, and cardiovascular tissues," in *Lasers in cardiovascular medicine and surgery: Fundamentals and techniques*, G.S. Abela, ed. (Norwell, MA: Kluwer Academic Publishers, 1990).

R. A. J. Groenhuis, J. J. Ten Bosch, and H. A. Ferwerda, "Scattering and absorption of turbid materials determined from reflection measurements. 1: Theory," *Applied Optics*, volume 22, 16 1983, pp. 2456-2462.

G. M. Hale and M. R. Querry, "Optical-constants of water in 200-nm to 200-μm wavelength region," *Applied* Optics, volume 12, 3 1973, pp. 555 -563.

L. G. Henyey and J. L. Greenstein, "Diffuse radiation in the galaxy," *Astrophysical Journal*, volume 93, 1941, pp. 70-83.

H. C. van de Hulst, *Multiple Light Scattering, Vol. 2* (New York: Academic Press, 1980).

D. E. Hyde, T. J. Farrell, M. S. Patterson, and B. C. Wilson, "A diffusion theory model of spatially resolved fluorescence from depth-dependent fluorophore concentrations," *Physics in Medicine and Biology*, volume 46, 2 2001, pp. 369 - 383.

A. Ishimaru, *Wave Propagation and Scattering in Random Media*. (New York: Wiley-IEEE Press, 1997).

M. Keijzer, S. L. Jacques, S. A. Prahl, and A. J. Welch, "Light distributions in artery tissue: Monte Carlo simulations for finite-diameter lasers beams," *Lasers in Medicine and Surgery*, volume 9, 1989, pp. 148-154.

A. Kienle, M. S. Patterson, L. Ott, and R. Steiner, "Determinatino of the scattering coefficient and the anisotropy factor from laser Doplper spectra of liquids including blood", *Applied Optics*, volume 35, 19 1996, pp. 3404 – 3412.

H. Liu, D. A. Boas, Y. Zhang, A. G. Yodh, and B. Chance, "Determination of optical properties and blood oxygenation in tissue using continuous NIR light," *Physics in Medicine and Biology*, volume 40, 1995, pp. 1983 -1993.

K. Malfait, "The properties and evolution of the dusty disks surrounding Herbig Ae/Be stars" (Leuven: Catholic University of Leuven, doctoral thesis, 1999).

V. G. Peters, D. R. Wyman, M. S. Patterson, and G. L. Frank, "Optical properties of normal and diseased human breast tissue in the visible and near infrared," *Physics in Medicine and Biology*, volume 35, 9 1990, pp. 1317-1334.

S. A. Prahl, M. Keijzer, S. L. Jacques, and A. J. Welch, "A Monte Carlo model of light propagation in tissue," in *SPIE Proceedings of Dosimetry of Laser Radiation in Medicine and Biology*, volume IS 5, G. J. Müller and D. H. Sliney, ed. (1989).

S. A. Prahl, "Charts to Rapidly Estimate Temperature following Laser Irradiation," in *Laser-Tissue Interaction VI*, S. L. Jacques ed., Proceedings of SPIE 2391, pp. 499-511, (1995).

L. O. Reynolds and N. J. McCormick, "Approximate two-parameter phase function for light scattering," *Journal of Optical Society of America*, volume 70, 1980, pp. 1206-1212.

A. Roggan, M. Friebel, K. Dörschel, A. Hahn, and G. Müller, "Optical properties of circulating human blood in the wavelength range 400-2500 nm," *Journal of Biomedical Optics*, volume 4, 1 1999, pp. 36 -46.

J. Schotland, J. C. Haselgrove, and J. Leigh, "Photon hitting density," *Applied Optics*, volume 32, 4 1993, pp. 448-453.

H. W. Schrötter and H. W. Klöckner, "Raman scattering cross sections in gases and liquids," in *Raman Spectroscopy of Gases and Liquids,* A. Weber, ed. (New York: Springer-Verlag, 1979).

E. Sevick, B. Chance, J. Leigh, S. Nioka, and M. Maris, "Quantitation of time- and frequency-resolved optical spectra for the determination of tissue oxygenation," Analytical Biochemistry, volume 195, 2 1991, pp. 330-351.

V. Venugopalan, J. S. You, and B. J. Tromberg, "Radiative transport in the diffusion approximation: An extension for highly absorbing media and small source-detector separations," *Physical Review E*, volume 58, 2 1998, pp. 2395 –2407.

L.-H. Wang, S. L. Jacques, L.-Q. Zheng, "MCML - Monte Carlo modeling of photon transport in multi-layered tissues," *Computer Methods and Programs in Biomedicine*, volume 47, 1995, pp. 131 -146.

A. J. Welch, C. M. Gardner, R. Richards-Kortum, E. Chan, G. Criswell, J. Pfefer, and S. Warren, "Propagation of fluorescence light," *Lasers in Surgery and Medicine*, volume 21, 1997, pp. 174-189.

J. Wu, "Modeling light-tissue interaction: applications to diffuse reflectance and fluorescence spectroscopy of human tissue" (Cambridge: Massachusetts Institute of Technology, master thesis, 1992).

J. Wu, M. S. Feld, and R. P. Rava, "Analytical model for extracting intrinsic fluorescence in turbid media," *Applied Optics*, volume 32, 1993, pp. 3585 –3595.

A. N. Yaroslavsky, I. V. Yaroslavsky, T. Goldbach, and H.-J. Schwarzmaier, "The optical properties of blood in the near infrared spectral range," in *Optical*

diagnostics of living cells and biofluids, D. L. Farkas, R. C. Leif, A. V. Priezzhev, T. Asakura, and B. J. Tromberg, eds., Proceedings of the Society of Photo-Optical Instrumentation Engineers 2678, 314-324 (SPIE, Bellingham, 1996).

W. G. Zijlstra, A. Buursma, and W. P. Meeuwsen var der Roest, "Absorption spectra of human fetal and adult oxyhemoglobin, de-oxyhemoglobin, carboxyhemoglobin, and methemoglobin," *Clinical Chemistry*, volume 37, 9 1991, pp. 1633-1638.

Chapter 4

Raman spectra of biological samples and linear multivariate analysis

4.1 Overview

As discussed previously, Raman spectroscopy provides quantitative spectral information about sample composition. Intensities of spectral features, called bands, are due to specific vibrations of molecules. Intensities of bands contain information about molecular concentrations. However, it is often difficult to interpret Raman spectra of biological samples due to the complexity of these samples. The presence of multiple components results in many overlapping Raman bands. Severe background noise also complicates any attempt to use Raman peak intensities for accurate quantitative analysis. Thus, more sophisticated analysis techniques are required to extract the information contained in the Raman spectra. Techniques to analyze multivariable data sets have been well studied by statisticians and analytical chemists, and such techniques are known as multivariate analysis methods [Sharma 1996] or chemometrics [Kramer 1998]. This chapter discusses certain multivariate regression[1] techniques. By using multivariate techniques, Raman

[1] Regression is a functional relationship among experimental data. Such relationship is typically used to predict quantities of interest when other quantities are known.

spectra of human serum and whole blood were better understood. Also, the effect of signal-to-noise ratio (S/N) on prediction accuracy was studied.

4.2 Background

Certain assumptions are necessary in order to use linear multivariate techniques in the analysis of Raman spectra. First, a Raman spectrum is assumed to be a linear superposition of the Raman spectra of the components. Thus, Raman spectrum of a mixture of chemicals would be the weighted sum of each of the chemicals' Raman spectra. Also, the signal intensity of a chemical's Raman bands are assumed to be linearly proportional to the chemical concentration. The linearity of Raman spectra in biological tissue was experimentally established [Manoharan 1992]. In this study, mixtures of cholesterol powder and barium sulfate powder were used for spectral collection. The intensity ratios of the cholesterol peak at 1440 cm^{-1} and the barium sulfate peak at 987 cm^{-1} were plotted against the weight percentage of cholesterol in the mixture. The intensity ratios and the weight percentage were found to be linear, with a correlation coefficient of 0.997. This implies that Raman spectra of tissue can be described as a linear superposition of individual chemicals, as long as the scattering and absorption properties of tissue do not significantly distort the signal.

Since changes in scattering and absorption properties are not significant in whole blood (Chapter 3), Raman spectra can be modeled as a linear superposition of component spectra, and linear techniques can be used to analyze Raman spectra. For whole blood, the linear superposition can be formulated as

$$
\begin{aligned}
S_{\text{whole blood}} &= c_{\text{albumin}} \cdot P_{\text{albumin}} \\
&+ c_{\text{triglycerides}} \cdot P_{\text{triglycerides}} \\
&+ c_{\text{urea}} \cdot P_{\text{urea}} + c_{\text{glucose}} \cdot P_{\text{glucose}} \\
&+ \cdots
\end{aligned}
\tag{4.1}
$$

where $S_{\text{whole blood}}$ is the Raman spectrum of whole blood, c_i is the concentration of component i, and P_i is the Raman spectrum of component i normalized by its concentration. For a single Raman spectrum, Eq. (4.1) can be expressed in vector form:

$$S = C \cdot P, \tag{4.2}$$

where S is the Raman spectrum of the sample, C is the component concentrations in a row vector, and $\boldsymbol{P}$ is the matrix of component spectra, with each spectrum occupying a row of wavelengths. In matrix notion, Eq. (4.2) can be written, for a set of samples, as:

$$\mathbf{S} = \mathbf{C} \cdot \mathbf{P}, \tag{4.3}$$

where $\boldsymbol{S}$ is the matrix of Raman spectra, $\boldsymbol{C}$ is the matrix of component concentrations in the samples, and $\boldsymbol{P}$ is the matrix of component spectra. When the number of samples is n, the number of components is p, and the number of wavelength points in each spectrum is m, $\mathbf{S}$ is an $n \times m$ matrix, $\mathbf{C}$ is an $n \times p$ matrix, and $\mathbf{P}$ is a $p \times m$ matrix.

There are numerous multivariate analysis algorithms. This section discusses basic regression techniques and multivariate analysis algorithms for concentration measurements: ordinary least squares (OLS) regression, classical least squares (CLS) regression, principal component regression (PCR), partial least squares (PLS) regression, and hybrid linear

analysis (HLA). In concentration measurements, the goal of these techniques is to find a projection vector that extracts concentration information from spectra:

$$C = S \cdot B, \tag{4.4}$$

where B is the projection vector. For each analyte in every data set, there exists only one ideal projection vector that models the data set most accurately. When the multivariate techniques are carefully applied, the projection vectors (B's) obtained with different multivariate techniques should all closely approximate the ideal projection vector.

4.2.1 Calibration, prediction and validation

Multivariate analysis for extracting concentrations is performed in two steps: calibration and prediction. Calibration is the process of developing a mathematical relationship between physical quantities (e.g. spectra and concentrations). Prediction is the process of applying the mathematical model developed during calibration to extract concentration information from spectra.

In calibration, a mathematical model is developed to describe the spectral composition of a data set or the relationship between chemical concentrations and Raman spectra. Various multivariate techniques require different information to build models. For example, the ordinary least squares regression model is built by obtaining a complete set of the component spectra. Principal component regression and partial least squares regression require concentrations of the target chemical in all samples and spectra of all samples to build a model that can extract concentration information.

It is necessary to check the accuracy of a model after it is built. An independent data set, which does not include the data used for the model building, is often used for testing the robustness of a model. If the concentrations obtained by using a model and the concentrations measured by an accurate and independent technique are statistically similar ($r > 0.9$), the model is validated and considered clinically accurate [Pincus 1996]. This process of testing a model is called validation. [2]

Although it is desirable to use an independent data set for validation, this requires a large number of samples. When the number of samples is not sufficient to perform an independent validation, cross-validation can be performed. Cross-validation allows for the efficient use of a data set, because only a small number of samples are reserved, and the spectra of the remaining samples are used for calibration. The calibrated model is then used to extract concentration information from the spectra of the reserved samples, and the extracted concentrations are compared with reference measurements. Different groups of spectra are then reserved, and the calibration-validation process is repeated until the concentrations of all of the samples are predicted. Since the data set used for calibration and the data set used for validation are independent, the validation is performed without bias. When a statistically sufficient number of spectra are used for calibration, the models obtained from different calibration data sets should be similar.

Different strategies can be employed to group spectra for calibration and validation. For example, a single sample is spared from each calibration in a "leave-one-sample-out"

---

[2] This is a schematic description of the validation process. Further details of the validation process are discussed in Martens and Næs (1989).

cross-validation, and the calibration and validation process is repeated as many times as the number of samples in the data set. The predicted concentrations in the validation data set are compared with the concentrations measured by an accurate and independent technique. Other grouping strategies, such as "leave-one-subject-out" or "leave-half-out", are available. In any form of calibration, efforts are made to separate the calibration data set and the validation data set.

In calibration and validation, accurate and independent measurement techniques play a critical role. Such techniques are called reference techniques, since they provide concentration information that is used as a reference in validation. Concentration information provided by a reference technique is used in two ways. First, concentrations are used to build a model during calibration. Any error in reference information may lead to inaccurate models, and thus erroneous predictions. Second, concentration information is used in the validation process. Significant errors in reference information may result in misleading prediction errors. This will be discussed in further detail below. Therefore, an accurate reference technique is required to build a robust model and to precisely assess the prediction error in a data set.

In concentration predictions, prediction errors indicate the quality of concentration predictions. For each sample, the prediction error is the difference between the predicted concentration and the concentration measured by a reference technique. This is formulated as

$$\Delta c_i = \left| c_{prediction,i} - c_{reference,i} \right|, \tag{4.5}$$

where Δc_i is the prediction error for the i-th sample, $c_{prediction,i}$ is the predicted concentration for the i-th sample, and $c_{reference,i}$ is the concentration measured by the reference technique for the i-th sample. For a set of samples, the prediction error for a data set is the standard deviation of the prediction errors for all samples:

$$\Delta c = \sqrt{\frac{\sum_{i}^{N}\left(c_{prediction,i} - c_{reference,i}\right)^2}{N}}, \tag{4.6}$$

where Δc is the predicted error for the data set and N is the number of samples in the data set. Δc is also called the root mean standard error of prediction (RMSEP). The prediction accuracy is defined as the ratio of the mean concentration to the prediction error ($c/\Delta c$).

Since the prediction error is defined as the difference between the predicted concentration and the reference concentration, the prediction error is affected by the error in the reference technique, as well as the error in the prediction technique. Had we known the actual concentrations, we could precisely calculate the error in the reference technique. Unless the reference technique is free from any error, the reference concentration and the actual concentration are not identical. If we introduce the actual concentration terms into Eq. (4.5), the effect of the error in the reference technique is accentuated:

$$\Delta c = \sqrt{\frac{\sum_{i}^{N}\left[\left(c_{prediction,i} - c_{actual,i}\right) + \left(c_{actual,i} - c_{reference,i}\right)\right]^2}{N}}, \tag{4.7}$$

where c_{actual} is the actual concentration in the i-th sample. When the error in the reference measurements and the error in the predictions are statistically independent, Eq. (4.7) is reduced to

$$\Delta c = \sqrt{\frac{\sum_{i}^{N}\left(c_{prediction,i} - c_{actual,i}\right)^2}{N} + \frac{\sum_{i}^{N}\left(c_{actual,i} - c_{reference,i}\right)^2}{N}} \quad (4.8)$$

In the case in which the prediction technique provides actual concentrations, the prediction error may not be zero unless the reference technique also provides actual concentrations without error. Thus, the prediction error of any prediction technique cannot be smaller than the error of the reference technique, even when the prediction technique provides more accurate information than the reference technique. This emphasizes the need for employing an accurate reference technique.

4.2.2 Ordinary Least Squares (OLS) Regression

In some studies, it is necessary to find out the concentrations of all important components present in the mixtures (samples). OLS regression can be used if the Raman spectra of all important components are known, and Raman spectra of samples can be measured.

When the number of spectra and the number of variables in the spectra are equal and the matrix $\boldsymbol{P}$ is invertible[3], we can directly obtain concentration from $\mathrm{C} = \mathrm{S} \cdot \mathrm{P}^{-1}$. However, the number of spectra and the number of variables in the spectra are rarely equal. To obtain the concentrations in this case, we multiply Eq. (4.3) by the transpose of $\boldsymbol{P}$:

$$\mathbf{S} \cdot \mathbf{P}^{\mathbf{T}} = \mathbf{C} \cdot \mathbf{P} \cdot \mathbf{P}^{\mathbf{T}}. \quad (4.9)$$

If $(\mathbf{P} \cdot \mathbf{P}^{\mathbf{T}})$ is invertible, we can derive an equation for the concentration matrix, $\boldsymbol{C}$:

---

[3] When there are samples of identical composition in the same data set, $\boldsymbol{P}$ or $(\mathbf{P} \cdot \mathbf{P}^{\mathbf{T}})$ cannot be inverted, or the inverted matrix may include significant numerical error.

$$\mathbf{C} = \mathbf{S} \cdot \mathbf{P}^{\mathbf{T}} \cdot (\mathbf{P} \cdot \mathbf{P}^{\mathbf{T}})^{-1}. \tag{4.10}$$

From comparison of Eq. (4.4) and Eq. (4.10), we find that

$$B = P^T \cdot (P \cdot P^T)^{-1}. \tag{4.11}$$

OLS is a simple, yet powerful technique in spectral analysis. However, it requires the knowledge of the number of important components and the Raman spectra of all the important components. In studies of biomedical samples, it may be difficult to ascertain the number of components due to the complexity of many biomedical samples. An error in the number of components can result in erroneous regression results. Additionally, spectra of certain chemicals vary depending on environmental changes, and this can lead to inaccurate OLS analysis.

4.2.3 Classical Least Squares (CLS) Regression

When it is necessary to find out the Raman spectra of all the components in the samples, CLS regression can be used if the concentrations of all the components can be measured, and the Raman spectra of samples are known.

By multiplying Eq. (4.3) by the transpose of ***C***, we get

$$\mathbf{C}^{\mathbf{T}} \cdot \mathbf{S} = \mathbf{C}^{\mathbf{T}} \cdot \mathbf{C} \cdot \mathbf{P}. \tag{4.12}$$

If $(\mathbf{C} \cdot \mathbf{C}^{\mathbf{T}})$ is invertible, we can derive an equation for the component spectra matrix, ***P***:

$$\mathbf{P} = (\mathbf{C}^{\mathbf{T}} \cdot \mathbf{C})^{-1} \cdot \mathbf{C}^{\mathbf{T}} \cdot \mathbf{S}. \tag{4.13}$$

CLS can extract the Raman spectra of components when the concentrations of each component in the spectral data set are known. In some samples, it may be difficult to chemically separate individual components, but it may be possible to measure or estimate

the concentration of all the components. Without single component samples, Raman spectra of the individual components cannot be measured. CLS is useful when it is difficult to measure the Raman spectra of all the individual components.

OLS and CLS are complementary techniques. OLS calculates concentrations from a known set of component spectra, and CLS calculates component spectra from a known set of component concentrations. The component spectra obtained by CLS can be used for OLS analysis of a new data set, as long as the two data sets have the same component spectra. In a similar manner, the component concentrations obtained by OLS can be used for CLS analysis of a new data set.

However, performing a CLS analysis requires the knowledge of the number of important components and the concentrations of each component. In biomedical studies, it may be difficult to know the exact number of important components due to the complexity of many biomedical samples. Furthermore, concentrations of certain chemicals are difficult to measure accurately. These can all lead to additional error in CLS analysis.

4.2.4 Principal Component Regression (PCR)

When the Raman spectra of all the components are known, OLS can be employed for spectral analysis. When the concentrations of all the samples are known, CLS can be employed. However, both OLS and CLS require *a priori* knowledge of all concentrations or all component spectra about the samples, and it is not always possible to use OLS or CLS. By using PCR or PLS (which is discussed in the next section), it is possible to analyze Raman spectra without demanding a complete set of information. PCR and PLS

require Raman spectra of samples and concentrations of only the component of interest, to calculate the projection vector, B. However, Raman spectra of individual components are not provided by PCR or PLS.

The main advantage of principal component analysis is its ability to compress data or extract key components. The eigenvectors represent spectral changes in the data set. If spectra are plotted in a multi-dimensional space, each eigenvector represents each direction of changes (variance) (Figure 4.1). For example, when two wavelengths are measured for each sample, we can plot the first wavelength against the second wavelength and calculate the eigenvectors. The first eigenvector, or the first principal component, is the direction of the largest variance in the data set. The second eigenvector, or the second principal component, is perpendicular to the first principal component. If the samples have two chemical components and if the components can have different intensities of Raman features at the two wavelengths, both principal components are necessary to explain various composition of the samples. If the samples has one chemical component, only one principal component is necessary to explain the spectral variance, and the other principal component is probably due to noise or measurement error. In analysis of a large data set, many principal components can be calculated. However, not all the components are meaningful. Some are due to noise, and some may have insignificant meanings. There are multiple methods to select the number of principal components [Malinoiski and Howery 1980], and the main concept behind these methods is to select statistically significant and physically meaningful components. Since PCA can describe variations in a data set with

principal components (hopefully) fewer than the number of variables, it is considered a data compression technique.

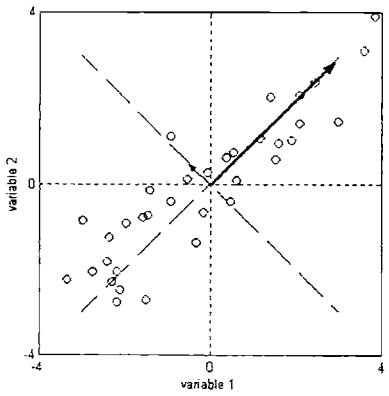

Figure 4.1. Direction of principal components in a two-variable data set. Mean-centered data are plotted (circles). The two variables (intensities at two wavelengths) appear to be correlated. The first principal component follows the direction of the largest variance (large arrow). The second principal component is perpendicular to the first component, and follows the direction of the second-largest variance (small arrow). The lengths of arrows indicate the variance of principal components. Note that the arrows are not principal components, as principal component vectors have unit length.

Building a PCR model is performed in three steps. First, the Raman spectra of samples are preprocessed. Preprocessing may include mean centering, intensity correction, background subtraction, normalization, scaling, smoothing, binning, cosmic-ray removal, and artifact removal. The details of these preprocessing steps are discussed below.

Second, the component spectra are obtained by calculating the eigenvectors of the $\boldsymbol{S}^T \cdot \boldsymbol{S}$, and the calculated eigenvectors are called principle components. This process alone is called principal component analysis (PCA) [Joliffe 1986]. Two methods are often used for the eigenvector calculation in PCR. The eigenvectors of the $\boldsymbol{S}^T \cdot \boldsymbol{S}$ can be calculated from the singular value decomposition (SVD) of the sample spectra, $\boldsymbol{S}$. Singular value

decomposition is robust and the numerical error in SVD is small. However, the singular value decomposition process is time-consuming for large-size matrices. Instead, nonlinear iterative partial least squares (NIPALS) can be used to obtain eigenvectors. NIPALS is an iterative algorithm and is faster than many other algorithms for eigenvector computations. NIPALS can compute only the desired number of principal components [Wold and Sjostrom 1977]. However, due to the iterative nature, NIPALS results may not converge to the principal components under certain numerical condition, and may not be able to compute all principal components.

Singular-value-decomposition decomposes a given matrix $\boldsymbol{S}$ into three matrices $\boldsymbol{U}$, $\boldsymbol{X}$, and V so that $S = U \cdot X \cdot V^T$. $\boldsymbol{X}$ is a diagonal matrix with non-negative elements, and the dimensions of $\boldsymbol{S}$ and $\boldsymbol{X}$ are equal. The diagonal elements of the matrix $\boldsymbol{X}$ are the square-root of the eigenvalues, and a large diagonal element implies that its corresponding principal component is statistically significant. $\boldsymbol{U}$ and V are unitary matrices, and hence, $U \cdot U^T = I$ and $V \cdot V^T = I$. The fit coefficients, which are also called scores, are $\boldsymbol{U}\cdot\boldsymbol{X}$. Each column of the matrix $\boldsymbol{V}^T$ is the component spectra of the matrix $\boldsymbol{S}$.

Once the data set is compressed into principal component scores, finally, an ordinary least squares regression is performed between the scores and the concentrations, so that

$$C = U \cdot X \cdot T, \tag{4.14}$$

where $\boldsymbol{C}$ is the matrix of concentrations, and T is the matrix that projects the scores onto concentration space ($T = \left[(U \cdot X)^T \cdot (U \cdot X)\right]^{-1} \cdot (U \cdot X)^T \cdot C$). For example, spectra of serum protein samples may have two major principal components: albumin and globulin.

Multi-wavelength data for each sample is compressed into two variables, scores for albumin and globulin. If the concentration of total protein, which is the sum of the albumin concentration and the globulin concentration[4], is of interest, the projection vector simply adds two scores and scales to the total protein concentration.

For a new data set, predictions can be made by extracting scores ($U \cdot X = S \cdot V$) and projecting the scores onto concentrations ($C = U \cdot X \cdot T$). This is equivalent to using the following equation:

$$C = S \cdot V \cdot T. \tag{4.15}$$

From comparison of Eq. (4.4) and Eq. (4.15), we find that

$$B = V \cdot T. \tag{4.16}$$

Again, the projection vector B's obtained from Eq. (4.11) and Eq. (4.16) are identical when both OLS and PCA can model the data set accurately.

4.2.5 Partial Least Squares (PLS) Regression

Partial least squares regression is another technique for concentration analysis. It is similar to PCR in that both techniques decompose the spectral data set and find the relationship between the decomposed spectra and the concentrations. The difference appears from the fact that PLS utilizes the concentration information in the decomposition process. The decomposition is performed with the covariance matrix of spectra and concentrations, the

---

[4] This example is only to illustrate the relation between scores and concentrations. In human blood samples, total protein includes other proteins as well.

benefit of which includes reducing the effect of noise and obtaining components that are better correlated to the concentrations of the component of interest. The use of the covariance matrix of spectra and concentrations allows the averaging of noise in spectral measurements by concentration measurements, or the averaging of error in concentration measurements by spectral measurements. PLS and PCR have similar performance if noise in the spectral data and errors in the reference concentration measurements are negligible. Otherwise, PLS generally provides better analysis than PCR [Thomas and Haaland 1990].

An important advantage of PLS and PCR over OLS or CLS is their ability to extract spectral components (called loadings in PLS and principal components in PCA/PCR) without knowledge of the actual number of components. OLS and CLS require knowledge of the number of components and build models with the known number of component spectra. In PLS and PCA, the number of spectral components is often determined during the calibration. This degree of freedom can sometimes be a challenge in obtaining accurate models, as both underfitting (calibrating with fewer components than necessary) and overfitting (calibrating with more components than necessary) can result in erroneous models [Kruse-Jarres 1990, Næes and Martens 1988]. However, this allows PLS and PCA to be a powerful tool in modeling spectral changes due to sources other than the known chemical components. Such sources include unknown chemical components, drift of the background, and other interfering signals from the system or the environment, all of which can be present in experimental data. While it is not impossible to model the non-chemical spectral components with OLS and CLS, it is often difficult to obtain their component

spectra and to quantify "concentrations" of such spectral components. This is why PLS and PCR are used in concentration measurements more often than OLS and CLS.

For further information, tutorial articles for PLS are available [Geladi and Kowalski 1986, Haaland and Thomas 1988].

4.2.6 Hybrid Linear Analysis (HLA)

Although PCR and PLS are powerful algorithms in spectral analysis, the accuracy of a model built by either technique depends on the quality of the spectral data set and the reference measurements. When the noise in the spectra reduces the accuracy of the model, the model can be improved by utilizing the accurate spectrum of the target chemical, if the spectrum of the target chemical can be measured accurately with high S/N. Hybrid linear analysis (HLA) combines OLS and PCA techniques, and employs the spectrum of the target chemical in the model building process.

HLA requires a spectral data set, knowledge of the concentrations of the target chemical, and the accurate spectrum of the target chemical. The S/N of the target chemical spectrum should be better than the S/N of each spectrum in the spectral data set. An HLA model is built in two steps. First, the spectral contribution of the target chemical is removed from the spectral data set. This can be formulated:

$$S' = S - c \cdot a \,, \tag{4.14}$$

where $\boldsymbol{S'}$ is the matrix of spectra which do not include any contribution of the target chemical, $\boldsymbol{c}$ are the concentrations of the target chemical, and $\mathbf{a}$ is the accurate spectrum of the target chemical at unit concentration. Second, the matrix of spectra $\boldsymbol{S'}$ is decomposed

by PCA, and the matrix of component spectra $\boldsymbol{P'}$ is obtained. The spectra in the matrix $\boldsymbol{P'}$ explain the changes in the spectral data set other than the change due to the target chemical. By combining the vector $\boldsymbol{a}$ as the first row and $\boldsymbol{P'}$, we obtain the matrix of all component spectra $\boldsymbol{P}$, which includes the spectrum of the target chemical. The rest of the model building process is similar to that in OLS, and the projection vector B is

$$B = P^T \cdot (P \cdot P^T)^{-1}. \tag{4.15}$$

After the model is built, the concentrations can be predicted by performing an OLS fit. The fit coefficient for the target chemical is the concentration of the target chemical.

HLA requires *a priori* knowledge of the target chemical spectrum. Thus, HLA cannot be applied when an accurate spectrum of the target chemical is not available. When the target chemical spectrum is available, HLA provides a more accurate and robust model than PLS or PCR [Koo et al. 1998]. The superiority of HLA over PLS and PCR is more apparent when the S/N of the spectral data set is relatively low. In a low S/N data set, the prediction error obtained by using HLA is smaller than the prediction error obtained by using PLS [Koo 1998]. This follows from the fact that the accurate spectrum of the target chemical improved the accuracy of the model. When the S/N of the data set is sufficiently high, both HLA and PLS provide similar projection vector B's and, therefore, similar results.

4.2.7 Preprocessing data

Spectral range selection

Multivariate methods attempt to find the spectral components with large variance. With the presence of a strong signal that is not associated with chemical concentrations, the algorithm may try to fit this strong signal, neglecting the variance in other regions. In addition, it is not helpful to use a spectral range that does not contain the spectrum of the specific chemical component.

In our studies, the spectral range, where the spectral features of the target analyte and no other dominating spectral features of other chemicals are present, was chosen and analyzed by the multivariate calibration algorithm. No special algorithm was devised for selecting the optimal spectral range other than thorough trials. The prediction errors were not significantly affected by varying the spectral range as long as the range included the key features of important component spectra.

Cosmic ray removal

A problem with CCD cameras is that cosmic ray signals degrade data (Figure 4.2) [Landsman 1997]. Cosmic rays hit random pixels of the CCD array at random times with arbitrary intensity. As a result, sharp spectral features of arbitrary intensities appear on top of Raman spectra. Since cosmic rays distort the intensity of the Raman bands, quantitative analysis of spectra may provide inaccurate results unless cosmic rays are removed.

Our solution for cosmic ray removal was to acquire spectral signals frame by frame and compare. When 300-second integration time was desired for a spectrum, 30 spectra of 10-second integration time each were collected. Each spectrum integrated over 10 seconds

was called a frame. A statistical algorithm was used to identify cosmic rays. The main assumption of this cosmic ray filtering method was that the spectrum does not change its intensity from frame to frame other than due to noise and cosmic rays, and a sudden change in the spectrum beyond typical noise is due to a cosmic ray.

Using a statistically significant number of frames, we calculated the median and the standard deviation of the set of pixel intensities in the frames. The median was close to the actual intensity, and the standard deviation was mainly due to noise and cosmic rays. The threshold for cosmic rays was the sum of the median and the standard deviation multiplied by a constant, which we call the weight factor. The weight factor determined what percentile of the pixels should be considered 'normal,' under the assumption that the noise in the data is random Gaussian noise. If there is no cosmic ray, only 0.1% of pixels are misclassified as cosmic rays, when the weight factor is 3. We varied the weight factor, but mostly used three standard deviations as the filtering criterion. Any pixel whose intensity is larger than this threshold was replaced with the median of the normal pixels in the remaining frames.

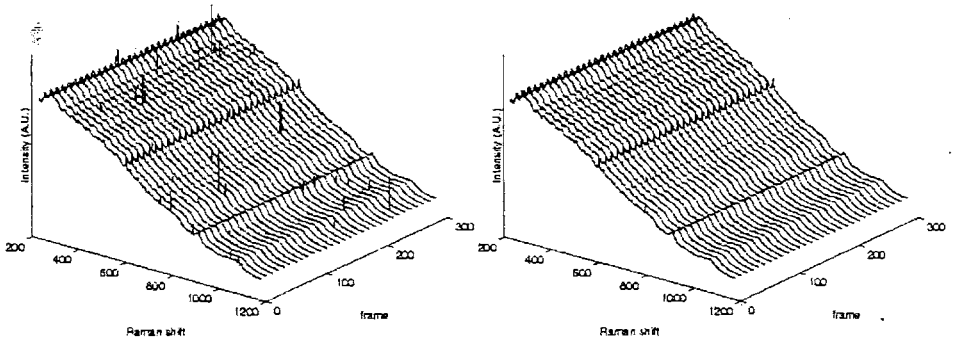

Figure 4.2 A set of raw spectra of a biological sample before cosmic ray filtering (left) and after (right). Spike shaped peaks are due to cosmic rays. A statistical algorithm was used to remove them.

Cosmic ray filtering has one weakness in its assumption. The variation of the signal in each pixel increases when there is an intensity change of the spectrum over the whole collection time due to physical or chemical changes in the sample. This increased variance may sometimes make it difficult to detect cosmic rays by employing this simple algorithm.

Background subtraction

Raman spectra of biological samples are often accompanies by strong fluorescence or other background. The fluorescence background is generated by optical components in the system, the quartz cuvette containing samples, and proteins and lipids in whole blood. The optical components and cuvettes are the dominant source of background fluorescence. Macromolecules, such as proteins and lipids, also contribute to the fluorescence background [Qu et al. 1999]. The strong fluorescence provides shot noise, and variation in the background interferes with multivariate analysis. While PLS and PCR can remove such backgrounds during calibration to some extent, they are not efficient in extracting concentrations in the presence of these backgrounds. Thus, it is desirable to remove this background before multivariate analysis when the background does not provide relevant information.

Since the fluorescence background has broader features than the Raman bands, it has been demonstrated that polynomial fits can sufficiently model fluorescence backgrounds [Baraga 1992, Brennan 1995]. The polynomial subtraction removed fluorescence backgrounds in Raman spectra of whole blood samples, and the background-subtracted spectra exhibit sharp Raman features (Figure 4.3). Some spectral bands have negative intensities as a result of the polynomial subtraction, but it does not affect data

analysis as it is the intensity relative to the baseline that is important in the data analysis. Both spectra before and after background subtraction were analyzed and better predictions were achieved by subtracting the backgrounds.

Mean centering

It is useful to mean-center the data before using many analytical algorithms other than OLS and CLS. Mean centering refers to subtracting the mean spectrum of the data set from each spectrum in the data set. Conceptually, mean centering accentuates the differences among spectra. Mathematically, it reduces the complexity of the data by one degree of freedom, and prevents certain spectra in the data set from being weighed more than other spectra. Statistically, it maps the data onto an abstract space where the mean of the mean centered data does not have any directionality [Kramer 1998]. For certain techniques, such as PCR and PLS, mean centering is recommended. Without mean centering, the first spectral component is the statistical mean of the data set, which is often not the information that is needed. In our studies, PLS was always performed after mean centering.

Noise suppression

Noise in the spectra can be filtered or reduced with mathematical tools or enhanced experimental setups. If the noise has a specific profile in the time domain (for example, flicker noise has a 1/f amplitude in the frequency domain) and if the frequencies of the noise and the signal are different, Fourier filters can be used to remove noise. Otherwise, experimental setup can be improved to reduce such noise or to increase the frequency of the signal to the level higher than the frequency of the noise. If the amplitude of the noise does not vary over the frequency domain, Fourier filters may be able to remove noise when the

spatial frequencies of the noise and the signal are different. However, many Raman spectra have sharp features, and both Raman features and high frequency noise appear in the same region in the spatial-domain Fourier space. It is difficult for Fourier filters to selectively remove noise without affecting the Raman signal. In practice, Fourier filters worsen prediction accuracy.

A moving average is a method essentially equivalent to Fourier filtering of high frequency noise. In a moving average, a spectral range called a "window" is selected. An average of the signal intensity at every data point in the window replaces the signal intensity at a data point in the center of the window. Then, a new window is selected by shifting the window by only one data point, and the averaging is again performed. This iterative process is repeated until the whole spectral range is covered. However, the moving average reduces the resolution of data, which can adversely affect prediction error.

Binning is a similar method of reducing noise. In binning, the window is shifted by the size of the window instead by one data point. As a result, the number of data points and the spectral resolution are reduced. Binning provides higher S/N data with fewer degrees of freedom, which can simplify the model and increase the robustness of multivariate analysis. Furthermore, binning can effectively compensate for spectral shifts, which is an artifact due to spectrograph drift. Thus, binning was selected as a method of noise reduction in our studies.

White light correction and wavenumber calibration

Additionally, white light correction is required to compare the spectral intensities collected with different systems. Various optical systems can have different spectral sensitivities, and it is difficult to compare intensities of spectra collected with different optical systems without correction. A white light spectrum can be used to correct for such variations. White light correction is performed by collecting a spectrum of a standard white light, and dividing spectra of samples with the white light spectrum.

Wavenumber calibration is also required to compare the frequencies of Raman bands collected with different systems, as various spectroscopy systems have different resolutions and dispersions. A well defined calibration light source (e.g. neon lamp or mercury lamp) is used to obtain accurate wavenumber information.

In analysis of data presented in this dissertation, spectral range selection, cosmic ray removal, and background subtraction were performed. For PLS analysis, mean centering was also performed. All spectra were wavenumber calibrated, and spectra are presented in wavenumbers. Since it was not intended to compare spectra collected with our system and spectra collected with other systems, white light correction was not performed.

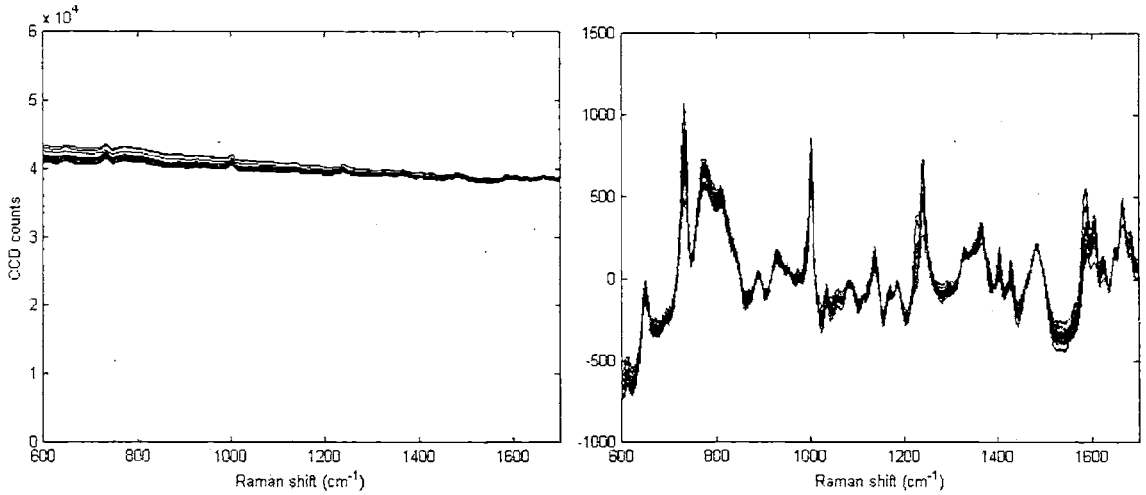

Figure 4.3. Raman spectrum of whole blood samples before background subtraction (left) and after (right). The background subtraction removed variations in fluorescence signals. Raman bands are more prominent after background subtraction.

4.3 Raman spectra of biological samples and components

Raman spectra provide information about molecular concentrations, but it is often difficult to interpret Raman spectra of biological samples, due to the complexity of these samples. The many overlapping Raman bands and the severe background noise complicates analysis of Raman spectra. Thus, more sophisticated analysis techniques are required to extract all the information contained in Raman spectra. In this section, multivariate techniques are used to analyze component spectra, and the findings from the spectral analysis of serum and whole blood spectra are discussed. The Raman spectra of 69 serum samples and 68 whole blood samples were obtained with the previous system in the manner described in Chapter 2.

First, a linear superposition of pure component spectra was calculated using OLS. The superposed spectra were obtained by multiplying the Raman spectra of important components by the physiological range of concentrations (total protein 6~7.8 g/dL, cholesterol 150~250 mg/dL, and triglycerides 10~190 mg/dL)and summing these weighted spectra. The superposed spectra and the Raman spectra of serum samples are similar (Figure 4.4). Most bands in the Raman spectra of serum samples are represented in the reconstructed spectra. Thus, we confirmed that the background subtracted Raman spectra are due to the Raman spectra of components and furthermore, are linear superpositions of the component spectra. In addition, we noticed that the contributions from simple molecules, such as glucose and urea, are small, and visual comparison in this scale cannot provide any information about the concentration of such molecules.

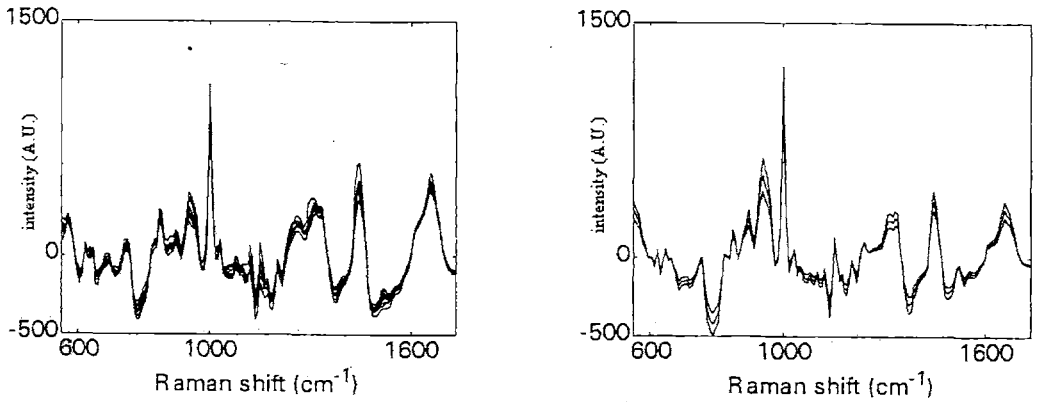

Figure 4.4. Raman spectra of 69 serum samples (left) and the superposed spectra of weighted components (right). The three superposed spectra represent physiological variations of chemical concentrations.

Second, we employed CLS to analyze the spectra of serum samples. Although CLS requires complete concentration information about a data set, the component spectra

obtained by CLS are closely related to the spectra of pure components. This is an advantage of CLS in spectral analysis. In contrast, the component spectra obtained by PCA or PLS do not require complete concentration information, but they are orthogonal to one another and often do not look similar to the spectra of pure components.

We used the concentrations of six chemical components in CLS analysis of 69 serum spectra. It was nearly impossible to know the exact number of chemicals present in each sample, so the concentrations of chemicals whose Raman signal intensities were larger than the noise were used. Those six chemicals were glucose, urea, cholesterol, triglyceride, total protein, and albumin[5]. The extracted spectrum of glucose and the measured Raman spectrum of pure glucose are similar (Figure 4.5), as are the spectra of urea (Figure 4.6). Also, the Raman spectra of glucose and urea match well with the published Raman spectra [Schrader 1989]. Several spectral features should be noted. The Raman band at 1011 cm^{-1} is the most significant band in the Raman spectrum of urea. However, the extracted Raman spectra are not identical to the pure component spectra. The dip in the extracted glucose spectrum at 1021 cm^{-1} is not seen in the Raman spectrum of pure glucose (Figure 4.5). A Raman band at 1177 cm^{-1} is not prominent in the extracted spectrum of urea (Figure 4.6). Furthermore, noise is present over the whole range of the extracted spectra. These differences are due to the presence of noise in the data set, the use

---

[5] The total protein concentration includes the concentration of albumin. Thus, when CLS was performed to obtain the spectrum of total protein, concentrations of albumin were not included. When the spectrum of albumin was to be obtained, the concentration of albumin was subtracted from the concentration of total protein.

of an incomplete set of concentrations, and the incapability of CLS in modeling spectral changes due to sources other than chemical components.

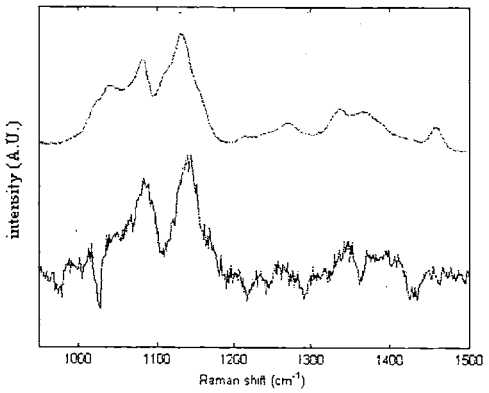

Figure 4.5. Raman spectrum of glucose experimentally measured (top) and Raman spectrum of glucose extracted by CLS from 69 serum samples (bottom). The spectra are offset for comparison.

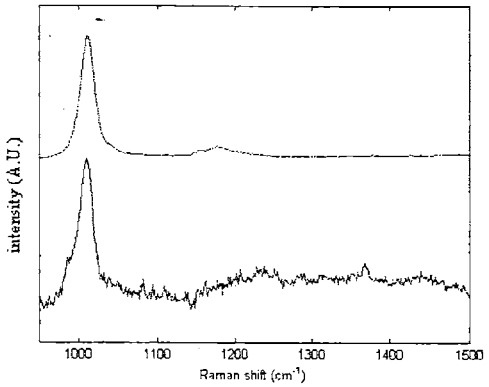

Figure 4.6. Raman spectrum of urea experimentally measured (top) and Raman spectrum of urea extracted by CLS from 69 serum samples (bottom). The spectra are offset for comparison.

Although the extracted Raman spectra and the measured Raman spectra of pure components are not completely identical, the extracted spectra contain the major spectral features of the pure chemicals. Moreover, CLS extracted spectral contributions of the six analytes, even when it was difficult to visually extract any information about glucose or urea at physiological concentrations. This demonstrates the capability of multivariate techniques in spectral analysis.

Finally, the Raman spectra of components in serum and whole blood were compared to confirm that the Raman spectrum of a given component remains the same in

serum and whole blood. The component spectra in serum were extracted from the Raman spectra of 69 serum samples, as described above. The component spectra in whole blood were extracted from the Raman spectra of 68 whole blood samples. The concentrations of glucose, urea, cholesterol, triglyceride, total protein, albumin, and hematocrit[6] were used. Raman spectra of glucose and urea extracted by CLS in whole blood did not have distinctive spectral features of pure glucose and urea. This is probably due to the small intensity of glucose and urea signals compared to the background noise and the presence of additional components in whole blood. For larger molecules, such as total protein, albumin, cholesterol, and triglyceride, Raman spectra extracted by CLS in serum and whole blood have similar spectral features (Figure 4.7). However, not all the extracted bands are identical. The Raman band at 1240 cm^{-1} in serum was shifted by 14 cm^{-1} in whole blood, and new bands around between 1340 cm^{-1} and 1390 cm^{-1} were seen in whole blood but are not present in serum. The incomplete concentration information about additional chemicals present in whole blood, the noise, and the signal changes, which are not modeled by CLS, may have induced these changes. Also, it can be noted that the signal intensity is lower by a factor of four in whole blood, which matches well with the decrease of glucose signal intensity in whole blood (see Chapter 2).

In summary, Raman spectra of serum and whole blood were analyzed. We confirmed that the Raman spectra of serum and whole blood are a linear superposition of component spectra. Although the spectral contributions of simple molecules were small,

---

[6] As discussed earlier, hematocrit is the volume fraction of red blood cells. The component spectrum extracted for hematocrit is related to the Raman spectrum of red blood cells.

CLS extracted their spectra. Also, many of the Raman spectra of components were closely related in serum and whole blood, and the signal intensity was smaller in whole blood. The effect of the intensity decrease is discussed in Section 4.4.

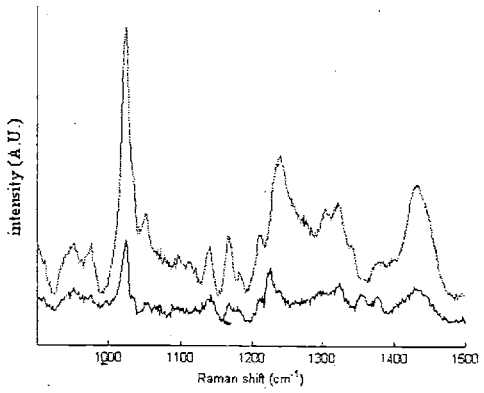

Figure 4.7. Raman spectra of total protein extracted by CLS in serum (top) and whole blood (bottom).

4.4 Estimation of prediction error

Section 4.2 discusses multivariate techniques and their application in concentration measurements. Furthermore, the mathematical definition of the prediction error (RMSEP) of a data set in concentration measurements was presented. In this section, we derive an analytical equation for prediction accuracy. The analytical equation explains which factors determine prediction error. By understanding prediction error better, efforts can be made to reduce prediction error systematically and scientifically, rather than using a trial-based approach. The importance of an analytical equation for prediction accuracy or prediction error has also been emphasized by other researchers [Kleinknecht 1996].

4.4.1 Derivation of the prediction error equation for a noise-limited data set

Assume that the noise in the spectral data set is the only source of error. The shot noise resulting from the fluorescence background is the dominant source of noise in the Raman spectrum of biological tissue, and the shot noise is the major source of error in studies of biological samples. We can use Eq. (4.4) to predict concentrations. In matrix notion, Eq. (4.4) can be written as

$$C = S \cdot B, \tag{4.15}$$

where $\boldsymbol{C}$ is the matrix of concentrations of components and $\boldsymbol{B}$ is the matrix of projection vectors. If we have an accurate $\boldsymbol{B}$ matrix, the noise in the matrix $\boldsymbol{S}$ induces error in concentrations:

$$C + \Delta C_{noise} = \left(S + S_N\right) \cdot B, \tag{4.16}$$

where $\boldsymbol{\Delta C_{noise}}$ is the matrix of error in concentration and $\boldsymbol{S_N}$ is the matrix of noise in the spectrum matrix $\boldsymbol{S}$. The ratio of $\boldsymbol{C}$ and $\boldsymbol{\Delta C}$ is the prediction accuracy. By subtracting Eq. (4.15) from Eq. (4.16), we get

$$\Delta C_{noise} = S_N \cdot B. \tag{4.17}$$

Since the projection vector $\boldsymbol{B}$ is universal, we can insert the projection vector for OLS, Eq. (4.11), into Eq. (4.17):

$$\Delta C_{noise} = S_N \cdot P^T \cdot \left(P \cdot P^T\right)^{-1}. \tag{4.18}$$

As discussed in Section 4.2, the prediction error of a data set is a standard deviation of the prediction error for each sample. By using the definition of standard deviation, the prediction error of the k-th element due to noise, $\Delta c_{noise,k}$, is

$$\Delta c_{noise,k} = \sqrt{diag_k\left(\Delta C_{noise}{}^T \cdot \Delta C_{noise}\right)/N}\,, \tag{4.19}$$

where $\mathrm{diag}_k(\boldsymbol{X})$ is the diagonal k-th element of a matrix $\boldsymbol{X}$. Each diagonal element of the $\Delta \boldsymbol{C}_{noise}{}^{T} \cdot \Delta \boldsymbol{C}_{noise}$ is related to the error in the concentration measurements of each component. Inserting Eq. (4.18) into Eq. (4.19), we obtain

$$\Delta c_{noise,k} = \sqrt{diag_k\left\{\left[\left(P \cdot P^T\right)^{-1}\right]^T \cdot P \cdot S_N{}^T \cdot S_N \cdot P^T \cdot \left(P \cdot P^T\right)^{-1}\right\}/N}\,. \tag{4.20}$$

In the covariance matrix of shot noise, the diagonal elements are dominant. By using an approximation, $S_N{}^T \cdot S_N \approx n^2 \cdot N \cdot I$ where n is the amplitude of the noise[7] and I is the N-by-N identity matrix, Eq. (4.20) can be greatly simplified.

$$\Delta c_{noise,k} \approx n\sqrt{diag_k\left\{\left(P \cdot P^T\right)^{-1}\right\}}. \tag{4.21}$$

The matrix of spectral components, $\boldsymbol{P}$, contains spectra of pure components at unit concentrations. We can expand the matrix $\boldsymbol{P}$ so that

$$Q = c_k \cdot P / s\,, \tag{4.22}$$

where Q is the matrix of generalized component spectra, s is the signal intensity, and c_k is the average concentration of the k-th component. The signal intensity s is the Euclidean

---

[7] Although this approximation is best in modeling white noise, it can also be used to model shot noise. If the noise is random white noise, n is the standard deviation of the noise.

norm [Strang 1988] of the spectrum of the k-th pure component, and $s = \sqrt{diag_k\left(P \cdot P^T\right)}$. Becausing of dividing by s, *P/s* is purely lineshape without intensity information. By inserting Eq. (4.22) into Eq. (4.21), we obtain

$$\frac{c_k}{\Delta c_{noise,k}} \approx \frac{s}{n} \cdot \frac{1}{\sqrt{diag_k\left\{\left(Q \cdot Q^T\right)^{-1}\right\}}}. \tag{4.23}$$

The ratio of concentration c_k and error Δc_k is the prediction accuracy, and Eq. (4.23) indicates that there are two significant factors that determine the prediction accuracy: S/N and spectral overlap. The first term (s/n) is the S/N of the target chemical spectrum. The prediction accuracy increases linearly with the S/N, which was confirmed in simulations [Berger and Feld 1997]. The second term, $1/\sqrt{diag\left\{\left(Q \cdot Q^T\right)^{-1}\right\}}$, describes the effect of the overlap in component spectra, and is called "overlap factor". When the covariance matrix of Q has dominant diagonal elements, the spectral overlap is small and the spectral overlap factor is close to 1, its maximum possible value. When the non-diagonal elements are comparable in magnitude to the diagonal elements, the spectral overlap is significant and the spectral overlap factor is close to 0. The spectral overlap is affected by the number of components present in the samples, the resolution of spectral data, and the spectral range of the data. When the overlap factors were calculated with the component spectra discussed in Section 4.3, the overlap factors were similar for all analytes. Thus, S/N was the major factor in concentration measurements in serum and whole blood.

One thing to note is that the prediction error equation (Eq. (4.21) and the prediction accuracy equation (Eq. (4.23)) are derived for OLS. If it is used to estimate the prediction

error in other multivariate techniques, such as PLS or PCR, the projection vectors for OLS and the other technique should be similar. If there are differences between the projection vectors, Eq. (4.21) and Eq. (4.23) will not provide accurate estimations. Eq. (4.23) was compared with prediction errors and prediction accuracies of OLS and PLS, and was validated in a numerical simulation (Appendix B).

4.4.2 Generalized equation of prediction error

In Eq. (4.23), which was derived on the assumption that the shot noise is the only source of error, the prediction error depends on the S/N and the spectral overlap of the spectral data set. In practice, other error sources contribute to the prediction error, as well. As discussed in Section 4.2, the error in reference measurements increases the total error. Changes in the optical system, such as laser power fluctuations and spectrograph drift, may also increase the prediction error. When concentration errors are due to error sources that are statistically independent, the errors can be added quadratically, as demonstrated in Eq. (4.8). Thus, the concentration error observed in an experiment is

$$\Delta c_{observed} = \sqrt{\Delta c_{noise}{}^2 + \Delta c_{reference}{}^2 + \Delta c_{others}{}^2}, \qquad (4.24)$$

where $\Delta c_{observed}$ is the concentration error observed in an experiment, Δc_{noise} is the error due to noise in the spectra, $\Delta c_{reference}$ is the error in reference measurements, and Δc_{others} is the error due to other error sources. Δc_{noise} is calculated from Eq. (4.23).

In our studies, only the error due to noise is strongly dependent upon the data collection time, out of all error sources. The reference error is independent of the data collection time. Other error sources, such as the system drift and the laser power

fluctuation, have different time constants. In our system, the system drift occurs over days or weeks, and its effect can be considered as a constant during a few hours of an experiment. Laser power fluctuation occurs on a period of up to a few seconds, and their effect is averaged over more than a minute data collection time. In Eq. (4.23), the S/N term is a function of the data collection time and the system sensitivity, while the overlap factor does not change over time. In our studies, Raman signals and backgrounds increased linearly with the data collection time, which are formulated as

$$s = s_0 \cdot t \text{ and} \tag{4.25}$$

$$B = B_0 \cdot t, \tag{4.26}$$

where s is the intensity of the collected Raman signal, s_0 is the intensity of the Raman signal collected for one second, B is the intensity of the background, and B_0 is the intensity of the background collected for one second, and t is the data collection time in seconds. In our data, $s << B$, since fluorescence backgrounds are much stronger than Raman signals. Thus, the shot noise of the background is larger than the shot noise of the Raman signal. From the statistics of shot noise, we know that the amplitude of the shot noise in the background is the square-root of the background. If we assume that the shot noise of the background is the major noise, we obtain

$$n = \sqrt{B}, \tag{4.27}$$

where n is the amplitude of noise. By inserting Eq. (4.26) into Eq. (4.27), we find

$$n = \sqrt{B_0 \cdot t}. \tag{4.28}$$

By dividing Eq. (4.25) by Eq. (4.28), we find that the S/N is also dependent upon the data collection time:

$$s/n = S_0\sqrt{t/B_0}\ . \tag{4.29}$$

In Eq (4.23), the prediction accuracy is linearly proportional to the S/N. The mean concentration of the component of interest does not change over time. From Eq (4.23), we find

$$\Delta c_k \approx \frac{1}{s/n}\cdot c_k\sqrt{diag_k\left\{\left(Q\cdot Q^T\right)^{-1}\right\}}, \tag{4.30}$$

and by inserting Eq. (4.29) into Eq. (4.30), we get

$$\Delta c_k \approx c_k\sqrt{\frac{B_0/{s_0}^2}{t}}\cdot\sqrt{diag_k\left\{\left(Q\cdot Q^T\right)^{-1}\right\}}. \tag{4.31}$$

The error due to noise in predicting the concentrations of the k-th component is inversely proportional to the square-root of the data collection time.

For simplicity, let's introduce two constants, a and b, so that

$$a = c_k\sqrt{B_0/{s_0}^2}\cdot\sqrt{diag_k\left\{\left(Q\cdot Q^T\right)^{-1}\right\}} \tag{4.32}$$

and

$$b = \sqrt{\Delta c_{reference}{}^2 + \Delta c_{others}{}^2}\ . \tag{4.33}$$

Then, Eq. (4.24) is reduced to

$$\Delta c_{observed} \approx \sqrt{a^2/t + b^2}\ . \tag{4.34}$$

This equation predicts how prediction errors improve with longer data collection times. It shows what data collection time is required to obtain what level of prediction error. From

Eq. (4.34), we can find t_0 which satisfies $a^2/t_0 = b^2$, or $t_0 = a^2/b^2$. When the collection time is t_0, the error due to the shot noise equals the error from other sources. The benefit of increasing the integration time beyond t_0 is small. At $2t_0$ the prediction error decreases by 13% from the prediction error at t_0, and at $4t_0$ the prediction error decreases by 21%. Eq. (4.34) also indicates that prediction errors cannot be zero, even with a very long data collection time, unless b is zero, as the prediction error cannot be lower than half of the prediction error at t_0. Thus, this equation explains the detection limit, how we can approach the detection limit, and what prediction error can be obtained with a practical data collection time. Eq. (4.34) is validated with experimental data in Chapter 6.

4.5 Discussion

Multivariate techniques are powerful tools in spectral analysis. The derivation of prediction error equations provides an insight into how to obtain further improvements. Noise was found to be the most significant source of error. The prediction error can be reduced by increasing the S/N of the data. The S/N can be improved by increasing the data collection time or employing a more sensitive collection system. Often, sensitivity and resolution of a system are associated, and a systematic approach is required to design an optimal system. The design of an optimal collection system is discussed in Chapter 5.

In Chapter 3, we discussed that light scattering and absorption in human blood reduce the intensity of the Raman signal. Since the S/N of the Raman signal was reduced by a factor of four in whole blood and the overlap factors in serum and whole blood are

similar, it was necessary to increase the S/N by factor of four to achieve prediction errors similar to those obtained in serum samples, which was the goal of the system design (Chapter 5). The new system achieved the design goal, and the prediction errors obtained with the new system in whole blood were comparable to the prediction errors obtained with the previous system in serum (Chapter 6).

References

J. J. Baraga, "In situ chemical analysis of biological tissue--vibrational Raman spectroscopy of human atheroschlerosis" (Cambridge: Massachusetts Institute of Technology, doctoral thesis, 1992).

A. J. Berger, T.-W. Koo, I. Itzkan, and M. S. Feld, "An enhanced algorithm for linear multivariate calibration," *Analytical Chemistry*, volume 70, 1998, pp. 623 –627.

A. J. Berger and M. S. Feld, "Analytical method of calculating chemometric prediction error," *Applied Spectroscopy*, volume 51, 50 1997, pp. 725 –732.

J. F. Brennan, "Near infrared Raman spectroscopy for human artery histochemistry and histopathology" (Cambridge, MA: Massachusetts Institute of Technology, doctoral thesis, 1995).

P. Geladi and B. R. Kowalski, "Partial least-squares regression: A tutorial," *Analytica Chimica Acta*, volume 185, 1986, pp. 1 –17.

D. M. Haaland and E. V. Thomas, "Partial least-squares methods for spectral analyses. 1. Relation to other quantitative calibration methods and the extraction of qualitative information," *Analytical Chemistry*, volume 60, 1988, pp. 1193 –1202.

I.T. Joliffe, *Principal* Component *Analysis* (New York: Springer-Verlag, 1986).

R. E. Kleinknecht, "Error estimation in PLS latent variable structure," *Journal of Chemometrics*, volume 10, 1996, pp. 687 -695.

T.-W. Koo, A. J. Berger, I. Itzkan, G. Horowitz, and M. S. Feld, "Reagentless Analysis of Glucose in Serum Using Near-infrared Raman Spectroscopy," *Diabetes Technology & Therapeutics*, volume 1, 2 1999, pp. 153 –157.

R. Kramer, *Chemometric Techniques for Quantitative Analysis* (New York: Marcel Dekker, 1998).

J. D. Kruşe-Jarres, G. Janatsch, and U. Gless, "Glucose and other constituents of blood determined by ATR-FTIR-spectroscopy," *Clinical Chemistry*, volume 36, 2 1990, pp. 401 –402.

W. Landsman, "Observed CCD Cosmic Ray Rates," Space Telescope Imaging Spectrograph Report, Goddard Space Flight Center, NASA, 1997.

E.H. Malinowski and D.G. Howery, *Factor Analysis in Chemistry* (New York: John Wiley & Sons, 1980).

H. Martens and T. Næs, *Multivariate Calibration* (Chichester: Wiley, 1989).

R. Manoharan, J. J. Baraga, M. S. Feld and R. P. Rava, "Quantitative Histochemical Analysis of Human Artery Using Raman-Spectroscopy," *Journal of Photochemistry and Photobiology B-Biology*, volume 16, 2 1992, pp. 211-233.

T. Næs and H. Martens, "Principal component regression in NIR analysis: viewpoints, background details and selection of components," *Journal of Chemometrics*, volume 2, 1988, pp. 155 –167.

M. R. Pincus, "Interpreting Laboratory Results: Reference Values and Decision Making," in *Clinical Diagnosis and Management by Laboratory Methods*, J. B. Henry, ed. (Philadelphia: W. B. Saunders Company, 1996).

J. N. Y. Qu, B. C. Wilson and D. Suria, "Concentration measurements of multiple analytes in human sera by near-infrared laser Raman spectroscopy," *Applied Optics*, volume 38, 25 1999, pp. 5491-5498.

S. Sharma, *Applied Multivariate Techniques* (New York: Wiley, 1996).

B. Schrader, *Raman/Infrared Atlas of Organic Compounds*, p. K1-03 (New York: VCH, 1989).

G. Strang, *Linear Algebra and its applications*, (Orlando: Harcourt College Publisher, 1988).

E. V. Thomas and D. M. Haaland, "Comparison of multivariate calibration methods for quantitative spectral analysis," Analytical Chemistry, volume 60, 1990, pp. 1091 –1099.

S. Wold and M. Sjostrom, *Chemometrics: Theory and Application*, Kowalski, B.R., Ed., (Washington, DC: American Chemical Society, 1977).

Chapter 5

Design of a high-sensitivity[1] system for Raman spectroscopy

One of the goals of this research was to develop a Raman technique to measure analyte concentrations in whole blood. Prior chapters discussed the challenges in making accurate measurements. Chapter 3 describes how turbidity reduces the intensity of the Raman signal in whole blood. Monte Carlo simulations were used to explain the mechanism of turbidity in signal reduction, and experiments were performed to confirm the turbidity effects. Overall, the intensity of the Raman signal was reduced by a factor of four, while the background noise did not decrease in whole blood, compared to the intensity in serum. Chapter 4 presents the effect of reduced intensities on prediction errors. Since a low signal-to-noise ratio (S/N) was the major source of prediction error, it was necessary to increase the S/N of Raman signals emerging from whole blood by a factor of four. This chapter describes in detail how a higher sensitivity system for Raman spectroscopy was developed and more than a factor of four improvement was made.

[1] Sensitivity is the ratio of the electrical output to the optical input in a system [Federal Standard 1037C]. In our studies, sensitivity is the ratio of the CCD counts to the excitation power for a specific analyte of unit concentration.

5.1 Overview

In the following subsections, the necessity of a high-sensitivity system is explained, and the design goal of four times higher signal-to-noise ratio (S/N) is presented. Fundamental concepts in radiometry, the study of radiation measurement, are described, and the methodology of the system design is discussed. Design of the new system required optimization of many optical components. Principles of optics and an optical design software used in the design process are also presented. After the new system was designed and built, its performance was demonstrated in an experiment. Finally, future directions are discussed.

Table 5.1. SI units employed for physical quantities in radiometry
[Nicodemus 1963, Boyd 1983, Holmes 1984, McCluney 1994, FS 1037C]

Quantity	Unit
Radiant energy	Joule
Radiant power (Radiant flux, Energy flow rate)	Watt
Plane angle	Radian
Solid angle	Steradian
Radiant intensity[2]	Watt/sr
Irradiance (Radiant emittance, Radiant exitance, Energy fluence rate)	$Watt/m^2$
Radiant exposure (Energy fluence)	$Joule/m^2$
Radiance	$Watt/m^2sr$
Radiant energy density	$Joule/m^3$

[2] This is not the "intensity of light," which is the amount of energy that crosses per second a unit area perpendicular to the direction of the flow [Born and Wolf 1980].

Physical quantities in radiometry have been named in different ways [Steel 1974, 1975]. For clarity, Table 5.1 summarizes key physical quantities in radiometry.

5.2 Background

As discussed earlier, the intensity of the Raman signals in whole blood was reduced by a factor of four, because hemoglobin absorbs photons and the system was not optimized to collect Raman signals emerging from a turbid medium. However, we did not see much change in background between serum and whole blood measurements. The major sources of the background fluorescence were optical components in the optical system, as many optical components, especially holographic filters, fluoresce strongly. A typical fluorescence background was much stronger than any Raman signal of blood analytes at physiological range. As the shot noise of the background was the dominant source of noise in spectra of serum and whole blood, noise levels were not much different in serum and whole blood. Accordingly, the signal to noise ratio (S/N) was also reduced by a factor of four in whole blood, and our immediate goal was to increase the S/N by a factor of four. We aimed to accomplish this goal by designing a new system for Raman spectroscopy of blood analytes. The sensitivity had to be enhanced, and perhaps the noise could be reduced as well. Another consideration in the system design was to make it modular so that any future improvements can be easily accommodated. Especially for future measurements in blood-tissue matrix, different light collection optics might be necessary, and the new collection optics can simply replace the current collection optics.

In addition to making a more sensitive instrument, there are other methods to increase the signal intensity and reduce the noise, such as increasing the excitation power, increasing the probability of the Raman scattering for each excitation photon, and filtering noise. These methods were carefully analyzed with considerations for safety, efficiency, and practicality.

Increasing the excitation power guarantees a signal increase. This is because more excitation photons are available for Raman scattering with increased excitation power. When more excitation photons impinge on the sample, more Raman-scattered photons emerge. However, high excitation power can damage the sample. In biological samples, photobleaching, protein denaturation, and photocoagulation are caused by high power laser excitation, and collected data cannot be trusted when samples are damaged. Therefore, it is not desirable to increase the excitation power beyond a certain level, since it increases the risk of photodamage. Considerations of excitation power are discussed further in Chapter 7.

The probability of Raman scattering for each excitation photon is a function of two parameters: concentrations of the molecules and Raman cross-sections. The probability can be enhanced by increasing any of these two terms. However, it may not be practical or feasible to increase these terms *in vivo*. The concentrations are the quantities to be measured, and they cannot be changed. In principle, surface enhanced Raman scattering (SERS) can increase the intensity of Raman signals [], but it requires SERS active particles, such as gold or silver colloids, making SERS measurements *in vivo* potentially unsafe.

In addition, there are other methods to improve S/N. Fourier filters may be employed to remove noise when the frequencies of the noise and the signal are different. However, Fourier filters worsened prediction accuracies in our studies, since it was difficult for Fourier filters to selectively remove noise without affecting the Raman signals (Chapter 4). Another method is to collect spectra for a longer period of time. Since the signal increases linearly with the collection time and the shot noise increases as the square root of the collection time, S/N improves with longer collection time.

However, other types of error sources, such as flicker noise, which has a strong low-frequency component, will become a dominant noise and reduce S/N if collection time is extended beyond a certain level. The flicker noise has strong noise at low frequencies [Yariv 1997], and its effect is more significant for long collection time. The flicker noise is due to instability in the system. It was observed in the previous system when the laser became unstable after its lifetime, but was eliminated by replacing the laser. The effect of flicker noise could be also reduced by frequency modulation [Haykin and Veen 1998].

Even if there were no flicker noise, it would be necessary to collect spectra for 80 minutes to increase S/N in whole blood by a factor of 4 from five-minute data, and 80-minute data collection is not practical in clinical settings.

Without severe flicker noise, the fluorescence background generates the dominant shot noise, and the fluorescence background is mainly generated by optical components and the quartz cuvette. In order to reduce the fluorescence generated by the quartz cuvette, several materials were tested to substitute quartz. It was found that certain types of magnesium fluoride (MgF_2) crystals (MooseHill, NJ) are optically clear for the wavelength

range of interest, and does not generate fluorescence. A cuvette was manufactured out of MgF_2. A regular cuvette was drilled, and a MgF_2 flat was attached by a soft glue. After each measurement, the MgF_2 flat was disassembled from the cuvette for cleaning and decontamination (of biohazard materials). However, a substantial background due to other optical components was still collected with the MgF_2 cuvette, and the difficulty of manufacturing the cuvette during clinical experiments discouraged further use of MgF_2 cuvettes.

Thus, we found that increasing the sensitivity of the system and reducing fluorescence background is a good method to increase the signals. This approach is independent of laser excitation power, and it does not require any manipulation of samples or introduction of additional chemicals to the samples. The collection efficiency is determined by the instrument, and advanced optical technologies can improve the collection efficiency.

As a result, developing a high sensitivity system is the most practical method to increase S/N and the best method to improve the prediction accuracy in whole blood. The following subsections discuss how such a system was designed and what performance the new system delivers.

5.3 Methodology

To develop a system with high sensitivity, we employed the following approach. First, we identified the efficiency of each component in the instrument. Second, a delivery geometry of excitation beam was selected which would confine the radiance distribution of Raman

signal to a small area at the sample surface. Although the sensitivity would increase with the confined radiance distribution, focused excitation radiance damages samples, and the sample damage threshold was also considered. Sample geometry was also considered. Since our samples consisted of whole blood contained in a cuvette, the sample geometry was simple and easily amenable to calculations. The surface distribution of Raman signals in whole blood was characterized. The radiance distribution measured in Chapter 4 was used. Third, the detector and spectrograph were analyzed. Both throughput and efficiency were considered. Fourth, an optical component was selected to transform the collected circular light to a linear beam. Fifth, an optimal collection geometry was calculated for the known radiance distribution of Raman signals. The optimal collection spot size and collection angle were the factors determining the collection geometry, based on the conservation of radiance. The calculation optimized the collection spot size and the optimal collection angle for the surface distribution of Raman signals in whole blood. Sixth, the optical components to collect signal within the given optimal collection geometry were selected. Many imaging optical components cannot collect light in the optimal collection geometry. The designed collection geometry was implemented by using non-imaging collection optics. The non-imaging optics that delivers the best collection efficiency was selected by using optical design software. Many commercially available non-imaging components were tested numerically, and we chose the component that provides the optimal collection efficiency and also collimates the collected light. Seventh, the collimated light was passed through a notch filter to block the excitation light, and the

filtered light was focused onto the fiber bundle. The new system was designed to be four times more sensitive than the previous system.

5.3.1 Conservation of radiance

The conservation of radiance is the main optical principle used in design of the new system. Two quantities, brightness and throughput, are defined in this discussion of conservation of radiance.

The conservation of radiance theorem is based on Abbe's sine condition in optical systems. For a well-corrected optical system Abbe states that

$$n_1 \sin\theta_1 h_1 = n_2 \sin\theta_2 h_2, \tag{5.1}$$

where n is the index of refraction, θ is the ray angle from the optical axis, and h is the height of the source or the image (Figure 5.1). The subscript 1 is for the source plane, and the subscript 2 is for the image plane. Abbe's theory can be derived via geometric optics [Klein 1986].

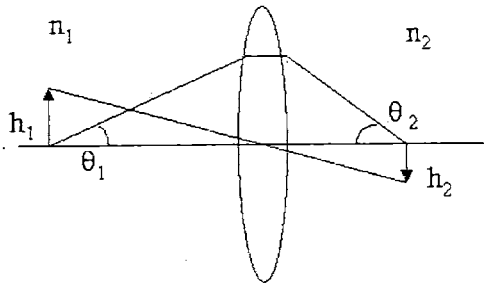

Figure 5.1. Diagram of Abbe's sine condition

From Eq. (5.1), we can take the squares of the both sides of the equation, and get

$$n_1^2 h_1^2 \sin^2\theta_1 = n_2^2 h_2^2 \sin\theta_2^2 . \quad (5.2)$$

For circular sources with axial symmetry (i.e. without dependence on the azimuthal angle) with radii h_1 and h_2, we can show that

$$A_1 = \pi h_1^2 \text{ and } A_2 = \pi h_2^2 , \quad (5.3)$$

where A_1 and A_2 are the areas of the circular sources. By inserting Eq. (5.3) into Eq. (5.2), we derive the throughput theorem,

$$n_1^2 A_1 \sin^2\theta_1 = n_2^2 A_2 \sin\theta_2^2 , \quad (5.4)$$

where each side of Eq. (5.4) is the throughput, T, of the system at each plane [Boyd 1983], and the throughput is sometimes called étendue or luminosity [Steel 1974, 1975]. The throughput at the source plane and the image plane are equal. Additionally, the throughput theorem can be derived by using a Hamiltonian [Born and Wolf 1980], and can be explained as an analogy of the Liouville theorem in statistical mechanics [Welford and Winston 1989].

In practice, a system is said to conserve throughput when there is no vignetting, or blocking of light, between the source plane and the image plane. In a system that conserves the throughput from the source plane to the image plane, the throughput should also be conserved at any plane between the source plane and the image plane along the optical axis. Thus, Eq. (5.4) is true for any two planes in a throughput conserving system.

Furthermore, we can consider the throughput theorem in terms of the energy of the light transmitted. Radiance (also called brightness) is the power of light transmitted through a unit area per unit solid angle. When all light is transmitted through the optical

system, the radiance is also conserved along the optical path, and this theorem is called the conservation of radiance. The throughput theorem and the conservation of radiance describe two different aspects of the same principle in terms of the instrument and the energy.

When the two planes are in the same medium (typically in air), the indices of refraction n_1 and n_2 are equal, and Eq. (5.4) is reduced to

$$\tau = A_1 \sin^2 \theta_1 = A_2 \sin^2 \theta_2, \tag{5.5}$$

where $\tau = T/n^2$ and $n = n_1 = n_2$. Eq. (5.5) shows the relationship between the collection area and the collection angle in an optical system that conserves the throughput. To simplify the equation, we can define the projected solid angle as $\Omega^* = \sin^2 \theta$.[3] Inserting this definition into Eq. (5.5), we get

$$\tau = A_1 \Omega_1^* = A_2 \Omega_2^*. \tag{5.6}$$

The throughput of an optical system is determined by the optical element with the lowest throughput. In a spectroscopy system, the spectrograph is often the element of the lowest throughput, and we wanted to use the spectrograph with the highest throughput.

5.3.2 Delivery of excitation beam

In highly turbid samples, such as whole blood, most Raman-scattered photons cannot penetrate more than a few millimeters, and they are strongly attenuated after transmitted through an optically thick sample. In such geometry, the most efficient method to collect

Raman-scattered photons in the optically thick sample is to collect photons from the same side on which the excitation photons impinge. When excitation and collection are performed on the same side of the sample, the geometry is called "single-ended". This single-ended geometry is also applicable to future *in vivo* studies, as Raman scattered photons rarely traverse through optically thick medium.

Delivery geometry plays an important role in determining the radiance distribution of excitation light and Raman signals. A narrow and focused beam can be used to obtain a confined distribution of Raman signals, while a broad and diverging beam can be used to obtain broadly distributed Raman signals. In order to collect light efficiently, it is desirable to confine the radiance distribution of Raman signals to a small region, as it is difficult to collect light efficiently with broadly distributed Raman signals, due to the limited throughput of the optical system. However, the number of Raman-scattered photons cannot be increased without affecting the number of absorbed photons in a given geometry. As Raman scattering is focused into a smaller region, thermal energy is deposited into a more focused region. In prior studies, thermal damage to whole blood samples was frequently observed with a 100 μm excitation spot at 300 mW. Thus, we decided to increase the excitation spot size to prevent sample damage. As a result, the collection efficiency was not as high as with a narrow beam excitation, but more reliable measurements were performed without damaging the samples. Collection efficiencies of narrow beam excitation and broad beam excitation are compared in Section 5.3.4.

---

[3] Ω^* is often mistaken for the geometric solid angle, $\Omega = 2\pi(1 - \cos\theta)$. For small angles, the projected solid angle and the geometric solid angle converge. For larger collection angles, the projected solid angle should be used for accurate throughput calculations.

5.3.3 Selection of spectrograph and detector

In a spectroscopy system, the spectrograph and the detector often play an important role in determining system throughput and the efficiency. Since we wanted to develop a high sensitivity spectroscopy system, a combination of a spectrograph and a detector that delivers the good throughput and efficiency was preferred.

We considered three types of spectrometers: dispersive, interferometric, and filter-based. In a dispersive spectrograph, the throughput is often determined by the slit width, the height of the active area in the detector (e.g. charge-coupled-device (CCD) array camera), and the acceptance angle of the optics. The advancement of volume holographic components made high throughput dispersive spectrographs available [Tedesco et al. 1993]. When combined with a large CCD camera, this type of spectrograph provides the highest throughput among the commercially available spectrographs, to the best of our knowledge. Holographic gratings also have a comparable efficiency (the ratio between incoming and emitted photons) to conventional gratings (up to ~80%). One issue in using a dispersive spectrograph is the collection of light emerging from a circular area with a narrow and long slit. Without proper transformation of light, a portion of the emitting light is blocked by the slit. The use of transforming optics can resolve this issue, and bring the efficiency of light transmission in a dispersive spectrograph to a value comparable to that in an interferometric spectrometer.

A typical interferometric spectrometer [Wilson 1995] has a throughput comparable to that of a dispersive spectrograph. The major benefit of employing an interferometric spectrometer is that a single channel detector, which is cheaper and enables faster data

reading than a multi-channel detector (e.g. a CCD camera), can be used. However, interferometric spectrometers often have moving components, which often require frequent alignment and raise difficulties in positioning the moving components with good reliability (the precision has to be well under the wavelength scale). Accordingly, interferometric spectrometers are more often used in wavelengths longer than the wavelength of our interest.

Filter-based instruments can deliver the highest throughput, since large size optical filters are available and filters can provide reasonable performance even for non-collimated light [Dou 1997]. The challenge in developing filter-based spectrometers is to provide high resolution multi-channel information to distinguish chemicals. The spectrograph in the current system provides 25 cm^{-1} resolution over the wavelength range between 830 nm and 1000 nm, and this would require at least 80 optical filters. Employing so many optical filters would be unwieldily expensive, and losses would greatly decrease the efficiency of such a system.

Thus, we chose to use a dispersive spectrograph with holographic components (Kaiser Optical). The spectrograph used in the previous experiment (Chapter 2) still remains as the state-of-the-art spectrograph. In our spectroscopy system, the throughput of the spectrograph limits the throughput of the system. The collection angel (15.5°) was limited by the optics in the spectrograph (f/1.8), and its corresponding Ω^* was 0.07 (Eq. 5.5). The limiting collection area was the product of the width and height of the optical slit. The slit height was limited to 15 mm by the optics and the grating in the spectrograph. As the magnification of the spectrograph was 1.13, the height of the slit corresponded with the

CCD detector height, 17 mm. We employed the largest CCD camera (25 mm x 17 mm) at a good efficiency (~ 25%). Although smaller CCD cameras with higher efficiency (as high as ~ 80% for the wavelength region of our interest) could be used with cylindrical lenses, aberrations and losses due to the use of such lenses would reduce the efficiency of the system.

The slit width determines the spectral resolution and the system throughput (Eq. 5.4). A too-wide slit results in a high-throughput low-resolution system. A high throughput system can collect signals more efficiently. The low-resolution spectra have many overlapping spectral features. While a lower S/N works favorably with respect to prediction accuracy, prediction accuracy can be adversely influenced due to spectral overlap (see Chapter 4), and the spectral overlap may become the dominant factor in prediction error. A too-narrow slit results in a high-resolution, low-throughput system. The high-resolution spectra have sharp, distinct spectral features. However, the S/N of spectra collected by a low throughput system is low. While the spectral features can be separated easily, low S/N may become the dominant error source (see Chapter 4). The optimal system can be found somewhere in between these two extremes.

In order to approximately determine the optimal slit width, a numerical simulation was performed. Instead of using optical slits of various widths, the Raman spectra of human serum samples were numerically binned with a range of bin sizes, and spectral data sets of various resolutions were obtained. PLS analysis (Chapter 4) was performed, and glucose concentrations in the spectral data sets were predicted.

Figure 5.2 shows the prediction error for various bin sizes. For the small bin size range, the prediction error decreases as the bin size increases, because increasing the bin size effectively reduces the influence of spectrograph drift and increases S/N of each data point. For the large bin size range, the prediction error increases as the bin size increases, because the spectral overlap becomes more significant with larger bin sizes. The previous system had an 8 cm^{-1} resolution with a 100 μm slit. While prediction error was the minimum with the eight pixel bin size, which corresponds to 16 cm^{-1} resolution, the prediction error increased by 10% from the minimum when the bin size was increased to 12 pixels, which corresponds to 25 cm^{-1} resolution. Instead of using a 100 μm slit and binning, the same 25 cm^{-1} resolution was achieved by using a 300 μm slit without binning. This increased the system throughput by factor of three, which can potentially improve the prediction accuracy by 73% (Chapter 4). Including the 10% prediction error increase due to the lower resolution, the net increase of the prediction accuracy was predicted to be 63%.

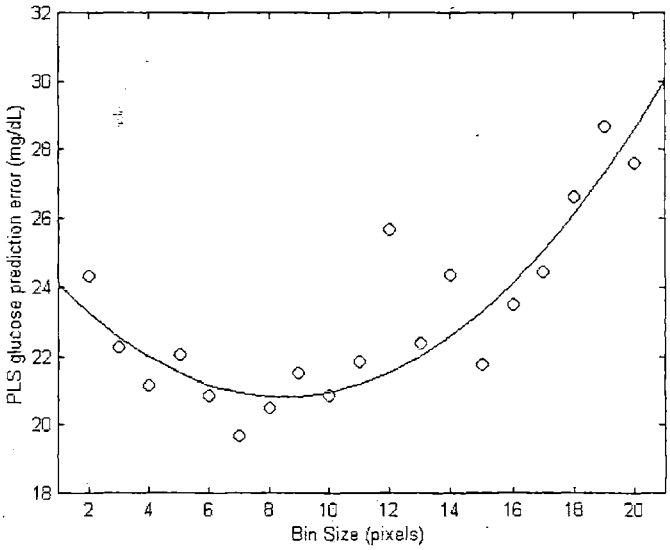

Figure 5.2. PLS prediction errors of glucose at various bin sizes (circle) and fit (line). The best prediction is available with the bin size of 8 pixels.

Based on this calculation, the slit width was determined to be 300 μm. The limiting collection area is then 4.5 mm^2, and the limiting collection angle is 15.5° for the f/1.8 spectrograph. The corresponding projected solid angle is 0.07. For an optical system whose throughput is limited by this spectrograph, Eq. (5.6) is reduced to

$$\begin{aligned} \tau &= A_1\Omega_1^* = A_2\Omega_2^* \\ &= 4.5\,\mathrm{mm}^2 \times 0.07 \\ &= 0.32\,\mathrm{mm}^2 \end{aligned} \tag{5.7}$$

5.3.4 Collection of Raman scattered light

For a given spectrograph throughput, the task was to design optics that collects Raman scattered light from whole blood. As the dispersive spectrograph was employed, we needed optics to transform the light emerging from a circular source to a line. An optical fiber bundle was used to serve as the transforming optics, and it was designed to conserve the throughput of the spectrograph. Within the limitation of the given spectrograph, the collection geometry was optimized. In the calculation of the optimized collection geometry, the surface distribution of Raman light obtained from an experiment and a Monte Carlo simulation (Chapter 3) was used.

Optical fiber bundle

The shape of the optimized slit did not match the shape of the spatial distribution of Raman signals. The shape of the new entrance slit was a narrow and tall rectangle (0.3 mm x 15

mm), whereas the spatial distribution of the Raman signal was axially symmetric (Chapter 3).

The rectangular slit is not an ideal aperture for transmitting light emerging from a circle, since it blocks most of light. If the new slit is used, 58% of light emerging from a circle of 0.9 mm diameter, which is the full-width-at-half-maximum (FWHM) of the Raman signals emerging from whole blood (Chapter 3), is blocked by the slit.

Therefore, as with the past system, an optical fiber bundle was used to covert the light emerging from a circular source into the narrow and tall image of the slit. The fiber bundle had the same collection area (4.5 mm^2 less the packing loss) and the same collection angle (15.5 °) as the spectrograph, and hence maintained the throughput of the system. Furthermore, the fiber bundle can be flexible, which is a desirable feature in future *in vivo* measurements.

The fiber bundle was custom made by Romack with 61 optical fibers in a five-layer structure (Figure 5.3). The core diameter of each optical fiber was 300 μm to match the slit width, the outside diameter of the cladding was 330 μm, and the outside diameter of the buffer (protective layer) was 360 μm. The fibers on the entrance side of the bundle were packed in a near-circle, and the fibers on the emitting side of the bundle were packed linearly. On the entrance side, the inner three layers were hexagonally packed to ensure the highest packing fraction (the ratio of the fiber core area to the total area), and the outer two layers were roundly packed to facilitate the assembly process. To increase the packing fraction, the buffer of each fiber was stripped. On the entrance side, the packing fraction of the fiber bundle without the buffer was 0.6224. The packing fraction would be 0.5230 if

the fibers were not stripped. On the emission side, the packing fraction of the stripped fiber bundle was 0.7151. If the fibers were not stripped, it would be 0.6545. As a result of stripping the buffer, optical fibers became fragile, and three optical fibers were damaged during the assembly of the bundle. However, the damaged optical fibers did not affect the collection efficiency in this system, since the current CCD detector can image only 45 fibers. Although the current CCD camera can image a vertical bundle of 45 330-μm fibers, the fiber bundle was made with 61 optical fibers for future employment of a taller CCD camera. The diameter of the entrance side of the fiber bundle was 3 mm, and the height and width of the output side of the bundle were 21 mm and 0.3 mm, for the active area. The NA of the fiber was 0.28, selected to match the NA of the spectrograph. This eliminated the need for any connection optics, and any optical loss associated with the connection optics was also eliminated.

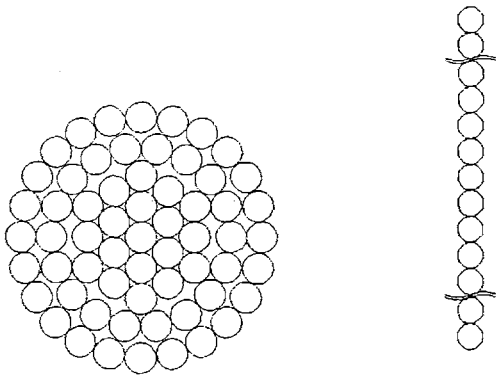

Figure 5.3. The input end (left) and output end (right) configuration of 61 fibers in the fiber bundle. The inner three layers are hexagonally packed (honeycomb packing), and the outer two layers are roundly packed in the input end. 61 fibers are arranged linearly in the output end.

Calculation to optimize the collection efficiency

In order to calculate and optimize collection efficiency, we had to know the radiance distribution on the sample surface of whole blood samples. However, radiance is a function of angle and position on the surface, and it was difficult to measure radiance at all angles and positions. In Chapter 3, we measured the radiance distribution of whole blood at certain angles and positions, and the Monte Carlo simulation results matched well with the radiance distribution. With an approximation in the coupling of the spatial and angular radiance distribution, collection efficiencies can be calculated from the limited measurement data. The collection efficiencies calculated with the measurement data and the simulation results provided similar collection efficiency curves.

With the system throughput determined, the optimal collection geometry can be calculated by trading off the collection spot size and the collection angle so that the throughput is conserved. The radiant power of Raman signals collected from the sample can be formulated as

$$S = P \int_{A_c} \int_{\Omega_c} R(r,\theta) dA d\Omega , \tag{5.8}$$

where S is the radiant power of the Raman signal (W), P is the radiant power of the excitation light (W), R is the radiance ($1/m^2sr$) distribution function of the Raman signal at the surface of the cuvette containing whole blood sample for 1 W excitation radiant power, r is the radial position on the surface (μm), and θ is the collection angle (degrees). The radiance of the Raman signal, R, is a function of r and θ. While R is also a function of the geometry and optical properties, for simplicity, it is assumed that the geometry is a single-ended semi-infinite medium and that the optical properties are fixed.

By replacing A and Ω with functions of r and θ, Eq (5.8) becomes:

$$S = P \int_{r_C} \int_{\theta_C} 2\pi r \cdot 2\pi \sin\theta \cdot R(r,\theta) \cdot dr d\theta . \tag{5.9}$$

The excitation radiant power is independent of the collection optics, and we can define a new variable, collection efficiency, ε, as $S/4\pi^2 P$. By inserting Eq. (5.9) into this definition, we derive:

$$\varepsilon = \int_{r_C} \int_{\theta_C} r \sin\theta \cdot R(r,\theta) \cdot dr d\theta . \tag{5.10}$$

If we assume that the Raman energy distribution function R can be expressed as a product of two separate terms, R_1 and R_2, Eq. (5.10) can be expressed as:

$$\varepsilon = \int_{r_C} \int_{\theta_C} r \sin\theta \cdot R_1(r) R_2(\theta) \cdot dr d\theta , \tag{5.11}$$

where R_1 is the normalized irradiance distribution function ($1/m^2$), or spatial distribution function, and R_2 is the normalized radiant intensity (1/sr), or angular distribution function, of Raman signal on the whole blood surface. Since R_1 is independent of θ and R_2 is independent of r, Eq. (5.11) can be rearranged into:

$$\varepsilon = \int_{r_C} r R_1(r) \cdot dr \int_{\theta_C} \sin\theta \cdot R_2(\theta) \cdot d\theta . \tag{5.12}$$

The spatial and angular distributions of Raman signal on the whole blood surface were measured in Chapter 3. If we aim to use a 100 μm diameter excitation beam, we can use the measured distribution functions as R_1 and R_2 in designing the collection optics for whole blood samples. The beam size affects the irradiance and the radiant exposure, which are related to sample damage. This is discussed further in a later part of this section.

As discussed earlier, the throughput is determined by the spectrograph, and the maximum signal intensity can be obtained by trading off the collection area and the collection angle. For a given radius of a spot, its area is defined as

$$A_c = \pi r^2 . \tag{5.12}$$

The corresponding collection angle within the system throughput can be calculated from Eq. (5.7):

$$\Omega_c^* = 0.32/A_c . \tag{5.13}$$

Figure 5.4 shows A_c and the collection angle calculated from Ω_c^* as functions of the radius of the collection spot r in an optical system whose throughput is limited by the throughput of the spectrograph. In single-end light delivery-collection geometry, the collection angle cannot be greater than 90°. The throughput is not conserved when a collection spot radius is less than 0.3 mm due to this geometrical constraint.

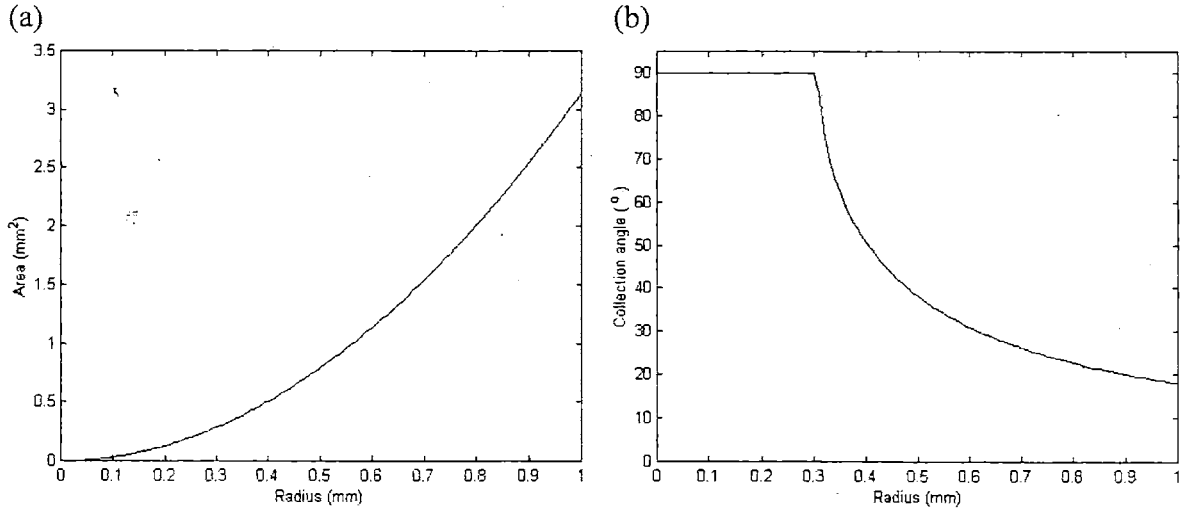

Figure 5.4. The area A_c (a) and the collection angle Ω_c^* (b) are functions of the radius of the collection spot, r, in an optical system whose throughput is limited by the throughput of the spectrograph. The throughput is 0.32 mm^2.

The area integration and the angular integration of the distribution of Raman signal on whole blood surface can be performed using the distribution functions measured in Chapter 3. Figure 5.5 displays the calculation of the area integral, $\int_{r_c} rR_1(r) \cdot dr$, and the angular integral, $\int_{\theta_c} \sin\theta \cdot R_2(\theta) \cdot d\theta$. Since Ω is always 1 when the spot radius r is less than 0.3 mm, the angular integral is also constant for the region where the radius is less than 0.3 mm.

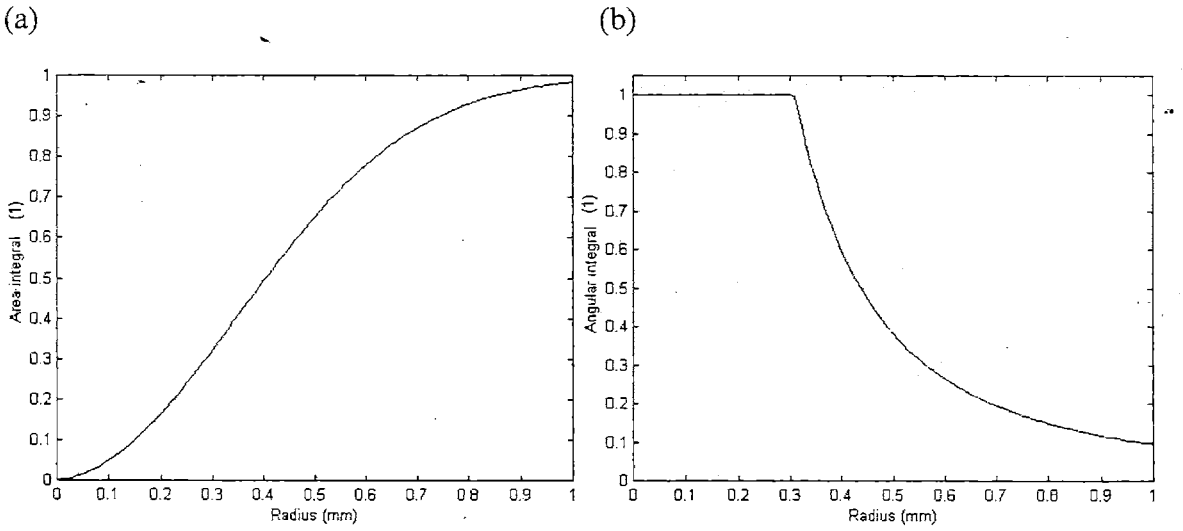

Figure 5.5. The area integral (a) and the angular integral (b) for Raman signals emerging from whole blood in an optical system whose throughput is limited by the throughput of the spectrograph.

As shown in Eq. (5.12), the collection efficiency ε is the product of the area integral and the angular integral; using the results of Figure 5.5, we obtain the collection efficiency curve of Figure 5.6. The maximum collection efficiency can be achieved by collecting signals from a 0.31 mm radius spot and its corresponding collection angle, 90 °. This is due to the fact that Raman light emerges from the whole blood surface at wide angles, the

maximum collection efficiency is available by collecting light from all angles and a small region of high radiance rather than from a spatially spread distribution and a narrow angle range. This optimal collection geometry collects 34% of the total Raman photons emerging from the whole blood surface. In a similar manner, the maximum collection efficiency of the previous system (throughput 0.11) was calculated to be 12% (Figure 5.7). However, the previous system was not operating with the maximum collection efficiency, and its collection efficiency was slightly lower, 11%. The maximum collection efficiency of the new system is a factor of 3 greater than the efficiency of the previous system.

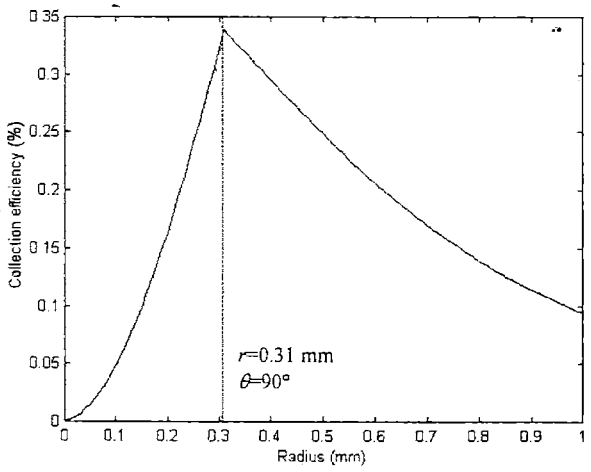

Figure 5.6. Collection efficiency of the new system for various collection geometry. The collection efficiencies were calculated using experimental results and Eq. (5.10). For the new system, the maximum collection efficiency is 34%.

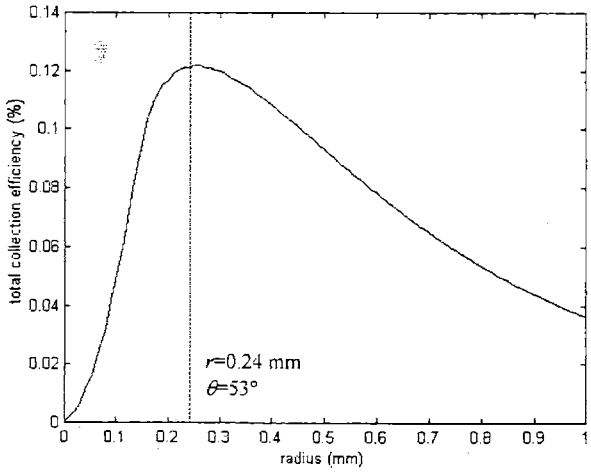

Figure 5.7. Collection efficiency for the previous system. The collection efficiencies were calculated using experimental results and Eq. (5.10). The maximum collection efficiency of the previous system was 12%.

In this calculation, we assumed that the spatial-angular distribution of Raman signals is the product of the spatial distribution and the angular distribution, and that the spatial distribution and the angular distribution are independent of each other. This assumption was made to simplify the calculation. However, the spatial distribution and the angular distribution are slightly coupled in turbid samples. The angular distribution of Raman signals near the excitation spot is narrower than the angular distribution at a point distant from the excitation spot. To test the accuracy of this simplified calculation, the collection efficiency curve was generated using Monte Carlo simulation results and compared. Since Monte Carlo simulations provided angular and spatial distributions of Raman signals for each angle and radius, the collection efficiency was calculated using Eq. (5.9), instead of using its approximate form, Eq. (5.12). Figure 5.8 shows the collection efficiency curve generated by using Monte Carlo simulation results. The 33% collection efficiency can be achieved by collecting signals from a 0.35 mm radius spot. This collection geometry is similar to the calculation results in Figure 5.6 obtained by using Eq. (5.12). Discontinuities in the large radius region (> 0.35 mm) are due to the discrete manner in which Monte Carlo simulation results are reported. At a larger radius (~1 mm), the collection efficiency obtained by the approximate calculation is about half of the collection efficiency obtained with the Monte Carlo simulation results. This indicates that the approximation does not hold for data points at large radii, as the angular distribution becomes dependent on the spatial distribution in such regions.

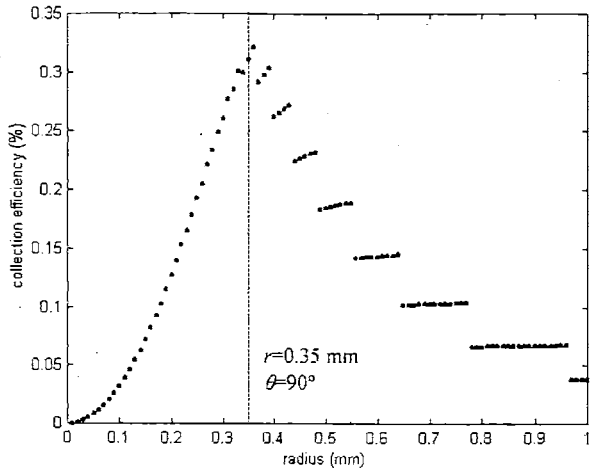

Figure 5.8. Collection efficiency of the new system for various collection geometry. The collection efficiencies were calculated using Monte Carlo simulation results. The maximum collection efficiency is 33%.

Optimization of the collection efficiency with consideration for sample damage issues

The calculation above assumed a 100 μm×100 μm square excitation beam geometry. The diode laser delivers a 280 mW excitation beam to the sample, and the irradiance can be as high as 2.8 kW/cm^2 when the excitation beam is focused onto a 100 μm×100 μm square region. In prior studies, this high irradiance beam easily damaged whole blood samples even at short exposure times (<10 second), and it was difficult to perform reliable measurements. Since we wanted to collect Raman signals for up to the same data collection time as in the previous experiment (300 seconds), we chose to increase the excitation beam spot size in the experimental setup to reduce the irradiance of the excitation beam on the sample surface close to the level (40 W/cm^2) tested for laser safety in *in vivo* applications at a similar near-infrared wavelength (785 nm) [Shim and Wilson 1996]. We could obtain a 28 W/cm^2 irradiance by expanding the excitation beam in the experimental setup to a 1 mm×1 mm spot. With this reduced irradiance, no visible damage was observed in whole blood samples. However, the excitation energy was distributed over a larger area,

and the Raman signal distribution was broader. Since the system could not collect photons from a larger area and at the same angle with the same efficiency, the broader distribution of Raman signals reduced the collection efficiency.

The collection efficiency was calculated for the 1 mm excitation beam. The spatial distribution of Raman signal R_I, measured for a narrow 100 μm excitation beam (Chapter 3), was numerically convoluted over a 1 mm×1 mm square area, and we obtained a new distribution function of Raman signal, R_I'. The computation of the area integral and the collection efficiency was performed using R_I' in the same manner as described above. Figure 5.9 shows the collection efficiency as a function of the collection spot radius.

The maximum collection efficiency was achieved by collecting the photons from a 0.31 mm radius spot and its corresponding collection angle, 90°. The maximum collection efficiency with a 1 mm excitation spot (21%) was reduced by 36%, compared to the collection efficiency with a narrow excitation beam (33%), but was still higher than the collection efficiency of the previous system (11%) (Chapter 2). However, the irradiance on the sample was lower, and the risk of sample damage was reduced. Further investigation of the safe level of irradiance and radiant exposure may reveal that an excitation spot smaller than 1 mm diameter at a higher irradiance could be applicable without sample damages, and it may lead to a large signal.

(a)

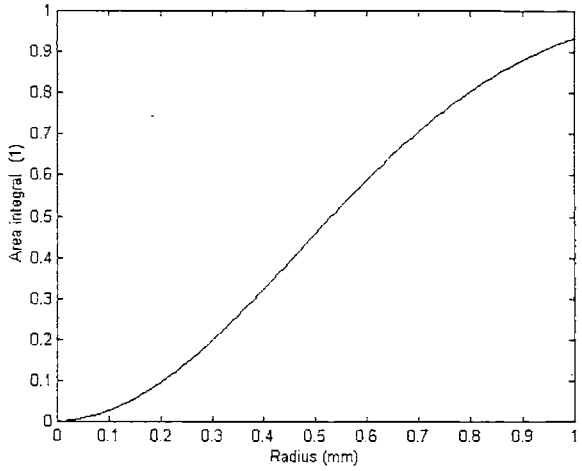

(b)

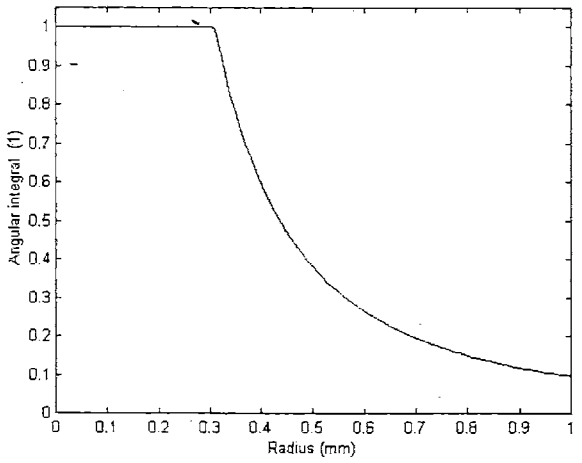

(c)

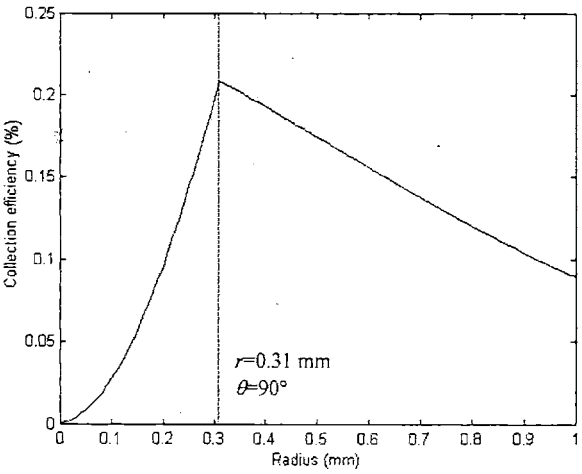

Figure 5.9. (a) The area integral of the Raman signal distribution function, R_I', (b) the angular integral, and (c) the collection efficiency calculated using the area integral of R_I'. The maximum collection efficiency was 21%, which is factor of 1.6 down from the collection efficiency with a narrow beam excitation (Figure 5.4).

5.3.5 Selection of optical components

Figure 5.15 shows the schematic diagram of the new experimental system. This section discusses selection of optical components based on the design specifications determined in the previous section.

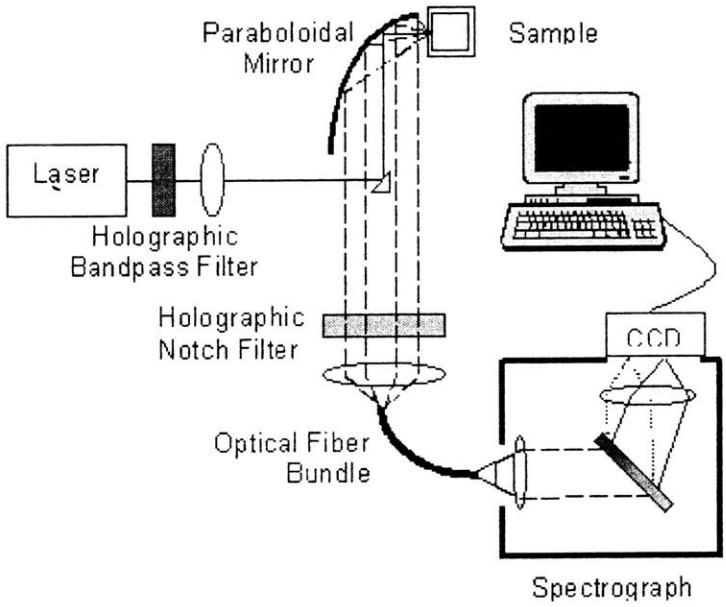

Figure 5.10. Schematic diagram of a new system employing a paraboloidal mirror for efficient light collection. The coupling optics between the optical fiber bundle and the spectrograph is also optimized.

From the collection efficiency calculations, it was concluded that the collection efficiency can be maximized by collecting Raman signal emerging from 0.31 mm radius spot with 90° collection angle. Although collection of light at 90° angle is not feasible in practice, the design goal was to find optical components that collect light in a manner close to the given geometry. This performance is not commonly available with many imaging

optical components. Single lenses can typically collect light up to 30°. Also, dry reflective objectives cannot collect light at a collection angle wider than 30° [Born and Wolf 1980]. Typical dry microscope objectives have a numerical aperture (NA) up to 0.7, which corresponds to a 45° collection angle. Many water-immersion or oil-immersion objectives can collect light up to a wider collection angle. However, such high angle collection optics have a limited field of view, and they cannot collect light from a spot with a diameter as large as 0.62 mm. A typical water-immersion microscope objective can collect light from a 200-μm diameter spot at 65° collection angle.

There are optical components that provide higher collection efficiencies. Those optics cannot deliver images, and thus, are called non-imaging optics [Welford and Winston 1989]. Among those, paraboloidal and ellipsoidal mirrors are commonly used in lighting instruments, as these can be manufactured easily. Paraboloidal mirrors collimate light emerging from a focal point, as in a searchlight, and focus collimated light onto a spot, as in certain types of telescopes. Ellipsoidal mirrors collect light emerging from a focal point and focus the collected light onto another focus. Compound parabolic concentrators (CPC's) are also powerful elements in radiometry. CPC's are designed to collect light at any desired collection geometry, and are often used as solar energy concentrators [Welford and Winston 1989]. They can, theoretically, collect light from a large area and at a wider angle. However, CPC's need to be manufactured with tight tolerance, and it is difficult and costly to make such a small precision optics [Tanaka 1996].

For our high-sensitivity system, a paraboloidal mirror was selected as the collection optics, since paraboloidal mirrors can collect light from a large angle and collimate the

collected light, as the collected light has to be collimated before being filtered by a holographic notch filter. Furthermore, paraboloidal mirrors are commercially available and easy to purchase. To place the sample at the focal point, one half of a paraboloidal mirror was used in an off-axis paraboloidal configuration (Figure 5.11).

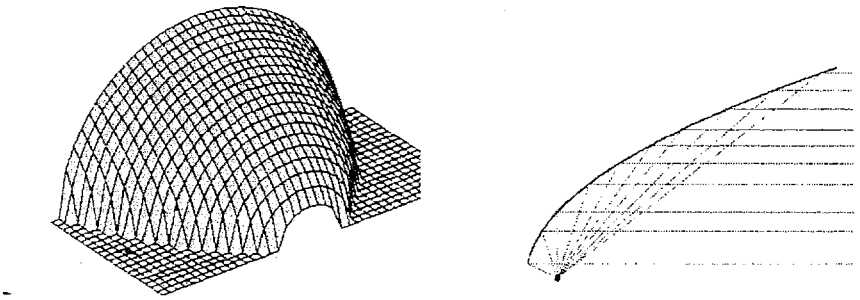

Figure 5.11. The diagram of one half of a paraboloidal mirror (left). The diagram of off-axis configuration of a paraboloidal mirror (right). The mirror (thickline) collimates rays (thin line) emerging from its focal point (dot).

An optical design software, Zemax (New-Focus Software, AZ), was used to select the optimal combination of a parboloidal mirror and a lens. The model of the optical system in Zemax included a light source (a spot of a given radiance distribution function), a paraboloidal mirror, a focusing lens, and a fiber bundle (Figure 5.12). We used the light source mimicking the measured surface distribution of the Raman scattered light emerging from the source (Chapter 3). The size of the detector was chosen to match the size of the fiber bundle for the new system. We varied the size and curvature of the paraboloidal mirror, and the size and power of the focusing lens. The size and curvature of commercially available paraboloidal mirrors were obtained from product catalogues. The size of the lens was varied between 1" to 3", and the NA of the lens was matched to the NA

of the fiber bundle (and the spectrograph), 0.28, in order to put limitations on the acceptance angle. Collection efficiencies were calculated by Zemax for a various combination of the variables.

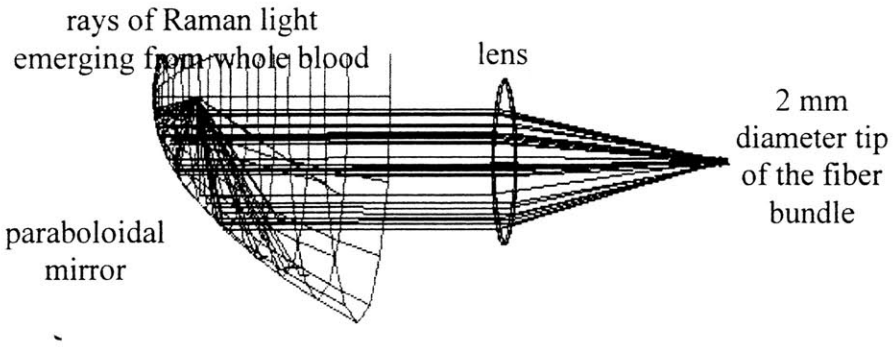

Figure 5.12. Zemax model of the collection optics. The optimal combination of a paraboloidal mirror and a lens was selected by Zemax calculations. See Figure 5.13 for the image of light collected on the tip of the fiber bundle.

Figure 5.13 shows some images of light collected on the entrance end of fiber bundle. When the generation of Raman scattered light is confined and the source is small (0.3 mm diameter circle), the collection optics can collect up to 54% of Raman scattered light emerging from the whole blood surface. When the source is broader and the surface distribution is close to that measured in blood (a 1.0 mm diameter circle), the collection optics can collect up to 36% of Raman scattered light, which matches well with the maximum collection efficiency calculated by the numerical approximation and the Monte Carlo simulation results (Figure 5.6 and Figure 5.8).

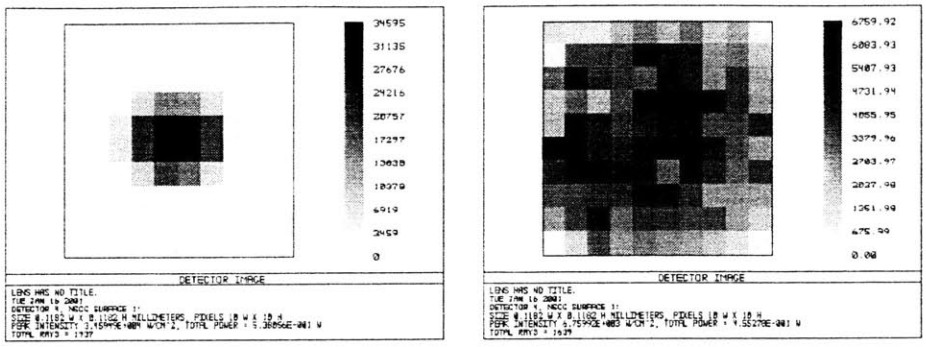

Figure 5.13. The image of light collected on the fiber bundle, from a 0.3 mm diameter source (left) and from a 1.0 mm diameter source (right) obtained by Zemax calculations.

The final design from the Zemax calculation included a paraboloidal mirror with its focal point placed 0.625" from the vertex, and the length of the mirror was 2.8" (3.01" from the vertex to the end) (Figure 5.14). The paraboloidal mirror (manufactured by ORC/PerkinElmer) was electroformed, and cut 0.5" inside the optical axis to facilitate placing a sample at the focal point of the mirror. As a result, the paraboloidal mirror could collect light from a 1 mm spot at up to 80° collection angle on the vertex side and up to 45° on the opposite side. The working NA of this paraboloidal mirror was 0.9 (Born and Wolf 1980]. The inside surface of the paraboloidal mirror was coated with gold to maintain high reflectivity for the target wavelength region between 830 nm and 1000 nm, and 85% reflectivity was obtained.

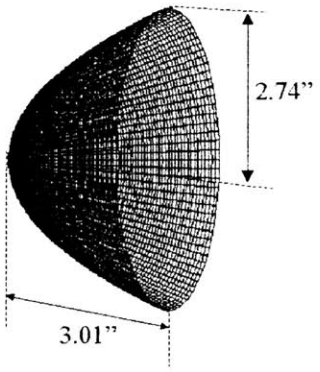

Figure 5.14. Zemax model of the paraboloidal mirror design

To block photons at the excitation wavelength in the collected light, a 2" diameter holographic notch filter (Kaiser Optical Systems) was placed. The light, nearly collimated by the paraboloidal mirror, was filtered the notch filter. A 2" aspheric lens (Melles-Griot) was used to focused filtered light onto the fiber bundle (Figure 5.15). The combination of the selected paraboloidal mirror and lens can deliver 36% collection efficiency for Raman signal from whole blood irradiated by a focused beam.

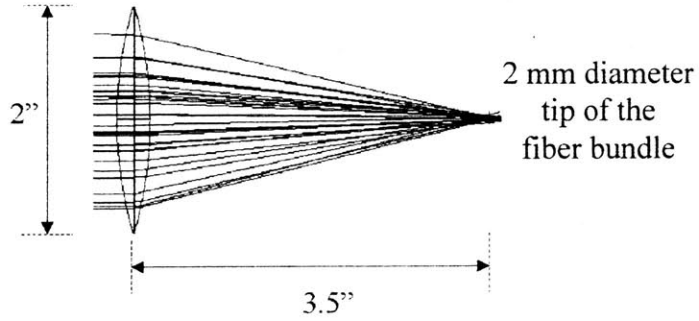

Figure 5.15. Zemax model of a typical focusing lens

5.3.6 System specifications

In the new system, the diode laser generates the excitation beam at 830 nm. The laser operates in multi-mode, and the beam is filtered to remove wavelengths other than 830 nm. A 100 mm focal length lens focuses the beam onto a prism. A small 1 mm×1 mm×1 mm prism was selected to minimize the shadowing of the collected Raman signals. Less than 3% of the collected Raman signals were blocked by the prism and its holder. The prism was located so that the excitation beam reflected by the prism was again focused by the paraboloidal mirror, and the beam size was 1 mm×1 mm at the focal plane of the mirror. The laser beam intensity was 280 mW at the sample plane. A sample was placed perpendicular to the optical axis, and the mirror collected Raman signals from the sample. A notch filter removed the excitation light, and the Raman photons were focused onto the optical fiber bundle. On the entrance side, the fibers were grouped in a hexagonal array to maximize the packing fraction (0.6224), and arranged in a line shape on the other side to match the shape of the slit of the spectrograph. The Raman signals were delivered to the spectrograph, and the grating dispersed light as a function of wavelength. The CCD camera converted the Raman photons to electrons and counted the number of electrons. The CCD counts were converted to spectra, which were analyzed with multivariate techniques, discussed in Chapter 4.

Table 5.2. Summary of system specifications

Component	*Specification*	*New system*	*Previous system*
Laser	Wavelength	830 nm	
	power output	480 mW	500 mW
Sample	Volume	1 ml	
	Excitation power on sample	280 mW	300 mW
	Excitation beam size	1 mm×1 mm	100 μm×100 μm
Collection optics	Optics type	Paraboloidal mirror	Reflective objective
	Focal length	15.9 mm	13.4 mm
	acceptance angle 1	80° (max on vertex side)	33° (maximum)
	acceptance angle 1	45° (max on open end side)	17° (minimum)
	NA	0.9	0.5
Fiber bundle	core diameter	300 μm	100 μm
	cladding diameter	330 μm	110 μm
	number of optical fibers	61	177
	packing fraction	0.6224	0.6125
	NA	0.28	0.22
	circular end diameter	3.0 mm	1.7 mm
	linear end height	20.1 mm	19.5 mm
Focusing lens	(Effective) focal length	90 mm	100 mm
	Diameter	51 mm	105 mm
Spectrograph	NA	0.27	
	Dispersion	16.5 m/cm^{-1}	
CCD detector	Height	17 mm	
	pixel size	22 μm x 22 μm	
	quantum efficiency	20% @ 900 nm	

5.4 Result and discussion

The new spectroscopy system was optimized for collecting signals from whole blood in a single-ended geometry. Increase in the system throughput, use of non-imaging optics for optimal collection, and elimination of the connection optics improved the sensitivity. Table 5.3 summarizes the factors contributing to the increased sensitivity. Using the high sensitivity spectroscopy system (Figure 5.16), the Raman signal in whole blood was increased by a factor of four in the new system (Figure 5.17).

Table 5.3 Factors contributing to the sensitivity

Factors	*New system*	*Previous system*	*Gain in signal*	*Miscellaneous*
Collection efficiency	21%	11%	×1.9	For a 1 mm excitation beam
Packing fraction	62%	61%	×1.0	Due to the use of an optical fiber bundle
Connection efficiency	~100%	~50%	× 2.0	Due to elimination of connection optics
AR coating	64%	64%	× 1	11 optical surfaces
CCD detector	20%	20%	× 1	quantum efficiency at 900 nm
Total	**~1.7%**	**~0.4%**	**× 3.9**	

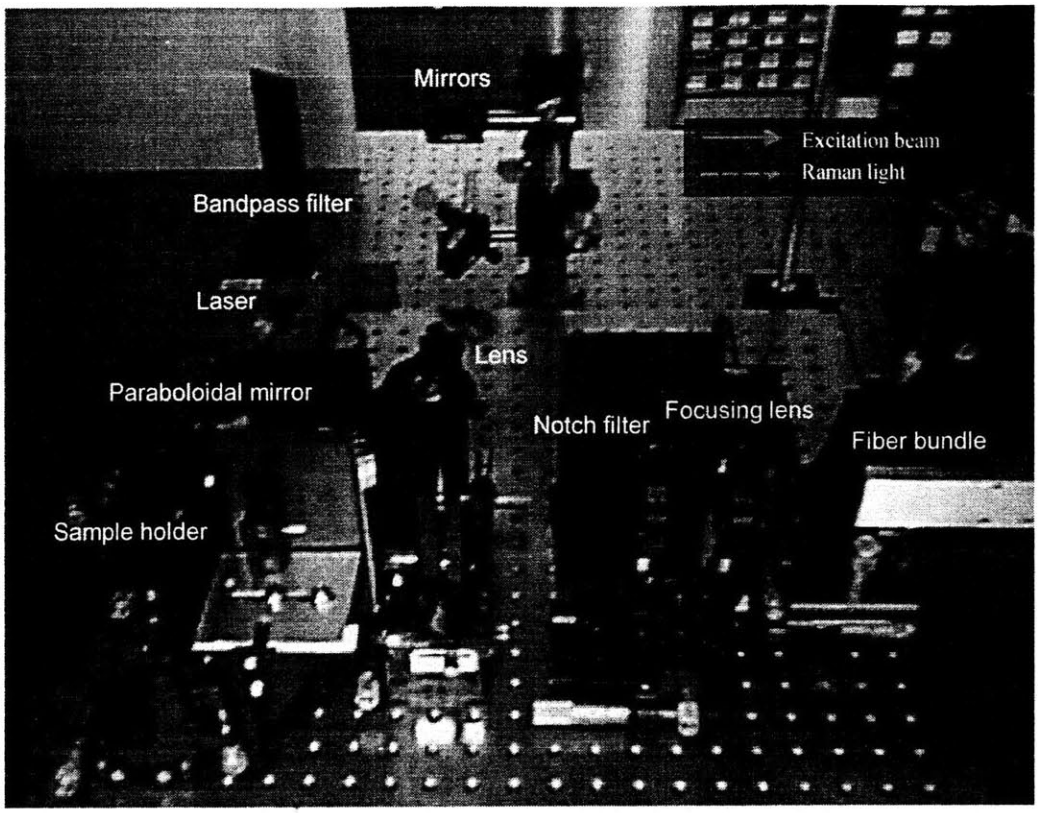

Figure 5.16. Photograph of the experimental setup

To quantify the sensitivity increase, we took the spectrum of glucose, as glucose is among our analytes of interest, and is a simple molecule. Furthermore, its signal at a physiological concentration (45~180 mg/dL or 2.5 to 10.0 mM) is relatively weak, and it serves as a good test case for demonstrating the high sensitivity of the new system. The Raman spectrum of glucose was obtained by subtracting a spectrum of whole blood (blank) from the spectrum of whole blood spiked with a unit concentration of glucose. The difference spectrum was normalized by the glucose concentration, and the normalized spectrum was compared with the spectrum of glucose obtained with the previous system in a similar manner (Figure 5.17). The Raman spectrum of 1 mM (18 mg/dL) glucose

obtained with the new system has 6 counts of peak intensity around 1117 cm^{-1} at 280 mW excitation for 10 seconds, whereas that obtained with the previous system has 1.7 counts of the peak intensity at 300 mW excitation for 10 seconds. Except for the intensity, all the Raman peaks of glucose are identically present for both systems with slightly different resolutions. These glucose spectra also match well with the published Raman spectrum of glucose [Vasko 1972, Schrader 1989].

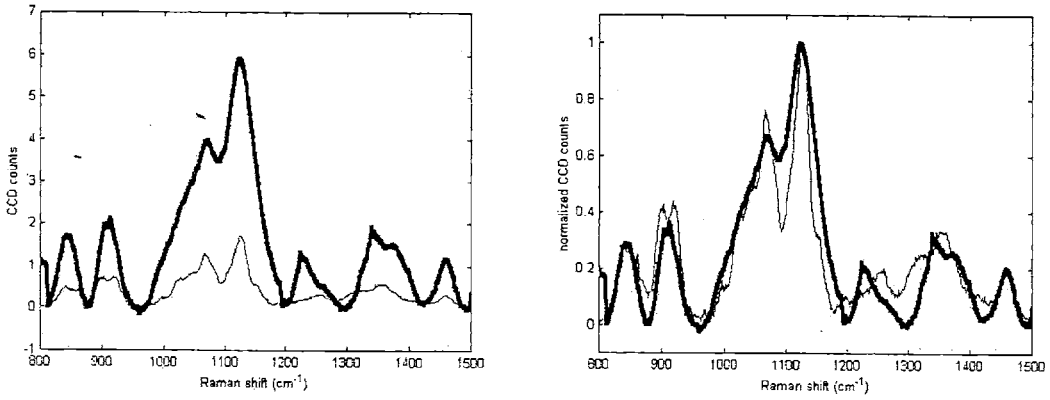

Figure 5.17. Raman spectra of glucose at unit concentration collected by the new system (thick line) and the previous system (thin line) for 10 seconds (left). The current system has four times higher sensitivity. The same spectra are normalized by their peak intensities around 1117 cm^{-1} (right). The current system has lower resolution than the previous system. Average spectra of 30 frames are presented.

Whereas the signal increased almost by a factor of four, the background decreased by half (Figure 5.18). This is because the optical components were the major sources of the fluorescence background (Figure 5.19), and the number of optical components were reduced in the new system. The fluorescence background generated by each optical element was measured from the spectra collected by placing a notch filter before and after the element. The spectral difference was assumed to be the fluorescence generated by the

optical element. As the fluorescence background decreased, the shot noise from the background also decreased by a factor of 1.4. The background fluorescence could be reduced further by using optical elements made out of a fluorescence-free material, such as MgF_2.

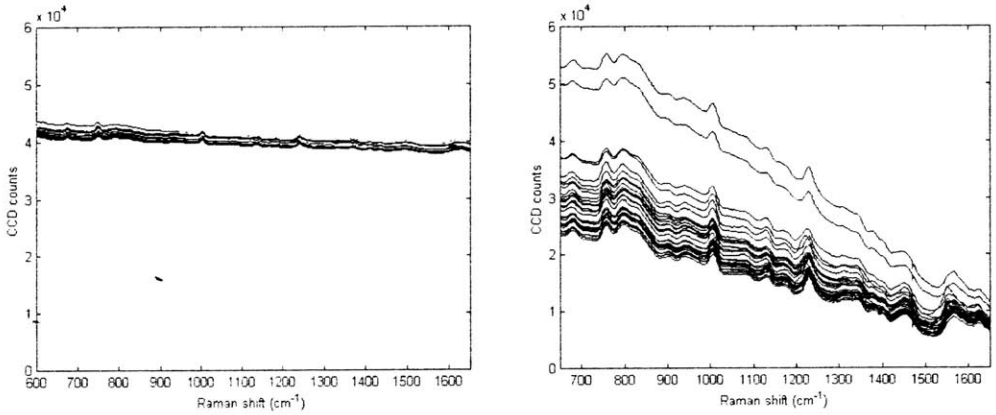

Figure 5.18. Raman spectra of whole blood samples collected with the previous system (left) and the new system (right).

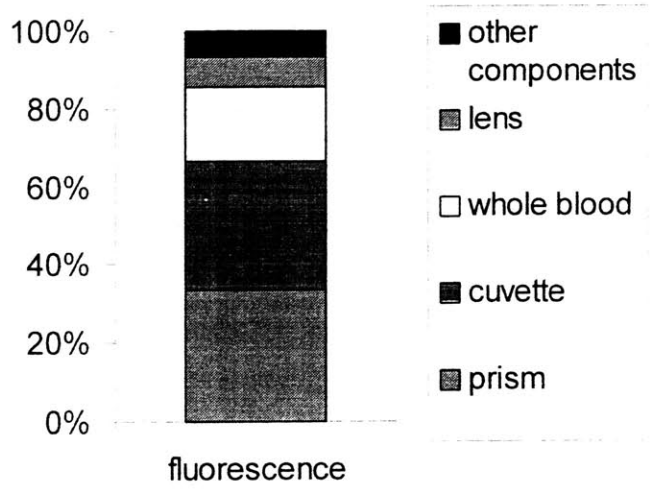

Figure 5.19. Sources of background fluorescence.

As the noise decreased, both the signal intensity and S/N in whole blood were improved by factor of five in the new system. For a spectrum of 10 mM glucose in whole blood collected for 10 seconds, the S/N increased from ~1 in the previous system to ~5 in the new system. To obtain data of a five times higher S/N with the previous system, 25 times longer collection time is required. We obtained higher S/N without increasing the collection time, and this is a major improvement for experiments in clinical settings.

5.5 Future directions

Increasing the system throughput, using optimal collection optics, and eliminating the connection optics increased the system sensitivity. Additional improvements can be made to further increase the system sensitivity. Table 5.4 summarizes the potential sensitivity increase in the future system.

The potential improvement in the immediate future is using a larger and more efficient CCD detector. The current CCD detector employs a front-illuminated CCD array chip. The quantum efficiency of the front-illuminated chip is less than 25% for the target wavelength region, between 830 nm and 1000 nm. CCD technology has advanced while this research was performed, and the state-of-the-art CCD camera with higher quantum efficiency and comparable size is now available. Such a CCD chip has up to 70% quantum efficiency for the target wavelength region. Employing such a CCD detector can increase the system sensitivity by additional factor of two or three. Also, micro-optic lenses focus light onto the active area of the CCD chip, and theoretically, can increase the sensitivity by

up to factor of two. Although such micro-lens arrays are not commercially available yet, they may become available in the future.

Near-term improvements can be also made with the reflection losses and packing loss. The current instrument has many optical components that are not anti-reflection (AR) coated. Each surface without AR coating reflects about 4% of incoming photons, and there were 11 optical surfaces that were not AR coated in the new system. As a result, 36% (=1-0.96^{11}) of the collected light was lost. By coating optical surfaces with anti-reflection layers (e.g. magnesium fluoride at $\lambda/2$ thickness), the reflectivity the system sensitivity can increase by another factor of 1.4.

The packing loss is due to the fiber bundle area that do not transmit light. The new system loses about 38% of the collected light due to the packing loss. A transforming optics with less packing loss will increase the sensitivity. Theoretically, a CPC can function as a transforming optics without any packing loss.

Also, efforts can be made to reduce the background fluorescence and noise in the system. The prism, which generated 30% of the background fluorescence, can be eliminated in different delivery schemes. For transcutaneous measurement, the cuvette, which also generated more than 30% of the background fluorescence, is not used. However, for transcutaneous measurements, the fluorescence from the skin layer is much stronger than the fluorescence from the system (Chapter 7), and the reduction of fluorescence and noise in the system would not be as important as the increase of the sensitivity.

Further improvements are expected as optical technologies advance and many components become more affordable. Continued improvements will enable faster collection of good S/N data, leading to more accurate blood analyte concentration measurements.

Table 5.4 Factors of the potential sensitivity increase in the future system

Factors	*Future system*	*Current system*	*Gain in signal*	*Miscellaneous*
Collection efficiency[1]	>21%	21%	>×1	Better collection optics for a 1 mm excitation beam
Packing fraction	62~100%	62%	×1.0~1.6	New transforming optics
Connection efficiency[1]	~100%	~100%	× 1.0	Due to elimination of connection optics
AR coatings	90%	64%	× 1.4	Reduced reflection loss on 11 optical surfaces
CCD detector	100%	20%	× 5.0	Increased efficiency and throughput
Total	**> 12~19%**	**~0.4%**	**> × 7~11**	

[1] These are already accomplished in the new system.

References

M. Born and E. Wolf, *Principles of optics. Electromagnetic theory of propagation interference and diffraction of light* (New York: Cambridge University Press, 1980).

R. W. Boyd, *Radiometry and the Detection of Optical Radiation* (New York: Wiley & Sons, 1983).

J. Courtial, B. A. Patterson, W. Hirst, A. R. Harvey, A. J. Duncan, W. Sibbett, and M. J. Padgett, "Static Fourier-transform ultraviolet spectrometer for gas detection," *Applied Optics*, volume 36, 13 1997, pp. 2813 -2817.

M. P. Dierking and M. A. Karim, "Solid-block stationary Fourier-transform spectrometer," *Applied Optics*, volume 35, 1 1996, pp. 84 -89.

X. Dou, Y. Yamaguchi, H. Yamamoto, S. Doi and Y. Ozaki, "A highly sensitive, compact Raman system without a spectrometer for quantitative analysis of biological samples," *Vibrational Spectroscopy*, volume 14, 2 1997, pp. 199-205.

Federal Standard 1037C, *Glossary of Telecommunications Terms*.

S. S. Haykin and B. V. Veen, *Signals and Systems*, (New York: John Wiley & Sons, 1998).

M. G. Holmes, "Radiation measurement," in *Techniques in Photomorphogenesis*, H. Smith and M. G. Holmes, ed. (Orlando, FL: Academic Press, 1984).

M. V. Klein and T. E. Furtak, *Optics* (New York: John Wiley & Sons, 1986).

E. N. Lewis, P. J. Treado, and I. W. Levin, "A miniaturized, no-moving-parts Raman spectrometer," *Applied Optics*, volume 47, 5 1993, pp. 539 -543.

R. McCluney, *Introduction to Radiometry and Photometry* (Norwood, MA: Artech House, Inc., 1994).

F. E. Nicodemus, "Radiance," *American Journal of Physics*, volume 31, 5, 1963, pp. 368 –377.

B. Schrader, *Raman/Infrared Atlas of Organic Compounds*, p. K1-03 (New York: VCH, 1989).

M. G. Shim and B. C. Wilson, "The effects of *ex vivo* handling procedures on the near-infrared Raman spectra of normal mammalian tissues," volume 63, 5 1996, pp. 662 -671.

W. H. Steel, "Luminosity, throughput, or etendue?," *Applied Optics*, volume 13, 4 1974, p. 704.

W. H. Steel, "Luminosity, throughput, or etendue? further comments," *Applied Optics*, volume 14, 2 1975, p. 252.

K. Tanaka, M. T. T. Pacheco, J. F. Brennan III, I. Itzkan, A. J. Berger, R. R. Dasari, and M. S. Feld, "Compound parabolic concentrator probe for efficient light collection in spectroscopy of biological tissue," *Applied Optics*, volume 35, 4 1996, pp. 758 -763.

J. M. Tedesco, H. Owen, D. M. Pallister, and M. D. Morris, "Principles and spectroscopic applications of volume holographic optics," *Analytical Chemistry*, volume 65, 9 1993, pp. A441-A449.

P. D. Vasko, J. Blackwell and J. L. Koenig, "Infrared and Raman spectroscopy of carbohydrates. Part II: Normal coordinate analysis of alpha-D-glucose," *Carbohydrate Research*, volume 23 1972, pp. 407-416.

W. T. Welford and R. Winston, *High Collection Nonimaging Optics* (San Diego, CA: Academic Press, 1989).

R. G. Wilson, *Fourier Series and Optical Transform Techniques in Contemporary Optics: An Introduction* (New York: John Wiley & Sons, 1995).

A. Yariv, *Optical Electronics in Modern Communications*, (Oxford, UK: Oxford University Press, 1997).

Chapter 6

Experiments to measure analytes in whole blood using the high-sensitivity system for Raman spectroscopy

6.1 Overview

One of the goals of this thesis research was to develop a Raman technique to measure analyte concentrations in whole blood. Chapter 4 discusses the key factors that determine the prediction accuracy and the necessity to improve the signal-to-noise ratio (S/N). In Chapter 5, a methodology to design a sensitive spectroscopy system is presented. This chapter describes experiments performed with the high-sensitivity system to measure analyte concentrations in whole blood samples.

Two experiments were performed with human whole blood samples. The first experiment demonstrated that the high sensitivity of the new system improved the signal collection efficiency for whole blood and, hence, the prediction accuracy in whole blood samples from a single donor. The second experiment verified that the new system also provides improved prediction accuracy for whole blood samples from multiple donors.

Analyte concentrations were measured with prediction accuracies comparable to the prediction accuracies achieved in human serum samples (Chapter 2).

6.2 Measurement of glucose in whole blood from a single donor

To demonstrate the performance of the new system, the first experiment was performed with whole blood from a single donor. The goal was to measure various concentrations of glucose in the presence of a constant background. Glucose was selected as the target analyte mainly because measurement of glucose is an indication of a good prediction capability. The signal intensity of glucose is strong enough to be detected. However, physiological concentration of glucose is low (45~180 mg/dL, or 2.5~10 mM) compared with the concentration of major blood constituents, and an accurate determination of glucose concentration is not trivial. In addition, glucose is a simple molecule, and its Raman spectrum is well defined and distinct. Finally, glucose is commercially available.

6.2.1 Experimental procedures

The samples were prepared in the following way. A uniform batch of whole blood was withdrawn from a single donor, and ethylenediaminetetraacetic acid (EDTA) was added. EDTA prevents the coagulation of whole blood, and was necessary for the storage of whole blood until measurements. Although EDTA interferes with determination of electrolytes, it does not significantly affect determination of our target analytes (glucose, urea, cholesterol, triglycierde, albumin, total protein, hemoglobin, and hematocrit) [Henry and Kurec 1996].

The batch was split into two equal volumes, and one part was spiked with a calculated amount of glucose. As a result, the glucose concentration in the spiked volume was 20 mM (360 mg/dL) higher than the other. Before measurement, each sample was prepared by mixing calculated amounts of the two volumes. All samples were identical, except for the different concentrations of glucose. The glucose concentrations were calculated from the volume ratios of whole blood from the spiked batch and the other batch. The concentrations ranged from 2 mM (36 mg/dL) to 18 mM (324 mg/dL). The reference error was set by the errors in pipetting the two volumes. Based on the pipetting precision and accuracy tested by the pipette manufacturer (Eppendorf), the standard deviation of the pipetting errors for all the samples was 2 mg/dL.

During the experiment, the whole blood samples were kept at room temperature until measurement to slow down metabolism of blood cells, since the blood cells in whole blood metabolize glucose into lactate at a rate of 0.4 mM/dL per hour (7 mg/dL per hour) at room temperature [Threatte and Henry 1996]. The reference concentrations were corrected with the known consumption rate and the time between the sample preparation and measurements.

6.2.2 Analysis

Raw spectra from whole blood samples were collected and preprocessed, as explained in Chapter 4. For each sample, 30 frames of 10-second spectra were taken, and the total collection time was 300 seconds. The excitation beam power was 280 mW on the sample, and the beam was 1 mm x 1 mm square. The spectra were cosmic ray filtered and

fluorescence background subtracted in the manner described in Chapter 4. Multiple frames were averaged to improve the S/N of the spectral data.

As mentioned in Section 4.2, the unprocessed spectra from whole blood samples have a strong fluorescence background. The raw data from this experiment is shown in Figure 6.1, and the preprocess data is shown in Figure 6.2. The spectral changes due to different glucose concentrations are not obvious to visual inspection, because Raman spectra of proteins dominate the whole spectra.

After the preprocessing, the partial least squares (PLS) regression was performed with "leave-one-sample-out" calibration (see Chapter 4). The concentrations predicted with PLS are discussed below.

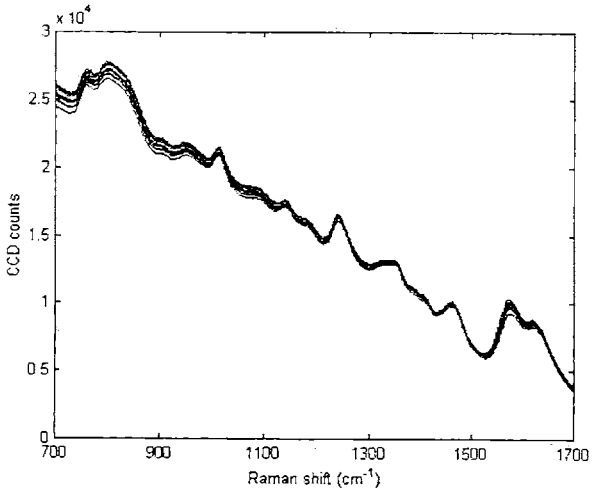

Figure 6.1. Raman spectra of nine whole blood samples. The overall slope is fluorescence backgrounds.

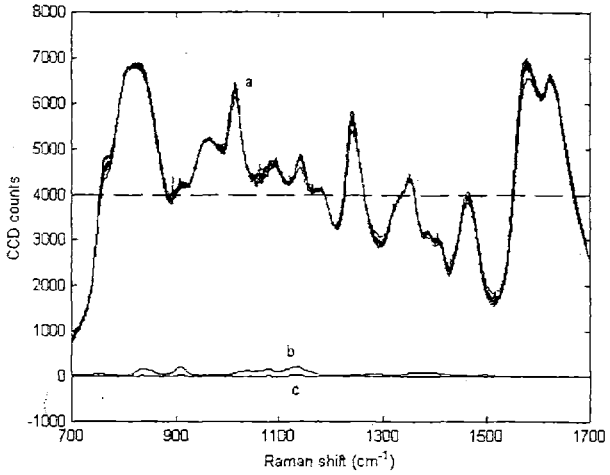

Figure 6.2. Raman spectra of nine whole blood samples after preprocessing (a). For comparison, Raman spectra of glucose at (b) 10 times higher than physiological normal concentration, 50 mM (900 mg/dL), and (c) physiological normal concentration, 5 mM (90 mg/dL), are shown. Most Raman features are due to proteins.

6.2.3 Results

Concentrations of glucose in the nine samples were predicted using the PLS regression method. The prediction error was 2 mg/dL (0.12 mM) for 300 second data and 4 mg/dL (0.22 mM) for 120 second data. Accurate measurements were performed with only 120 second data collection. For 300 second data collection, the prediction error and the reference error are equivalent. This indicates that the prediction error is limited by the reference error (see Chapter 4), and the prediction accuracy can improve by employing a more accurate reference technique. The prediction plot (Figure 6.3) shows that all the predictions are located near the zero-prediction-error line. When we compare this prediction plot and the prediction plot of glucose in the single donor whole blood made for the same collection time (300 seconds) by using the previous system (Chapter 2), the

current system provides better prediction accuracy, both quantitatively and qualitatively (Figure 6.4). The root-mean-squared prediction (RMSEP) error was 34 mg/dL (1.9 mM).

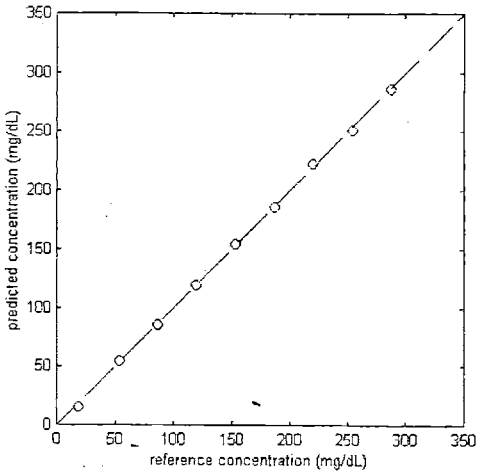

Figure 6.3. Prediction plot of glucose in whole blood samples from a single donor. Each data point was collected for 300 seconds at 280 mW excitation. Predictions are near the "zero-prediction-error" line. The root-mean-squared prediction error was 2 mg/dL (0.12 mM).

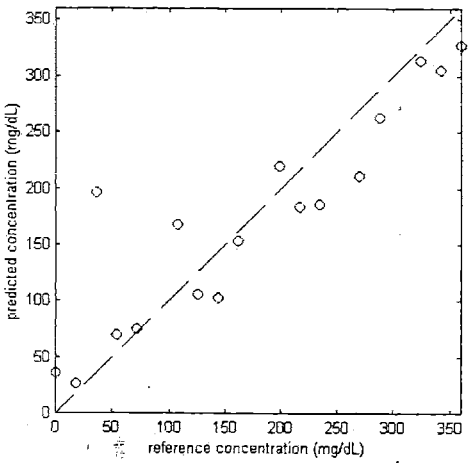

Figure 6.4. Prediction plot of glucose in whole blood samples from a single donor, obtained by using the previous system. Each data point was collected for 300 seconds at 300 mW excitation. The root-mean-squared prediction error was 34 mg/dL (1.9 mM).

Table 6.1 compares the prediction errors in the previous system and the new system. The S/N of glucose in single-donor serum measured with the previous system was lower by factor of 1.4 than that in single-donor whole blood measured with the new system, for the same concentration and collection time. Thus, the 300 second spectra of serum collected with the previous system had a S/N similar to that in 150 second data of whole blood

collected with the new system, which can be calculated using Eq. (4.29). The prediction error for glucose in serum collected for 300 seconds with the previous system was 5 mg/dL [Berger 1998] and the prediction error for glucose in whole blood collected for 150 seconds with the new system was also 5 mg/dL (Figure 6.5). Furthermore, the coefficient a in a fit to Eq. (4.34) was 46 $sec^{1/2}$ mg/dL, which is close to a=69 $sec^{1/2}$ mg/dL obtained from Eq. (4.32). t_0 was 1,200 seconds, which indicates that we can benefit from a longer collection time.

Table 6.1. Comparison of prediction errors in the previous system and the new system

S/N @ 10 mM	medium	*prediction error with previous system* (mg/dL)	*integration time* (seconds)	medium	*prediction error with new system* (mg/dL)	*integration time* (seconds)
16	serum	5 mg/dL	300	whole blood	5 mg/dL	150
4.4	whole blood	34 mg/dL	300	whole blood	15 mg/dL	~10

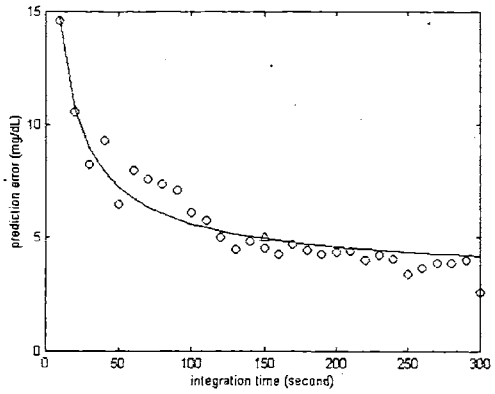

Figure 6.5. Prediction errors of glucose in single-donor whole blood for various integration time. The circles are the empirical results and the line is a fit to Eq. (4.34). The prediction error of glucose in single-donor whole blood at 150 seconds is comparable to the prediction error of glucose in single-donor serum collected for 300 seconds (the triangle).

However, the prediction error in single-donor whole blood obtained with the previous system and that with the new system do not match well. Since the new system has five higher S/N than the previous system for analytes in whole blood, 12 second data obtained with the new system had a S/N comparable to that in 300 second data obtained with the previous system, which can be calculated using Eq. (4.29). The prediction error for glucose in 10 second whole blood data obtained with the new system was 15 mg/dL, while the prediction error obtained with the previous system for 300 seconds was 34 mg/dL. This indicates that there were additional sources of error in the single donor whole blood experiment with the previous system. In fact, whole blood samples were frequently damaged by the focused excitation beam in the single-donor experiment with the previous system, and that was probably the source of additional error.

6.2.4 Summary

The new Raman spectroscopy system can measure concentrations of blood analytes in whole blood samples from single subject with better accuracy (2 mg/dL) than the previous system (34 mg/dL). At 300 second, the prediction error in whole blood with the new system is limited by the reference error. Accurate measurements were made at a shorter collection time, 60 seconds. The prediction error improvement is comparable to the improvement expected from the signal-to-noise theory.

6.3 Measurement of analytes in whole blood from multiple donors

To demonstrate the performance of the new system in clinical settings, the experiment was performed with whole blood from multiple donors. The goal was to measure various concentrations of multiple analytes. The overlap of the target chemical spectrum and the spectra of other analytes of various concentrations adds more challenges. Nine analytes were selected as the target analytes: glucose, urea, bilirubin, total protein, cholesterol, triglycerides, hematocrit, and hemoglobin. Some analytes, such as total protein and albumin, have higher signal intensities than glucose in whole blood, and it would be expected that such analytes can be measured with high prediction accuracy. In contrast, the physiological concentration of bilirubin is orders of magnitude lower than the physiological concentration of glucose in whole blood, and it would be expected that the prediction accuracy for measuring bilirubin would be lower.

6.3.1 Experimental procedures

Figure 6.5 is the diagram of the experimental procedure. The whole blood samples were withdrawn at the Beth Israel Deaconess Medical Center (BIDMC). The samples were delivered to the MIT, and Raman spectra of the samples were collected. Plasma was extracted from each sample after measurement, and plasma samples were sent to BIDMC for reference measurements. The reference concentrations and the Raman spectra were analyzed with multivariate techniques. The details are described below.

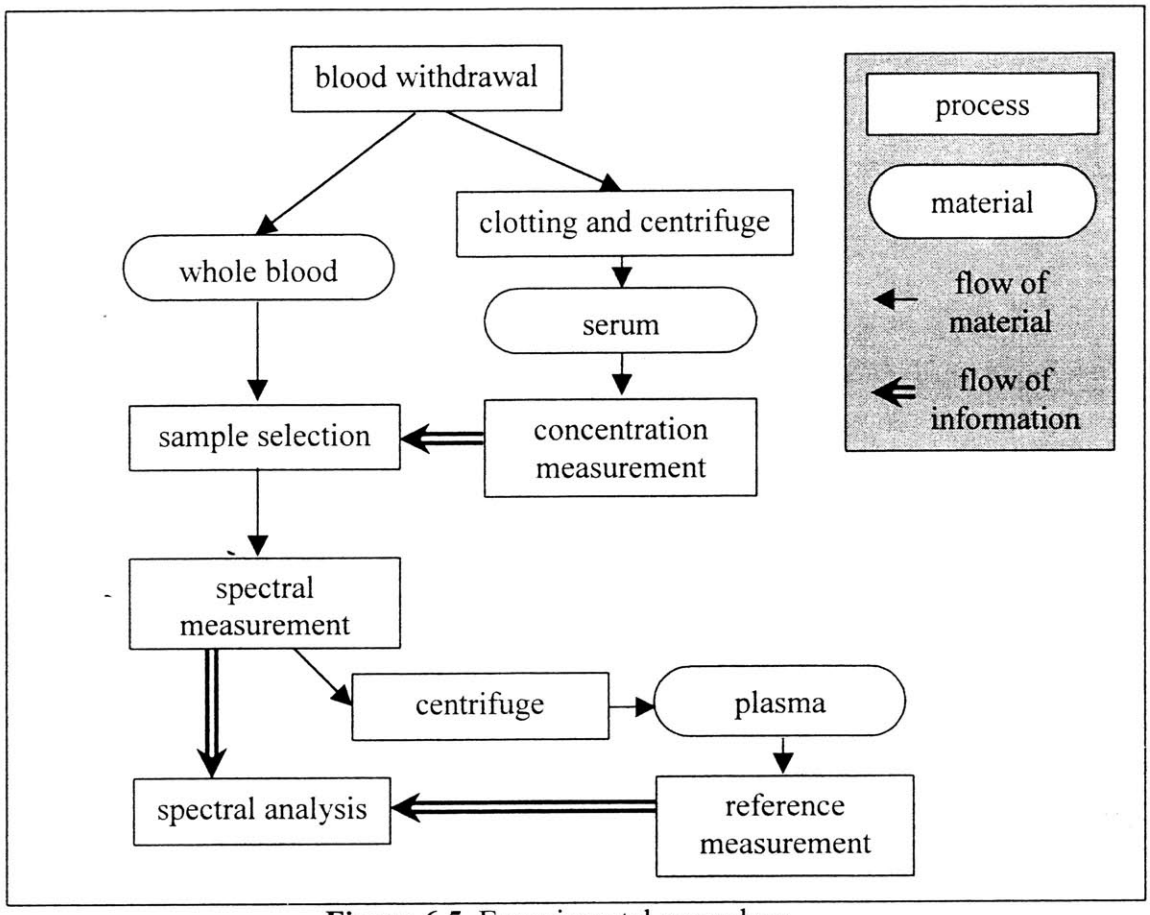

Figure 6.5. Experimental procedure

The multiple donor experiment was performed over two days with thirty one human whole blood samples, as it was demonstrated that a good calibration was achieved with thirty samples from multiple donors [Berger et al. 1999]. Three days before the experiment, whole blood samples were withdrawn from subjects at Beth Israel Deaconess Medical Center (BIDMC). As whole blood samples were withdrawn for clinical diagnosis purposes, not for our studies, samples had to be retained in the hospital clinical laboratory

for three days. This was because some clinical diagnoses were repeated to check for accuracy, and sometimes additional analytes needed to be measured in the same sample.

Samples that were relevant to our studies were whole blood samples, which were mixed with EDTA as an anticoagulant, and matching (withdrawn from the same subject at the same time) serum samples, which were obtained from whole blood samples without anticoagulants. Since no blood cells were present in serum, analytes in serum were stable and their concentrations did not change significantly over time. However, anticoagulants added to whole blood samples did not prevent cell metabolism, and therefore, many analytes were metabolized by blood cells. It was expected that concentrations of certain analytes (e.g. glucose) in whole blood would be change over the three days.

In a preliminary study, it was found that many whole blood samples did not have any glucose in them after three days. This is because glucose was broken down due to cell metabolism, which is called glycolysis. The glycolysis in whole blood is the reason we obtained low glucose concentration samples. Blood cells consume glucose at the rate of 0.4 mM/hour (7 mg/dL per hour) at room temperature, and 0.1 mM/hour (2 mg/dL per hour) at 4°C [Threatte and Henry 1996]. Glucose must have been digested by blood cells during the three days the samples were retained at the BIDMC. This emphasizes the need for a better experimental protocol to control the glucose concentrations better. To deal with glucose consumption in whole blood, a strict rule in sample selection was implemented in this experiment. Samples with high (>200 mg/dL, or >11 mM) serum glucose concentrations were selected to insure that a physiological concentration of glucose would remain in whole blood after three days' glycolysis. Furthermore, plasma were extracted immediately before

and after spectral data collection at MIT, in order to obtain accurate reference concentrations.

On each days of the experiment, fifteen or sixteen samples were selected to represent a range of glucose concentrations, based on the glucose concentrations in matching serum samples. Hemoglobin concentrations and hematocrit, the volume fraction of red blood cells, were first measured at BIDMC using a hematology analyzer.

Samples were delivered to MIT and stored at 4°C to slow down blood cell metabolism. One hour before spectral collection, each sample was placed at room temperature to facilitate plasma separation in centrifugation. 2 cc of the same whole blood sample was placed in a cuvette. Thirty frames of Raman spectra were taken from each sample at 280 mW excitation, and each frame was collected for 10 seconds. The actual run-time was seven minutes per sample (five minutes for spectrum integration and two minutes for CCD readout). This process allowed us to remove the cosmic rays by using a statistical filter, and to obtain spectra of various integration times. Ten-second spectra were obtained by simply using one-frame spectra, and 300-second spectra were obtained by summing all 30 frames of spectra. During the measurements, a stirring magnet inside the cuvette prevented blood cells from settling and kept the sample homogenous throughout the measurements.

Immediately after spectral collection, 1 cc of whole blood was taken out of the cuvette and placed into a centrifuge tube. The centrifuge tube was spun at 3,000 g in an Eppendorf Centrifuge 5415 for five minutes, to separate plasma and blood cells. A nomogram was used to determine the speed of the centrifuge [Henry and Kurec 1996] to

achieve the proper centrifugal force. The plasma was extracted using a Pasteur pipette and stored in a plasma tube.

The plasma samples were sent to BIDMC after the two-day experiment for reference measurements. Concentrations of glucose, urea, bilirubin, total protein, albumin, cholesterol, and triglycerides were measured using a spectrophotometer.

6.3.2 Analysis

Findings from reference measurements

Concentrations of analytes in plasma samples were obtained from the Hitachi blood analyzer at BIDMC. The reference measurements were used to quantify the damage to samples and the distribution of analyte concentrations. The details of the findings are discussed below.

First, there was insignificant damage to the red blood cells. Hemoglobin concentrations in plasma samples were 30 mg/dL, on average. Hemoglobin is normally present inside erythrocytes (red blood cells). When the cell membranes of erythrocytes are damaged, hemoglobin is released into the plasma. The non-zero hemoglobin concentration in plasma indicates that the red blood cells were damaged during the measurements. However, the normal concentration of hemoglobin in whole blood is 15 g/dL, and it can be estimated that about 0.2 % of red blood cells were damaged during the measurements. The effect of this small blood cell damage on multivariate calibration was insignificant.

In a separate study, the mechanism of red blood cell damage was investigated. Two potential causes of damage, stirring and laser heating, were suggested. To identify the cause, whole blood samples were tested under two conditions. In one case, the whole blood sample was exposed to laser excitation, without any stirring mechanism, for 7 minutes. In the other test, the remaining whole blood sample was put into a cuvette with a stirring magnet for 7 minutes, and there was no laser exposure. Plasma was extracted from both samples. By comparing the hemoglobin concentrations in plasma tubes from both samples, it was indicated that the magnet stirring is the major cause of damage to red blood cells. This indicates that a better stirring mechanism can be employed, if necessary, in future studies to minimize the damage to red blood cells, and that the damage due to laser exposure was insignificant.

Second, many samples had good ranges of analyte concentrations. Especially, all samples had a good range of glucose concentrations, spanning from normal (45 ~ 180 mg/dL or 2.5 ~ 10 mM) samples to hyperglycemic, higher than normal glucose level, samples. This demonstrates that the new protocol, selecting samples with serum glucose concentrations higher than 200 mg/dL, solved the problem of zero glucose samples.

Preprocessing spectra

Raw spectra from whole blood samples were preprocessed, as discussed in Section 6.2. The unprocessed spectra from whole blood samples have a strong fluorescence background (Figure 6.6). Figure 6.6 also shows that spectra have different fluorescence backgrounds. This is due to changes in collection geometry, especially due to the use of different

cuvettes, and the different compositions of proteins and lipids in samples. The difference in the fluorescence background can be subtracted. The preprocessing removed cosmic rays and subtracted fluorescence backgrounds in the standard manner. As before, after the preprocessing, the Raman features are more prominent (Figure 6.7). The preprocessed spectra were analyzed with the PLS algorithm.

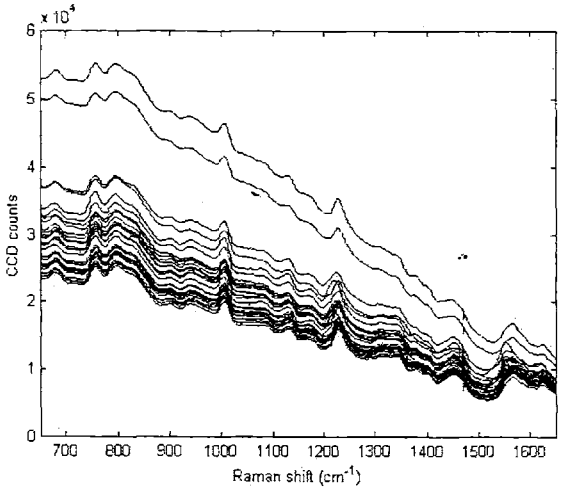

Figure 6.6. Raman spectra of 31 whole blood samples from 31 human subjects. The major difference among the spectra is the background fluorescence only, and is mainly due to the different compositions of proteins and lipids in samples.

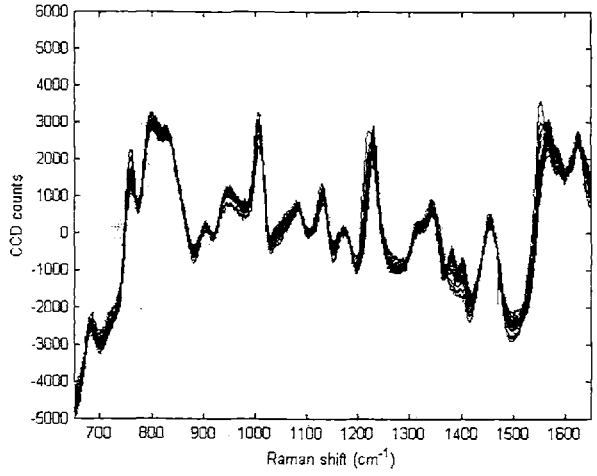

Figure 6.7. Raman spectra of 31 whole blood samples from 31 human subjects after preprocessing. After fluorescence background subtraction, the spectra display similar Raman features.

6.3.3 Results

Prediction accuracy

By performing PLS analysis with a "leave-one-sample-out" cross-validation method, concentration predictions were calculated for all the analytes. The predictions have better prediction accuracies than the previous experiment, discussed in Chapter 2. In addition, all the predictions are insensitive to minor changes in the analysis parameters, such as bin size, number of loading vectors, and integration time.

Table 6.2 summarizes the prediction results for nine analytes in whole blood. The collection time was 300 seconds for all the analytes. The prediction errors obtained with the new system in whole blood are close to the prediction errors obtained with the previous system for serum, and thus we have achieved the design goal. For total protein and albumin the prediction errors and reference errors are comparable, and the errors due to sources other than the reference errors are small. This indicates that the Raman technique may provide more accurate concentration information than the reference technique (see Chapter 4). The comparison of the prediction errors in whole blood with the new system and the prediction errors in whole blood with the previous system also shows that all the prediction errors are reduced with the new system.

The correlation coefficient, r, indicates how two variables are correlated. A correlation coefficient close to 1 indicates close correlation between the variables, r close to 0 indicates little correlation, and r close to -1 indicates inverse correlation. In Figure 6.8

and Figure 6.9, r is the correlation coefficient between the reference concentrations and the predicted concentrations. r^2 values are presented to show how close correlation coefficients are to 1, the maximum value. Since the correlation coefficients are higher than 0.9 for all analytes except for cholesterol, these are considered to be clinically accurate or near-clinically accurate [Pincus 1996].

In addition to prediction errors, it is helpful to use prediction plots in evaluating the quality of predictions. The prediction plots for the seven analytes are presented in Figure 6.8 and Figure 6.9. The x-axis of each plot represents concentrations of each analyte measured by the reference technique. The y-axis of each plot represents concentrations of each analyte predicted by the Raman technique. The dashed lines are for "zero-prediction-error" data points, and the magnitude of the vertical distance from each data point to the line is the prediction error for that data point. Thus, a perfect prediction plot with zero prediction-error would have all the data points on the dashed line. All the prediction plots indicate that there are good correlations between the reference concentrations and the predicted concentrations.

Table 6.2. Prediction errors of analyte concentration measurements

Analyte (unit)	*Whole blood with the new system (r^2)*	*Whole blood with the previous system (r^2)*	*Serum with the previous system[6] (r^2)*
Glucose (mg/dL)	19 (0.95)	77 (0.15)[2]	26 (0.83)
Urea (mg/dL)	4.9 (0.94)	6.5 (0.59)	3.8 (0.74)
Bilirubin (mg/dL)	N/A[1,2]	N/A[3]	N/A[3]
Cholesterol (mg/dL)	30 (0.66)	45 (0.12)[2]	12 (0.83)
Triglyceride (mg/dL)	39 (0.93)	81 (0.56)	29 (0.88)
Total Protein (g/dL)	0.26 (0.95)	0.38 (0.55)	0.19 (0.77)
Albumin (g/dL)	0.10 (0.99)	0.21 (0.76)	0.12 (0.86)
Hemoglobin (g/dL)	0.41 (0.94)	N/A[3]	N/A[4]
Hematocrit (%)	1.3 (0.96)	1.5 (0.92)	N/A[5]

[1] Samples did not have a representative range of analyte concentrations.

[2] No predictability was achieved due to low S/N.

[3] This analyte was not measured in the previous measurements.

[4] Hemoglobin is not present in serum samples.

[5] Hematocrit, the volume fraction of red blood cells, is always zero in serum samples, since red blood cells are not present in serum samples. Determination of hematocrit in serum does not have any statistical or clinical significance.

[6] Serum results are from 60 second data obtained with the previous system [Berger 1999]. The prediction errors from 300 second data are similar.

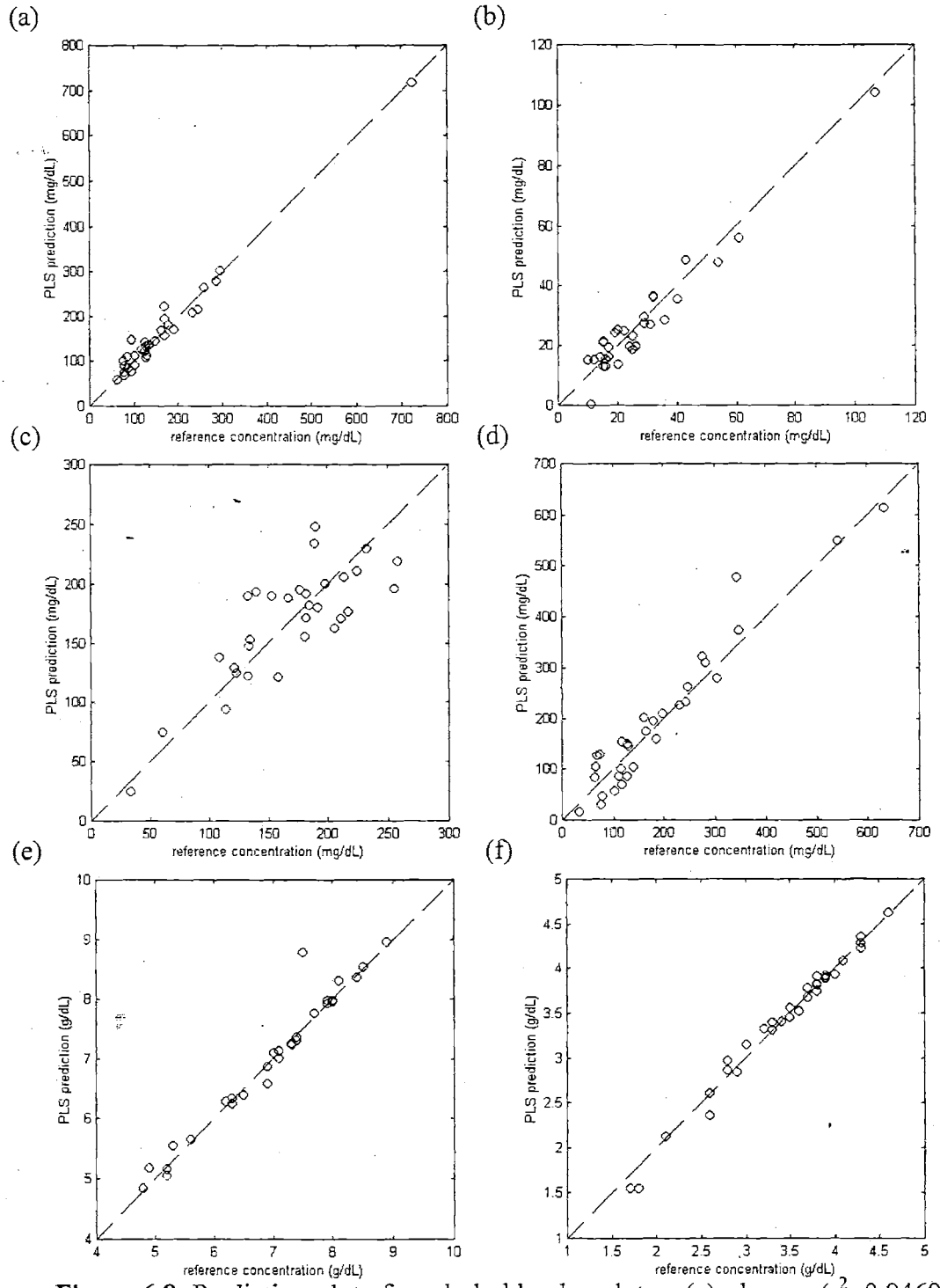

Figure 6.8. Prediction plots for whole blood analytes: (a) glucose (r^2=0.9469), (b) urea (BUN) (r^2=0.9372), (c) cholesterol (r^2=0.6589), (d) triglyceride (r^2=0.9303), (e) total protein (r^2=0.9497), and (f) albumin (r^2=0.9857).

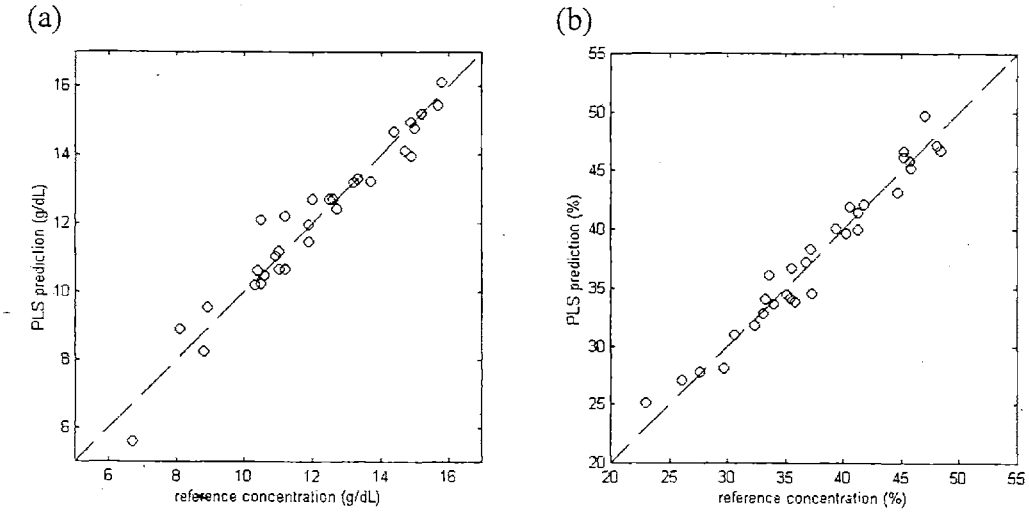

Figure 6.9. Prediction plots for whole blood analytes: (a) hemoglobin (r^2=0.9438) and (b) hematocrit (r^2=0.9613).

To evaluate the clinical accuracy of glucose monitoring systems, Clarke et al developed a method called error grid analysis (EGA) [Clarke 1987]. EGA divides glucose prediction plots into five regions, and each region has a different clinical meaning. Zone A represents "clinically accurate" data; zone B covers "benign" values; zone C includes "overcorrection" results; any data point in zone D indicates dangerous failure to detect and treat;" and data points in zone E can lead to "erroneous treatment." A clinical glucose monitoring system should not have any data point in zone C, D, or E [Cox 1997]. When our glucose predictions are plotted on the error grids, 27 out of 31 samples from the Raman experiment fall only in zones A, and the remaining 4 are in zone B (Figure 6.10). This implies that the Raman technique can provide clinically accurate information.

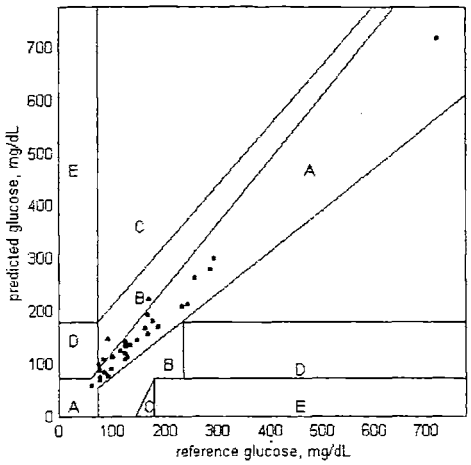

Figure 6.10. Glucose predictions plotted on error grid. 27 data points are in zone A, the region of clinically accurate data, and 3 data points are in zone B. No data points are located in zone C,D, or E.

Analysis of 51 samples

The number of 31 samples was chosen, because an accurate calibration could be performed with 30 samples from multiple donors [Berger et al. 1999]. To test if this was an acceptable number of samples, Raman spectra of 20 additional samples were taken in a manner similar to that described above. However, the samples were randomly selected, and their serum glucose concentrations were not used. As a result, many of these samples did not have enough glucose concentrations.

All 51 Raman spectra and analyte concentrations in 51 samples were analyzed with the standard PLS algorithm. The prediction errors are summarized in Table 6.3. The prediction errors were comparable when the number of samples was either 31 or 51. For most analytes, the prediction errors slightly increased with 51 samples, and it is probably

due to long term system drifts, as the spectra of 20 samples and 31 samples were taken three weeks apart.

Table 6.3. Prediction errors of analyte concentrations for various sample sizes

Analyte (unit)	*Whole blood with 31 samples*	*Whole blood with 51 samples*
Glucose (mg/dL)	19	26
Urea (mg/dL)	4.9	5.4
Bilirubin (mg/dL)	N/A	N/A
Cholesterol (mg/dL)	30	32
Triglyceride (mg/dL)	39	43
Total Protein (g/dL)	0.26	0.36
Albumin (g/dL)	0.10	0.21
Hemoglobin (g/dL)	0.41	0.69
Hematocrit (%)	1.3	2.4

Prediction errors for various integration times

Throughout this research, the S/N is assumed to be the dominant factor in determining the prediction errors. This assumption was tested by calculating the prediction errors for various S/N. Thirty frames of spectra were taken from each sample, and each frame was collected for 10 seconds. By adding various numbers of frames, spectra of a range of integration time were obtained. The signal increases linearly with the integration time, and the noise increases as the square root of the integration time, as discussed in Chapter 4. Based on the relationship between the integration time and S/N, Eq. (4.34) described the prediction error as a function of the integration time:

$$\Delta c = \sqrt{a^2/t + b^2}\,, \tag{4.34}$$

where Δc is the prediction error, t is the integration time, and a and b are fit coefficients.

When the prediction errors for various integration times are plotted along with their fit to this equation, the prediction errors improved following Eq. (4.24). Figure 6.11 and Figure 6.12 show the prediction errors as functions of integration time, and fits to Eq. (4.31).

For glucose and urea, the prediction errors do not follow the fit for short integrations times ($\lesssim$ 70 seconds). Due to the nature of the PLS algorithm, the predictions cannot be worse than a random guess. The prediction errors of glucose do not exceed 90 mg/dL and those of urea do not exceed 9 mg/dL. Again, the prediction errors of glucose cannot be reduced below 11 mg/dL and those of urea cannot be reduced below 1.1 mg/dL simply by improving S/N.

Fitting data to Eq. (4.31) showed that the prediction errors improve with longer integration times, as suggested by the signal-to-noise theory in Chapter 4. The fits in Figure 6.11 and 6.12 also show what prediction errors can be achieved by improving S/N. Furthermore, prediction errors for 60 second data collection were comparable to prediction errors for 300 second data for many analytes (Table 6.4), which indicates that for clinical applications, 60 second data collection provides adequate accuracy.

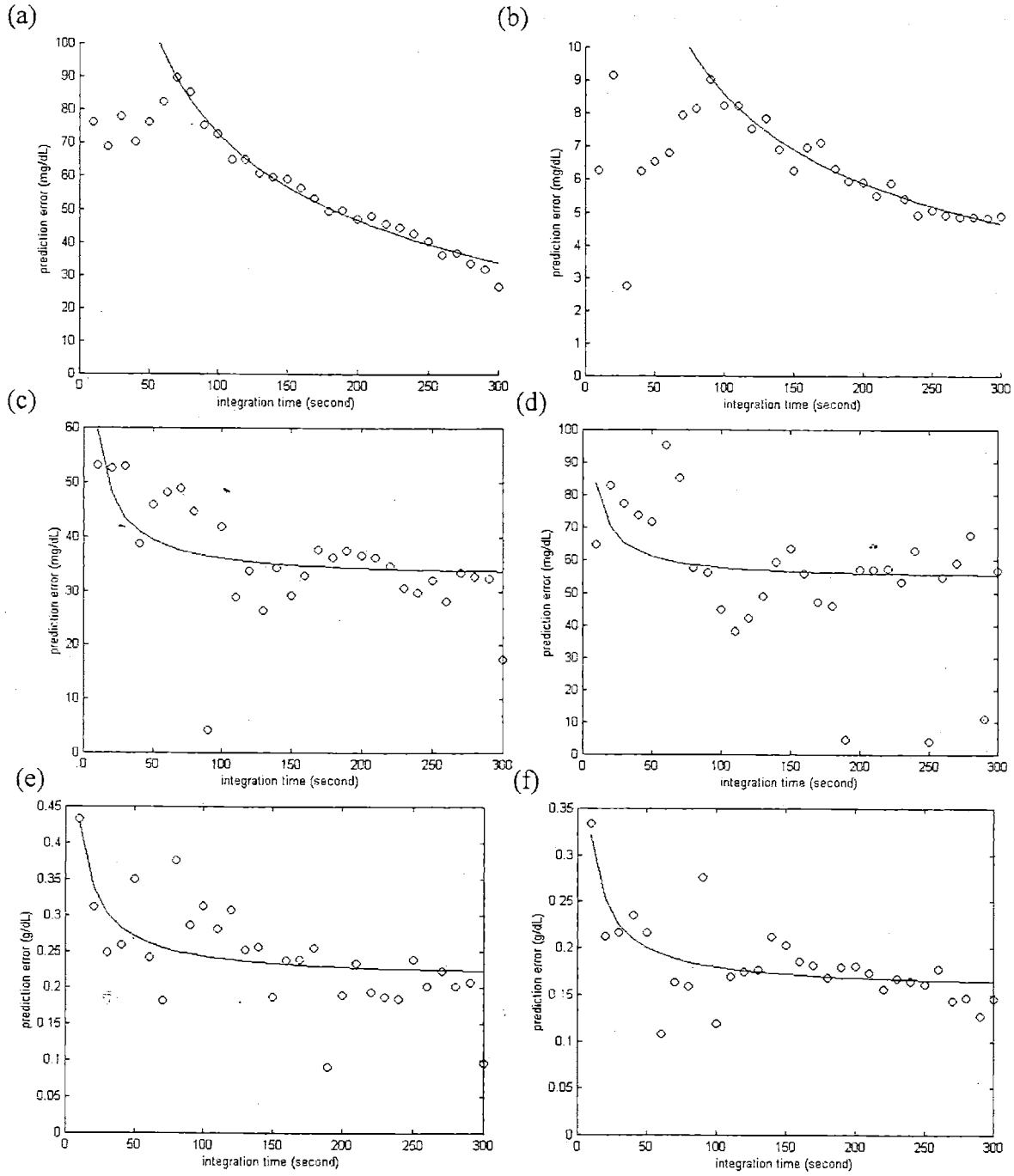

Figure 6.11. Prediction plots of whole blood analytes for various integration times: (a) glucose, (b) urea, (c) cholesterol, (d) triglyceride, (e) total protein, and (f) albumin. Circles are actual prediction errors, and lines are fits to Eq. (4.24).

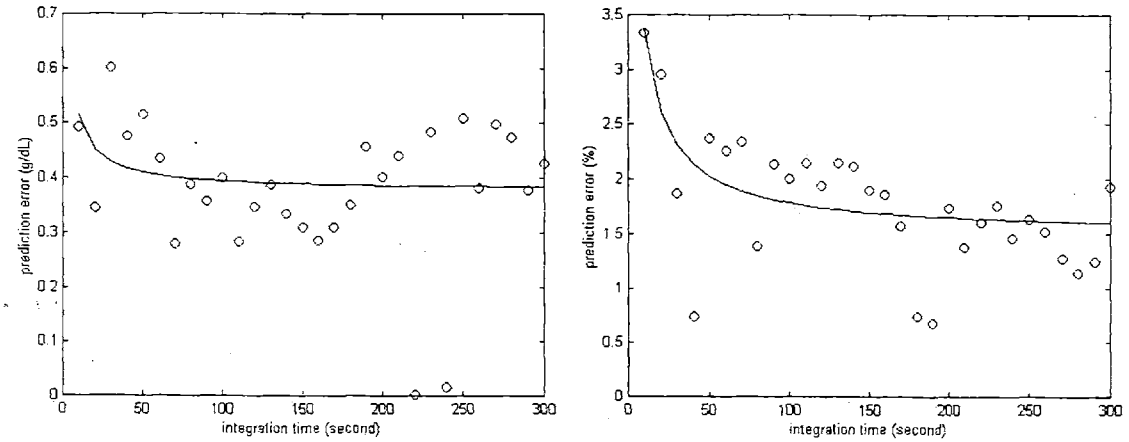

Figure 6.12. Prediction plot of hemoglobin (left) and hematocrit (right) in whole blood for various integration times. Circles are prediction errors and the line is the fit to Eq. (4.24).

Table 6.4. Prediction errors of analyte concentrations for various integration time

Analyte (unit)	*Whole blood at 300 seconds*	*Whole blood at 60 seconds*
Glucose (mg/dL)	19	75*
Urea (mg/dL)	4.9	9.1*
Cholesterol (mg/dL)	30	38
Triglyceride (mg/dL)	39	60
Total Protein (g/dL)	0.26	0.25
Albumin (g/dL)	0.10	0.18
Hemoglobin (g/dL)	0.41	0.41
Hematocrit (%)	1.9	2.0

* For these analytes, prediction errors at 60 second do not have predictability. Prediction errors for 90 second data are presented.

The fit coefficient a in Eq. (4.34) is the rate at which the prediction error is reduced with time. a can be directly obtained from using Eq. (4.32) by calculating S/N and overlap

factors. Table 6.5 compares the fit coefficient *a* obtained by fitting data with Eq. (4.34) and calculated by using Eq. (4.32). It indicates that the two *a* values are closely related.

Table 6.5. Comparison of the fit coefficient *a* and Eq. (4.32)

Analyte	*a* from fitting	*a* from Eq. (4.32)	difference
Glucose	147	205	-58
Urea	87	93	-6
Cholesterol	124	85	39
Triglyceride	188	162	26
Total protein	1.2	0.5	0.7
Albumin	0.95	0.4	0.55

The fit coefficient *b* in Eq. (4.34) is the prediction error that is not dependent upon integration time or SNR, and the prediction error cannot be improved below the fit coefficient *b* simply by improving S/N. Table 6.6 compares the fit coefficient *b* and the reference error for each analyte.

Table 6.6 indicates that the fit coefficient *b* and the reference error are similar for many analytes except for cholesterol and triglyceride. The difference between the fit coefficient *b* and the reference error is due to other sources of errors discussed in Chapter 4. In addition, it can be noted that the fit coefficient *b* is much larger than the reference error for predictions of cholesterol and triglycerides. This is probably due to the fact that the reference concentrations were measured in plasma, while the analytes were measured in whole blood using Raman spectroscopy. Our reference techniques could measure cholesterol and triglyceride concentrations only in serum or plasma. In the process of

converting whole blood to serum or plasma, blood cells were centrifuged and removed. The plasma membrane of blood cells contain high concentrations of cholesterol [Segal et al. 1984] and triglycerides [Stryer 1995]. The presence of additional cholesterol and triglycerides could increase prediction errors. An employment of reference techniques that measure cholesterol and triglyceride concentrations in whole blood can eliminate this discrepancy and reduce prediction errors.

Table 6.6. Comparison of the fit coefficient b and the reference error

Analyte	b	reference error[1]	b - (reference error)
Glucose	6 mg/dL	3 mg/dL	3 mg/dL
Urea	1.1 mg/dL	0.9 mg/dL	0.2 mg/dL
Cholesterol	34 mg/dL	4 mg/dL	30 mg/dL
Triglyceride	55 mg/dL	3 mg/dL	52 mg/dL
Total protein	0.23 g/dL	0.1 g/dL	0.13 g/dL
Albumin	0.16 g/dL	0.09 g/dL	0.07 g/dL
Hemoglobin	0.38 g/dL	0.17 g/dL	0.21 g/dL
Hematocrit	1.5 %	0.4 %	1.1 %

Additionally, we calculated the time constant t_0 from the fit coefficients (Table 6.7). Again, the benefit of increasing the collection time beyond t_0 is often small. The prediction error cannot be lower than half of the prediction error with collection time t_0. The time constants for many analytes indicate that good prediction accuracy can be achieved with

[1] The reference errors are obtained from day-to-day errors in reference techniques. Since our prediction errors includes day-to-day errors and sample-to-sample errors, the reference errors are underestimated. The sample-to-sample errors in the reference techniques were not available.

less than 1 minute collection time. For glucose and urea, longer collection time could reduce the prediction error further.

Table 6.7. Time constant t_0 for analytes in whole blood

Analyte	a	b	t_0 (seconds)
Glucose	147	6	600
Urea	87	1.1	6000
Cholesterol	124	34	13
Triglyceride	188	55	12
Total protein	1.2	0.23	27
Albumin	0.95	0.16	35

6.3.4 Summary

Near-infrared Raman spectroscopy can measure concentrations of many blood analytes in whole blood samples from multiple subjects, most in 60 seconds. With the improved sensitivity, the new system determined concentrations more accurately than the previous system. The whole blood predictions with the new system are comparable to the serum predictions with the previous system.

6.4 Conclusion

A series of experiments was performed to demonstrate that blood analyte concentrations can be determined by using Raman spectroscopy. For many analytes, clinical accuracy was achieved with data collection for 60 seconds. For other analytes, the prediction errors improved with longer integration times, and followed the prediction error equation

discussed in Chapter 4. According to the prediction error equation, a more sensitive system will enable accurate measurements in less collection time.

Whole blood measurements can be improved in the following ways:

1. Better reference techniques
2. Better S/N for analytes having small signals

As discussed in Section 6.3, the predictions errors of total protein and albumin were comparable to the reference errors. Although it is possible that the Raman spectroscopy technique is more accurate than the reference technique, this cannot be demonstrated. A more accurate reference technique may show that prediction errors of the Raman spectroscopy technique are lower than the values listed in Section 6.3 and 6.4. Furthermore, there were discrepancies between the samples analyzed by the Raman spectroscopy technique and the samples measured by the reference techniques. The reference techniques employed in this study could measure analytes in serum or plasma only, while the Raman spectroscopy measured analytes in whole blood. Although plasma concentrations and whole blood concentrations are similar for many analytes, plasma concentrations of cholesterol and triglycerides deviate from their whole blood concentrations. A reference technique that measures concentrations in whole blood is more desirable in assessing prediction errors of the Raman spectroscopy technique in whole blood.

Furthermore, there are other analytes that provide diagnostic information, in addition to the analytes discussed in this chapter. For example, concentrations of HDL and LDL determine the risk of cardiovascular diseases. While HDL and LDL concentrations

could not be measured with the previous system, it may be feasible to measure theirs concentrations with the new system, as we find that concentrations of LDL and HDL cholesterols are comparable to those of analytes that we measured according to Table 2.3. Bilirubin provides the diagnostic information about the liver function [Pincus and Schaffner 1996]. It has weaker signals than the analytes already measured. A development of a more sensitive system or an increase in the collection time will enable concentration measurements of these analytes, and expand the horizon of Raman spectroscopy applications.

References

A. J. Berger, "Measurement of analytes in human serum and whole blood samples using near-infrared Raman spectroscopy," (Cambridge: Massachusetts Institute of Technology, doctoral thesis, 1998).

A. J. Berger, T. W. Koo, I. Itzkan, G. Horowitz and M. S. Feld, "Multicomponent blood analysis by near-infrared Raman spectroscopy," *Applied Optics*, volume 38, 13 1999, pp. 2916-2926.

W. L. Clarke, D. Cox, L. A. Gonder-Frederick, W. Carter, and S. L. Pohl, "Evaluating clinical accuracy of systems for self-monitoring of blood glucose," *Diabetes Care*, volume 10, 1987, pp. 622 –628.

D. J. Cox, L. A. Gonder-Frederick, B. P. Kovatchev, D. M. Julian, and W. L. Clarke, "Understanding error grid analysis," *Diabetes Care*, volume 20, 1997, pp. 911 – 912.

J. B. Henry and A. S. Kurec, "The Clinical Laboratory: Organization, Purposes, and Practice," in *Clinical Diagnosis and Management by Laboratory Methods*, J. B. Henry, ed. (Philadelphia: W. B. Saunders Company, 1996).

M. W. Morris and J. B. Henry, "Basic Examination of Blood," in *Clinical Diagnosis and Management by Laboratory Methods*, J. B. Henry, ed. (Philadelphia: W. B. Saunders Company, 1996).

M. R. Pincus, "Interpreting Laboratory Results: Reference Values and Decision Making," in *Clinical Diagnosis and Management by Laboratory Methods*, J. B. Henry, ed. (Philadelphia: W. B. Saunders Company, 1996).

M. R. Pincus and J. A. Schaffner, "Assessment of Liver Function," in *Clinical Diagnosis and Management by Laboratory Methods*, J. B. Henry, ed. (Philadelphia: W. B. Saunders Company, 1996).

P. Segal, P. S. Bachorik, B. M. Rifkind, and R. I Levy, "Lipids and Dyslipoproteinemia," in *Clinical Diagnosis and Management by Laboratory Methods*, J. B. Henry, ed. (Philadelphia: W. B. Saunders Company, 1984).

L. Stryer, *Biochemistry* (New York: W. H. Freeman and Co., 1995).

G. A. Threatte and J. B. Henry, "Carbohydrates," in *Clinical Diagnosis and Management by Laboratory Methods*, J. B. Henry, ed. (Philadelphia: W. B. Saunders Company, 1996).

J. Woo and J. B. Henry, "Metabolic Intermediates and Inorganic Ions," in *Clinical Diagnosis and Management by Laboratory Methods*, J. B. Henry, ed. (Philadelphia: W. B. Saunders Company, 1996).

Chapter 7

Toward transcutaneous measurements

We hope that the technique discussed in this thesis can be applied to non-invasive measurements. In this chapter, we aim to provide groundwork and suggestions for future research in non-invasive measurements.

The target of measurement is now the blood-tissue matrix, which is a medium quite different from serum or whole blood, and there are issues to be considered in non-invasive measurements. The first part of this chapter discusses these issues. The second part of this chapter discusses preliminary results of a transcutaneous experiment. Raman spectra of typical body parts were collected and analyzed. The third part of this chapter discusses the predictions based on the analysis of the preliminary data and provides guidelines for the future directions of this research.

7.1 Considerations

Differences between the blood-tissue matrix and previously studied media raise issues for non-invasive measurements. The complex nature of the blood-tissue matrix composition is described. Due to the structural and chemical differences, the blood-tissue matrix has various optical properties, and the effect of the changes in the optical properties is discussed. Several methods of measuring reference concentration for transcutaneous studies are presented. Finally, the safe level of laser radiation is discussed.

7.1.1 Structural and chemical composition of a blood-tissue matrix

While whole blood samples are uniform mixtures of blood cells and plasma, the structural and chemical composition of blood-tissue matrix is inhomogeneous and varies from body part to body part. The structural composition of the blood-tissue matrix affects the scattering patterns, and also determines the distribution of certain analytes. Since there will be favorable regions and non-favorable regions for transcutaneous measurement, the selection of the body part is an important task in transcutaneous measurements.

The skin is a multi-layered system, and largely consists of two layers: epidermis and dermis (Figure 7.1). The epidermis has multiple layers: stratum corneum, stratum lucidum, stratum granulosum, stratum malpighii (also called stratum spinosum), and stratum germinativum (or stratum basale) [Gray 1977]. The thickness of the epidermis varies. The thickness normally range from 40 to 150 μm (thin in lips) and is greater in palms of hands and soles of feet (800 ~ 1400 μm). Keratin is the major protein in human epidermis, hair, and nail [Williams et al. 1994]. For example, the stratum corneum, the outer layer of the epidermis, mainly consists of keratin (*ca.* 65%) and some lipids (*ca.* 10%), such as sphingolipids, ceramides, cholsterol sulphate, neutral lipids, and polar lipids [Barry et al. 1992]. Water, salts, and lipids are also found in epidermis [Kardong 1998].

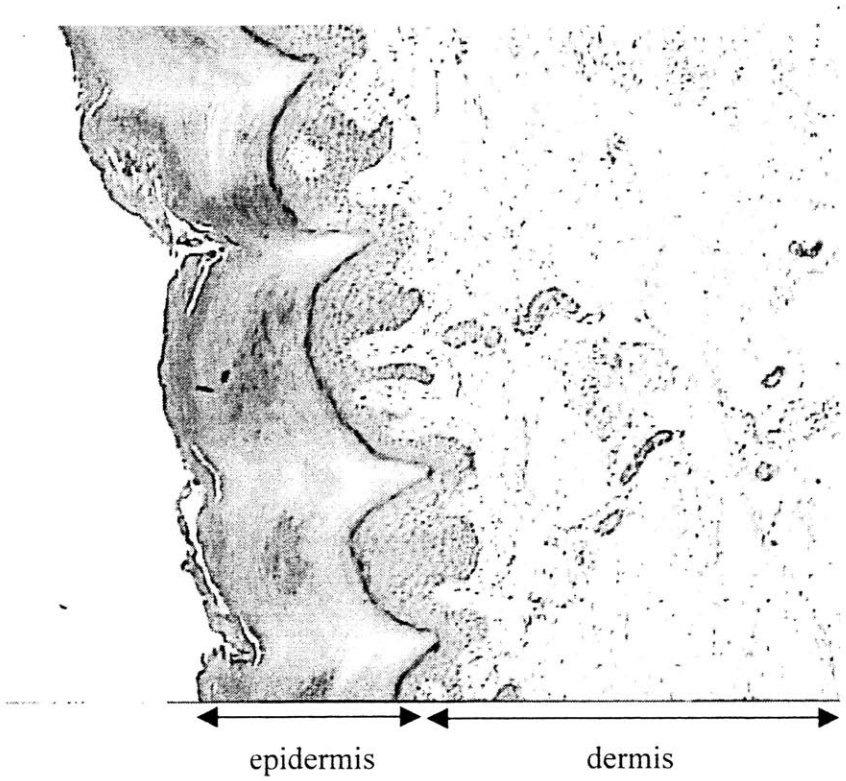

Figure 7.1. Epidermis and dermis in finger skin (© McGill University Histology Review)

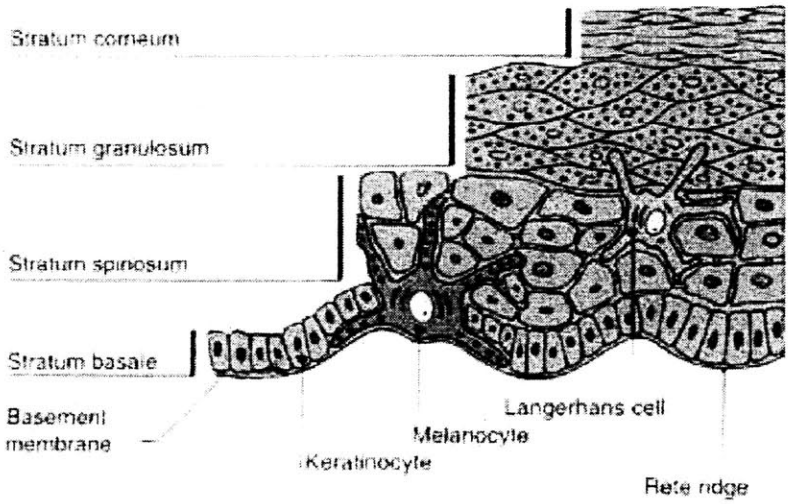

Figure 7.2. Epidermis structure (© W.B. Saunders Company 1997) [Gawkrodger 1997]

The dermis also has multiple layers: reticular layer and papillary layer. The dermis varies in thickness. The thickness typically ranges from 1 to 2 mm. It is very thick in the

palms and heels (3 mm or more), and thin in the eyelids and scrotum (0.6 mm) [Gray 1977]. The dermis consists of connective tissue, elastic fibers, blood vessels, lymphatics, and nerves. Collagen is the major constituent of dermis (70%), followed by elastin.

Interstitial fluid is another component in the blood-tissue matrix. Interstitial fluids fills the space between cells in epidermis and dermis, while whole blood is present in blood vessels in dermis which is located deeper than epidermis. Thus, measurements of analytes in interstitial fluids may be easier than measurements of analytes in whole blood. Certain analytes are diffused into interstitial fluids, and glucose is one of them.

There has been an extensive study of glucose in interstitial fluid, and in this chapter, we will use glucose as an example of analytes in the blood-tissue matrix. The concentration of glucose in whole blood and that in the blood-tissue matrix are not identical [Roe and Smoller 1998, Waynant and Chenault 1998]. Table 7.1 presents the relative concentrations and volume fraction of three types of fluids in the blood-tissue matrix. The glucose concentration in the interstitial fluid is lower than the glucose concentration in plasma by factor of 0.82. The glucose concentration in the intracellular fluid is only 10% of the glucose concentration in plasma. The glucose concentration in the blood-tissue matrix is the volume-weighted-average of the glucose concentrations in three types of biological fluids, and the glucose concentration in the blood-tissue matrix is 23% of the glucose concentration in plasma. Furthermore, if we aim to measure concentrations of whole blood glucose (or plasma glucose), the Raman signal of the whole blood glucose would be much smaller than that of the plasma glucose, since only 6% of the blood-tissue matrix is occupied by plasma.

Table 7.1. Concentrations and volume fractions of biological fluids in the blood-tissue matrix

	*volume fraction (L/L)**	*typical glucose concentration (mM)*	*typical amount of glucose (~mmole)*
Intracellular fluid	37%	0.5	0.19
Interstitial fluid	16%	4.1	0.66
Plasma	6%	5.0	0.30
Non-liquid component	41%	0	0
Blood-tissue matrix	100%	1.15	1.15

* The relative volume fractions are given by Roe and Smoller (1998). The absolute volume fraction was obtained from Guyton (1997).

The best strategy for the maximum signal collection might be to collect the glucose signal in a relatively large area of blood tissue matrix with a high numerical aperture (NA) objective. If we collect the glucose signal from interstitial fluid only, the glucose concentration is not much reduced, but interstitial fluid exists in the space between cells, and it would be a challenge to collect signal only from interstitial fluid. Typically, the interstitial fluid occupies less than 16% of the blood-tissue matrix [Guyton 1997]. Although the relative concentration of glucose in the blood-tissue matrix is lower than that in plasma, the overall the ratio between the signal and the shot noise would be higher when a spectrum is collected from a large area of the blood-tissue matrix. Furthermore, this would reduce the effect of local variations of the blood-tissue structure, and provide more reliable measurements.

7.1.2 Turbidity in blood-tissue matrix

The optical properties of the blood-tissue matrix are quite different from those of serum or whole blood. The surface distribution of Raman scattered light in the blood-tissue matrix will be also different from that in serum or whole blood. Also, the penetration depth is important in the blood-tissue matrix. Since whole blood is a relatively uniform mixture of plasma and blood, the penetration depth is normally not as important in whole blood measurements. In the blood-tissue matrix, it is important to probe the region in which analytes are present, and the penetration depth should be carefully examined.

In Chapter 3, it was demonstrated that an increase in both absorption and scattering properties reduced the fluence of the Raman signal. At 830 nm excitation, we expect that absorption in the blood-tissue matrix is, in fact, smaller than the absorption property in whole blood, since the volume fraction of plasma (and whole blood) is small. This implies that the Raman signal intensity of glucose may be larger in the blood-tissue matrix than that in whole blood, due to the lower absorption.

A Monte Carlo simulation was performed to calculate the intensity of Raman signal in the blood-tissue matrix. The optical properties of a typical skin were used to model human skin [Cheong et al. 1990]. The model predicts that the intensity of the Raman signal in skin is three times higher than that in whole blood, which promises a potentially more accurate measurements in skin. In the future, the optical properties of various body locations can be tested with detailed chemical and structural compositions.

7.1.3 Reference measurements

Another issue of consideration is the method of reference concentration measurements. When a multivariate analysis is performed for concentration measurements, the predicted concentrations are often compared with the reference concentrations to calculate the prediction error. Also, the reference measurement is necessary with certain multivariate analysis techniques (e.g. PLS or PCR).

The things to consider for reference measurement in the blood-tissue matrix are the selection of medium, or tissue, in which the reference concentrations are determined. Reference measurements are commonly performed with serum or plasma obtained from whole blood in vein, artery, and capillary. Measurements in interstitial fluid are also possible.

Whole blood can be collected by puncture of vein, artery, and skin. Certain analytes have comparable concentrations in these media, but there are analytes (e.g. blood gases) whose concentrations vary drastically. While whole blood obtained from venous puncture or arterial puncture needs to be analyzed with a hospital blood analyzers, certain analytes, such as glucose and cholesterol, in whole blood obtained from a finger prick can be analyzed with portable blood analyzers. Although hospital instruments are more accurate and capable of measuring more analytes than the portable analyzers, the convenience of measuring analytes on-site makes the portable blood analyzers a useful tool for reference measurements. Determination of analytes in blood provides concentrations in the manner common among the medical community. However, analytes in the blood-tissue matrix and in whole blood may have different scales of concentrations. Concentrations in

the blood-tissue matrix may also have delayed readings. Thus, concentrations in whole blood may need corrections to serve as reference in the blood-tissue matrix.

Interstitial fluid is already present in the blood-tissue matrix, and concentrations in the interstitial fluid may not need such correction when they are compared with those in the blood-tissue matrix. However, if the concentrations in interstitial fluid is to be compared with concentrations in whole blood, which is what the medical community is more familiar with, proper conversion may be necessary. For glucose, its concentration in interstitial fluid is about 82% of the concentration in plasma (Table 7.1). Again, analyte concentrations in interstitial fluids are expected to have a time lag over the analyte concentrations in whole blood. This lag may present a problem when rapid and accurate measurements of analyte concentrations are needed.

7.1.4 Allowable radiant energy to patient

Finally, the determination of the excitation laser power is an important issue in terms of the patient safety. A high energy excitation beam is desired for high signal intensity, but it increases the risk of tissue damage. It is needless to say that it is necessary to keep the power below the level of damage in measurements *in vivo*. The safe level of excitation power also varies for different body parts. It is crucial to have a good understanding of the laser excitation power in order to prevent any damage in subjects and increase the signal by using the maximum allowable power.

The safe levels of irradiation are expressed in terms of radiant exposure (J/cm^2) or irradiance (W/cm^2). If the irradiance of an excitation beam is high and the irradiated body

part cannot quickly transport the energy away from the irradiated body part, a damage will occur in a short period of time. As the energy deposited into the body part remains in the irradiated location on the time scale of damage, the radiant exposure would be a good measure of the damage risk. If the irradiance of the excitation beam is not high enough to cause immediate damage, the energy deposited into the body part will be partially transported via heat transfer mechanisms. As the energy level in the irradiated body part will increase over time, the irradiance and the exposure time would determine the risk of tissue damage.

We aim to use around 300 mW irradiance in a 1 mm x 1 mm square beam geometry for measurements in skin (30 W/cm^2 irradiance). This is the level comparable to what was used in other *in vivo* tissue studies. This power can be obtained from a compact diode laser and the collection efficiency for this excitation geometry is acceptable (21% in whole blood).

The American National Standards Institute (ANSI) set a guideline for safe use of lasers and laser systems [ANSI.Z136-1, ANSI Z136-3]. For an exposure to an 830 nm excitation beam for longer than 10 seconds, the ANSI standard recommends less than 0.4 W/cm^2 irradiance on skin as a level of "comfort". Our design goal is above the ANSI guideline.

However, the irradiance levels in the ANSI standard are not the levels of skin damage. The ANSI standard does not address the absorption parameters of various tissues or the blood perfusion in a blood-tissue matrix. For therapeutic purpose, irradiance higher than the ANSI standard is often used. In a diagnostic study, there are reports of skin

exposure for 30 seconds to a 40 W/cm^2 irradiance beam (760 μm diamter) at 785 nm, which is higher than the ANSI standard, and it was reported that no sensible damage was observed [Shim and Wilson 1997]. These led us to investigate the safe level of irradiance.

The mechanism of the laser damage for various excitation wavelengths is well known (University of Waterloo Laser Safety Manual, International Commission on Illumination). The laser damage due to a continuous excitation beam at 830 nm is thermal damage. An excitation beam at the wavelength between the 200 to 280 nm range produce sunburn (erythema), skin cancer, and accelerated skin aging. An excitation beam in the range of 280 to 400 nm can result in increased pigmentation. Photosensitization and thermal damage to skin can result from the exposure to light from 310 to 700 nm. The severity of thermal damage ranges from a mild reddening, which is normally healed within hours, to blisters and charring. An extremely high powered laser may result in depigmentation, ulceration, and scarring of the skin, and damage to underlying organs. Mild to severe thermal damage can be observed in histology.

In a preliminary experiment (Motz and Sasic at MIT), parts on an artery tissue type were exposed to a focused beam (200 μm diameter) of 280 mW radiant power for up to 600 seconds. When the histology of the tissue samples were studied, no thermal damage was found. Our desired irradiance and radiant energy were lower than the irradiance and radiant energy used in this experiment and those used by Shim and Wilson, and thus, our irradiance might be safe for skin exposure. Although we cannot directly compare this experiment with *in vivo* measurements, the experimental data seems to indicate that a higher level of irradiation may be safe.

The future refinement of this artery experiment may address the following issues. The temperature in the tissue samples was lower than the body temperature If a thermal damage occurs when a small part of the tissue sample reaches a certain temperature, the samples should be initially kept at the body temperature to study the damage threshold. Then, a higher level of the safe may be established.

7.2 Measurement of tissue spectra

This section discusses measurements of Raman spectra of various body parts and its preliminary analysis. The new system developed for whole blood measurements (Chapter 5) was used. Although it was optimized for collecting Raman scattered light emerging from whole blood, it could collect Raman scattered light efficiently from other turbid biological tissues. The collected spectra were analyzed with an ordinary least squares regression method.

7.2.1 Preliminary experiment

As a preliminary study of the blood-tissue matrix, Raman spectra of various body parts were collected using the new system. The body parts were chosen to represent various body parts. The fingers were chosen, because they are easy to access and are the regions of finger prick blood withdrawal. The spectrum of a fingernail was collected to approximate keratin, because pure keratin was not easy to obtain. Epidermis of a lip is relatively thin and thus, it would be easier to probe blood by using the lip. The earlobe also has thin skin layer and a good supply of arterial blood. Table 7.2 lists the body parts whose Raman

spectra were collected. In each measurement, the selected body part was placed at the focal plane of the collection optics, and the spectrum was integrated for 10 seconds.

Table 7.2. List of body parts whose Raman spectra were collected

sample number	body part
1	ventral (inside) thumb
2	dorsal (outside) thumb
3	dorsal (outside) index finger
4	nail + dorsal (outside) index finger
5	ventral (inside) palm
6	ventral (inside) webbing
7	dorsal (outside) hand
8	ventral (front) earlobe
9	inside lower lip

7.2.2 Preliminary tissue model and fit

As a preliminary step toward transcutaneous measurements, the Raman spectra of typical body parts were collected and analyzed with OLS. Raman spectra of nine chemicals were used as component spectra. Those analytes were whole blood, water, fat, cholesterol, collagen, elastin, and keratin. The Raman spectrum of the whole blood was obtained from the whole blood experiment of multi-donors (Chapter 6). The Raman spectrum of the keratin was obtained by subtracting the spectrum of a finger from the spectrum of a fingernail where keratin is abundant, because pure keratin was not commercially available.

However, this is probably not pure keratin, and it does not match well with the published spectrum of keratin [Williams 1994]. This can be further investigated. The other component spectra were obtained from chemical models of human breasts [Shafer 2001]. The chemical models of breast were developed to distinguish the chemical composition of normal, benign, and malignant breast tissue, and included Raman spectra of many chemicals: calcium oxalate, calcium hydroxyapatite, carbonate, phospatidyl choline, myosin, tropomyosine, actin, and beta-carotene, in addition to the chemical listed above. However, many of these chemicals are not present in the blood-tissue matrix, and thus, were not used in the chemical model of the blood-tissue matrix.

The Raman spectrum of the inside thumb (Figure 7.3) matches well with the published Raman spectrum of human skin [Caspers et al. 1998]. We fit the measured spectrum with the Raman spectra of the chemical components in our model. The fit coefficients were related to the concentration of the chemicals. However, the chemical model was not calibrated for concentrations, and we could not obtain absolute concentrations of components, nor could we compare concentrations of one chemical and another on the absolute scale. Instead, the fit coefficients of each chemical were normalized by the maximum fit coefficient of that chemical observed in our experiment, and we could compare the relative abundance of each chemical in different body parts.

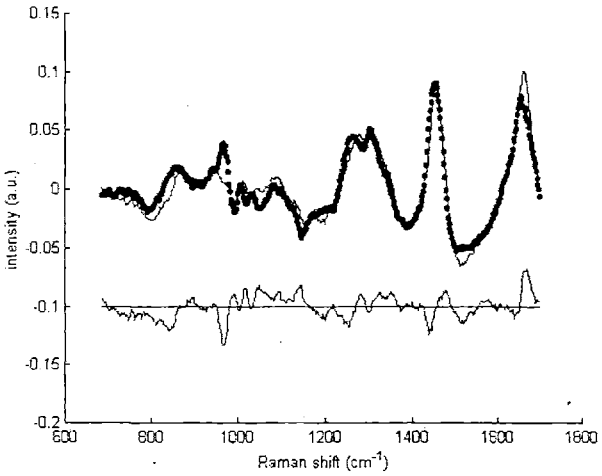

Figure 7.3. Raman spectrum of the inside thumb and the model fit. The line is the spectrum, and the dots are the fit. The residual is plotted offset. Water, fat, cell nucleus and cytoplasm, collagen, elastin, and "keratin" are the constituents.

Table 7.3. Coefficients for the model fit of the inside finger (Figure 7.3)

component	Water	Fat	Cholesterol	Collagen	Elastin	Keratin
concentration	59.0	47.4	10.8	13.8	60.2	34.6

The Raman spectrum of the fingernail (Figure 7.4) had a strong peak at 968 cm^{-1}. The normalized fit coefficients indicated that the fingernail had the highest concentration of keratin among the body parts measured, which corresponded well with the known chemical composition of fingernails [Burkitt et al. 1996]. The fit coefficients for collagen, elastin, cholesterol, and fat were non-zero, and this seemed to indicate that we were probing skin under the fingernail.

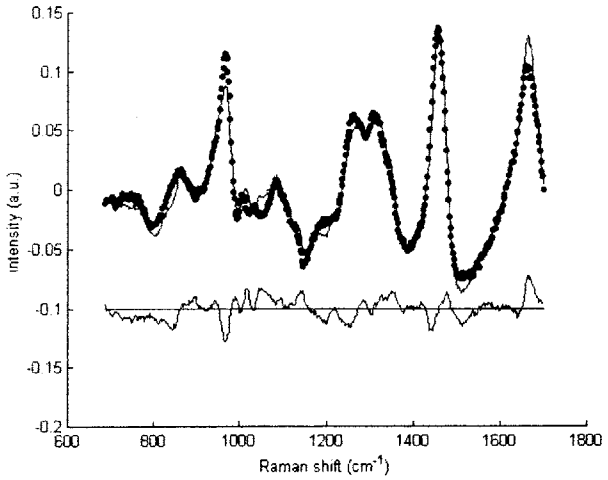

Figure 7.4. Raman spectrum of the fingernail and the model fit. The line is the spectrum, and the dots are the fit. The residual is plotted offset. Water, fat, cell nucleus and cytoplasm, collagen, elastin, and "keratin" are the constituents. The Raman band at 968 cm^{-1} is strong.

Table 7.4. Coefficients for the model fit of the fingernail (Figure 7.4)

component	Water	Fat	Cholesterol	Collagen	Elastin	Keratin
concentration	50.9	34.5	9.0	18.8	58.1	100

The Raman spectrum of the earlobe (Figure 7.5) was quite different from the spectrum of the skin. The fit coefficient for keratin was much small compared to that for the skin, and this may be an indication of thinner epidermis in the earlobe. Also, it was the only body part the spectrum of which had any contribution from whole blood. Thus, the earlobe may be the best body part for *in vivo* measurements of analytes in blood. The maximum fit coefficients of cholesterol and fat were observed in the earlobe. The earlobe might be an ideal body part for tissue cholesterol measurements.

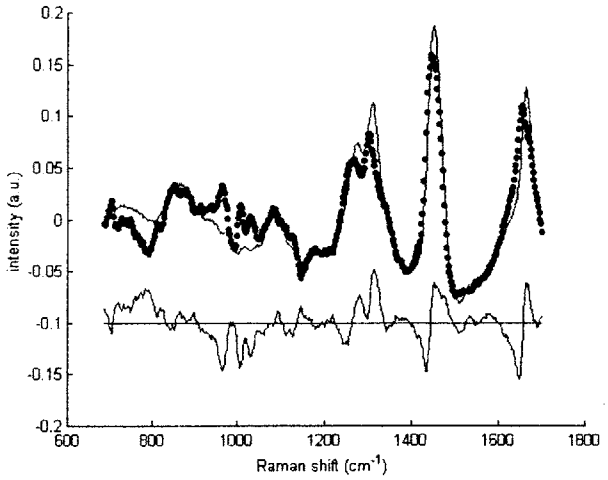

Figure 7.5. Raman spectrum of the earlobe and the model fit. The line is the spectrum, and the dots are the fit. The residual is plotted offset. Whole blood, water, fat, cell nucleus and cytoplasm, collagen, elastin, and "keratin" are the constituents. It is notable that the contribution of whole blood was only observed in the earlobe.

Table 7.5. Coefficients for the model fit of the earlobe (Figure 7.5)

component	Whole Blood	Water	Fat	Cholesterol	Collagen	Elastin	Keratin
concentration	100	74.1	100	100	10.7	93.9	22.8

The Raman spectrum of the inner lip (Figure 7.6) had the least concentration of keratin. This seemed to be related to the fact that lips have thin epidermal layer. In addition, the keratin concentrations seem to be related to the known thickness of epidermis in various body parts. The keratin concentration was the highest in the fingernail, followed by the finger, earlobe, and the lip. If this observation is true, the lip may be an ideal body part for measurements of dermal interstitial fluid, as the interference of the epidermis on dermis measurements will be the minimum in lips.

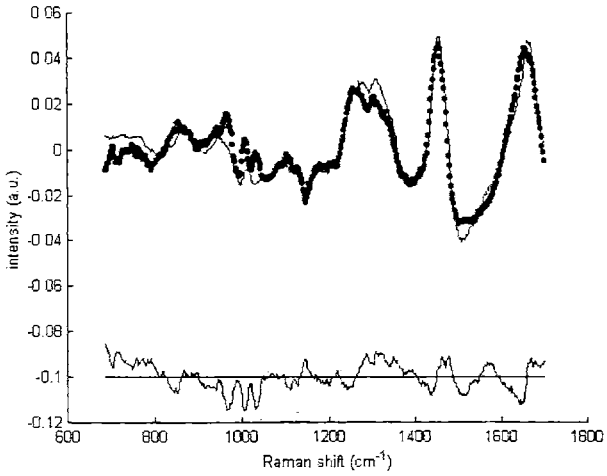

Figure 7.6. Raman spectrum of the inner lip and the model fit. The line is the spectrum, and the dots are the fit. The residual is plotted offset. Water, fat, cell nucleus and cytoplasm, collagen, elastin, and "keratin" are the constituents. There are peaks that cannot be fit with the model components between 940 and 1040 cm^{-1}.

Table 7.6. Coefficients for the model fit of the inner lip (Figure 7.6)

component	Water	Fat	Cholesterol	Collagen	Elastin	Keratin
concentration	48.4	11.8	28.1	16.6	43.1	13.1

However, we did not observe any contribution from whole blood, and this may be investigated further. The Raman peaks between 940 and 1040 cm^{-1} were not fit well with the model components. This seemed to indicate that additional components were necessary to completely model the Raman spectrum of the human inner lip. Although this chemical model has not been validated yet for the blood tissue matrix, some findings match well with the known compositions of various body parts. Further investigation will provide more insight into non-invasive transcutaneous measurements.

7.2.3 Summary

Raman spectra of various body parts were collected and analyzed. The Raman spectra of many chemical components were used in the analysis. The analysis seems to indicate that the earlobe may be the best body part for *in vivo* whole blood measurements, and the lip may the best body part for interstitial fluid measurements. This has to be validated with further investigation.

7.3 Predictions for transcutaneous measurement of blood analytes

In Chapter 4, we derived Eq (4.23) that estimates the prediction accuracies with the signal-to-noise ratios (S/N) and the line shapes of the constituent spectra:

$$\frac{c_k}{\Delta c_k} \approx \frac{S}{n} \cdot \frac{1}{\sqrt{diag_k\left\{\left(Q \cdot Q^T\right)^{-1}\right\}}}. \tag{4.23}$$

With experimental data and our knowledge about blood-tissue matrix, we can estimate the prediction accuracy of analyte concentration measurements in the blood-tissue matrix. Although our measurements are not limited to glucose, we continue to use glucose as an example of a target molecule.

In general, we expect that more Raman scattered light emerges from the blood-tissue matrix than from whole blood, because the blood-tissue matrix has much lower absorption than whole blood [Cheong et al. 1990]. In a recent experiment (Enejder, Sasic, and Oh at MIT), three times more Raman scattered light was collected from a medium

whose optical properties are similar to those of skin, than from whole blood. This also matched with a Monte Carlo simulation model of skin (Enejder). As we discussed in the previous section, concentrations of glucose in the blood-tissue matrix are only 23% of those in whole blood. Thus, the intensity of light Raman-scattered by glucose in the blood-tissue matrix is 70% of that in whole blood.

The fluorescence background and its shot noise is stronger in the blood-tissue matrix than in whole blood (Figure 7.7). The fluorescence background increased by factor of 8 in lip and 17 in finger. If we eliminate the fluorescence generated by optical components (Figure 5.19), the fluorescence background increase would be 7 times in lip and 16 times in finger. The shot noise would increase by factor of 2.6 in lip and a factor of 4 in the finger. This fluorescence background originates from the body and would be difficult to eliminate in CW measurements.

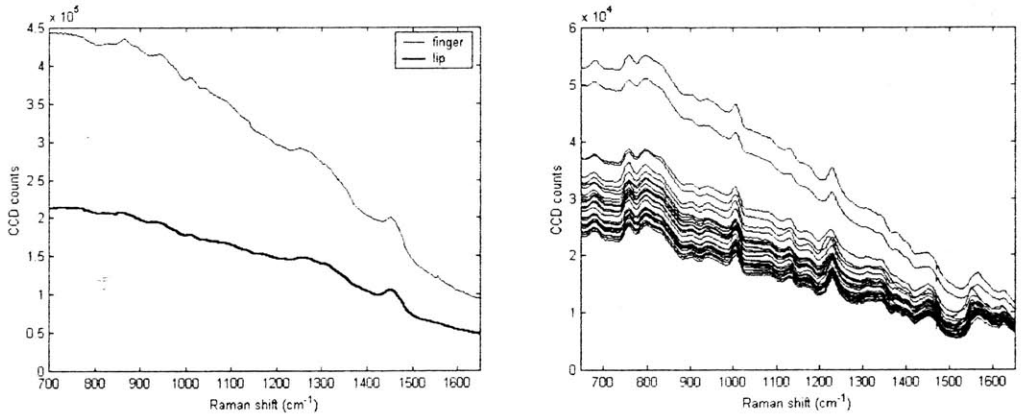

Figure 7.7 Fluorescence background in Raman spectra of finger and lip (left). Raman spectra of body parts have the background at least ten times stronger than that of whole blood (right).

The signal intensity in the blood-tissue matrix was 70% of that in whole blood. The noise increased at least by factor of 2.6. Accordingly, the S/N in the blood-tissue matrix is 3.7 times smaller than that in whole blood. The overlap factor was also reduced in the blood-tissue matrix. It was 0.69 in whole blood and 0.64 in the blood-tissue matrix. As a result, the prediction accuracy is expected to be 4 times lower in the blood-tissue matrix according to Eq. (4.23), predicting 4 mM prediction error for glucose.

To enhance the prediction accuracy, the system sensitivity needs to be improved further. As the fluorescence background originates from the body part, the fluorescence background will also increase in a more sensitive system. Thus, an improvement of the system sensitivity by factor of 16 is needed to achieve the prediction accuracy obtained in the whole blood measurement. In Chapter 5, potential enhancement in the system sensitivity was discussed (Table 5.4), and up to factor of 11 enhancement can be made. Although this is short of the required factor of 16, glucose can be measured with slightly reduced prediction accuracy. Thus, transcutaneous measurements of blood analytes appear to be feasible.

7.4 Future directions

The future work for the transcutaneous measurement may include the following. The Monte Carlo simulation model for the blood-tissue matrix will provide information about light propagation in the blood-tissue matrix. The instruments can be improved for faster and more accurate measurements. Since the surface distribution of light is different in the blood-tissue matrix from the whole blood, an optimization of the collection optics may

further increase the sensitivity in measurements of the blood-tissue matrix. The installation of a larger and more efficient detector will also increase the sensitivity of the instrument. Further study of the blood-tissue matrix may find skin analytes, which cannot be measured easily with conventional techniques, and may provide important clinical information. All this work will lead to the non-invasive transcutaneous measurements of blood analytes.

References

American National Standards Institute, Z136-1, *Safe Use of Lasers*, 2000

American National Standards Institute, Z136-3, *Safe Use of Lasers in Health Care Facilities*, 1996

B. W. Barry, H. G. M. Edwards, and A. C. Williams, "Fourier Transform Raman and Infrared Vibrational Study of Human Skin: Assignment of Spectral Bands," *Journal of Raman Spectroscopy*, volume 23, 1992, pp. 641 -645.

G. Burkitt, A. Stevens, J. Lowe, and B. Young,*Wheater's Basic Histopathology*, (New York: Churchill Livingston, 1996).

P. J. Caspers, G. W. Lucassen, R. Wolthuis, H. A Bruining, and G. J. Puppels, "*In vitro* and *in vivo* Raman spectroscopy of human skin," *Biospectroscopy*, volume 4, 1998, pp. S31 –S39.

P. J. Caspers, G. W. Lucassen, H. A Bruining, and G. J. Puppels, "Automated depth-scanning confocal Raman microspectrometer for rapid in vivo determination

of water concentration profiles in human skin," *Journal of Raman spectroscopy*, volume 31, 2000, pp. 813 –818.

W.-F. Cheong, S. A. Prahl, and A. J. Welch, "A review of the optical properties of biological tissues," *IEEE Journal of Quantum Electronics*, volume 26, 12, 1990, pp. 2166 –2185.

M. J. C. van Gemert, J. S. Nelson, T. E. Milner, D. J. Smithies, W. Verkruysse, J. F. de Boer, G. W. Lucassen, D. M. Goodman, B. S. Tanenbaum, L. T. Norvang, and L. O. Svaasand, "Non-invasive determination of port wine stain anatomy and physiology for optimal laser treatment strategies," Physics in Medicine and Biology, volume 42, 1997, pp. 937 –950.

D. J. Gawkrodger, *Dermatology: An Illustrated Colour Text*, (Philadelphia: W. B. Saunders Company, 1997).

H. Gray, *Descriptive and Surgical Anatomy*, T. P. Pick and R. Howden, ed. (New York: Bounty Books, 1977).

A. C. Guyton, J. E. Hall, and W. Schmitt, *Human Physiology and Mechanisms of Disease* (Philadelphia: W. B. Saunders Company, 1997).

K. V. Kardong, *Vertebrates: Comparative Anatomy, Function, and Evolution* (New York: McGraw-Hill, 1998).

L.-G. Lindberg and P. A. Öberg, "Optical properties of blood in motion," *Optical Engineering*, volume 32, 2 1993, pp. 253 -257.

McGill University Histology Laboratory, Molson Medical Informatics Project, Histology Review Site, http://sprojects.mmip.mcgill.ca/histo/introduction.htm.

S. Pilotto, M. T. T. Pacheco, L. Silveira Jr., A. B. Villaverde, and R. A. Zangaro, "Analysis of near-infrared Raman spectroscopy as a new technique for a transcutaneous non-invasive diagnosis of blood components," Lasers in Medical Science, volume 16, 1, 2001, pp. 2 –9.

J. N. Roe and B. R. Smoller, "Bloodless glucose measurements," *Critical Reviews in Therapeutic Drug Carrier Systems*, volume 15, 3 1998, pp. 199 -241.

K. E. Shafer, "Chemical basis for breast cancer diagnosis using Raman spectroscopy" (Cambridge, MA: Massachusetts Institute of Technology, 2001).

M. G. Shim and B. C. Wilson, "Development of an in vivo Raman spectroscopic system for diagnostic applications," *Journal of Raman* Spectroscopy, volume 28, 2-3 1997, pp. 131-142.

N. W. Tietz, "Carbohydrates," in *Fundamentals of Clinical Chemistry*, N. W. Tietz, ed. (Philadelphia: W. B. Saunders Company, 1970).

R. W. Waynant and V. M. Chenault, "Overview of non-invasive fluid glucose measurement using optical techniques to maintain glucose control in diabetes mellitus," *IEEE LEOS Newsletter*, volume 12, 2 1998.

A. C. Williams, H. G. M. Edwards, and B. W. Barry, "Raman spectra of human keratotic biopolymers: skin, callus, hair and Nail," *Journal of Raman Spectroscopy*, volume 25, 1994, pp. 95 –98.

Chapter 8

Conclusion

8.1 Review of goals and accomplishments

As discussed in Chapter 1, the principal goal of this thesis research was to measure blood analytes in whole blood with clinical accuracy. The results presented in Chapter 6 demonstrate that this goal has been achieved. From a Raman spectrum of whole blood, the concentrations of eight analytes (glucose, urea, cholesterol, triglyceride, albumin, total protein, hemoglobin, and hematocrit) can be extracted with clinical accuracy.

We also wanted to derive an analytical equation for prediction error. The analytical equation derived in Chapter 4 provides a better understanding of the prediction error. The equation indicated that noise is the major source of error, and efforts were made to design a spectroscopy system with a maximum sensitivity. Based on the prediction error equation, we assume that as the S/N in the spectrum increases, the number of analytes that can be predicted will increase (e.g. bilirubin).

We needed a high-throughput spectroscopy system to achieve high S/N data rapidly. The new system designed in Chapter 5 had a five times higher S/N than the previous state-of-the-art system. An optimization of system resolution and throughput, Monte Carlo simulation results, calculation of the collection geometry, and optimal component selection by an optical design software were performed to design the new system.

Another goal was to develop a tool to study Raman scattering and light propagation in turbid biological media. A Monte Carlo simulation model was developed and validated, and the model provided important parameters in designing the new optical system. The application of the simulation model is not limited to whole blood. Given proper optical properties, it can model various parts of skin in different geometry. Thus, we developed a versatile tool for studying Raman scattering in turbid media.

These studies have been the first of their kind. No other group, to our knowledge, has presented research in which the study of Raman scattering in turbid media, the study of prediction error, and the design of a new Raman spectroscopy system were all combined to improve prediction accuracy in whole blood.

8.2 Final statement

In conclusion, this thesis research has shown the accuracy of Raman spectroscopy as a technique for monitoring blood analytes. Multiple analyte concentrations have been measured, and more analytes will be measured as instrumentation continues to improve. Practical applications of this methodology would include whole blood analyzer clinical laboratories, indwelling catheter for online measurements in intensive-care-unit, noninvasive blood analyte monitors for in-patient units, physicians' offices, and patients' home. Furthermore, accurate measurements of skin analytes *in vivo* may have the potential for expanding the horizon of medicine.

Appendix A

Light propagation in whole blood calculated by Monte Carlo simulation and diffusion approximation with delta-Eddington phase function

Light propagation in turbid media can be described by many mathematical tools. This section compares the light propagation in whole blood calculated by two methods: Monte Carlo simulation and diffusion approximation with delta-Eddington phase function.

The Monte Carlo simulation model is a statistical approach to model radiative transfer equation. There are many Monte Carlo simulations models develop to study light propagation in turbid media, including the one described in Chapter 3. We used our Monte Carlo simulation model for the study in this section. Monte Carlo simulation models can model various optical properties in different geometries, and calculate many physical quantities of interest.

The use of diffusion approximation with delta-Eddington phase function was suggested to better describe forward scattering photons [Groenhuis et al. 1983] than the use of diffusion approximation alone. The delta-Eddington phase function has two terms: forward scattered light and diffused light. For highly forward scattering media (high

anisotropy, g), the intensity of the diffused light is negligible to that of the forward scattered light. This method was used to describe propagation of elastically-scattered and Raman-scattered light in whole blood [Berger 1998]. It found that the intensity of the diffused light was negligible when compared with that of the forward scattered light, and suggested an interesting model for light propagation in whole blood: excitation light is exponentially attenuated without spreading in whole blood and Raman-scattered light emerges ballistically, which is not an accurate description of light propagation in whole blood.

The light propagation calculated by the Monte Carlo simulation differs from that calculated by the delta-Eddington diffusion approximation (Figure B.1). The Monte Carlo simulation used Reynolds-McCormick phase function (Chapter 3). Both were computed using the same optical properties of whole blood (μ_a 1.04/mm, μ_s 216/mm, and g 0.990 [Roggan et al. 1999]).

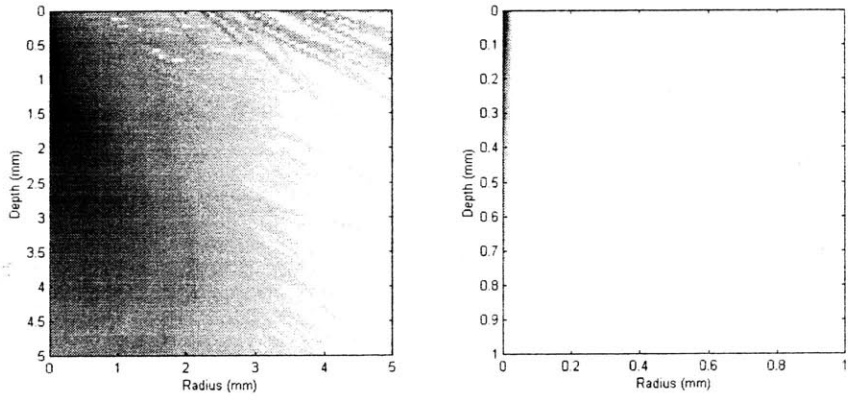

Figure A.1. The distribution of excitation light absorbed by the media, calculated by the Monte Carlo simulation model (left) and the delta-Eddington diffusion approximation (right).

Also, the surface distribution of Raman scattered light calculated by the Monte Carlo simulation model differs from that calculated by the delta-Eddington diffusion

approximation. The full-width at half-maximum (FWHM) of the Raman scattered light from a pencil beam excitation was 0.9 mm according to the Monte Carlo simulation (Figure 3.7) and 0.04 mm according to the delta-Eddington diffusion approximation [Berger 1998]. This is probably because the delta-Eddington phase function overestimates the forward scattered light for values of g close to 1.

The delta-Eddington diffusion approximation is not accurate in modeling light propagation in whole blood. Although the accuracy of such an approximation method could be improved by employing an accurate phase function, they are often limited to specific geometries (e.g. semi-infinite medium). A Monte Carlo simulation model would be a better tool to study light propagation in a turbid medium, in general.

Reference

A. J. Berger, "Measurement of analytes in human serum and whole blood samples by near-infrared Raman spectroscopy" (Cambridge: Massachusetts Institute of Technology, doctoral thesis, 1998).

R. A. J. Groenhuis, J. J. Ten Bosch, and H. A. Ferwerda, "Scattering and absorption of turbid materials determined from reflection measurements. 1: Theory," *Applied Optics*, volume 22, 16 1983, pp. 2456-2462.

A. Roggan, M. Friebel, K. Dörschel, A. Hahn, and G. Müller, "Optical properties of circulating human blood in the wavelength range 400-2500 nm," *Journal of Biomedical Optics*, volume 4, 1 1999, pp. 36 -46.

Appendix B

Numerical validation of the prediction accuracy equation

The prediction error equation and the prediction accuracy equation derived in Chapter 4 can be numerically tested. The prediction accuracy equation was:

$$\frac{c_k}{\Delta c_k} \approx \frac{s}{n} \cdot \frac{1}{\sqrt{diag_k\left\{\left(Q \cdot Q^T\right)^{-1}\right\}}} \tag{4.23}$$

We wrote a code for Matlab (Mathworks, MA) in order to numerically simulate Raman spectra and various mixture of chemicals. For each trial, one hundred samples were numerically prepared, and each sample was considered as a mixture of ten chemicals. Spectra of the ten chemicals (Figure B.1) and their concentrations in 100 samples were randomly generated assuming a Gasussian distribution. Then, the spectra of all the samples can be computed as linear superpositions. The known amplitude of noise was added to model the noise in the real system. Ordinary least squares (OLS) and partial least squares (PLS) were used to analyze each set of spectra. The prediction accuracy was calculated from the prediction accuracy equation and was compared with those obtained by OLS and PLS. The prediction accuracy of 100 samples in 10 trials, calculated by three methods, are listed in Table B.1.

Figure B.2. demonstrates that the prediction accuracy of a chemical, present in 100 samples with other nine chemicals, obtained by Eq. (4.23) (line), OLS analysis (circle), and PLS analysis (triangle). The prediction accuracy calculated by the three methods match well with one another. Furthermore, the prediction accuracy increases as the signal-to-noise-ratio (S/N) of the spectra. The small deviation for OLS and PLS from the prediction accuracy equations is due to the statistical nature of OLS and PLS.

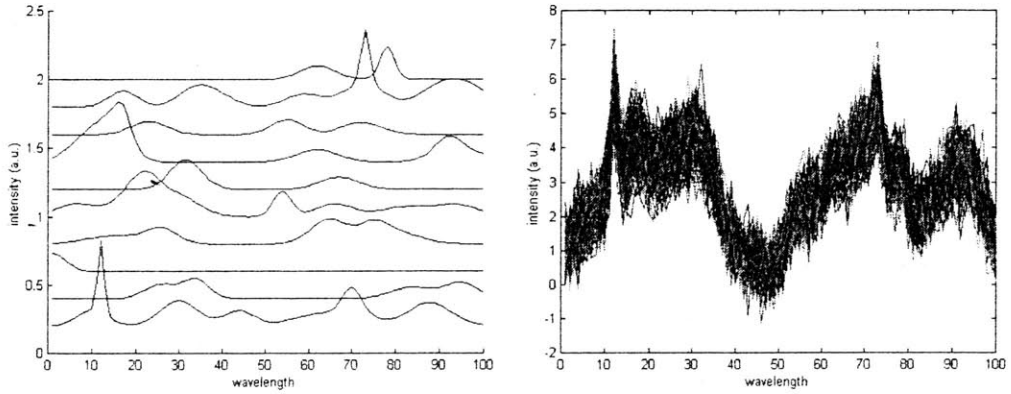

Figure B.1. A typical set of ten randomly generated spectra (left). The spectra are displayed offset. The spectra of 100 mixture samples with noise.

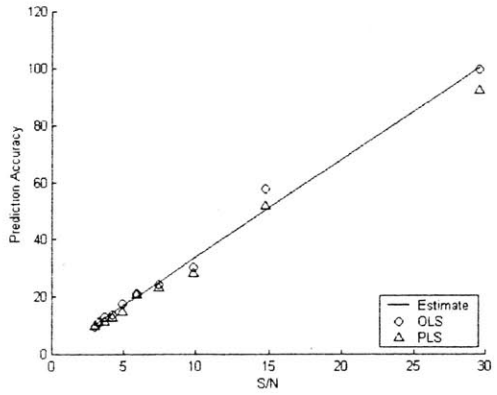

Figure B.2. Prediction accuracy increases as a function of the signal-to-noise-ratio.

However, the prediction accuracy of PLS does not always follow the prediction accuracy equation. The prediction accuracy equation indicates that the prediction error is large when the S/N is low and the overlap factor (OLF) is large. Thus, when the

amplitude of noise increases, the prediction error will increase accordingly, according to the prediction accuracy equation. On the other hand, the prediction error of PLS does not follow the prediction accuracy equation when the error becomes large. Due to the nature of PLS, its maximum prediction error is the standard deviation of the concentrations, which is the prediction error when all predictions are the average concentrations. Since the prediction accuracy is inversely proportional to the prediction error, the minimum prediction accuracy can be also calculated. In one set of simulation data, the mean concentration of analytes was 5 mM and the standard deviation of analyte concentrations was 1 mM. Thus, the prediction error of PLS could not exceed 1 mM, and the prediction accuracy could not be less than 5. This explains why the prediction accuracy deviates from the prediction accuracy equation sometimes (Figure B.3). The prediction accuracy plateaus around 5. As the prediction accuracy was always higher than 5 in Figure B.1., we did not observe such deviations.

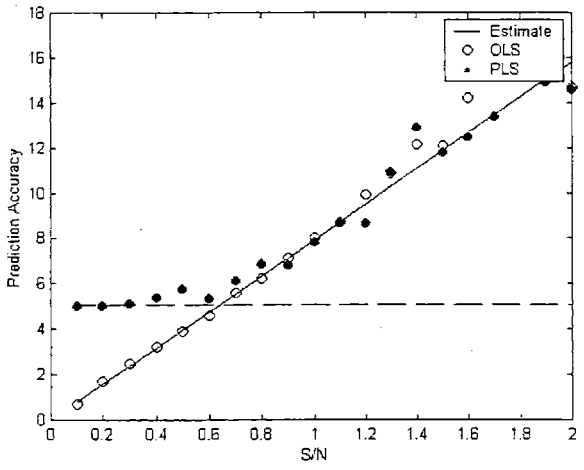

Figure B.3. Prediction accuracy of partial least squares does not always follow the prediction accuracy equation when the signal-to-noise-ratio is low. The dashed line is drawn at 5.3 prediction accuracy.

The analysis of this simulation result demonstrates that the prediction accuracy equation is accurate for OLS analysis. For PLS analysis, the prediction accuracy equation can be fairly accurate, but it would be prudent to compare the calculated prediction accuracy with the standard deviation of concentrations.

The following is the Matlab code to test the prediction accuracy equation.

```
C=random('norm',10,2,100,10);
P2=zeros(10,100,10);
for i=1:10, % i is related to the degree of overlap
  fprintf(1, 'processing %d out of 10\n', i);
  P=zeros(10,100);
  for j=1:10, % j is the index of components
    n=unidrnd(i); % n is the number of peaks
    for k=1:n, % k is the index of peaks
      m=unidrnd(100);
      w=normrnd(4,1);
      P(j,:)=P(j,:)+normpdf([1:100],m,w);
    end;
  end;
  S=C*P;
        P2(:,:,i)=P;
  B=P'*inv(P*P');
        OLF=sqrt(diag(inv(P*P')));

  for j=1:10; % j is related to the degree of noise
    S2=S+random('norm',0,j/50,100,100); % noise = j/50
    for k=1:10, % k is the index of components
      R=candp_quiet(S2,C(:,k),10,1,100,1,[],[1:100]);
      for l=1:11,
        tmp(l)=rmsep(C(:,k),R(:,l));
      end;
      error_pls(i,j,k)=min(tmp);
      error_ols(i,j,k)=rmsep(C(:,k),S2*B(:,k));
      error_est(i,j,k)=j/50*OLF(k);
    end;
  end;
end;
```

Table B.1. Prediction accuracy calculated from the prediction accuracy estimation equation, ordinary least squares analysis, and partial least squares analysis.

S/N	OLF	EST	OLS	PLS	S/N	OLF	EST	OLS	PLS	S/N	OLF	EST	OLS	PLS
0.87	0.72	0.63	0.62	0.96	3.42	0.29	0.99	0.96	1.66	7.24	0.63	4.53	4.47	4.30
0.97	0.72	0.70	0.76	1.04	3.42	0.26	0.88	0.84	1.87	7.24	0.41	2.99	3.02	2.90
1.08	0.43	0.46	0.48	1.25	3.43	0.68	2.34	2.17	2.13	7.27	0.65	4.69	4.97	4.55
1.09	0.72	0.79	0.81	1.02	3.45	0.51	1.77	1.73	1.85	7.29	0.42	3.03	3.51	3.30
1.11	0.46	0.51	0.54	1.13	3.46	0.48	1.66	1.92	1.59	7.30	0.58	4.27	3.89	4.01
1.12	0.19	0.21	0.22	1.05	3.47	0.61	2.12	2.21	2.15	7.31	0.79	5.75	5.99	5.82
1.14	0.70	0.80	0.75	1.14	3.48	0.41	1.41	1.39	1.49	7.31	0.32	2.34	2.27	2.52
1.14	0.46	0.53	0.54	1.15	3.48	0.60	2.09	1.95	1.86	7.34	0.29	2.13	2.22	2.28
1.14	0.52	0.60	0.54	1.01	3.49	0.32	1.11	1.15	1.50	7.35	0.53	3.90	3.92	3.33
1.17	0.35	0.41	0.37	1.00	3.49	0.29	1.00	0.88	1.44	7.37	0.34	2.47	2.39	2.56
1.17	0.94	1.09	1.24	1.13	3.50	0.56	1.95	1.98	1.86	7.37	0.47	3.45	3.26	4.37
1.20	0.43	0.51	0.53	1.03	3.50	0.45	1.57	1.52	1.91	7.38	0.43	3.17	3.09	3.07
1.21	0.63	0.76	0.73	1.11	3.50	0.66	2.32	2.23	2.69	7.40	0.66	4.89	4.73	4.50
1.21	0.63	0.76	0.94	1.22	3.51	0.40	1.41	1.45	2.01	7.40	0.59	4.37	4.50	4.08
1.23	0.58	0.71	0.77	1.04	3.54	0.54	1.92	1.88	2.41	7.43	0.43	3.17	2.66	3.02
1.23	0.46	0.56	0.62	1.22	3.56	0.59	2.09	2.17	2.16	7.46	0.41	3.02	3.05	2.84
1.24	0.19	0.24	0.26	1.05	3.57	0.60	2.13	2.13	2.03	7.46	0.39	2.91	3.10	2.71
1.24	0.72	0.90	0.87	1.20	3.59	0.43	1.54	1.61	2.03	7.48	0.59	4.39	3.83	3.63
1.26	0.70	0.88	0.78	1.11	3.60	0.57	2.06	1.80	2.00	7.48	0.57	4.28	4.57	4.78
1.26	0.34	0.43	0.44	1.08	3.62	0.63	2.26	2.15	2.39	7.57	0.65	4.94	4.88	4.61
1.27	0.46	0.59	0.58	1.10	3.62	0.41	1.49	1.35	1.50	7.61	0.32	2.42	2.26	2.20
1.27	0.52	0.66	0.64	1.01	3.63	0.31	1.12	1.15	1.21	7.65	0.34	2.62	2.56	2.81
1.28	1.00	1.28	1.16	1.37	3.63	0.65	2.35	2.58	2.21	7.67	0.45	3.43	3.45	3.24
1.29	0.91	1.18	1.23	1.24	3.63	0.45	1.62	1.69	2.22	7.68	0.48	3.71	3.86	3.63
1.30	0.35	0.46	0.43	1.01	3.64	0.42	1.52	1.66	1.90	7.69	0.41	3.16	3.31	3.78
1.30	0.94	1.22	1.15	1.19	3.64	0.98	3.58	3.39	3.53	7.69	0.12	0.92	1.11	1.28
1.30	0.82	1.07	1.19	1.68	3.65	0.32	1.17	1.26	1.52	7.74	0.51	3.92	4.30	4.14
1.31	0.59	0.78	0.85	1.37	3.68	0.53	1.95	1.96	2.08	7.77	0.65	5.05	5.13	4.70
1.32	0.95	1.26	1.32	1.21	3.69	0.72	2.67	2.95	3.00	7.78	0.23	1.77	1.77	2.34
1.32	0.87	1.16	1.10	1.25	3.70	0.66	2.45	2.56	2.17	7.80	0.19	1.51	1.52	1.99
1.33	0.44	0.58	0.60	1.08	3.70	0.59	2.18	2.35	2.21	7.81	0.51	3.96	4.03	3.73
1.34	0.63	0.85	0.97	1.22	3.70	0.46	1.69	1.78	2.01	7.83	0.33	2.55	2.57	2.68
1.34	0.63	0.85	0.80	1.12	3.70	0.32	1.18	1.29	1.57	7.90	0.20	1.61	1.62	1.99
1.35	0.43	0.58	0.61	1.11	3.72	0.43	1.58	1.64	1.98	7.94	0.56	4.48	4.05	3.74
1.36	0.29	0.39	0.40	1.28	3.72	0.23	0.87	1.08	1.42	7.96	0.62	4.93	4.53	4.23
1.36	0.58	0.79	0.81	1.24	3.73	0.19	0.71	0.66	1.12	7.98	0.26	2.04	1.91	2.35
1.39	0.46	0.63	0.65	1.18	3.74	0.59	2.20	2.29	2.08	8.01	0.31	2.49	2.54	2.40
1.39	0.41	0.56	0.57	1.00	3.74	0.57	2.14	2.04	2.34	8.02	0.48	3.86	3.87	4.11
1.40	0.32	0.45	0.45	1.11	3.74	0.56	2.09	2.00	2.24	8.03	0.60	4.80	4.40	4.28
1.40	0.29	0.40	0.44	1.06	3.75	0.48	1.78	1.69	1.93	8.10	0.61	4.96	5.41	4.91
1.40	0.19	0.27	0.26	1.05	3.78	0.53	1.99	1.92	2.17	8.10	0.34	2.72	2.72	2.36
1.41	0.34	0.48	0.46	1.17	3.78	0.65	2.47	2.50	2.04	8.11	0.62	5.03	4.57	4.42
1.42	0.70	1.00	1.12	1.22	3.78	0.24	0.92	0.92	1.87	8.13	0.60	4.88	4.76	4.20
1.42	1.00	1.42	1.38	1.44	3.79	0.70	2.65	2.65	2.46	8.13	0.43	3.52	4.00	4.56
1.43	0.46	0.66	0.66	1.13	3.79	0.52	1.95	2.00	2.47	8.17	0.31	2.51	2.39	2.30
1.43	0.52	0.75	0.72	1.06	3.80	0.32	1.21	1.07	1.33	8.18	0.66	5.40	5.01	4.55
1.43	0.91	1.31	1.33	1.20	3.81	0.46	1.77	1.86	1.83	8.18	0.45	3.65	3.42	3.34

S/N	OLF	EST	OLS	PLS	S/N	OLF	EST	OLS	PLS	S/N	OLF	EST	OLS	PLS
1.44	0.57	0.82	0.77	1.20	3.81	0.52	1.99	1.90	1.89	8.20	0.98	8.06	7.89	7.70
1.44	0.82	1.19	1.15	1.49	3.82	0.34	1.31	1.33	1.76	8.22	0.58	4.81	5.13	4.79
1.45	0.41	0.60	0.64	1.03	3.84	0.48	1.86	1.81	2.07	8.25	0.20	1.63	1.62	1.75
1.45	0.72	1.05	1.04	1.19	3.84	0.41	1.58	1.57	2.22	8.30	0.47	3.89	3.97	4.35
1.46	0.35	0.52	0.55	1.08	3.85	0.12	0.46	0.41	1.04	8.34	0.40	3.31	3.43	3.04
1.46	0.59	0.86	0.82	1.26	3.87	0.51	1.96	1.77	1.87	8.37	0.23	1.96	1.77	1.95
1.46	0.94	1.37	1.45	1.60	3.87	0.42	1.65	1.55	1.99	8.40	0.38	3.15	3.41	2.91
1.47	0.95	1.40	1.31	1.38	3.88	0.59	2.27	2.35	2.75	8.41	0.39	3.28	3.71	3.45
1.47	0.53	0.78	0.76	1.33	3.88	0.61	2.36	2.39	2.67	8.43	0.64	5.39	5.70	5.06
1.47	0.87	1.28	1.37	1.40	3.89	0.35	1.38	1.47	1.83	8.44	0.11	0.94	1.11	1.27
1.47	0.44	0.65	0.70	1.17	3.90	0.94	3.65	3.43	3.08	8.45	0.48	4.01	4.17	3.54
1.51	0.29	0.44	0.53	1.11	3.90	0.19	0.75	0.80	1.60	8.51	0.53	4.48	4.85	4.79
1.51	0.63	0.96	1.10	1.30	3.93	0.68	2.67	2.57	2.62	8.51	0.24	2.07	1.83	2.29
1.51	0.63	0.96	0.93	1.32	3.94	0.51	2.02	2.11	2.36	8.52	0.52	4.39	4.09	3.53
1.53	0.58	0.88	0.89	1.03	3.94	0.65	2.58	2.54	2.39	8.54	0.29	2.49	2.83	2.64
1.54	0.12	0.18	0.18	1.03	3.95	0.48	1.90	1.87	1.79	8.57	0.29	2.48	2.70	2.68
1.54	0.43	0.66	0.65	1.36	3.95	0.20	0.81	0.87	1.69	8.71	0.72	6.29	7.29	6.85
1.55	0.41	0.63	0.56	1.01	3.96	0.59	2.32	2.51	2.22	8.73	0.56	4.87	5.62	5.03
1.55	0.51	0.78	0.80	1.10	3.97	0.56	2.24	2.22	2.01	8.77	0.79	6.90	7.71	7.03
1.55	0.32	0.50	0.51	1.20	3.99	0.26	1.02	0.93	2.11	8.84	0.34	2.97	2.78	2.84
1.55	0.29	0.44	0.46	1.18	4.00	0.56	2.23	2.06	2.14	8.85	0.43	3.80	3.68	3.62
1.58	0.34	0.54	0.61	1.17	4.00	0.31	1.25	1.06	1.53	8.86	0.54	4.81	5.54	5.18
1.59	0.46	0.72	0.63	1.35	4.00	0.45	1.80	1.75	2.16	8.89	0.23	2.02	1.97	2.84
1.60	0.19	0.31	0.29	1.16	4.01	0.40	1.61	1.70	1.81	8.90	0.59	5.23	5.45	4.89
1.60	0.57	0.92	0.90	1.30	4.02	0.60	2.40	2.39	2.30	8.95	0.41	3.63	3.57	3.39
1.60	1.00	1.60	1.66	1.70	4.02	0.63	2.55	2.61	2.40	8.96	0.39	3.49	3.04	2.83
1.61	0.41	0.66	0.64	1.17	4.03	0.63	2.55	2.21	2.25	9.02	0.48	4.34	5.00	4.56
1.61	0.91	1.47	1.57	1.53	4.04	0.65	2.61	2.58	2.64	9.06	0.61	5.50	4.82	4.90
1.62	0.62	1.01	0.92	1.37	4.05	0.42	1.68	1.54	1.97	9.09	0.65	5.87	5.84	5.49
1.62	0.70	1.14	1.15	1.40	4.05	0.61	2.48	2.49	2.74	9.11	0.42	3.79	3.69	3.62
1.62	0.82	1.34	1.32	1.61	4.05	0.34	1.36	1.24	1.60	9.13	0.33	2.97	3.14	2.90
1.63	0.46	0.76	0.75	1.27	4.05	0.62	2.52	2.18	2.23	9.16	0.68	6.24	6.22	5.78
1.63	0.52	0.85	0.77	1.08	4.07	0.60	2.44	2.42	2.11	9.19	0.51	4.71	4.89	5.07
1.63	0.53	0.87	0.96	1.45	4.09	0.58	2.36	2.54	2.27	9.20	0.45	4.11	4.13	4.46
1.64	0.59	0.97	1.09	1.53	4.09	0.31	1.26	1.29	1.62	9.21	0.48	4.43	4.47	3.88
1.65	0.20	0.33	0.34	1.20	4.09	0.66	2.70	2.69	2.77	9.22	0.72	6.66	6.37	6.23
1.65	0.95	1.57	1.62	1.58	4.09	0.45	1.82	1.81	2.73	9.26	0.32	2.96	3.31	3.13
1.65	0.87	1.45	1.47	1.42	4.10	0.98	4.03	4.48	4.17	9.29	0.62	5.76	6.16	5.69
1.66	0.44	0.73	0.72	1.29	4.12	0.20	0.81	0.86	1.37	9.29	0.43	3.96	3.71	3.46
1.67	0.35	0.59	0.52	1.28	4.13	0.43	1.76	1.80	2.19	9.29	0.43	4.02	3.68	4.48
1.67	0.94	1.56	1.84	1.73	4.15	0.59	2.44	2.57	2.41	9.32	0.65	6.05	6.94	5.85
1.68	0.38	0.63	0.71	1.18	4.17	0.40	1.65	1.62	1.79	9.33	0.56	5.20	4.64	4.40
1.69	0.11	0.19	0.17	1.02	4.18	0.32	1.33	1.28	1.75	9.34	0.59	5.49	6.06	5.63
1.69	0.29	0.49	0.45	1.23	4.19	0.23	0.98	1.18	1.37	9.34	0.45	4.19	4.36	4.43
1.71	0.29	0.50	0.58	1.30	4.20	0.38	1.58	1.51	1.52	9.37	0.40	3.76	3.65	4.04
1.71	0.12	0.21	0.20	1.03	4.20	0.39	1.64	1.83	1.86	9.37	0.51	4.76	4.44	4.23
1.72	0.51	0.87	0.99	1.18	4.22	0.34	1.45	1.41	1.60	9.39	0.58	5.49	6.01	5.41
1.72	0.63	1.09	1.01	1.06	4.22	0.64	2.69	2.62	2.70	9.48	0.47	4.44	4.10	4.68
1.73	0.63	1.09	1.11	1.23	4.22	0.11	0.47	0.43	1.09	9.68	0.42	4.11	3.64	3.72
1.74	0.41	0.70	0.69	1.07	4.22	0.48	2.01	2.20	2.34	9.69	0.59	5.68	5.39	5.21

S/N	OLF	EST	OLS	PLS	S/N	OLF	EST	OLS	PLS	S/N	OLF	EST	OLS	PLS
1.74	0.72	1.26	1.15	1.31	4.23	0.66	2.80	2.68	2.49	9.75	0.32	3.11	2.77	2.40
1.74	0.32	0.56	0.64	1.23	4.25	0.53	2.24	2.39	2.51	9.85	0.65	6.44	6.72	5.95
1.75	0.29	0.50	0.57	1.05	4.26	0.24	1.04	1.07	1.79	9.86	0.66	6.52	5.90	5.50
1.75	0.58	1.01	0.94	1.11	4.26	0.52	2.20	2.14	2.05	9.97	0.57	5.71	6.44	5.88
1.77	0.54	0.96	1.08	1.45	4.27	1.00	4.27	4.59	4.55	10.01	0.31	3.12	3.18	3.17
1.80	0.43	0.77	0.79	1.22	4.27	0.29	1.24	1.30	1.68	10.09	0.65	6.59	6.29	6.00
1.80	0.57	1.03	1.04	1.52	4.27	0.57	2.45	2.26	2.14	10.13	0.34	3.40	3.43	3.33
1.80	0.62	1.12	1.16	1.63	4.30	0.91	3.92	4.36	4.41	10.20	0.34	3.49	3.41	3.18
1.81	0.34	0.62	0.64	1.31	4.32	0.65	2.82	2.81	2.46	10.24	0.48	4.95	5.68	5.31
1.81	0.41	0.75	0.71	1.19	4.33	0.82	3.56	4.00	3.84	10.28	0.29	2.98	3.13	2.90
1.83	1.00	1.83	1.81	1.60	4.34	0.63	2.72	2.87	2.70	10.31	0.48	4.97	5.34	5.04
1.83	0.20	0.36	0.39	1.28	4.36	0.72	3.15	3.13	2.95	10.37	0.23	2.36	2.23	2.96
1.84	0.53	0.98	1.05	1.58	4.36	0.56	2.44	2.44	2.31	10.43	0.40	4.13	4.44	4.37
1.84	0.72	1.33	1.34	1.66	4.37	0.34	1.50	1.41	1.96	10.51	0.39	4.10	4.03	4.02
1.84	0.91	1.68	1.85	1.61	4.37	0.59	2.59	2.47	2.42	10.54	0.64	6.73	6.21	6.29
1.85	0.46	0.85	0.84	1.33	4.38	0.79	3.45	3.58	3.20	10.71	0.60	6.40	6.99	6.13
1.85	0.32	0.59	0.58	1.25	4.39	0.48	2.12	2.20	2.22	10.77	0.43	4.62	4.94	4.19
1.86	0.82	1.53	1.61	1.87	4.40	0.95	4.19	3.98	3.72	10.84	0.43	4.69	4.66	4.65
1.86	0.19	0.36	0.37	1.16	4.41	0.87	3.85	3.89	3.94	10.85	0.63	6.79	7.10	5.81
1.87	0.38	0.70	0.73	1.22	4.42	0.44	1.95	2.15	2.13	10.90	0.31	3.35	3.14	2.94
1.87	0.59	1.11	1.15	1.63	4.42	0.34	1.48	1.51	1.83	10.90	0.45	4.86	5.44	5.10
1.88	0.11	0.21	0.20	1.18	4.43	0.43	1.90	1.82	2.20	10.93	0.98	10.75	9.82	9.58
1.89	0.95	1.79	1.76	1.70	4.43	0.54	2.40	2.22	2.43	10.96	0.33	3.57	3.64	3.44
1.89	0.87	1.65	1.86	1.74	4.44	0.59	2.62	2.78	2.56	10.96	0.58	6.41	6.34	5.69
1.89	0.70	1.33	1.13	1.23	4.45	0.31	1.39	1.56	1.97	10.96	0.79	8.62	8.69	7.88
1.89	0.44	0.84	0.71	1.25	4.45	0.59	2.62	2.59	2.70	11.06	0.34	3.71	4.33	3.80
1.90	0.29	0.55	0.59	1.34	4.48	0.41	1.81	2.02	2.02	11.06	0.47	5.18	5.25	5.26
1.90	0.46	0.88	0.84	1.30	4.48	0.39	1.75	1.82	1.91	11.07	0.43	4.75	4.85	4.55
1.91	0.52	1.00	1.02	1.23	4.50	0.34	1.51	1.50	1.78	11.10	0.59	6.55	6.97	6.36
1.92	0.12	0.23	0.23	1.03	4.52	0.29	1.31	1.30	1.59	11.10	0.46	5.07	5.01	4.94
1.94	0.51	0.98	1.03	1.21	4.53	0.61	2.75	2.89	2.68	11.14	0.62	6.91	6.53	6.22
1.94	0.29	0.56	0.49	1.25	4.54	0.65	2.93	2.87	2.45	11.16	0.23	2.61	2.67	2.31
1.94	0.42	0.82	0.80	1.35	4.55	0.42	1.89	1.91	2.10	11.19	0.19	2.14	1.83	1.76
1.94	0.59	1.14	1.22	1.69	4.57	0.32	1.45	1.58	1.55	11.19	0.41	4.54	4.15	3.92
1.94	0.35	0.69	0.67	1.24	4.58	0.68	3.12	2.76	2.58	11.20	0.39	4.36	4.49	3.60
1.95	0.94	1.82	1.78	1.75	4.59	0.60	2.74	2.69	2.77	11.26	0.48	5.35	5.20	4.62
1.97	0.54	1.07	1.18	1.63	4.59	0.51	2.36	2.39	2.36	11.35	0.53	5.97	6.62	5.69
1.97	0.65	1.29	1.42	1.35	4.60	0.45	2.06	2.15	2.50	11.35	0.24	2.76	2.69	3.28
1.99	0.41	0.81	0.84	1.15	4.61	0.48	2.22	2.25	2.18	11.36	0.70	7.96	8.52	8.20
1.99	0.32	0.64	0.64	1.22	4.61	0.72	3.33	3.06	3.01	11.37	0.52	5.85	5.36	5.08
2.00	0.29	0.57	0.50	1.10	4.61	0.41	1.90	1.85	2.42	11.41	0.32	3.63	3.48	3.45
2.01	0.63	1.27	1.30	1.59	4.63	0.32	1.48	1.56	1.61	11.42	0.46	5.30	6.28	5.66
2.02	0.63	1.27	1.31	1.47	4.63	0.40	1.84	1.98	2.07	11.43	0.52	5.97	6.29	5.53
2.03	0.62	1.26	1.29	1.72	4.64	0.41	1.88	1.82	1.67	11.50	0.45	5.14	5.77	5.58
2.04	0.58	1.18	1.23	1.66	4.64	0.43	1.98	2.03	2.31	11.53	0.41	4.74	5.34	4.96
2.05	0.72	1.48	1.36	1.51	4.65	0.32	1.49	1.44	1.53	11.65	0.65	7.57	7.46	7.03
2.06	0.57	1.18	1.23	1.53	4.66	0.29	1.33	1.44	1.66	11.67	0.35	4.13	4.18	3.61
2.06	0.32	0.66	0.64	1.33	4.66	0.65	3.03	3.31	2.79	11.69	0.94	10.94	11.92	10.87
2.06	0.20	0.41	0.40	1.22	4.67	0.56	2.60	2.71	2.56	11.70	0.19	2.26	2.68	2.72
2.07	0.41	0.85	0.90	1.20	4.67	0.39	1.82	1.81	1.67	11.72	0.51	5.95	6.24	5.18

S/N	OLF	EST	OLS	PLS	S/N	OLF	EST	OLS	PLS	S/N	OLF	EST	OLS	PLS
2.10	0.38	0.79	0.82	1.19	4.67	0.31	1.44	1.76	1.67	11.85	0.20	2.42	2.81	2.82
2.10	0.53	1.12	1.16	1.66	4.67	0.59	2.74	3.06	3.02	11.87	0.59	6.97	7.34	6.73
2.11	0.34	0.72	0.82	1.21	4.67	0.45	2.10	2.01	1.95	11.91	0.56	6.72	7.98	7.48
2.11	0.11	0.23	0.24	1.13	4.67	0.45	2.08	1.90	2.48	11.98	0.26	3.06	2.84	3.19
2.14	1.00	2.13	1.90	1.89	4.68	0.19	0.90	0.83	1.69	12.02	0.48	5.79	5.81	5.85
2.14	0.29	0.62	0.66	1.32	4.68	0.40	1.88	2.00	1.90	12.07	0.63	7.65	8.89	8.44
2.15	0.91	1.96	2.28	2.17	4.68	0.64	2.99	3.21	3.12	12.09	0.63	7.65	7.66	7.49
2.15	0.42	0.91	0.91	1.64	4.69	0.98	4.61	4.53	4.07	12.12	0.65	7.82	7.79	7.29
2.15	0.43	0.92	0.83	1.45	4.69	0.51	2.38	2.33	2.43	12.15	0.42	5.05	5.32	4.93
2.15	0.59	1.26	1.20	1.70	4.74	0.20	0.97	0.86	1.64	12.15	0.61	7.44	7.03	6.61
2.17	0.82	1.78	1.75	1.84	4.76	0.56	2.69	3.18	2.66	12.20	0.60	7.33	7.72	7.23
2.17	0.63	1.36	1.28	1.90	4.78	0.23	1.12	1.10	1.50	12.26	0.58	7.08	7.24	6.74
2.18	0.72	1.57	1.55	1.40	4.79	0.26	1.23	1.25	2.19	12.27	0.66	8.11	8.56	7.78
2.19	0.59	1.30	1.29	1.64	4.80	0.57	2.75	2.46	2.66	12.39	0.43	5.28	5.55	5.60
2.19	0.65	1.43	1.50	1.53	4.83	0.48	2.29	2.25	2.28	12.45	0.23	2.83	3.08	2.95
2.20	0.12	0.26	0.31	1.03	4.83	0.41	1.99	1.85	1.94	12.46	0.59	7.32	7.51	6.58
2.20	0.95	2.09	1.90	1.95	4.84	0.42	2.06	1.84	2.33	12.65	0.34	4.35	4.09	4.09
2.21	0.87	1.93	2.25	2.22	4.85	0.59	2.84	2.88	3.47	12.81	1.00	12.80	12.67	12.13
2.21	0.44	0.97	0.87	1.36	4.86	0.61	2.97	2.99	2.84	12.85	0.29	3.72	3.82	3.34
2.21	0.51	1.12	0.97	1.27	4.86	0.53	2.56	2.65	2.79	12.91	0.91	11.77	12.69	11.70
2.21	0.54	1.20	1.23	1.77	4.86	0.24	1.18	1.25	1.65	13.00	0.82	10.69	10.62	9.03
2.22	0.59	1.31	1.29	1.69	4.87	0.79	3.83	4.37	4.36	13.01	0.43	5.63	6.08	5.62
2.22	0.46	1.01	0.94	1.54	4.87	0.52	2.51	2.54	2.39	13.09	0.56	7.31	7.85	7.11
2.24	0.19	0.43	0.41	1.08	4.87	0.32	1.56	1.65	1.87	13.12	0.59	7.78	9.48	8.35
2.26	0.29	0.66	0.65	1.36	4.88	0.60	2.93	2.93	2.86	13.15	0.58	7.69	8.05	7.64
2.27	0.70	1.59	1.60	1.72	4.90	0.53	2.60	3.03	3.11	13.21	0.95	12.56	11.93	10.84
2.28	0.32	0.73	0.71	1.38	4.91	0.66	3.24	3.18	3.21	13.24	0.87	11.56	11.67	10.08
2.28	0.46	1.06	1.05	1.31	4.91	0.34	1.65	1.65	1.84	13.26	0.44	5.85	6.51	5.93
2.29	0.52	1.19	1.19	1.36	4.92	0.43	2.11	2.11	2.10	13.27	0.47	6.22	6.79	6.15
2.30	0.72	1.67	1.65	1.70	4.93	0.65	3.22	3.17	3.06	13.34	0.31	4.16	4.05	3.43
2.31	0.41	0.95	1.04	1.47	4.93	0.66	3.26	3.41	2.86	13.50	0.34	4.53	4.43	3.93
2.32	0.32	0.74	0.79	1.26	4.97	0.41	2.02	2.20	2.05	13.55	0.29	3.94	3.72	3.21
2.32	0.62	1.44	1.45	1.81	4.98	0.39	1.94	1.87	1.89	13.59	0.61	8.26	8.30	7.55
2.32	0.41	0.94	0.90	1.14	4.99	0.57	2.85	2.99	3.31	13.69	0.33	4.46	4.34	3.88
2.33	0.32	0.74	0.84	1.31	5.00	0.31	1.56	1.83	1.78	13.74	0.68	9.36	9.09	8.56
2.33	0.29	0.67	0.63	1.26	5.04	0.65	3.29	3.16	2.97	13.78	0.51	7.07	7.04	6.38
2.33	0.35	0.83	0.91	1.16	5.06	0.34	1.70	1.82	1.85	13.82	0.48	6.65	6.66	6.07
2.34	0.94	2.19	2.23	2.13	5.09	0.59	2.99	2.61	2.59	13.90	0.40	5.51	5.20	5.21
2.34	0.19	0.45	0.49	1.49	5.10	0.34	1.75	1.65	1.88	13.91	0.41	5.64	5.89	5.60
2.36	0.20	0.47	0.44	1.32	5.11	0.45	2.29	2.39	2.77	13.93	0.62	8.63	9.77	8.58
2.37	0.20	0.48	0.55	1.45	5.12	0.48	2.47	2.60	2.58	13.96	0.32	4.46	4.13	3.91
2.38	0.56	1.34	1.36	1.26	5.13	0.12	0.62	0.77	1.23	13.97	0.29	3.99	4.26	3.64
2.40	0.26	0.61	0.63	1.82	5.14	0.29	1.49	1.51	1.67	14.00	0.56	7.80	7.85	7.32
2.40	0.57	1.37	1.39	1.61	5.16	0.51	2.62	2.60	2.27	14.01	0.39	5.46	5.23	4.48
2.40	0.38	0.90	0.88	1.36	5.18	0.65	3.36	3.27	2.72	14.02	0.45	6.29	5.73	5.06
2.41	0.11	0.27	0.31	1.12	5.19	0.65	3.35	3.57	3.23	14.05	0.40	5.65	5.66	5.26
2.41	0.63	1.51	1.47	1.79	5.21	0.42	2.16	2.11	2.28	14.05	0.64	8.98	8.90	7.68
2.41	0.41	1.00	0.98	1.32	5.21	0.51	2.64	2.37	2.57	14.39	0.57	8.24	8.84	8.54
2.41	0.63	1.53	1.69	1.74	5.21	0.40	2.07	2.20	2.39	14.43	0.48	6.95	6.73	6.26
2.42	0.63	1.53	1.49	1.50	5.24	0.56	2.92	2.82	2.80	14.49	0.41	5.97	6.58	6.37

S/N	OLF	EST	OLS	PLS	S/N	OLF	EST	OLS	PLS	S/N	OLF	EST	OLS	PLS
2.42	0.42	1.03	1.11	1.60	5.25	0.39	2.05	2.20	1.95	14.61	0.79	11.50	10.92	9.49
2.42	0.59	1.42	1.30	1.69	5.27	0.64	3.37	3.42	3.56	14.62	0.32	4.67	5.03	4.87
2.43	0.61	1.49	1.40	1.41	5.31	0.43	2.26	2.24	2.23	14.70	0.53	7.81	7.73	7.07
2.44	0.60	1.47	1.28	1.57	5.34	0.59	3.14	3.33	3.41	14.74	0.34	4.95	5.19	5.37
2.44	0.29	0.71	0.66	1.29	5.36	0.60	3.20	3.17	2.88	14.75	0.43	6.34	6.50	6.31
2.45	0.53	1.30	1.24	1.66	5.39	0.43	2.31	2.47	2.38	14.79	0.66	9.79	11.28	10.10
2.45	0.58	1.42	1.41	1.49	5.40	0.62	3.36	3.37	3.33	14.92	0.41	6.05	5.72	5.10
2.45	0.66	1.62	1.73	2.02	5.43	0.63	3.40	3.34	3.34	14.93	0.39	5.82	6.08	5.80
2.46	0.65	1.61	1.72	1.68	5.44	0.61	3.30	3.15	3.23	14.96	0.57	8.56	9.83	8.44
2.47	0.59	1.46	1.49	1.63	5.45	0.31	1.68	1.87	2.13	15.13	0.65	9.88	8.95	8.53
2.53	0.34	0.87	0.90	1.50	5.45	0.45	2.43	2.34	2.87	15.30	0.34	5.24	4.66	4.68
2.53	0.54	1.37	1.34	1.94	5.47	0.98	5.37	4.90	4.65	15.33	0.45	6.86	7.06	6.37
2.54	0.32	0.81	0.85	1.41	5.48	0.33	1.78	2.00	2.37	15.36	0.48	7.42	6.63	6.57
2.56	1.00	2.56	2.29	2.27	5.48	0.79	4.31	4.91	4.10	15.38	0.12	1.85	1.89	2.06
2.56	0.41	1.05	1.19	1.50	5.50	0.68	3.74	3.67	3.94	15.49	0.51	7.85	8.12	7.20
2.56	0.12	0.31	0.28	1.03	5.50	0.20	1.09	1.06	1.37	15.53	0.65	10.09	10.82	10.20
2.58	0.51	1.31	1.22	1.47	5.51	0.51	2.83	2.67	2.82	15.56	0.23	3.54	3.55	3.69
2.58	0.91	2.35	2.74	2.42	5.53	0.34	1.85	1.67	1.78	15.62	0.51	7.93	9.09	8.61
2.60	0.19	0.50	0.52	1.51	5.53	0.48	2.66	3.13	2.74	16.07	0.60	9.60	10.27	9.59
2.60	0.82	2.14	2.00	2.10	5.53	0.43	2.38	2.57	2.61	16.21	0.62	10.07	11.28	10.48
2.62	0.56	1.46	1.70	1.98	5.55	0.59	3.27	3.34	3.47	16.26	0.43	7.04	6.97	7.39
2.62	0.59	1.56	1.52	1.81	5.55	0.46	2.54	2.84	2.69	16.35	0.31	5.03	4.94	4.48
2.63	0.72	1.90	2.00	1.88	5.57	0.62	3.45	3.54	3.20	16.36	0.45	7.30	8.34	7.38
2.63	0.20	0.54	0.55	1.44	5.58	0.23	1.30	1.29	1.49	16.40	0.98	16.12	16.02	15.02
2.64	0.95	2.51	2.31	2.10	5.59	0.19	1.07	1.12	1.34	16.44	0.58	9.61	10.56	9.91
2.65	0.32	0.84	0.92	1.25	5.60	0.41	2.27	2.25	2.49	16.49	0.20	3.26	3.34	3.49
2.65	0.56	1.49	1.59	1.60	5.60	0.39	2.18	2.08	2.23	16.59	0.47	7.77	9.10	8.38
2.65	0.87	2.31	2.00	1.94	5.60	0.56	3.12	3.20	2.98	16.74	0.23	3.91	4.13	3.77
2.65	0.44	1.17	1.16	1.53	5.60	0.38	2.10	1.93	2.03	16.80	0.38	6.31	6.43	6.20
2.66	0.26	0.68	0.73	1.96	5.61	0.45	2.52	2.73	2.87	16.88	0.11	1.88	1.84	1.99
2.69	0.43	1.16	1.09	1.72	5.62	0.40	2.26	2.07	2.38	16.89	0.48	8.02	7.56	6.86
2.70	0.61	1.65	1.61	1.70	5.63	0.11	0.63	0.72	1.20	17.02	0.53	8.96	8.73	7.99
2.70	0.62	1.68	1.67	2.08	5.63	0.48	2.67	2.57	2.81	17.03	0.24	4.14	3.59	3.77
2.71	0.60	1.63	1.69	1.53	5.67	0.53	2.99	3.10	3.21	17.05	0.52	8.78	8.56	8.04
2.71	0.29	0.79	0.81	1.46	5.68	0.24	1.38	1.40	1.67	17.09	0.29	4.97	5.19	4.93
2.71	0.63	1.70	1.66	1.97	5.68	0.70	3.98	4.08	3.72	17.14	0.29	4.96	4.74	4.46
2.72	0.61	1.65	1.69	1.71	5.68	0.52	2.93	3.11	2.96	17.72	0.54	9.62	10.62	8.74
2.73	0.66	1.80	1.63	1.89	5.70	0.29	1.66	1.74	2.08	17.81	0.59	10.46	10.22	8.81
2.75	0.68	1.87	1.99	2.05	5.71	0.32	1.82	1.73	1.74	18.04	0.48	8.69	8.66	7.73
2.75	0.20	0.54	0.52	1.19	5.71	0.46	2.65	2.43	2.33	18.17	0.65	11.74	11.29	11.19
2.76	0.51	1.41	1.35	1.74	5.71	0.29	1.65	1.72	1.95	18.22	0.42	7.58	6.74	6.86
2.76	0.48	1.33	1.40	1.36	5.72	0.52	2.99	3.22	2.78	18.26	0.33	5.95	6.03	5.87
2.77	0.42	1.18	1.18	1.51	5.72	0.31	1.78	1.62	1.93	18.43	0.72	13.33	13.86	13.02
2.77	0.59	1.62	1.65	1.71	5.75	0.45	2.57	2.59	3.04	18.52	0.32	5.91	5.55	5.25
2.77	0.59	1.64	1.79	2.13	5.76	0.41	2.37	2.58	2.84	18.57	0.62	11.51	11.90	11.32
2.78	0.46	1.27	1.30	1.66	5.79	0.34	1.94	1.94	2.14	18.58	0.43	7.92	7.75	7.25
2.78	0.41	1.13	1.18	1.49	5.83	0.65	3.78	3.97	3.49	18.69	0.59	10.98	13.12	11.53
2.79	0.32	0.89	0.99	1.51	5.83	0.35	2.07	1.88	1.83	19.37	0.42	8.23	9.39	9.09
2.79	0.29	0.80	0.78	1.29	5.84	0.94	5.47	5.19	4.71	19.39	0.59	11.35	11.44	10.27
2.80	0.19	0.54	0.51	1.11	5.85	0.32	1.87	2.12	2.05	19.70	0.65	12.89	13.41	13.03

S/N	OLF	EST	OLS	PLS	S/N	OLF	EST	OLS	PLS	S/N	OLF	EST	OLS	PLS
2.80	0.56	1.56	1.45	1.58	5.85	0.19	1.13	1.09	1.93	20.01	0.31	6.23	6.04	5.30
2.80	0.38	1.05	1.02	1.28	5.86	0.51	2.97	3.14	3.08	20.25	0.34	6.80	6.36	5.68
2.80	0.45	1.26	1.30	1.61	5.91	0.54	3.21	3.73	3.18	20.75	0.23	4.72	4.57	4.59
2.81	0.40	1.13	1.24	1.54	5.92	0.66	3.91	4.12	4.02	20.85	0.40	8.27	8.95	8.67
2.81	0.11	0.31	0.27	1.12	5.93	0.20	1.21	1.14	2.06	21.02	0.39	8.20	8.39	7.95
2.81	0.65	1.84	1.88	1.88	5.94	0.59	3.49	4.42	3.80	21.08	0.64	13.47	17.26	15.96
2.84	0.70	1.99	1.93	1.95	5.95	0.56	3.36	3.13	2.64	21.69	0.43	9.39	8.70	7.78
2.85	0.29	0.83	0.81	1.50	5.96	0.40	2.36	2.43	2.54	21.71	0.63	13.58	13.78	12.49
2.85	0.32	0.91	0.95	1.38	5.98	0.57	3.42	3.41	3.38	21.91	0.58	12.82	11.45	10.41
2.85	0.46	1.33	1.14	1.54	5.99	0.26	1.53	1.59	2.29	21.92	0.79	17.25	17.53	16.33
2.86	0.52	1.49	1.49	1.49	6.01	0.39	2.34	2.50	2.40	22.11	0.34	7.42	8.04	7.78
2.88	0.57	1.65	1.41	1.77	6.02	0.64	3.85	4.06	4.20	22.12	0.47	10.36	9.00	8.77
2.88	0.41	1.19	1.34	1.78	6.04	0.63	3.82	4.06	3.34	22.13	0.43	9.51	10.18	9.31
2.90	0.41	1.19	1.14	1.56	6.05	0.63	3.82	3.65	3.76	22.20	0.59	13.10	12.12	11.25
2.90	0.72	2.10	2.44	2.43	6.05	0.65	3.95	3.96	3.98	22.38	0.41	9.07	9.83	9.16
2.91	0.56	1.62	1.75	1.75	6.06	0.65	3.91	4.42	3.97	22.39	0.39	8.73	8.35	7.63
2.92	0.35	1.03	0.95	1.39	6.07	0.42	2.53	2.43	2.62	22.83	0.32	7.27	8.41	7.98
2.92	0.94	2.74	2.45	2.55	6.08	0.61	3.72	3.70	3.80	23.00	0.45	10.29	9.70	9.15
2.92	0.32	0.93	0.98	1.34	6.09	0.33	1.98	2.21	2.34	23.06	0.41	9.49	9.58	9.22
2.92	0.19	0.56	0.57	1.57	6.10	0.60	3.66	3.47	3.05	23.30	0.65	15.14	15.99	15.03
2.94	0.53	1.56	1.64	1.59	6.12	0.34	2.10	2.18	2.16	23.39	0.19	4.52	4.51	3.82
2.95	0.54	1.60	1.52	1.93	6.13	0.58	3.54	3.73	3.32	23.44	0.51	11.89	11.21	10.19
2.96	0.66	1.96	1.84	1.90	6.13	0.66	4.05	3.69	3.68	23.71	0.20	4.83	5.01	4.25
2.96	0.20	0.60	0.60	1.73	6.14	0.48	2.97	2.78	2.85	23.82	0.56	13.44	13.52	12.50
2.98	0.56	1.68	1.51	1.63	6.14	0.72	4.44	4.69	4.14	23.95	0.26	6.13	6.30	6.53
2.99	0.57	1.71	1.68	2.01	6.17	0.32	1.97	1.97	2.02	24.05	0.48	11.59	11.55	10.03
2.99	0.26	0.77	0.73	1.99	6.19	0.62	3.84	3.24	3.23	24.30	0.61	14.87	15.59	14.42
3.02	0.63	1.91	1.75	1.73	6.19	0.43	2.64	2.59	2.71	24.39	0.60	14.65	13.85	12.14
3.02	0.61	1.83	1.94	2.08	6.22	0.23	1.42	1.49	2.30	24.53	0.66	16.21	16.14	15.24
3.02	0.63	1.91	1.86	1.84	6.23	0.59	3.66	3.59	3.44	25.71	0.29	7.44	7.53	7.20
3.03	0.65	1.98	1.82	1.95	6.26	0.79	4.93	4.80	4.29	26.18	0.56	14.61	15.86	14.78
3.04	0.61	1.86	2.07	2.14	6.32	0.34	2.12	2.03	2.32	27.18	0.61	16.51	17.75	16.20
3.05	0.60	1.83	1.83	2.04	6.32	0.43	2.72	2.58	2.46	27.39	0.33	8.92	9.81	9.25
3.05	0.68	2.08	2.16	2.23	6.32	0.34	2.17	2.32	2.12	27.48	0.68	18.71	19.12	18.20
3.06	0.34	1.05	1.02	1.77	6.39	0.41	2.59	3.01	2.87	27.57	0.51	14.13	15.65	14.64
3.06	0.51	1.57	1.49	1.66	6.40	0.39	2.49	2.35	2.27	27.64	0.48	13.30	14.44	13.30
3.06	0.58	1.77	1.68	1.69	6.41	1.00	6.40	6.76	6.08	27.86	0.62	17.27	15.89	14.65
3.07	0.66	2.03	2.09	2.29	6.43	0.29	1.86	2.13	2.29	27.99	0.56	15.61	17.17	16.23
3.07	0.48	1.48	1.70	1.66	6.43	0.60	3.84	4.09	3.65	28.03	0.45	12.58	13.72	12.49
3.07	0.48	1.48	1.46	1.65	6.45	0.91	5.89	6.11	5.74	28.10	0.40	11.29	11.91	10.71
3.07	0.72	2.22	2.25	2.01	6.46	0.42	2.74	2.51	3.11	29.24	0.32	9.34	10.88	9.60
3.08	0.12	0.37	0.35	1.03	6.46	0.59	3.78	3.60	3.90	29.58	0.66	19.57	19.43	17.96
3.09	0.32	0.99	0.90	1.39	6.50	0.82	5.34	5.14	4.66	29.92	0.57	17.12	19.03	17.79
3.10	0.51	1.57	1.68	1.49	6.51	0.43	2.82	2.77	3.48	30.26	0.65	19.76	17.85	16.90
3.10	0.63	1.94	1.69	1.90	6.54	0.31	2.01	2.03	1.84	30.60	0.34	10.48	12.21	11.40
3.11	0.56	1.73	1.84	1.73	6.54	0.45	2.92	2.72	3.21	30.72	0.48	14.85	16.64	17.03
3.11	0.45	1.40	1.54	1.89	6.55	0.56	3.65	3.83	3.36	31.12	0.23	7.08	6.57	6.63
3.12	0.40	1.25	1.26	1.52	6.56	0.98	6.45	7.16	6.65	32.13	0.60	19.21	19.61	18.29
3.16	0.34	1.09	1.13	1.45	6.56	0.59	3.89	3.50	3.53	32.53	0.43	14.08	13.14	14.14
3.17	0.59	1.87	1.71	1.84	6.57	0.65	4.30	4.58	4.56	32.70	0.31	10.05	12.16	11.12

S/N	OLF	EST	OLS	PLS	S/N	OLF	EST	OLS	PLS	S/N	OLF	EST	OLS	PLS
3.20	1.00	3.20	3.33	3.10	6.57	0.45	2.94	2.89	3.15	32.71	0.45	14.59	14.51	13.08
3.21	0.60	1.92	1.86	2.16	6.57	0.58	3.85	3.72	3.72	32.80	0.98	32.25	33.24	31.80
3.23	0.91	2.94	2.74	2.49	6.60	0.95	6.28	5.49	5.17	32.87	0.58	19.23	20.65	18.76
3.23	0.42	1.37	1.35	1.86	6.62	0.87	5.78	5.86	4.91	33.19	0.47	15.54	15.51	15.63
3.23	0.59	1.89	1.79	2.37	6.63	0.44	2.92	3.19	3.01	33.49	0.23	7.82	9.68	8.74
3.24	0.62	2.01	1.90	2.16	6.64	0.47	3.11	2.85	3.53	33.78	0.48	16.05	17.98	16.97
3.25	0.32	1.04	1.21	1.38	6.66	0.65	4.32	4.25	3.85	34.04	0.53	17.91	21.76	21.39
3.25	0.82	2.67	2.84	2.60	6.67	0.31	2.08	1.92	2.21	34.05	0.24	8.29	9.36	8.95
3.26	0.32	1.04	1.04	1.37	6.70	0.51	3.40	3.02	3.07	34.10	0.52	17.56	18.51	17.62
3.27	0.31	1.01	1.13	1.26	6.70	0.23	1.56	1.73	1.69	35.61	0.59	20.92	20.85	20.26
3.27	0.45	1.46	1.45	2.17	6.75	0.34	2.27	2.25	2.28	36.07	0.48	17.38	16.59	14.42
3.27	0.56	1.83	1.76	1.79	6.76	0.48	3.21	3.10	2.64	36.35	0.65	23.47	24.65	22.83
3.28	0.98	3.22	3.28	2.87	6.78	0.29	1.97	2.37	2.36	36.44	0.42	15.15	17.99	16.88
3.28	0.59	1.95	1.75	2.16	6.80	0.61	4.13	3.24	3.48	37.16	0.43	15.84	16.86	15.27
3.28	0.65	2.15	2.33	2.18	6.81	0.53	3.58	3.48	3.25	37.38	0.59	21.95	21.75	20.32
3.29	0.66	2.17	2.11	2.20	6.81	0.24	1.66	1.44	1.95	40.03	0.31	12.47	13.00	11.88
3.29	0.41	1.36	1.35	1.93	6.82	0.52	3.51	3.52	3.39	40.51	0.34	13.59	15.11	13.94
3.30	0.20	0.65	0.65	1.29	6.85	0.33	2.23	2.34	2.65	41.70	0.40	16.53	14.20	13.69
3.30	0.95	3.14	3.22	3.21	6.87	0.68	4.68	4.67	4.25	42.04	0.39	16.39	17.62	16.34
3.31	0.87	2.89	3.06	3.22	6.89	0.51	3.53	3.73	3.82	42.16	0.64	26.93	28.78	26.03
3.31	0.44	1.46	1.38	1.57	6.91	0.48	3.33	3.34	2.97	43.83	0.79	34.50	32.41	30.11
3.32	0.57	1.90	2.06	1.77	6.92	0.23	1.57	1.55	2.64	44.22	0.34	14.84	14.23	14.23
3.34	0.19	0.65	0.59	1.46	6.95	0.40	2.76	3.09	2.93	44.26	0.43	19.01	17.73	15.69
3.35	0.23	0.78	0.78	1.37	6.95	0.41	2.82	2.64	2.37	44.76	0.41	18.14	18.87	16.81
3.36	0.38	1.26	1.33	1.52	6.96	0.62	4.32	4.55	4.05	44.78	0.39	17.45	16.77	15.49
3.36	0.65	2.20	2.11	2.09	6.98	0.32	2.23	2.27	2.04	46.00	0.45	20.57	20.22	18.51
3.38	0.11	0.38	0.34	1.08	6.98	0.29	2.00	1.96	2.07	46.60	0.65	30.27	29.25	27.64
3.38	0.48	1.60	1.68	1.75	7.00	0.56	3.90	3.92	3.48	46.87	0.51	23.78	22.53	20.72
3.39	0.20	0.69	0.63	1.51	7.01	0.39	2.73	3.08	2.96	51.41	0.29	14.89	16.21	14.02
3.39	0.29	0.99	0.87	1.43	7.01	0.45	3.15	3.00	3.08	54.78	0.33	17.84	19.27	16.92
3.40	0.61	2.06	2.13	2.34	7.03	0.40	2.82	2.30	2.54	55.71	0.62	34.54	34.25	32.26
3.40	0.34	1.16	1.09	1.75	7.03	0.64	4.49	4.33	4.62	62.24	0.23	14.16	16.60	15.74
3.40	0.56	1.92	2.00	1.91	7.12	0.59	4.18	4.92	4.27	65.06	0.43	28.16	28.39	26.75
3.40	0.53	1.79	1.62	2.12	7.20	0.57	4.12	3.72	3.71	65.74	0.58	38.45	38.33	35.67
3.41	0.24	0.83	0.80	1.46	7.21	0.48	3.48	3.45	3.71	66.37	0.47	31.08	30.58	30.45
3.41	0.52	1.76	1.71	1.60	7.23	0.43	3.13	3.15	4.54	72.15	0.48	34.76	38.09	36.89